October 1982

LIDS-TH-1251

Research Supported By:

National Science Foundation
Grant ECS-8012668

Reconstruction From Projections Based On Detection and Estimation of Objects

David John Rossi

October, 1982 LIDS-TH-1251

RECONSTRUCTION FROM PROJECTIONS BASED ON DETECTION AND ESTIMATION OF OBJECTS

by

David John Rossi

This report is based on the unaltered thesis of David John Rossi, submitted in partial fulfillment of the requirements for the degree of Doctor of Philosophy at the Massachusetts Institute of Technology in August, 1982. The research was conducted at the M.I.T. Laboratory for Information and Decision Systems, with support from the National Science Foundation under Grant ECS-8012668.

Laboratory for Information and Decision Systems
Massachusetts Institute of Technology
Cambridge, MA 02139

RECONSTRUCTION FROM PROJECTIONS

BASED ON

DETECTION AND ESTIMATION OF OBJECTS

by

DAVID JOHN ROSSI

Submitted to the Department of Electrical Engineering and Computer Science on 30 August 1982 in partial fulfillment of the requirements for the Degree of Doctor of Philosophy

ABSTRACT

The problem of reconstructing a multi-dimensional field from noisy projection measurements is approached using an object-based stochastic formulation. Objects within the cross-section are characterized (e.g. location, shape, size) using a finite-dimensional set of parameters, which are estimated directly from the projection measurements (rather than post-processing a reconstructed image) using nonlinear maximum likelihood (ML) parameter estimation. Object localization involves obtaining the log likelihood function by a convolution back-projection operation, using a convolving kernel that is specified in the optimal solution to the location estimation problem. The performance of object location and geometry estimation is investigated, as is the robustness to a variety of modeling errors. Several computer simulations are included which illustrate the difference between the image representation of a localization log likelihood function and a reconstructed image obtained using conventional reconstruction techniques.

Thesis Supervisor: Alan S. Willsky

Title: Associate Professor of Electrical Engineering

ACKNOWLEDGEMENTS

I would like to express my sincere gratitude to Prof. Alan Willsky, for initially suggesting the idea of detection in tomography and for providing many valuable insights and suggestions, and most of all for his enthusiasm in this research. I would also like to thank Drs. Robert Tenney and Berthold Horn for their many discussions, suggestions and encouragement.

I am indebted to Prof. Derek Rowell for making available his Ramtek image display unit for the simulations in this thesis, to Ms. Virginia Klema for the very generous use of her word processing equipment, and to the Department of Aeronautics and Astronautics for the use of their computer system in developing the simulations and figures in this thesis. I would like to thank Dwayne Mann for his enthusiastic computer programming assistance, and Mr. Arthur Giordani for his help in preparing many of the figures.

I would especially like to thank my wife, Holly Stack, for her unbounded patience, encouragement and sense of humor; her support during this project was truly invaluable.

This research was conducted at the Laboratory for Information and Decision Systems, M.I.T. with support from the National Science Foundation under Grant No. ECS-8012668.

TABLE OF CONTENTS

LIST OF FIGURES

LIST OF TABLES

CHAPTER 1

1.0 INTRODUCTION

The problem of reconstructing an n-dimensional function from its (n-1)-dimensional projections is a well-studied problem arising (typically in the context of cross-sectional imaging of a medium) in a diversity of disciplines including radio astronomy, medicine, nondestructive testing, geophysics, and oceanography (Gordon, 1974; Klyuev et al., 1980; Munk and Wunsch, 1979; Bracewell, 1956). To make the problem of reconstruction precise, let $f(x)$ represent the value of the n-dimensional function at the point $x \in \mathbb{R}^n$. Suppose that the values of line integrals

$$g(L_i) = \int_{L_i} f(x)\,ds \tag{1.1}$$

are available along a (possibly infinite) number of lines L_i in $\mathbb{R}^n$. The reconstruction problem, stated generally, is then: given a set of projection line integrals $g(L_i)$, determine an estimate $\hat{f}(x)$ of the function $f(x)$. Mathematically, the problem of reconstruction is an inverse problem since the measurements are obtained by a projection operation which must be inverted during reconstruction.

In practice the reconstruction problem arises in conjunction with the internal imaging of a three-dimensional medium. There are two ways to perform three-dimensional imaging, either approximately by successive cross-sectional imaging on closely spaced parallel planes, or by direct three-dimensional reconstruction (Kowalski, 1979). In reconstructing the interior of a medium, the function f(x) corresponds to some spatially distributed parameter of the medium, for example density or refractive index. In the reconstruction problem, it is not possible to observe f(x) directly; instead, it must be inferred from external projection measurements. These measurements can be modeled under ideal circumstances as integrals of f(x) along straight lines, obtained by measuring energy exiting the medium along the various lines. To simplify the discussion we consider throughout this thesis only the planar imaging problem, in which case f(x) is two-dimensional and the lines L_i lie in the imaged plane. At the expense of more complicated notation, the ideas to follow may be extended easily to the three-dimensional reconstruction problem.

The source of the energy, typically electromagnetic or acoustic, is either external to or internal to the medium, giving rise to active and passive reconstruction problems, respectively. In the active problem, an

external source transmits energy through the medium; in the passive problem, the energy (e.g. thermal energy) is spatially distributed within the medium.

In most applications, the ultimate objective of the reconstruction process is to extract specific information about the cross-section. Typically, projection measurements are used to obtain an approximate reconstruction which is subsequently processed (perhaps by humans) to remove artifacts and extract the information of interest. For example, considerable work has been done in the area of automated and semi-automated analysis of medical CAT scan reconstructions, for the purpose of detecting and delineating the boundaries of organs, bones, lesions and fluid spaces (Belanger et al., 1979; Selfridge and Prewitt, 1981). This post-processing step is effectively the utilization of a priori information about the medium being imaged to enhance and extract information about the cross-section.

In this thesis, we describe a method for utilizing a priori information directly in the inverse problem. Direct utilization of a priori information offers the potential for significant improvements in applications where (1) attempts to perform direct inversion result in severely degraded reconstructions and (2) the ultimate goal of the processing is to obtain a few specific pieces

of information concerning the cross-section. To develop a framework for utilizing a priori information in the processing of projection measurements, we focus in this thesis on a relatively simple version of the problem in two dimensions; at the end of this thesis we discuss ways in which the framework we have developed can be (and is being) extended.

1.1 APPLICATIONS OF RECONSTRUCTION

Currently, the application of reconstruction techniques spans a wide range of disciplines, including:

- medicine -- the attenuation of X-radiation transmitted through biological tissue is related to the line integral of the tissue X-ray absorption density; this reconstruction procedure is currently employed in Computerized Axial Tomography (CAT) scanners (Cormack, 1963, 1964; Hounsfield, 1973). Time-of-flight measurements with ultrasound provide path integrals of the tissue refractive index; this procedure is particularly well suited to mammography (Glover and Sharp, 1977; Greenleaf et al., 1978). In passive imaging, radionuclides are injected into the body and selectively accumulate in certain organs and neoplasms; emitted positrons or gamma rays are used to reconstruct the spatial distributions of both the

energy source and the tissue absorption density (Gullberg and Budinger, 1981; Brownell et al., 1977).

- electron microscopy -- the micrograph, or electron microscope image, represents a projection of the spatial density distribution of a specimen onto a plane; reconstruction techniques are used to determine the three-dimensional density distribution from multiple micrographs (DeRosier and Moore, 1970).

- geophysics -- cross-borehole electromagnetic probing provides measurements related to the path integral of either attenuation or propogation velocity; these techniques are potentially useful in energy resource mapping and in detecting hazardous regions ahead of a mine face (Radcliff and Balanis, 1979; Dines and Lytle, 1979)

- oceanography -- the velocity of acoustic energy in water is temperature dependent, and time-of-flight measurements may be used to obtain underwater temperature profiles (Munk and Wunsch, 1979; Spindel, 1979). Such techniques are potentially useful in mapping and tracking large thermal water masses, e.g. Gulf Stream cold-core rings (Backus et al., 1981). In the passive problem, acoustic sources such as ships or submarines in the ocean generate an acoustic field whose line integrals may be observed

via multiple acoustic arrays (Rockmore, 1980).

- radio astronomy -- in this passive problem, a radio telescope aimed at the sky measures the integral of radio brightness temperature along strips; these integral data are used in radio contour mapping (Bracewell, 1956).

- refractive index mapping -- holographic interferometry is used to measure the optical pathlength (related to the line integral of the refractive index) through a transparent medium (Sweeney and Vest, 1973).

- meteorology -- in the passive reconstruction problem, satellite-borne microwave spectrometers measure the line integral of thermal radiation at different levels in the atmosphere, which may be used to determine atmospheric temperature profiles (Ledsham and Staelin, 1978).

- target association -- objects in a medium, such as airplanes in flight, reflect energy from active sources such as radar or laser. If the measurements (reflected energy vs. bearing angle) are modeled as integrals of a reflectance field, reconstruction of this reflectance field may be used to infer the location of objects (Denton et al., 1978).

- nondestructive testing -- reconstruction techniques have been employed in nondestructive detection of cracks in nuclear reactor cooling water piping (Morris et al., 1979), for nondestructive mapping of refractive index profiles and cross-sectional geometry of optical-fiber preforms (Chu and Saekeang, 1979), and for nondestructive mapping of residual stress fields inside metals (Hildebrand and Harrington, 1981).

- target shape estimation -- using spatially distributed radar, the cross-sectional area of a convex object in three-space may be measured at a number of view angles; these measurements may be used to reconstruct the three-dimensional shape of the object (Das and Boerner, 1978; Rockmore et al., 1979).

In addition to these applications, many others are presently under investigation. In particular, the well-publicized success of reconstruction from projections in CAT scanners, as well as in radio astronomy and electron microscopy, has recently led to suggestions to apply reconstruction techniques to a wide variety of novel and technologically demanding tasks, e.g. real-time monitoring of very high production rate manufacturing processes and "stop action" internal imaging of very rapidly changing media (McKinnon and Bates, 1981; Klyuev

et al., 1980)

1.2 OBJECT-BASED RECONSTRUCTION

The major emphasis of research and applications in the area of reconstruction from projections has been on producing accurate, high resolution cross-sectional images from projection measurements. In practice, these images are either observed directly and interpreted by a human inspector or are post-processed by a computer (see for example Belanger et al., 1979) to extract important information about the cross-section. It is well known (Mersereau and Oppenheim, 1974), however, that creating an accurate, high resolution image of a cross-section by reconstruction demands a large number of high signal-to-noise ratio (SNR) line integral measurements.

One way to see this is to note that in any application, what is obtained is a digital reconstruction of $f(x)$. Consequently, what is really being reconstructed is a set of parameters $\underline{f}$ which form a digital representation of $f(x)$. For example, if $f(x)$ is represented using a standard pixel image representation, the vector $\underline{f}$ consists of the complete set of pixel intensities. Similarly, in practice only a finite set of line integral measurements can be taken. If $\underline{g}$ denotes this vector, then one can use (1.1) to arrive at a set of

linear equations of the form

$$\underline{g} = H\underline{f} \tag{1.2}$$

where H is a matrix (see Gordon (1974) for a more detailed discussion). In this setting the problem is to invert the relationship (1.2) to reconstruct $\underline{f}$.

Although this representation for the problem is attractive because the measurement model is linear, in many applications the dimension of $\underline{f}$ is very large (e.g. for a 256x256 pixel image representation, the dimension of $\underline{f}$ exceeds 65,000). Often, considerably fewer than 65,000 line integral measurements are available, which results in an underdetermined set of equations having a nonunique solution, i.e. reconstructions that contain "suspect features" (Gordon, 1973). In such cases, a variety of ad hoc techniques are generally used to post-process the reconstructed image in order to remove suspect features; this step essentially involves incorporating a priori information about the cross-section <u>after</u> the reconstruction is performed. Furthermore, as discussed by Vest and Radulovic (1977), if measurements can not be made at angles that span the full range from 0 to π, the matrix H is poorly conditioned, resulting in reconstruction artifacts.

In their work, Mersereau and Oppenheim (1974) show that one of the most popular reconstruction algorithms (the convolution back-projection algorithm, to be discussed in Section 1.3) is very sensitive to both a reduced number of measurement line integrals and to errors or noise in the line integral data. In particular, the sensitivity of this algorithm to noise manifests itself in the reconstructed image as a mottled or speckled appearance. This effect arises primarily because high frequency components in the projection data are emphasized during the reconstruction by a convolution operation that accentuates high frequencies in the projections. This leads to computational errors in the reconstruction similar to those introduced by numerical differentiation.

Although accurate, high-resolution image reconstruction requires a large number of high SNR projection measurements taken over a wide angle, in many cases, particularly with many of the recently suggested applications, this may be neither practical nor possible. This may be due to

- economic constraints that limit the total number of measurement transducers -- e.g. oceanographic transducers are sophisticated, low power units that are costly to build, place and maintain.

- time constraints that limit measurement quality -- e.g. limited measurement time interval in "stop action" imaging of very rapid events, or in nondestructive testing of high production rate processes such as steel manufacturing (McKinnon and Bates, 1981; Klyuev et al., 1980)

- safety and operating constraints that limit the measurement quality -- e.g. high temperature and/or caustic operating environments in certain process monitoring applications may limit sensor accuracy and signal to noise performance.

- geometrical or physical constraints that limit the view angle -- e.g. in ultrasonic imaging, where bony structures limit view angles, or in nondestructive testing of certain large objects.

- inaccuracy of the measurement model -- the line integral measurement model in (1.1) is an idealization that does not incorporate, for example, the effects of refraction, diffraction, scattering, and polychromaticity (Dennis et al., 1977).

As mentioned, when one or more of these factors limits the overall view angle or the total number or SNR of line integral measurements, the reconstructed image is known to have artifacts, poor resolution and/or high noise levels.

This in turn may make image evaluation by a human inspector or a computer inconsistent and unreliable.

In a variety of applications, however, the final goal of the signal processing is often far more modest than obtaining a high resolution image of the cross-section. For example, in nondestructive testing, the final goal of processing projection data may be simply to determine whether a certain type of flaw or defect is present within the cross-section of a homogeneous material. Or, the goal may be to determine where within the cross-section some sort of object (such as an oceanographic cold-core ring (Backus et al., 1981)) is located.

In such cases, because the signal processing goals are relatively modest, high quality imaging may not be necessary for the ultimate goal of detecting and characterizing objects within the cross-section from projection data. Acceptable object detection and characterization may be possible instead by replacing the current combination of image reconstruction followed by visual or automated interpretation with more sophisticated decision-directed signal processing algorithms.

If the goal of the processing of projection measurements is simply to detect and characterize one or more objects in a cross-section, conventional image reconstruction methods may also not represent the best

approach because they do not take full advantage of the available a priori information about the properties and structure of the cross-section. Typically, nominal properties of the cross-section are well defined a priori either statistically or deterministically. For example, a flaw- or defect-free homogeneous material may correspond to a constant internal density, or a cross-section of the ocean that does not contain a cold-core ring may have a particular well-known statistical characterization. In many cases, it is the goal of the signal processing to seek well-defined deviations from this nominal state, where the variety and complexity of possible deviations is limited and known a priori. Said another way, the number of degrees of freedom associated with the problem of detecting, locating, and characterizing objects such as flaws in materials or cold-core rings in the ocean are far fewer than the number of degrees of freedom in the full image reconstruction problem.

Since in these types of problems a great deal is often known a priori about the cross-section, and the signal processing goals are relatively specific, one approach toward designing signal processing algorithms for these problems is to utilize all available information concerning the cross-section under examination and to optimize performance in terms of the reliability and accuracy of object detection and estimation, not in terms

of image quality.

For example, if it is believed that there exists an object within the cross-section, characterized a priori by a set of random or unknown parameters (corresponding to, say, location, shape, orientation, and/or density), then one may utilize all available a priori information about the cross-section and apply hypothesis testing and parameter estimation algorithms to detect and characterize the object. As will be shown, parameters characterizing the object location, size and geometry enter the problem in a nonlinear way, resulting in a nonlinear estimation problem of relatively small dimensionality. This is in contrast to full image reconstruction, in which a linear estimation problem of high dimensionality is solved.

A number of authors have considered specific problems of detecting constant density regions in a field and estimating the boundaries of these regions (e.g. Hanson, 1978; Belanger et al., 1979; Selfridge and Prewitt, 1981). All of these approaches have involved post-processing a reconstructed function using automated or semi-automated image boundary detection and estimation techniques. Unfortunately, such an approach does not reduce the number of degrees of freedom associated with the preliminary image reconstruction, and consequently, a large quantity of high SNR projection data is still

required. Also, even if the line integral measurement noise is white, the reconstructed image noise is nonwhite (Riederer et al., 1978), which complicates the post-processing operation. In this thesis, we similarly consider detecting objects contained within a cross-section and estimating their boundaries. Unlike previous work in this area, however, we propose to perform statistical detection and estimation using the noisy projection data directly, rather than post-processing a reconstructed image.

We develop a framework for incorporating a priori information into the reconstruction problem by employing an object-based, probabilistic description for the cross-sectional density function f(x). In practice, varying amounts of a priori information may be available regarding objects in a cross-section -- for example one may or may not have information concerning their number, location, shape, orientation, and density. In the framework to be presented, available detailed a priori information is incorporated into the object detection and estimation problem only when it is known where to focus it. For example, as a first step in an object localization and estimation problem, one may conceive of the direct use of noisy projection measurements to solve a coarse detection problem such as determining whether or not an object having simple boundary shape is present at a

hypothesized location; similarly, one may attempt to determine the object location as well. Here only a modest amount of a priori information is used, namely, the possible presence of an object, and a very rough estimate of its shape. If an object is determined to be present at some location, then finer details of a priori information (e.g. information about probable object shapes) may be incorporated into the subsequent problem of estimating the object boundary geometry.

We investigate the estimation performance, that is, the accuracy with which an object's location and geometry can be estimated, as a function of the measurement noise level and scanning geometry. The estimation accuracy, besides depending on the measurement noise and geometry, clearly also depends upon the accuracy of the mathematical model for the cross-section, the object, and the measurements. Consequently, we investigate not only the performance, but also the robustness or sensitivity of the estimation procedure to various types of modeling errors, e.g. attempting to estimate an object's geometry when its location is imprecisely known, or when there exists an unmodeled object in the cross-section.

Robustness analysis plays an important role in assessing the utility of object-based reconstruction in any particular application, since the incorporation of a

priori information directly into the inverse problem implies that the resulting procedure will be reliable only if it is not sensitive to inaccuracies in the details of this a priori information. The approach to be pursued in this thesis allows systematic investigation into the robustness issue, because the models to be employed clearly display the assumptions which have been made, and which are therefore the focus of attention in the robustness analysis.

In this thesis, rather than developing a general algorithm for processing projection data from arbitrarily complex cross-sections, we instead investigate several specific problems in order (1) to develop some insight into the structure of the resulting detection and parameter estimation computations, and (2) to assess the performance of the parameter estimator and the dependence of the performance on measurement geometry. These investigations establish a framework for more detailed studies and indicate how one can incorporate information and critically evaluate performance in a systematic manner.

We focus our attention on two particular problems, namely analyzing noisy projection data (1) to locate a single object whose shape, orientation and density are known, but which lies at some unknown point in the

cross-section, and (2) to estimate the geometry (e.g. size, shape and orientation) of a single object whose location is known. The object location and geometry will be estimated, for the case of projection measurements corrupted by additive white Gaussian noise, by maximum likelihood (ML) parameter estimation. In this case, the computation associated with the log likelihood function evaluations can be shown to have the same form as the computation associated with one solution to the full image reconstruction problem, namely the convolution back-projection inversion formula (to be discussed in Section 1.3). This fact will allow existing theoretical results about the convolution back-projection inversion to be employed in assessing the performance of the ML parameter estimation problem.

It should be noted that a closely related problem is object detection, that is, using projection measurements to determine whether or not an object is present in the cross-section. It is well known (Van Trees, 1968) that the types of calculations and analyses that must be performed in solving a detection problem are essentially identical to the calculations involved in the solution to the estimation problem. In this analysis, we do not carry out these detection calculations explicitly, as we have found that the estimation problem has provided an excellent focus for obtaining insight into object-based

reconstruction. Once ML estimates are available for the object parameters, hypothesis testing (to detect the presence of an object) may be performed by using, for example, the generalized likelihood ratio test (GLRT) (Van Trees, 1968; Willsky and Jones, 1976).

1.3 THE RECONSTRUCTION PROBLEM

1.3.1 Geometry

As a prelude to our development, we review the reconstruction problem in two dimensions. Let (x_1,x_2) be the Cartesian coordinates of a point x in the cross-section being imaged, and let f(x) represent the value of the spatially-distributed property of the medium being imaged (hereafter referred to as the density) at the point x. A line lying in the cross-section, as shown by $l(t,\theta)$ in Figure 1.1, is specified by the polar coordinates (t,θ) of its normal vector, and is given by

$$l(t,\theta) \triangleq \{x: x_1\cos\theta + x_2\sin\theta = t\} = \{x: \underline{x}'\underline{\theta} = t\} \qquad (1.3)$$

$$(t,\theta)\in\mathcal{Y} \triangleq \{(t,\theta): \; -\infty < t < \infty, \; 0 \le \theta < \pi\}$$

Here, $\underline{x}' = (x_1 \; x_2)$, and $\underline{\theta} = (\cos\theta \; \sin\theta)'$ is a unit vector at angle θ to the x_1 axis.

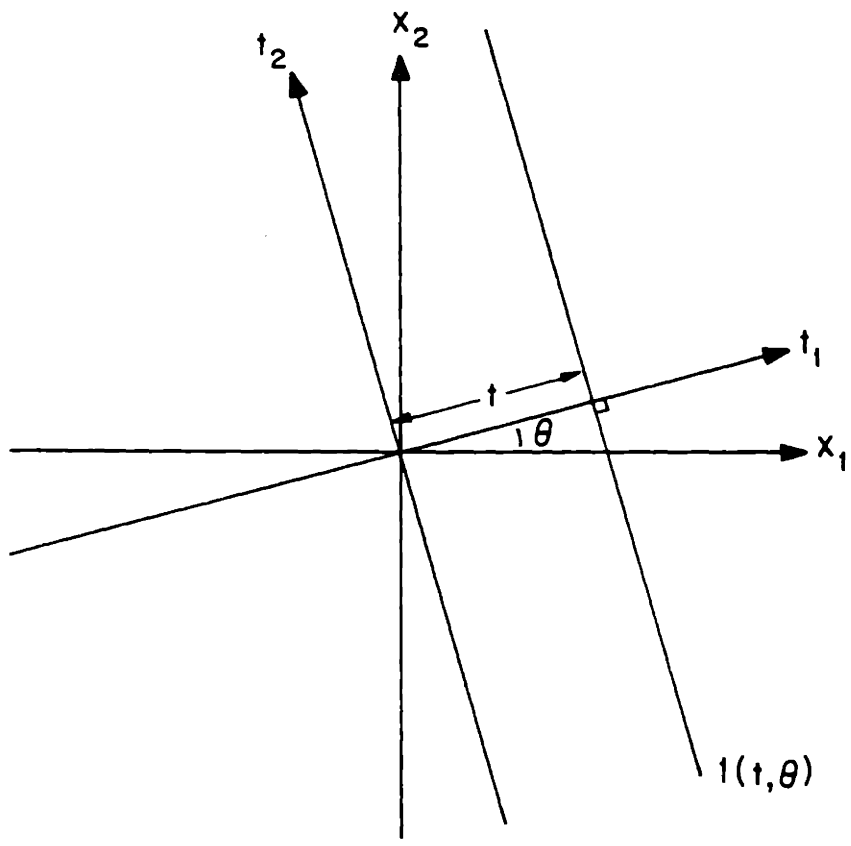

Figure 1.1 Measurement geometry.

1.3.2 The Radon transform

In reconstruction problems, $f(x)$ can be observed only via its projections in various directions, and the reconstruction problem corresponds to estimating the value of the function $f(x)$, for $x \in \mathbb{R}^2$, from projection measurements. The projection of $f(x)$ at any angle θ is a one-dimensional (1D) function denoted by $g(t,\theta)$ as shown in Figure 1.2. For any value of projection angle θ, the

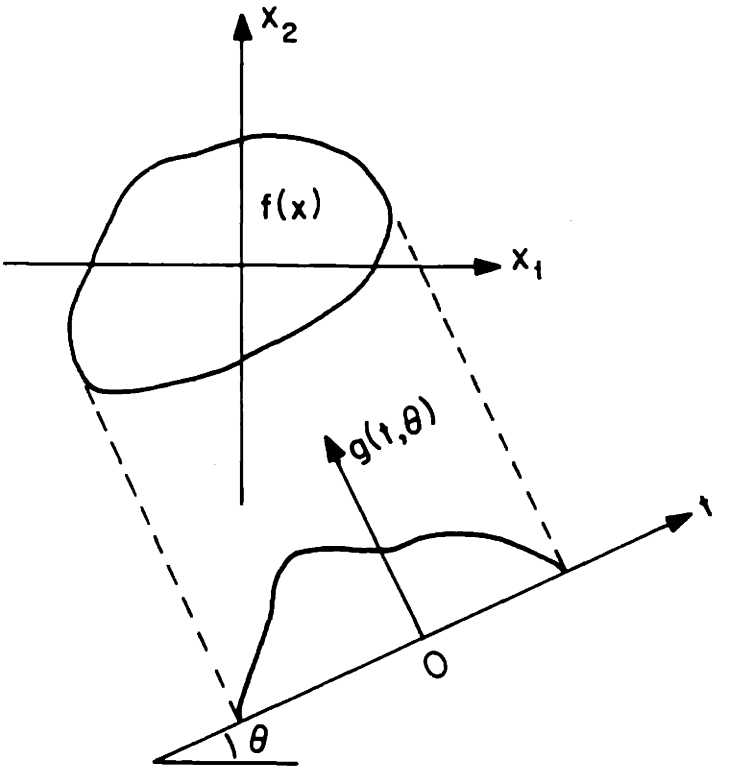

Figure 1.2 Projection at angle Θ.

projection $g(t,\theta)$, evaluated at the point t, is the line integral of the function $f(x)$ along the line $l(t,\theta)$

$$g(t,\theta) = \int_{-\infty}^{\infty}\int_{-\infty}^{\infty} f(x)\,\delta(t - x_1\cos\theta - x_2\sin\theta)\,dx_1dx_2$$

$$= \int_{\underline{x}'\underline{\theta}=t} f(x)\,ds \qquad (1.4)$$

where $\delta(t)$ is the Dirac delta function.

In terms of the notation introduced thus far, reconstruction of $f(x)$ from its projections $g(t,\theta)$ corresponds mathematically to inverting the integral equation in (1.4). One form of the solution to this problem, known as the inverse Radon transform, was derived by the Austrian mathematician Johann Radon (1917). Radon's derivation assumes the availability of noise-free projections at all possible projection angles, in which case $g(t,\theta)$ can be thought of as a function $g:\mathcal{Y}\rightarrow\mathbb{R}$, where $\mathcal{Y}$ is defined in (1.3). In his honor, the linear operator in (1.4) mapping the function $f:\mathbb{R}^2\rightarrow R$ into the function $g:\mathcal{Y}\rightarrow R$ is referred to as the Radon transformation, and g is called the Radon transform of f, denoted here as $\mathcal{R}f$.

Although by assumption g is defined for $(t,\theta)\in\mathcal{Y}$, it may be evaluated at any (t,θ) value, and because of the nonunique parameterization of a line

$$l(t,\theta) = l(-t,\theta + (2k+1)\pi) = l(t,\theta + 2k\pi) \quad k=0,\pm1,... \tag{1.5}$$

$g(t,\theta)$ satisfies the following periodicity properties

$$\begin{aligned} &1)\ g(t,\theta) = g(-t,\theta + (2k+1)\pi) && k=0,\pm1,... \\ &2)\ g(t,\theta) = g(t,\theta + 2k\pi) && k=0,\pm1,... \end{aligned} \tag{1.6}$$

By the Radon transformation in (1.4), a density function has two mathematical representations, $f(x)$ and $g(t,\theta)$, which are referred to as its object space and Radon space representations, respectively. The Radon transform maps the object space representation f into the Radon space representation g, and the various exact and approximate reconstruction techniques are concerned with mapping the Radon space representation into the object space representation.

Certain geometric relationships exist between points (x_1,x_2) in object space and points (t,θ) in Radon space under the Radon transformation and will be important in the discussions to follow. According to (1.3), these four variables are related by

$$t = x_1 \mathrm{Cos}\theta + x_2 \mathrm{Sin}\theta = \underline{x}'\underline{\theta} \qquad (1.7)$$

First, consider a given point (t,θ) in Radon space. The corresponding set of points x in object space satisfying (1.7) is the line $l(t,\theta)$ in (1.3). Next, consider a point $x = (x_1,x_2)$ in object space. The corresponding set of points in Radon space satisfying (1.7), that is the set of (t,θ) so that $l(t,\theta)$ passes through the point x, specify a cosinusoid $\mathscr{C}(x)$, see Figure 1.3, with magnitude $\|x\|$ and phase equal to the $\arctan(x_2/x_1)$; i.e.

$$\mathscr{C}(x) \triangleq \{(t,\theta): \; x_1 \mathrm{Cos}\theta + x_2 \mathrm{Sin}\theta = t\} \qquad (1.8)$$

In summary, then, lines in object space correspond to points in Radon space; points in object space correspond to cosinusoids in Radon space.

1.3.3 Reconstruction techniques

Mathematically, determining f(x) from the integrals in (1.4) is a problem of inverting an integral equation, and currently, there exist a number of exact and approximate reconstruction techniques. As already mentioned, the mathematical problem of reconstructing a 2D function f(x) given a set of noise-free integrals taken at all possible orientations was first solved by J. Radon (1917); his solution is referred to as the inverse Radon transform.

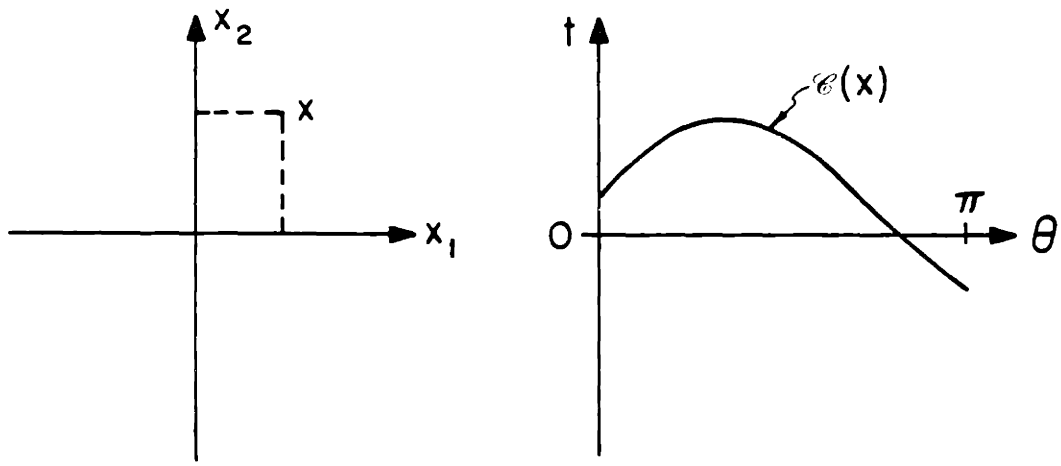

Figure 1.3 Point x in object space and corresponding cosinusoid in Radon space.

More recently, Fourier transform analysis has led to the projection-slice theorem (Mersereau and Oppenheim, 1974) which states that $g(t,\theta)$, the projection at angle θ, has a 1D Fourier transform that is a central slice at angle θ of the 2D Fourier transform of $f(x)$. The projection-slice theorem can be used for reconstruction by first taking 1D Fourier transforms of the projection measurements to estimate slices of the 2D Fourier transform of $f(x)$, and then inverting the Fourier transform to obtain an estimate of $f(x)$ (Stark et al., 1981). The projection-slice theorem also suggests a representation for $f(x)$ directly in terms of its Radon transform $g(t,\theta)$, that is, it provides a second

representation for the solution to the integral equation in (1.4); this solution is referred to as the convolution back-projection (CBP) inversion formula.

The CBP inversion formula is an exact solution to the reconstruction problem that, like the inverse Radon transform, assumes the availability of noise-free projection measurements at all projection angles. The CBP inversion formula is given by

$$\hat{f}(x) = \int_0^{\pi} \int_{-\infty}^{\infty} g(t,\theta) v(t - \underline{x}'\underline{\theta}) dt d\theta \triangleq \int_0^{\pi} q(\underline{x}'\underline{\theta},\theta) d\theta \quad (1.9)$$

where for perfect reconstruction from noise-free projections, the Fourier transform of the convolving kernel $v(t)$ is $V(\omega) = |\omega|$. Details regarding the derivation of (1.9) may be found in Bracewell (1956), Shepp and Logan (1974), Snyder and Cox (1977) and Rowland (1979).

The name convolution back-projection arises because (1.9) corresponds to a two-step procedure for reconstructing $f(x)$:

1. Along lines of constant θ in Radon space, filter or convolve $g(t,\theta)$, the projection at angle θ, with the function $v(-t)$ to form a convolved projection $q(t,\theta)$. The set of all convolved projections $q(t,\theta)$, $\theta \in [0,\pi)$

may be thought of as the function $q:\mathcal{Y}\rightarrow R$ in Radon space.

2. The so-called back-projection operation is performed in the integration with respect to θ in (1.9); back-projection corresponds to 1D integration with respect to the differential $d\theta$ of the 2D function $q:\mathcal{Y}\rightarrow R$, over the set of (t,θ) points in $\mathcal{Y}$ sweeping out the cosinusoidal path $\mathscr{C}(x)$ in Radon space (see (1.8)).

This procedure may be interpreted in object space as well:

1. At each projection angle θ, filter the 1D projection $g(t,\theta)$ with $v(-t)$ to obtain $q(t,\theta)$.

2. For each θ value, "back-project" $q(t,\theta)$ into a 2D function that is constant along points x on parallel lines $l(t,\theta)$.

3. Integrate the back-projections from step (2) over $\theta\in[0,\pi)$.

Steps (2) and (3) of this procedure to reconstruct f at a point x are known as the back-projection operation, which is shown schematically in Figure 1.4. The back-projection operator maps the function $q:\mathcal{Y}\rightarrow R$ into the 2D function $\hat{f}:\mathbb{R}^2\rightarrow R$; $\hat{f}$ is called the back-projection of q and is denoted $\mathscr{B}q$. For a more complete discussion of the

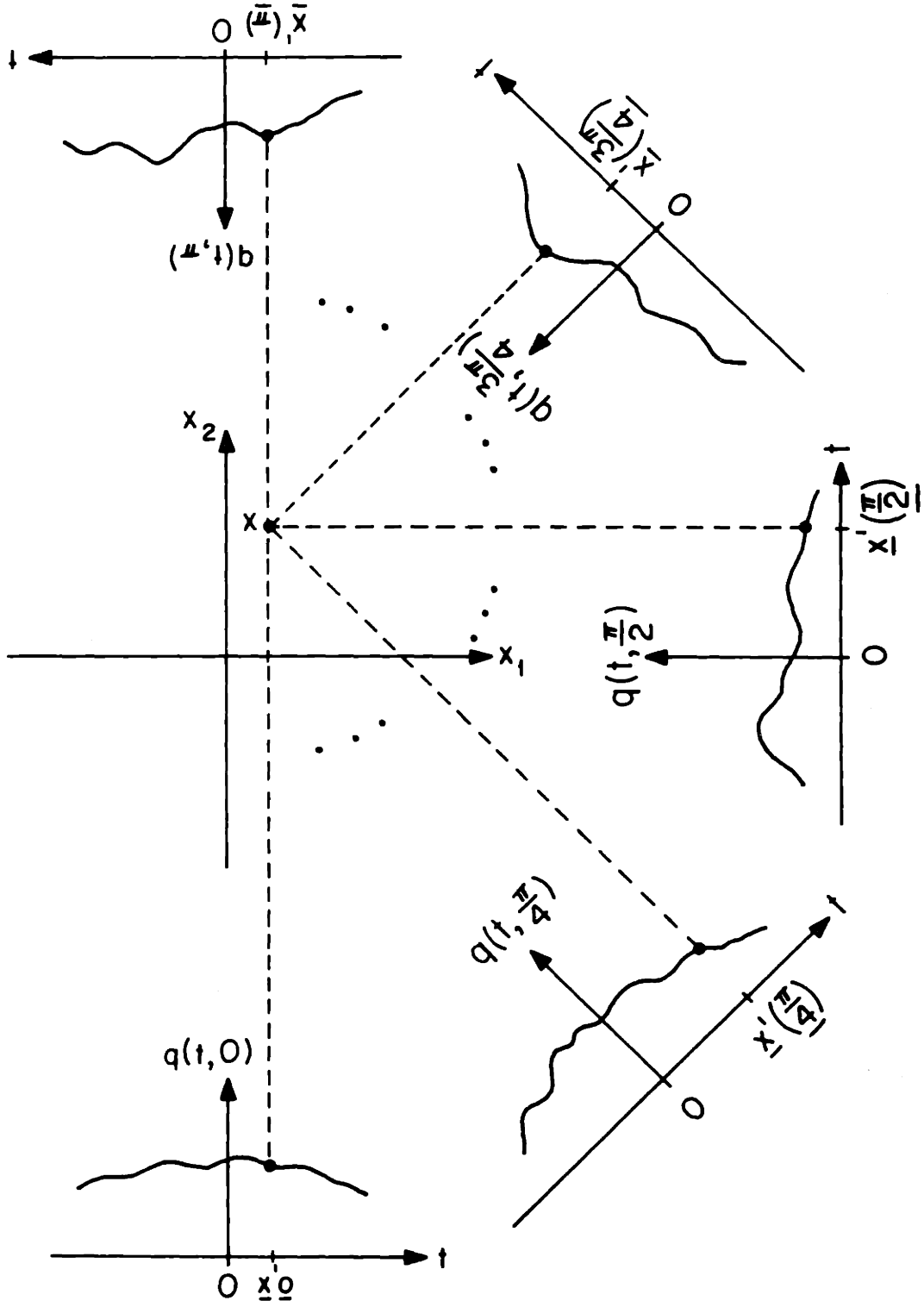

Figure 1.4 Back-projection operation.

back-projection operator, see for example Rowland (1979).

The exact reconstruction formulas in the inverse Radon transform and the CBP in (1.9) require an infinite amount of noise-free projection data. To apply these formulas in practice when only a finite number of projection measurements are available, the integrals associated with these formulas are approximated by finite sums. Lakshminarayanan (1975) and Horn (1978) have investigated the discrete approximation to the inverse Radon transform, and Bracewell (1956) and others have investigated the discrete approximation to the CBP solution in (1.9).

Although these discrete approximations can be determined for any given set of measurement lines (i.e. any given set of measurement sample points in Radon space), in the case where the line integrals in every projection are taken along parallel lines (the so-called parallel-ray measurement geometry), these analyses provide the same approximate reconstruction formula, known as the convolution back-projection reconstruction algorithm:

$$\hat{f}(x) = \frac{\Delta}{2N_\theta} \sum_{k=0}^{N_\theta-1} \sum_{j=-N_t}^{N_t} g(j\Delta,\theta_k)\ \tilde{v}(j\Delta - \theta_k) \qquad (1.10)$$

where

$$\theta_k = k\pi / N_\theta$$

Δ = sample spacing in t

N_θ = number of angular increments

N_t = largest integer $\leq T/\Delta - 1/2$

$\tilde{v}$ = an appropriately selected weighting function

The weighting function $\tilde{v}$ is the function v(t) in (1.9) with Fourier transform $V(\omega) = |\omega|$, multiplied by some window function that attenuates high frequencies. Various tradeoffs between reconstructed image resolution and noise sensitivity arise in selecting the weighting function $\tilde{v}$, and are discussed in Shepp and Logan (1974), Horn (1978), and Rowland (1979). Equation (1.10) is the type of reconstruction algorithm currently employed in medical CAT scanners; it is a simple, explicit formula that provides rapid, quality reconstructions when a large number of high SNR line integral measurements are available at a full range of viewing angles.

It should be noted that the term "back-projection" has so far been used in two distinct ways. First, it has been used in naming the convolution back-projection reconstruction formula in (1.9) and the approximate reconstruction algorithm in (1.10). Second, it has been used to refer to the operation of integration along a cosinusoid in Radon space, which in object space corresponds to the integrated effect of a continuum of two-dimensional back-projected functions, each of which is constant along parallel lines. In the latter use, back-projection corresponds to an operator mapping a 2D function in Radon space into a 2D function in object space (Rowland, 1979). In this thesis, we have occasion to use the term back-projection in the sense of an operator. Also, in this thesis, the term "convolution back-projection" is used to refer to a somewhat more general two-step procedure than that shown in (1.9) (convolution in the t variable followed by back-projection); in particular, $V(\omega)$, the 1D Fourier transform of the convolving kernel, is not be restricted to only equal $|\omega|$, and in fact is allowed to be different for different values of θ.

The convolution back-projection algorithm in (1.10) resulted from discrete approximation of the exact reconstruction formula (1.9). The so-called <u>series expansion reconstruction algorithms</u> also result from an

approximation, in particular, the cross-sectional density function f(x) is approximated by a finite number of terms in a series expansion on a known basis set $\{\phi_i\}$

$$f(x) \simeq \sum_{i=1}^{N} f_i \phi_i(x) \tag{1.11}$$

For example, in a pixel representation for f(x), the ϕ_i are indicator functions on square-shaped subsets that result from horizontal and vertical tesselation of the plane.

This type of series expansion representation gives rise to a linear measurement equation (as in (1.2); see Gordon (1974) for details), and reconstruction corresponds to a matrix inversion problem which has been approached by numeric relaxation (ART, see Gordon, 1974; Herman, 1973), minimum norm (Kashyap and Mittal, 1973), generalized inverses (Krishnamurthy et al., 1974), and least squares (Cho and Burger, 1977), and, in cases where measurement noise is explicitly modeled, by Bayesian analysis (Herman and Lent, 1976), maximum likelihood estimation (Rockmore and Macovski, 1976; Tasto, 1976), and minimum variance estimation (Wood and Morf, 1981). For a comparison of the CBP and series expansion algorithms, see Rohler and Krishnaprasad (1981).

1.4 THESIS OUTLINE

As mentioned in Section 1.2, we focus our attention in this thesis on several specific problems involving a probabilistic object-based representation for the cross-sectional density f(x). In particular, in Chapter 2, we develop the general problem of using noisy projection measurements to determine maximum likelihood (ML) and maximum aposteriori (MAP) estimates of the density, location and geometry of a single object located within a cross-section. Several specific examples of objects are discussed, including a constant density object on a disk and a Gaussian object. In Chapters 3 and 4, the single object location estimation problem is addressed; the estimation performance analysis machinery is developed in Chapter 3 and then illustrated with two examples in Chapter 4. The location estimation log likelihood function is shown to have the same form as the CBP inversion formula in (1.10), where the convolving kernel does not satisfy $V(\omega) = |\omega|$, but instead is specified in the solution to the optimal object localization problem. In Chapter 4 several computer simulations are also presented which illustrate the distinction between log likelihood function evaluation and conventional image reconstruction from noisy projection data.

In Chapter 5, issues related to model sensitivity are addressed; in particular, the sensitivity of the location estimation performance to errors in the modeled object geometry, as well as to the presence of multiple objects is investigated. In Chapter 6, the problem of estimating the geometry of a single object with known location is addressed. In this chapter, one approach toward the ML estimation of object geometry (size, angular orientation, and extent of elongation or eccenticity) is developed, estimation performance is assessed, and several questions of practical importance are answered. In the conclusion to Chapter 6, we discuss ways in which one might structure an iterative algorithm for the problem of estimating the location and geometry of one or more objects in a cross-section from a set of noisy projection measurements. Finally, in Chapter 7, we conclude by summarizing the results of the location and geometry estimation problem, and discuss ways in which the framework developed in this thesis can be extended.

CHAPTER 2

AN OBJECT-BASED APPROACH TO RECONSTRUCTION

2.0 INTRODUCTION

Suppose that a cross-sectional density profile f(x), whose projections are being measured, can be approximately represented as some known background field $f_b(x)$, superimposed upon which are N "objects" -- an object will be modeled as a 2D function that is an additive component of the overall cross-sectional density. The object-based approach to reconstruction will involve using noisy projections of the overall density function f(x) to determine information about each of its component two-dimensional objects. As discussed in Chapter 1, the information desired about each object may include the object location within the cross-section, its density or contrast (with respect to the background), and information about the detailed variation of the two-dimensional object density profile. In addition, information concerning the number of objects may also be desired.

While many object density profiles are possible, all of the representations to be considered in this thesis will satisfy the following:

1. the brightness or contrast of the object will be characterized by a scalar multiplier of the function representing the object. That is, the function corresponding to the object (which need not be constant) corresponds to some relative density variation within the object; the contrast is simply the overall scaling. The jth object contrast or density scaling factor will be denoted $d_j \in R$.

2. the location of the object will enter the representation by a shift in the 2D variable x; the jth object location will be denoted $c_j \in R^2$

3. the profile of the object (that is, the detailed variations in the 2D object) may, in view of points (1) and (2) above, be completely specified by knowledge of the profile of a unit contrast object located at the origin. This will be called the relative profile of the object since it is the unit contrast profile of the object relative to its location point c. Such object properties as size, shape and orientation will be incorporated into the relative profile description, as we discuss in Section 2.1. While a wide variety of representations for relative profiles are possible, in the interest of estimating an object profile using finite dimensional optimal estimation techniques, we will suppose that

the relative profile belongs to some finitely parameterized class of 2D functions of unit contrast situated at the origin. The jth object relative profile will then be characterized by some finite dimensional parameter v_j.

As an example, an object might correspond to a region of the field having constant density d relative to the background, where the region is a subset K(c) of the plane with its centroid at the point $c \in \mathbb{R}^2$. In this case, the object is given by

$$d\chi_{K(c)}(x) = d\chi_{K(0)}(x - c) \tag{2.1}$$

where χ_K is the indicator function on the set K,

$$\chi_K(x) = \begin{cases} 1 & \text{if } x \in K \\ 0 & \text{otherwise} \end{cases} \tag{2.2}$$

From (2.1), the relative profile is $\chi_{K(0)}$, an indicator function of the set K(0) (a unit contrast function located at the origin). In Sections 2.1.1 and 2.1.2, we will discuss several general types of possible relative profiles.

By characterizing each of the N objects as just described, the jth object may be represented as $d_j f_o(x-c_j;v_j)$ where $f_o(x;v_j)$ is the object's relative profile. The overall cross-sectional density function may then be represented as

$$f(x) = f_b(x) + \sum_{j=1}^{N} d_j f_o(x - c_j;v_j) \qquad (2.3)$$

In the object-based reconstruction problem with such a field, one is interested in analyzing noisy projections of f(x) to determine such things as how many objects are present in a cross-section, and for each object detected, determining an optimal estimate for its parameters d_j, c_j, and v_j (with respect to some optimization criterion) . In order to establish some intuition into the estimation of object parameters, we will focus our attention in this thesis on the parameter estimation problem assuming only a single object is present within the cross-section. The single object problem, a natural precursor to the N-object problem, will provide us with intuition into the underlying task of estimating the location and profile of an object from noisy projection data, without becoming involved at this point in the problem of reconciling data from two or more objects. Also, it will provide insight into a number of areas we wish to explore, including

- estimator structure -- interpretation of the estimation computations, and methods for efficiently and/or approximately performing the computations

- estimation performance -- how well can objects be located and characterized versus SNR? To what extent do the values of particular parameters influence our ability to estimate other parameters; for example, how does an object's shape affect the accuracy with which its location or orientation can be estimated?

- the effect of limited projection data -- in what ways does performance degrade when the total number of projections or the total view angle is reduced?

- robustness to modeling errors -- determining the impact of particular modeling errors, such as the effect on the location estimation problem of inaccuracies in the assumed object size or shape.

While these issues arise for each object in the N-object problem, they are much more clearly assessed in the single-object case. Consequently, we will develop the problem of using noisy projection measurements to estimate the density, location and relative profile for a single object in a cross-section represented as

$$f(x) = f_b(x) + d \cdot f_o(x - c;v) \qquad (2.4)$$

This investigation into the single object problem not only uncovers much about the areas of interest just mentioned, but also establishes a systematic approach which extends to the N-object case and to other model-based signal processing problems.

The relative profile for the object in (2.4) is $f_o(x;v)$; in the next section we discuss several potentially useful parametric representations for this profile, and investigate the Radon transform of (2.4) in Section 2.2.

2.1 THE OBJECT RELATIVE PROFILE

As discussed in the previous section, the object relative profile $f_o(x;v)$ is a unit contrast 2D function correponding to an object situated at the origin of the cross-sectional coordinate system. While this function has been constrained to be finitely parameterized, it is otherwise completely arbitrary. In any application, a priori information about the type of objects likely to occur in a cross-section should serve as a guide in appropriately selecting the class of modeled relative profile functions. Generally speaking, the various choices may be split into two groups, namely discontinuous and continuous functions, and in the next three sections

we present several possible profiles, as well as some specific examples that will be further analyzed in the course of this thesis.

2.1.1 Discontinuous relative profiles

In a number of applications, automated or semi-automated delineation of boundaries in reconstructed images is currently being accomplished by partitioning the cross-section into regions (e.g. bone, kidney, airspaces), where the density variations within any region are small, but where the variation between regions may be great (Belanger et al., 1979; Selfridge and Prewitt, 1981). Any such region may be either exactly or approximately represented as a constant density object, i.e. an object having a relative profile that is an indicator function on some set K situated (e.g. centroid location) at the origin.

The unknown information in such a relative profile is the boundary ∂K of the set K; ∂K is a closed curve in the plane which is represented parametrically. The problem of stochastic curve representation has been treated by a number of authors (Anastassiou and Sakrison, 1981; Cooper et al., 1980). Since the projection of an indicator function on a set K is a constant times the chord length of intersection of the line $l(t,\theta)$ with the set K, we

desire a finite dimensional parametric representation for ∂K that is amenable to easy chord length of intersection calculation. A variety of representations are possible, including the following:

- If ∂K can be well approximated by a simple geometric element (e.g. rectangle, ellipse), it may be approximately specified by a small number of parameters, e.g. side length or semi-axis lengths.

- If K is convex, ∂K can be completely described by its support function, which is periodic in 2π (Santalo, 1976). This periodic function can be approximated by a finite number of terms in a series expansion, e.g. a Fourier series, in which case ∂K is parameterized by a finite number of coefficients in a truncated series.

- The boundary ∂K can be approximately represented by a sequence of horizontally and vertically directed edge segments, corresponding to a binary pixel representation for the set K (Elliott and Srinivason, 1981; Cooper et al., 1980). In this case, K is represented by the finite set of parameters characterizing the sequence of edge segments.

Each of these representations (as well as others not listed), has relative advantages and disadvantages, such as the simplicity of computation, or the goodness of fit to the actual boundary ∂K for a given number of parameters, and in any application, a priori information would be taken into account in making an appropriate choice of parameterization for the curve ∂K. The indicator function on a disk is a simple relative profile that we will use frequently in this thesis to illustrate a number of points about the parameter estimation problems being investigated.

2.1.2 Continuous relative profiles

In some applications, a discontinuous density function may be an inappropriate model. For example, oceanographic thermal or salinity profiles do not have infinite gradient values because of mixing at the interface between regions of different temperatures or salinities. In such cases, a continuous object is a more appropriate model. A smooth circularly shaped object of radius "R" may, for example, be described by a Gaussian object, $f_o(x;R) = \exp(-\|x\|^2/R^2)$, where $\|x\|$ is the magnitude of the point x.

Such an object profile is clearly an approximation to an actual object, since the Gaussian object is nonzero at arbitrarily large distances from the location point. The Gaussian object is a very good approximate profile, however, since its density value decreases rapidly to a small value with increasing distance from the location point. This profile will be used in this thesis to illustrate many of the parameter estimation techniques, and is attractive because the corresponding calculations are in most cases simple and analytic.

2.1.3 Size, eccentricity and orientation

A potentially rich class of object relative profiles may be obtained from any given profile $f_o(x;v)$ by considering the effect of applying scaling, stretching and rotation transformations to the x coordinate system. For example, by using such a representation, an indicator function on an ellipse may be easily expressed in terms of the circularly symmetric indicator function on a disk. Specifically, let

$$\tilde{x} = Q(R,\lambda,\phi)x$$

$$\triangleq \begin{bmatrix} \cos\phi & \sin\phi \\ -\sin\phi & \cos\phi \end{bmatrix} \begin{bmatrix} \sqrt{\lambda} & 0 \\ 0 & 1/\sqrt{\lambda} \end{bmatrix} \begin{bmatrix} R & 0 \\ 0 & R \end{bmatrix} x \qquad (2.5)$$

In this case, the relative profile $f_o(Q^{-1}(R,\lambda,\phi)\tilde{x};v)$

is the relative profile $f_o(x;v)$ isotropically magnified by a size factor R, stretched in the x_1 direction and compressed in the x_2 direction by a factor $\sqrt{\lambda}$, and rotated by the angle $\emptyset$. This relative profile representation is particularly attractive because it leads to analytically tractable evaluation of some interesting specific examples. The transformation in (2.5) will find application in Chapter 6 of this thesis, where we consider the problem of using limited noisy projection data to estimate the geometry of a single object, specifically, the problem of estimating object size, eccentricity and orientation.

2.2 THE RADON TRANSFORM

The cross-sectional density f(x) can be observed only via its projections, i.e. via its Radon transform, where the Radon transform (equation 1.4) of f(x) in (2.4) is

$$\int_{\underline{x}'\underline{\theta}=t} f_b(x)ds + d\int_{\underline{x}'\underline{\theta}=t} f_o(x - c;v)ds \qquad (2.6)$$

Since the background field is assumed known, the first term in (2.6) may be subtracted from the Radon transform to leave that part due solely to the object, namely

$g(t,\theta;d,c,v) =$

$$d \cdot g(t,\theta;c,v) = d \int_{\underline{x}'\underline{\theta}=t} f_o(x - c;v)ds \tag{2.7}$$

Notice that the contrast parameter d, which affects the density function in object space linearly, also affects the Radon transform linearly. Thus, in order to see how c and v affect the Radon transform, it is sufficient to look at the case where d=1. We will use the notation $g_0(\cdot)$ to denote the Radon transform of a relative profile, namely

$$g_0(t,\theta;v) \triangleq \int_{\underline{x}'\underline{\theta}=t} f_o(x;v)ds \tag{2.8}$$

Finally, the Radon transform of a relative profile which has been shifted to the point c is

$$g(t,\theta;c,v) = \int_{\underline{x}'\underline{\theta}=t} f_o(x - c;v)ds$$

$$= \int_{\underline{x}'\underline{\theta}=t-\underline{c}'\underline{\theta}} f_o(x;v)ds = g_0(t - \underline{c}'\underline{\theta},\theta;v) \qquad (2.9)$$

Shifting a relative profile from the origin to the point c in object space causes its Radon transform to experience a shift in the t variable in Radon space, the magnitude of the shift depending sinusoidally on θ.

EXAMPLE 1 -- Pillbox Object

Consider the problem of using projection measurements to locate a constant density object on a disk (this 2D function is often referred to as the pillbox function). Let the object be given by a weighted indicator function on the disk $D(R) \triangleq \{x: \|x\| \leq R\}$,

$$d \cdot f_o(x;R) = \begin{cases} d & \text{if } \|x\| \leq R \\ 0 & \text{otherwise} \end{cases} \qquad (2.10)$$

which is illustrated in Figure 2.1a. For any value of θ, the projection is a half-ellipse centered at t=0,

$$d \cdot g_0(t,\theta;R) = \begin{cases} 2d\sqrt{R^2 - t^2} & \text{if } |t| < R \\ 0 & \text{otherwise} \end{cases} \qquad (2.11)$$

The Radon transform, viewed as a 2D Radon space function is the θ-independent function shown in Figure 2.1b. It should be noted that whenever the density function is

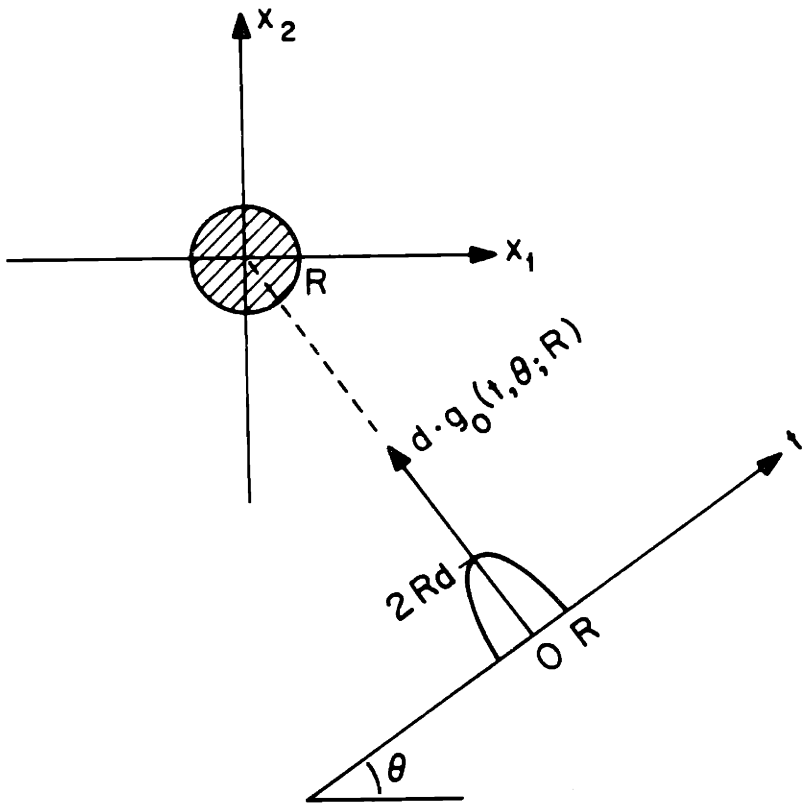

Figure 2.1 (a) Projection at angle Θ.

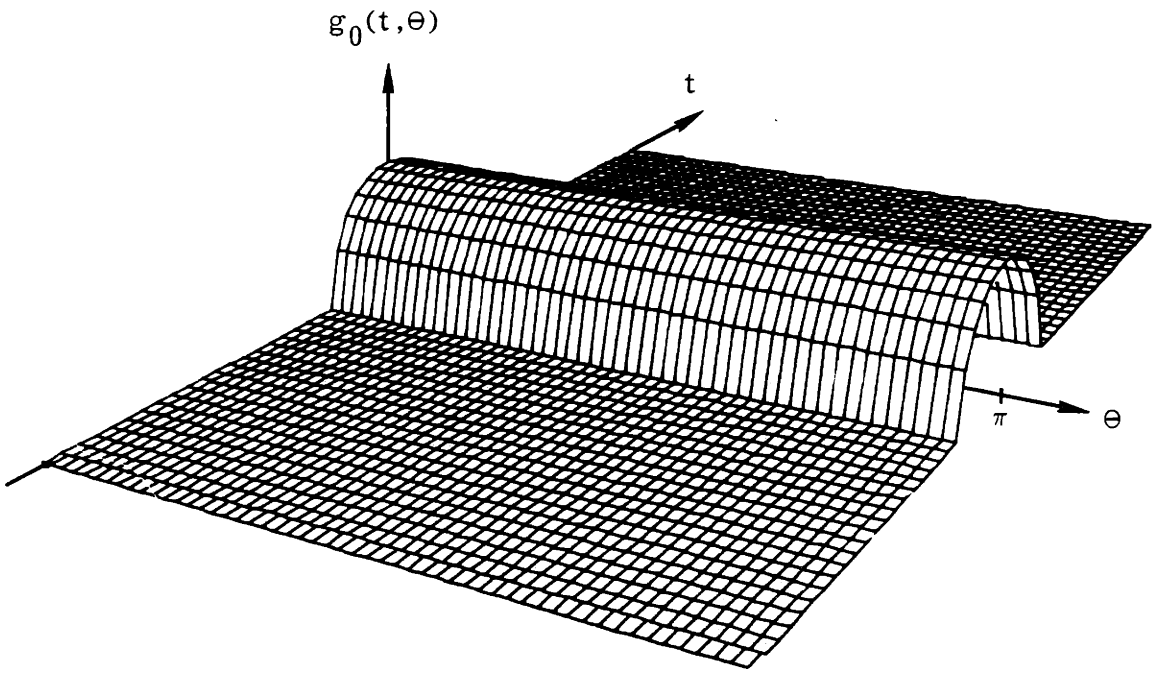

Figure 2.1 (b) Radon transform for a single pillbox object located at the origin.

circularly symmetric, as it is in this example, the Radon transform is θ-independent, and is also referred to as the Abel transform (Bracewell, 1965).

Consider now the case where the object is situated at an arbitrary point $c \in \mathbb{R}^2$ in the cross-section. As indicated by (2.9), the projection at the angle θ is the 1D function $d \cdot g_0(t - \underline{c}'\underline{\theta}, \theta; R)$, which from (2.11) is a half-ellipse centered at the point $t = \underline{c}'\underline{\theta} = c_1 \cos\theta + c_2 \sin\theta$, as shown in Figure 2.2a. The projection has the following properties:

1. The projection at angle θ, sampled at the point t, is equal to the product of d times the chord length of intersection of line $l(t,\theta)$ with the disk D(R) centered at c.

2. The area under the projection at any angle θ equals the product of d and the cross-sectional area of the disk D(R).

3. The centroid of the projection at angle θ is located at the point $\underline{c}'\underline{\theta}$, which is the projection at angle θ of the object centroid c. This is true not only for circular objects, but for <u>any</u> object.

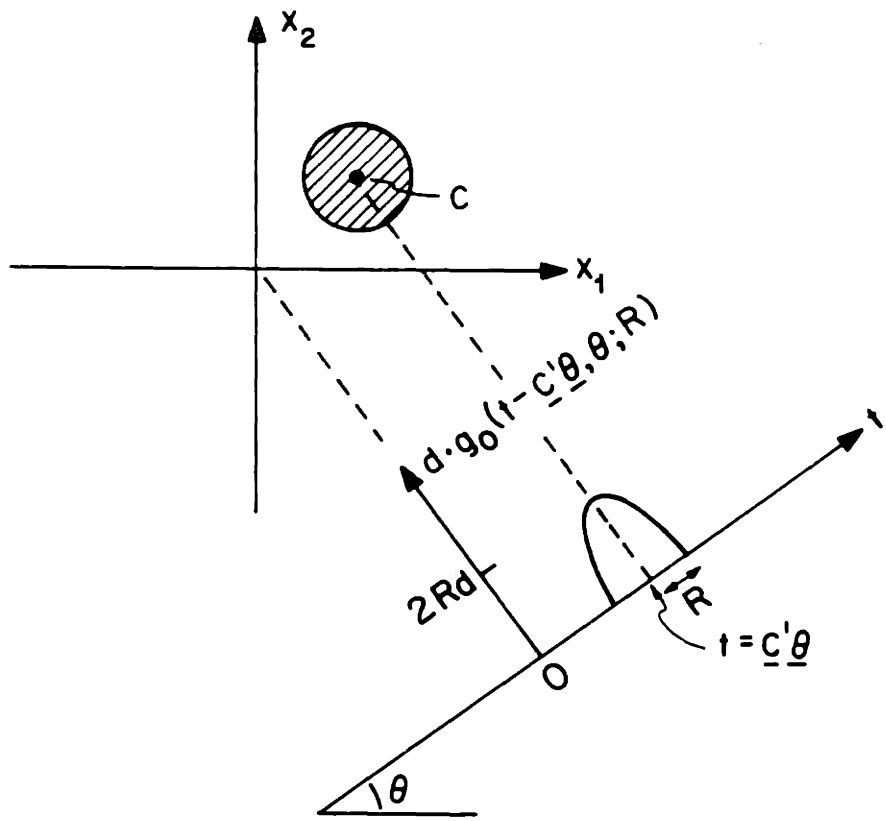

Figure 2.2 (a) Projection at angle Θ.

4. For all θ, the projection is symmetric about the point $\underline{c}'\underline{\theta}$. This is true not only for objects that are indicator functions on circularly-shaped sets, but for relative profile that is centrally symmetric, i.e. one satisfying $f_o(q;v) = f_o(-q;v)$ for all $q \in \mathbb{R}^2$.

5. The projections at all angles are the same relative to the point $\underline{c}'\underline{\theta}$; this is true whenever the relative profile is circularly-symmetric.

6. While this discontinuous object has a continuous projection, the first partial derivative $\partial g(t,\theta)/\partial t$ has points of discontinuity. This is more generally true for indicator functions on any set K having a boundary ∂K following a curve with a finite radius of curvature (Galvin and Bjarngard, 1975). The first partial derivative is discontinuous at (t,θ) points corresponding to the line tangent to the boundary at points of finite radius of curvature.

The Radon transform of the pillbox object located at c, viewed as a function $g:\mathcal{Y} \rightarrow R$, is the θ-dependent function shown in Figure 2.2b, which is related to the Radon transform in Figure 2.1b by a sinusoidal shift in the t variable. The problem of estimating the object location $c \in \mathbb{R}^2$ in object space, therefore, is the same as estimating the sinusoidal shift of its Radon transform in

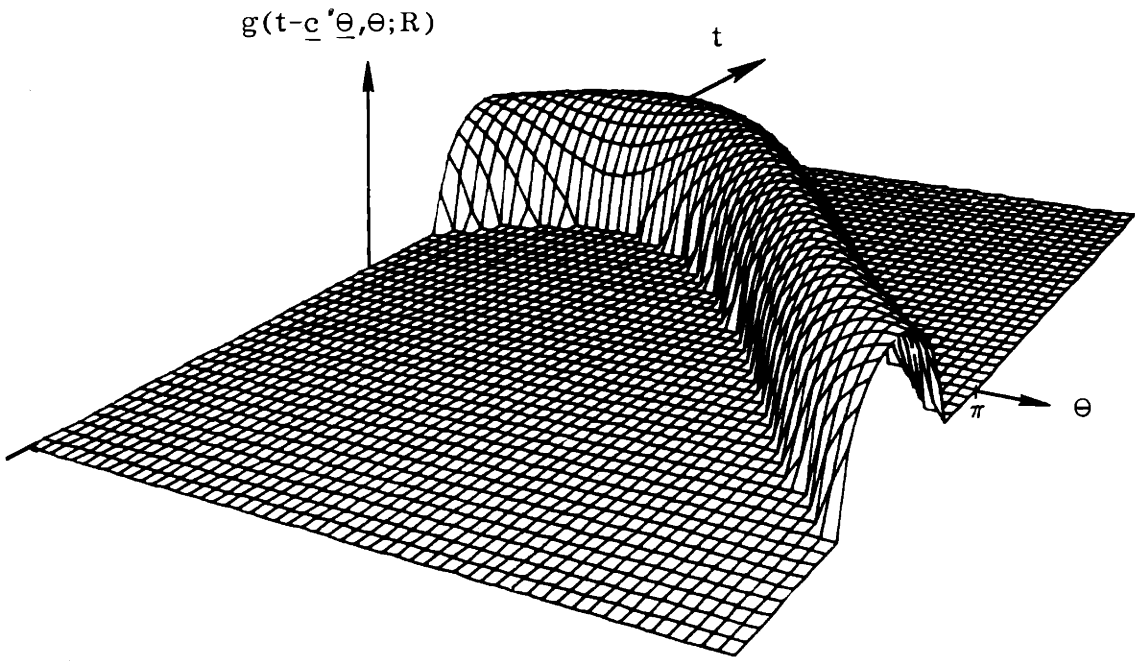

Figure 2.2 (b) Radon transform for a single pillbox object located at the point c.

Radon space.

EXAMPLE 2 -- Box Object

Consider now an object that is a weighted indicator function on a square with sides of length L parallel to the x axes, centered at the point c, and having constant density d. In this case, the object is given by

$$d \cdot f_o(x - c; L) = d \, \chi_{I(L)}(x - c) \tag{2.12}$$

as illustrated in Figure 2.3a, where $I(L) \triangleq \{x: |x_1| \leq L$ and $|x_2| \leq L\}$.

The projection at angle Θ is a trapezoid, as shown in Figure 2.3a, where

$$h(\Theta) = Ld/\mathrm{Cos}(\pi/4 - \delta)$$

$$w_1(\Theta) = (L/\sqrt{2})\,\mathrm{Sin}\,\delta$$

$$w_2(\Theta) = L\mathrm{Sin}(\pi/4 - \delta)$$

$$\delta = |\ (\Theta \bmod \pi/2) - \pi/4\ | \tag{2.13}$$

As was the case in Example 1, the centroid of the projection is the projection of the centroid, and the projection is symmetric about the centroid. The Radon transform of the square object is shown in Figure 2.3b as

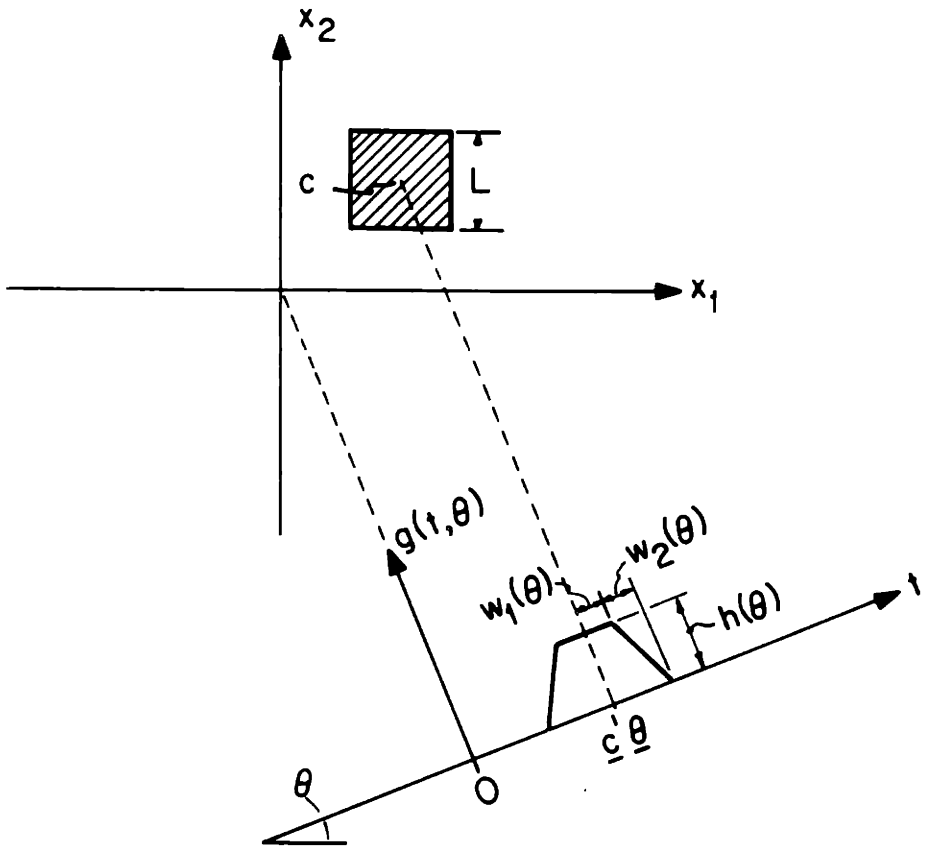

Figure 2.3 (a) Projection at angle Θ.

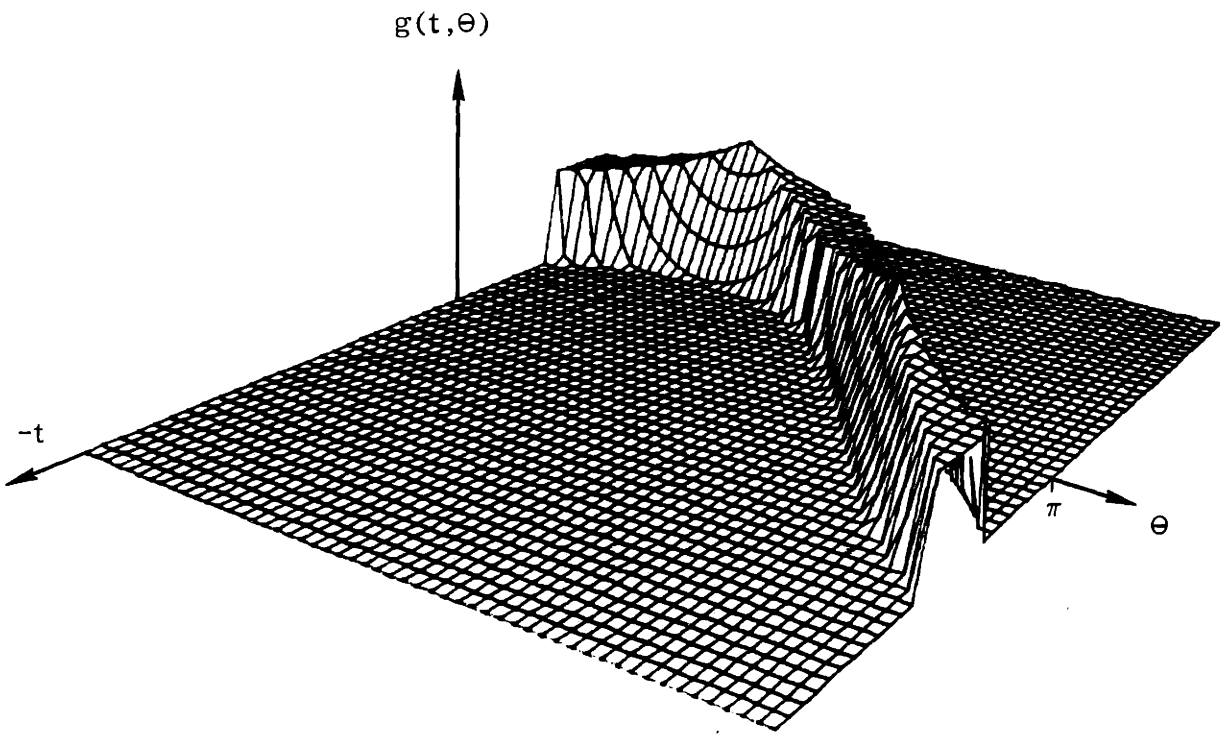

Figure 2.3 (b) Radon transform for a single box object.

a two-dimensional function on $\mathcal{Y}$. It should be noted that since the relative profile is not circularly-symmetric, the projection, relative to its centroid $\underline{c}'\underline{\theta}$, has a shape that is not independent of the projection angle θ. Also, for certain projection angles, the projection is seen to be a discontinuous function; this is true for any profile that is an indicator function on a set having a boundary containing straight lines.

EXAMPLE 3 -- Gaussian Object

In this final example, consider the Gaussian object of size R presented in Section 2.1.2, having relative profile

$$f_o(x;R) = \exp(-\|x\|^2/R^2) \tag{2.14}$$

The projection of a 2D Gaussian function is a 1D Gaussian, and the Radon transform is the θ-independent function

$$g_0(t,\theta;R) = \sqrt{\pi}\, R \exp(-t^2/R^2) \tag{2.15}$$

Again, the centroid of the projection is the projection of the centroid, and the projection is symmetric about its centroid. Also, the projection is continuous, and has a continuous first partial derivative with respect to t.

Example summary

The object-space structure in the profile $d \cdot f_o(x-c;v)$ is seen to translate directly into structure in its Radon transform -- a "cosinusoidally-displaced" two-dimensional function, where the centroid of the projection at angle θ sweeps out the cosinusoid $\mathscr{C}(c)$ in Radon space. The Radon space representation of the densities for Examples 1 and 2, shown in Figures 2.2b and 2.3b, are completely described by the variables c, d, R, and L. Variable c affects only the projection centroid cosinusoid $\mathscr{C}(c)$, variables R and L affect the shape of the projection at every θ value, and the contrast parameter d affects only the magnitude of the Radon transform (in a linear manner).

These simple examples serve to illustrate the perspective being taken in this thesis -- the problem of searching for an object in object space (Figures 2.2a and 2.3a) may be approached by searching in Radon space (i.e. measurement space) for a highly structured cosinusoidally displaced Radon transform (Figures 2.2b and 2.3b).

2.3 THE MEASUREMENT MODEL

In practice, only noisy samples of the Radon transform are available as measurements, and two stochastic measurement models are commonly used:

1. Poisson process model -- in the case of low-level electromagnetic probing of an attenuating field, sensors measure the rate at which photons escape the field along straight lines. If a narrow beam of photons with rate λ_o is directed through the field along the line $l(t,\theta)$, the escaping photons obey a Poisson process model with rate

$$\lambda(t,\theta) = \lambda_o \exp(-g(t,\theta)) \tag{2.16}$$

where $g(t,\theta)$ denotes the Radon transform at the point (t,θ).

2. Additive noise model -- with acoustic or high level electromagnetic energy, the measurements are typically modelled as the Radon transform contaminated with zero-mean additive noise

$$y(t,\theta) = g(t,\theta) + w(t,\theta) \qquad (t,\theta)\in\mathscr{S} \tag{2.17}$$

Typically, $w(t,\theta)$ is a zero-mean white Gaussian noise

process, although other noise models have been used; for example, an additive correlated noise model arises by line integration of a homogeneous random field with exponential correlation (Tasto, 1974).

Throughout this thesis, we will employ the measurement model (2.17) with $w(t,\theta)$ a zero-mean white Gaussian process, $(t,\theta)\in\mathscr{S}$, where $\mathscr{S}$ denotes the subset of $\mathbb{Y}$ on which the measurements are taken. We will consider two types of measurements, specifically, projection measurements taken over a continuous interval of θ values and projection measurements taken at only a finite number of projection angles.

Case 1 Continuous-view Measurements

In the continuous-view case, measurements are taken over a total viewing angle of 2Δ centered at $\pi/2$, i.e. views are taken up to an angle Δ on either side of the x_1 axis (here $0<\Delta\leq\pi/2$). The measurement subset is given by

$$\mathscr{S} = \mathscr{S}_{\Delta}$$

$$\triangleq \left\{(t,\theta): -\infty<t<\infty,\ \frac{\pi}{2}-\Delta\leq\theta<\frac{\pi}{2}+\Delta\ \right\} \qquad (2.18)$$

In the continuous-view case, the additive noise $w(t,\theta)$ is a 2D zero-mean Gaussian random field on $\mathscr{S}$ with

covariance

$$E\{w(t,\Theta)w(\tau,\emptyset)\} = \frac{N_o}{2}\delta(t-\tau,\Theta-\emptyset) \qquad (t,\Theta)\in\mathcal{S} \tag{2.19}$$

where $\delta(t,\Theta)$ is a 2D impulse. The standard tomographic reconstruction problem, where (noise-free) measurements are assumed to be available at all possible projection angles, is the special case of continuous-view measurements with $\Delta=\frac{\pi}{2}$. We will refer to this as the full-view measurement case, and to the case $\Delta<\frac{\pi}{2}$ as the limited-view measurement case.

Case 2 Discrete-view measurements

In the discrete-view case, projections are measured at N angles that are uniformly spaced over the interval $[0,\pi)$. The measurement subset is

$$\begin{aligned}\mathcal{S} &= \mathcal{S}_N \\ &\triangleq \{(t,\Theta):\ -\infty<t<\infty,\ \Theta=\Theta_j=\frac{j\pi}{N},\ j=0,1,\ldots,N-1\}\end{aligned} \tag{2.20}$$

For each view angle Θ_j, the noise process $w(t,\Theta_j)$ is a 1D zero-mean Gaussian process with covariance

$$E\{w(t,\Theta_j)w(\tau,\Theta_j)\} = \frac{N_o}{2}\delta(t-\tau) \tag{2.21}$$

and the noise at different view angles Θ_i and Θ_j, $i\neq j$, is uncorrelated.

In practice, only a finite number of line integral measurements can be taken, in which case the Radon-space measurement set $\mathscr{S}$ corresponds to a finite set of points in $\mathcal{Y}$ (for example, in the so-called parallel-ray scanning geometry, $\mathscr{S}$ corresponds to a lattice of points uniformly spaced in $\theta\in[0,\pi)$ and $t\in[-T,T]$ for some value of T). In this thesis, we will not consider this case explicitly, because it is much simpler to expose the basic ideas by using projections that are continuous in the t direction. In the course of the analysis, however, a variation of the measurement equation in (2.17) will be introduced that involves a continuous projection which has been spatially bandlimited in the t direction; this analysis effectively considers t-direction sampling of the projections.

2.4 MAXIMUM LIKELIHOOD PARAMETER ESTIMATION

Suppose in the problem being considered that the parameters d, c and v are known a priori to belong to the sets D, C and V respectively. Given a set of continuous- or discrete-view measurements, we wish to estimate these object parameters by maximum likelihood (ML) estimation. The ML estimates are obtained by first using the projection measurements to compute a log likelihood function $\mathscr{L}(d,c,v)$ (Van Trees, 1968), and then finding the parameters $d\in D$, $c\in C$ and $v\in V$ that maximize $\mathscr{L}(d,c,v)$.

In the continuous-view case, the log likelihood function is given by

$$\mathscr{L}_{\Delta}(d,c,v) = \frac{2}{N_o} d \int_{\frac{\pi}{2}-\Delta}^{\frac{\pi}{2}+\Delta} \int_{-\infty}^{\infty} y(t,\theta) g(t,\theta;c,v) dt d\theta$$

$$- \frac{1}{N_o} d^2 \int_{\frac{\pi}{2}-\Delta}^{\frac{\pi}{2}+\Delta} \int_{-\infty}^{\infty} g^2(t,\theta;c,v) dt d\theta \qquad (2.22a)$$

and in the discrete-view case, it is given by

$$\mathscr{L}_N(d,c,v) = \frac{2}{N_o} \sum_{j=0}^{N-1} \int_{-\infty}^{\infty} d \cdot y(t,\theta_j) g(t,\theta_j;c,v) dt$$

$$- \frac{1}{N_o} \sum_{j=0}^{N-1} \int_{-\infty}^{\infty} d^2 \, g^2(t,\theta_j;c,v) dt \qquad (2.22b)$$

In each case, the log likelihood function is the difference between two terms, the first of which is obtained by a matched filtering operation (Van Trees, 1968) on the measurements using a Radon-space filtering template $g(t,\theta;c,v)$. The second term involves the Radon transform energy on the measurement subset. Maximum likelihood (ML) estimates for these parameters then satisfy

$$\begin{bmatrix} \hat{d} \\ \hat{c} \\ \hat{v} \end{bmatrix}_{ML} = \underset{\substack{d\in D \\ c\in C \\ v\in V}}{\operatorname{argmax}} \; \mathcal{L}(d,c,v) \tag{2.23}$$

If the parameters d, c and v, rather than being nonrandom unknown parameters, are instead random variables with joint a priori probability distribution p(d,c,v), then the maximum a posteriori (MAP) estimates for these variables satisfy

$$\begin{bmatrix} \hat{d} \\ \hat{c} \\ \hat{v} \end{bmatrix}_{MAP} = \underset{\substack{d\in D \\ c\in C \\ v\in V}}{\operatorname{argmax}} \; \mathcal{L}(d,c,v) + \ln p(d,c,v) \tag{2.24}$$

The cross-sectional field model in (2.4), together with the additive noise measurement model (2.17) and ML estimation equation (2.23) will comprise the focus of the investigation in this thesis. Since the Radon transform (2.7) and measurement model (2.17) are linear in the contrast d, this parameter is determined very simply once the optimal estimates $\hat{c}_{ML}$ and $\hat{v}_{ML}$ for the location and geometry are known; for example, in the full-view case

$$\hat{d}_{ML} = \frac{\int_0^{\pi} \int_{-\infty}^{\infty} y(t,\theta)\, g(t,\theta;\hat{c}_{ML},\hat{v}_{ML})\, dt d\theta}{\int_0^{\pi} \int_{-\infty}^{\infty} g^2(t,\theta;\hat{c}_{ML},\hat{v}_{ML})\, dt d\theta} \qquad (2.25)$$

For this reason, we will concentrate on estimating only the location and geometry parameters. In particular, as discussed earlier, we will split the problem of location and geometry estimation into two separate problems, so that we can systematically investigate the structure and the performance and robustness issues related to each problem independently. Such an approach will also allow us to assess the utility of an iterative approach to the problem of object-based reconstruction from projections in which we consider the introduction of additional cross-section detail in our model at each stage in the processing.

The problem of locating an object having a known relative profile $f_o(x;v)$ will be investigated in Chapters 3 and 4, and estimation robustness issues are discussed in Chapter 5. In Chapter 6, the problem of relative profile estimation is addressed through the use of the object size, eccentricity and orientation representation intoduced in Section 2.1.3. Also in the conclusion to Chapter 6, we interpret the significance of the results obtained in Chapters 3 through 6 in terms of

their implications for the feasibility and structure of an iterative approach to reconstruction; in particular to the use of projections to reconstruct a cross-section containing an unknown number of objects whose location and geometry are unknown.

CHAPTER 3

SINGLE OBJECT LOCALIZATION PERFORMANCE ANALYSIS

3.0 INTRODUCTION

In this chapter and the next, we consider the problem of locating a single object whose contrast and relative profile are known, but whose location within the cross-section is unknown. Given a set of continuous- or discrete-view measurements, we wish to estimate the object's location $c \in C$ by maximum likelihood (ML) estimation. The ML location estimate is obtained by first using the projection measurements to compute a log likelihood function $\mathscr{L}(c)$ (Van Trees, 1968) and then finding the 2D parameter $c \in C$ that maximizes $\mathscr{L}(c)$. The continuous- and discrete-view log likelihood functions may be obtained from (2.22), and are given by

$$\mathscr{L}_{\Delta}(c) = \frac{2}{N_o} d \int_{\frac{\pi}{2}-\Delta}^{\frac{\pi}{2}+\Delta} \int_{-\infty}^{\infty} y(t,\theta) g(t,\theta;c,v) dt d\theta$$

$$- \frac{1}{N_o} d^2 \int_{\frac{\pi}{2}-\Delta}^{\frac{\pi}{2}+\Delta} \int_{-\infty}^{\infty} g^2(t,\theta;c,v) dt d\theta \qquad (3.1a)$$

and in the discrete-view case, it is given by

$$\mathscr{L}_{N}(c) = \frac{2}{N_o} d \sum_{j=0}^{N-1} \int_{-\infty}^{\infty} y(t,\theta_j) g(t,\theta_j;c,v) dt$$

$$- \frac{1}{N_o} d^2 \sum_{j=0}^{N-1} \int_{-\infty}^{\infty} g^2(t,\theta_j;c,v)\,dt \qquad (3.1b)$$

In each case, the log likelihood function is the difference between two terms, the first of which is obtained by a matched filtering operation (Van Trees, 1968) on the measurements using a Radon-space filtering template $g(t,\theta;c,v)$. The second term involves the Radon transform energy on the measurement subset; by (2.9) and a change of variable

$$\int_{-\infty}^{\infty} g^2(t,\theta;c,v)\,dt = \int_{-\infty}^{\infty} g_0^2(t-\underline{c}'\underline{\theta},\theta;v)\,dt$$

$$= \int_{-\infty}^{\infty} g_0^2(\tau,\theta,v)\,d\tau \qquad (3.2)$$

The final integral in (3.2) is independent of c, so the Radon transform energy terms in (3.1) contribute only a constant to the log likelihood function, which has no effect on the location of the maximum. Ignoring these energy terms, as well as the first term scaling constants, and no longer writing the Radon transform explicitly as a function of v, the log likelihood function for each case becomes, by (2.9)

$$L_\Delta(c) = \int_{\frac{\pi}{2}-\Delta}^{\frac{\pi}{2}+\Delta} \int_{-\infty}^{\infty} y(t,\theta)\, g_0(t-\underline{c}'\underline{\theta},\theta)\,dt\,d\theta \qquad (3.3a)$$

and

$$L_N(c) = \sum_{j=0}^{N-1} \int_{-\infty}^{\infty} y(t,\theta)\, g_0(t-\underline{c}'\underline{\theta}_j, \theta_j)\, dt \qquad (3.3b)$$

In summary, the ML estimate for the object location $c \in C$ is determined by computing the log likelihood function $L_\Delta(c)$ ($L_N(c)$ in the discrete-view case) in (3.3), and determining the value of the two-dimensional parameter $c \in C$ at which the peak of the log likelihood function occurs,

$$\hat{c}_{ML} = \begin{cases} \underset{c \in C}{\operatorname{argmax}}\ L_\Delta(c) & \text{in the continuous-view case} \\ \underset{c \in C}{\operatorname{argmax}}\ L_N(c) & \text{in the discrete-view case} \end{cases} \qquad (3.4)$$

Consider first the full-view case $\Delta = \frac{\pi}{2}$, and notice the similarity between the log likelihood function in (3.3a) and the convolution back-projection inversion formula in (1.9). In (1.9), the noise-free projection measurements $g(t,\theta)$ are used to determine a reconstruction $\hat{f}: \mathbb{R}^2 \to R$ by convolution back-projection with a θ-independent convolving kernel $v(t)$. In contrast, in (3.3a) with $\Delta = \frac{\pi}{2}$, the noisy projection measurements $y(t,\theta)$ are used to determine a 2D log likelihood function $L_{\frac{\pi}{2}}: \mathbb{R}^2 \to R$ by convolution back-projection with a generally θ-dependent and nonsymmetric convolving kernel $g_0(t,\theta)$.

In the conventional use of the CBP operation for reconstruction as in (1.9), the convolving kernel v(t) is chosen to provide an accurate reconstruction, i.e. so that the reconstruction $\hat{f}(x)$ is "close" to f(x) in some sense. Said another way, the composite operation of Radon transformation followed by convolution back-projection with kernel v(t) corresponds to a mapping $f \rightarrow \hat{f}$; in the image reconstruction problem, the convolving kernel v(t) is chosen so that this mapping has an approximately impulsive point-spread function.

In contrast, although in the full-view case the operation in (3.3a) may be interpreted as a CBP, the resulting log likelihood function is <u>not</u> interpreted as a reconstructed image because the convolving kernel was not chosen with accurate reconstruction in mind. In fact, the full-view log likelihood function will be shown to be a noisy and blurred version of the original function f(x). The CBP operation in (3.3a) is used to obtain the log likelihood function $L_{\frac{\pi}{2}}(c)$, this being the first step in determining $\hat{c}_{ML}$, the ML estimate of the object location $c \epsilon C$. That is, the convolving kernel $g_0(t,\theta)$ is the correct one to use for the purpose stated, namely the optimal estimation of the location of the object.

In the limited-view case ($\Delta<\frac{\pi}{2}$), and in the discrete-view case, the log likelihood function in (3.3) still has the same general form as the CBP operation in (1.9), except that the integral with respect to θ for $\theta\epsilon[0,\pi)$ (i.e. the back-projection operation) is replaced by either an integral with respect to θ for $\theta\epsilon[\frac{\pi}{2}-\Delta,\frac{\pi}{2}+\Delta)$ or by an N-point sum over θ_j. These expressions resemble those associated with approximate convolution back-projection reconstruction algorithm in (1.10), which is used to compute approximate reconstructed images when measurements are available only on some subset of the full measurement set $\mathcal{Y}$ (note that (1.10) holds for a finite number of line integral measurements, whereas these log likelihood function expressions involve continuous projections). The distinction between reconstructing an image and evaluating a log likelihood function still applies; the approximate CBP reconstruction algorithms use a convolving kernel that provides approximate reconstructions, whereas in (3.3) the kernel is <u>not</u> chosen with accurate reconstruction in mind, but rather is chosen to obtain the log likelihood function from the measurements in each case.

It should be noted that in terms of computational complexity, for a given set of measurements both image reconstruction and log likelihood function evaluation require the same amount of computation. This is so

because each procedure involves the determination of a 2D function whose value at any point is given by an integral or sum of weighted projection data. If the goal of the signal processing, however, is to locate an object within a cross-section, the task is completed when the log likelihood function peak is found, whereas when a reconstructed image is formed, further image processing is required if the location of the object is to be determined. In fact, it is well known (Riederer et al., 1978) that if the projection measurement noise is white, the reconstructed image noise is nonwhite. Consequently, post-processing a reconstructed image is not a (relatively simple) problem of detection/estimation in white noise.

The problem of detecting a constant density object having known location by examination of a noisy reconstructed image has been considered by Hanson (1978), who empirically identified the relationship between minimum detectable contrast and object diameter. Hanson demonstrated that unless appropriate filtering is performed, human interpreters have difficulty in detecting large low contrast objects in the presence of the nonwhite noise in a reconstructed image. This "appropriate" filter essentially corresponds to a whitening filter (Van Trees, 1968), which undoes the noise correlating effect of the CBP operation. This is more complex than the direct approach being considered in this thesis, which involves

Radon-space (i.e. measurement-space) matched filtering in the presence of white noise.

In this chapter and the next, we investigate the accuracy of the ML location estimate $\hat{c}_{ML}$ in (3.4). Two sources of error contribute to the overall estimate error covariance, and these error sources are assessed in this chapter. In this development, we do not specifically discuss algorithmic or implementation issues such as efficient procedures for locating the log likelihood function peak; instead we focus on issues of how well one can do assuming the ML estimation procedures can be carried out exactly. In Chapter 4, several specific examples are presented for which the error covariance is evaluated as a function of signal-to-noise ratio (SNR) and object size. Also in Chapter 4, several computer simulations are presented in which limited amounts of noisy computer-generated projection data have been processed using a CBP algorithm with both a conventional image reconstruction kernel (to compute a reconstructed image) and the kernel $g_0(t,\theta)$ (to compute a log likelihood function).

3.1 PERFORMANCE ANALYSIS

The maximum likelihood estimate for the location of an object in the cross-section is obtained from projection measurements according to (3.4), by locating the peak of the 2D function $L_\Delta(c)$ in the continuous-view case, and the peak of $L_N(c)$ in the discrete-view case. The noise $w(t,\theta)$ in the measurements (2.17) affects the log likelihood function as shown in (3.3), and consequently affects the location $\hat{c}_{ML}$ of the log likelihood function peak. In this chapter, we investigate the way in which the statistical accuracy of the location estimate $\hat{c}_{ML}$ is affected by the measurement noise $w(t,\theta)$.

First, to see how the log likelihood function depends on the measurement noise, substitute (2.17) into (3.3) (the "a" subscripts correspond to the actual object)

$$L_\Delta(c) = \int_{\frac{\pi}{2}-\Delta}^{\frac{\pi}{2}+\Delta} \int_{-\infty}^{\infty} g(t,\theta;c_a)\, g(t,\theta;c)\, dt\, d\theta$$

$$+ \int_{\frac{\pi}{2}-\Delta}^{\frac{\pi}{2}+\Delta} \int_{-\infty}^{\infty} w(t,\theta)\, g(t,\theta;c)\, dt\, d\theta$$

$$\triangleq \bar{a}_\Delta(c,c_a) + n_\Delta(c) \qquad (3.5a)$$

$$L_N(c) = \sum_{j=0}^{N-1} \int_{-\infty}^{\infty} g(t,\theta_j;c_a)\, g(t,\theta_j;c)\, dt\, d\theta$$

$$+ \sum_{j=0}^{N-1} \int_{-\infty}^{\infty} w(t,\theta_j)\, g(t,\theta_j;c)\, dt$$

$$\triangleq \bar{a}_N(c,c_a) + n_N(c) \qquad (3.5b)$$

The log likelihood function in each case is the sum of two functions. The first function, $\bar{a}$, is the expected value of the log likelihood function, and is a deterministic function known as the generalized ambiguity function (Van Trees, 1971). The second term in the log likelihood function expression, n, depends on the measurement noise, and is a zero-mean correlated random field which, for the two measurement cases respectively, has covariance

$$E\{n_\Delta(c)\, n_\Delta(c')\} = \frac{N_o}{2}\, \bar{a}_\Delta(c,c') \qquad (3.6a)$$

$$E\{n_N(c)\, n_N(c')\} = \frac{N_o}{2}\, \bar{a}_N(c,c') \qquad (3.6b)$$

The ambiguity function, then, enters the log likelihood function in both its deterministic and random components. Consequently, the ambiguity function plays a key role in the analysis of estimator performance, in much the same way it does in the analysis of estimator

accuracy, ambiguity, and resolution in radar and sonar applications (Van Trees, 1971).

Although the ambiguity function is shown in (3.5) as a function of two values of $c \in \mathbb{R}^2$, it depends on the two values only through their difference. This can be seen, in the continuous-view case, from

$$\bar{a}_{\Delta}(c,c_a) = \int_{\frac{\pi}{2}-\Delta}^{\frac{\pi}{2}+\Delta} \int_{-\infty}^{\infty} g_0(t - \underline{c}_a'\underline{\theta},\theta)\, g_0(t - \underline{c}'\underline{\theta},\theta)\, dt\, d\theta$$

$$= \int_{\frac{\pi}{2}-\Delta}^{\frac{\pi}{2}+\Delta} \int_{-\infty}^{\infty} g_0(t,\theta)\, g_0(t - (\underline{c}-\underline{c}_a)'\underline{\theta},\theta)\, dt\, d\theta$$

$$\triangleq a_{\Delta}(c - c_a) \qquad (3.7a)$$

Similarly in the discrete-view case,

$$a_N(c - c_a) \triangleq \bar{a}_N(c,c_a) \qquad (3.7b)$$

The ambiguity function, then, depends only on the position of any given point c relative to the actual object location $c_a \in C$. One consequence of this is that the noise n(c) is stationary, so the covariance between two points depends only on the vector difference of their locations.

3.1.1 Overall estimation error covariance

In this subsection, we investigate the statistical accuracy of the location estimate $\hat{c}_{ML}$, by considering Λ_e, the error covariance matrix for the location estimate,

$$\Lambda_e = E\{ee'\} \qquad e \triangleq \hat{c}_{ML} - c_a \tag{3.8}$$

One technique for analyzing the error covariance of maximum likelihood parameter estimates in nonlinear estimation problems is to write the error covariance as a linear combination of conditional error covariances, where each term is conditioned on the event that the parameter estimate falls into a certain subset of the overall parameter space (Van Trees, 1968). This approach is attractive because in many cases approximate conditional error covariances may be determined quite easily.

To apply this technique to the object localization problem being considered, the set of possible parameter values C is partitioned into M nonoverlapping regions $C_0, C_1, \ldots, C_{M-1}$ (for example, rectangular subsets of the plane). If E_j denotes the event that the peak of the log likelihood function lies in region C_j, then the error covariance may be written as

$$\Lambda_e = \sum_{j=0}^{M-1} \Lambda_j p_j \tag{3.9}$$

where p_j is the probability of event E_j, and Λ_j denotes the estimate error covariance conditioned on E_j.

At this point, two approximations are made in order to simplify the analysis and provide an approximate expression for the error covariance Λ_e :

1. Let $\{c_j: \ c_j \in C_j \subset C, \ j=0,1,\ldots,M-1\}$ be a set of M points, one in each region, with $c_0 = c_a \in C_a$ assumed for simplicity. Let $L_j = L(c_j)$, that is L_j is the random variable equal to the log likelihood function in (3.3) evaluated at the point c_j. From (3.5), the random vector $\underline{L} = (L_0 \ L_1 \cdots L_{M-1})$ is Gaussian with density $p(\underline{L})$ and moments

$$E\{L_j\} = a(c_j)$$

$$E\{L_i L_j\} = a(c_i - c_j) \tag{3.10}$$

The first simplification is to approximate the log likelihood function L(c) as being constant on each of the M regions, taking on the value L_j at <u>all</u> points in the region C_j, j=0,1,...,M-1. For this approximation to be good, the regions C_j should be

small in size. When L(c) is approximated as being piecewise-constant, the computation of the probabilities $p_j = \text{Prob}\{E_j\}$ is simplified,

$$p_j = \text{Prob}\{l_j > l_i \ , \forall i \neq j\}$$

$$= \int_{-\infty}^{\infty} \left[\int_{-\infty}^{L_j} \cdots \int_{-\infty}^{L_j} p(\underline{L}) \, dL_0 \cdots dL_{M-1} \right] dL_j \qquad (3.11)$$

In practice, the p_j are computationally intensive to determine when the L_j are correlated, although some work on bounds is available (Gallager and Helstrom, 1969). In the case of uncorrelated L_j (which typically arises when the regions C_j are large in size), bounds are more easily obtained, see for example Van Trees (1968), p263.

2. The conditional error covariance Λ_j in (3.9) is given by

$$\Lambda_j = \iint_{C_j} ee' \, p_{e|E_j}(e|E_j) \, de_1 de_2 \qquad (3.12)$$

Conditioned on the event E_j, $j \neq 0$ (i.e. the event that the log likelihood function peak lies in an incorrect region C_j), and assuming that L(c) is constant on the region C_j, the peak location is

equally likely to be anywhere in the region. If c_j is a representative point in C_j (e.g. the centroid) then the conditional error covariance may be approximated as

$$\Lambda_j \simeq (c_j - c_0)(c_j - c_0)' \qquad j \neq 0 \tag{3.13}$$

When the preceeding approximations are made, the error covariance in (3.9) may be written

$$\Lambda_e = \begin{bmatrix} \sigma_{11}^2 & \sigma_{12}^2 \\ \sigma_{21}^2 & \sigma_{22}^2 \end{bmatrix} \simeq \Lambda_0 p_0 + \sum_{j=1}^{M-1} (c_j - c_0)(c_j - c_0)' p_j \tag{3.14}$$

In (3.14), Λ_0 is the error covariance conditioned on the event that the peak of the log likelihood function lies in C_0, the region containing the true location point. In the following subsection, we consider this local error covariance.

3.1.2 Local error analysis

If the region C_0 is small enough so that all points in C_0 are close to the true object location c_a, the Cramer-Rao bound (Van Trees, 1968) provides an accurate estimate of the covariance matrix Λ_0, and in particular, of its diagonal elements. Specifically, for

i=1,2

$$[\Lambda_0]_{ii} \geq [J^{-1}]_{ii} \tag{3.15}$$

where J is the 2x2 Fisher's information matrix

$$[J]_{ik} = -E\left\{\frac{\partial^2 \mathscr{L}(c)}{\partial c_i \partial c_k}\right\} \tag{3.16}$$

and $\mathscr{L}(c)$ is the log likelihood function in (3.1). By substituting g(t,Θ;c) from (2.9) into (3.1) and taking derivatives, (3.16) may be written in terms of the ambiguity function as

$$[J]_{ik} = -\frac{2}{N_0}\left[\frac{\partial^2 a(c)}{\partial c_i \partial c_k}\right]_{c=0} \triangleq -\frac{2}{N_o}\beta_{ik} \tag{3.17}$$

Equation (3.17) indicates that when the object location estimate $\hat{c}_{ML}$ lies in the vicinity of the true location c_a, the estimate error can be characterized in terms of β_{ik}, the second partial derivative of the ambiguity function evaluated at the origin.

In practice, evaluation of β_{ik} by taking two derivatives of the ambiguity function may be very tedious. This is particularly true when the object relative profile $f_o(x)$ is an indicator function on some set as in Example 1, since in this case, both the integrand and the limits of integration with respect to t in (3.5) depend on c. In

the following section, we employ frequency domain analysis to develop an expression for β_{ik} which is more easily evaluated than (3.17).

3.1.3 Evaluating β_{ik} using frequency domain analysis

In this subsection, we evaluate β_{ik} in (3.17) by using frequency domain analysis. Letting $\mathscr{F}_2^{-1}\{\cdot\}$ denote the 2D inverse Fourier transform (Bracewell, 1965), and using capital letters to denote Fourier transforms, where $\omega=(\omega_1,\omega_2)$ represents a point in the frequency domain,

$$a(c) = \mathscr{F}_2^{-1}\{A(\omega)\}$$

$$= \int_{-\infty}^{\infty}\int_{-\infty}^{\infty} A(\omega_1,\omega_2)\, e^{j2\pi(\omega_1 c_1 + \omega_2 c_2)}\, d\omega_1 d\omega_2 \qquad (3.18)$$

By taking derivatives of both sides, β_{ik} in (3.17) may be obtained in terms of $A(\omega)$, the Fourier transform of the ambiguity function $a(c)$

$$\beta_{ik} = \left[\frac{\partial^2 a(c)}{\partial c_i \partial c_k}\right]_{c=0} = -4\pi^2 \mathscr{F}_2^{-1}\{\omega_i \omega_k A(\omega)\}_{c=0} \qquad (3.19)$$

In a moment, we develop an expression for $A(\omega)$ as a product of several 2D Fourier transforms. In order to do so, we first show that for each of the measurement cases, the ambiguity function a(c) may be written as

$$a(c) = \mathcal{B}(\mathcal{R}f * \mathcal{R}\tilde{f} * \xi) \tag{3.20}$$

where $\tilde{f}(x_1,x_2) \triangleq f(-x_1,-x_2)$. In this equation, the Radon space function $\xi(t,\theta)$ is a sampling function that allows the limited-view CBP (with an integral over $\frac{\pi}{2}-\Delta<\theta<\frac{\pi}{2}+\Delta$) and the discrete-view CBP (with a sum over $\theta_j = j\pi/N$) to be written as a CBP over the continuous interval $0\leq\theta<\pi$.

Claim 1: In the continuous-view case, ξ in (3.20) is given by

$$\xi_\Delta(t,\theta) = \delta(t)\cdot \text{rect}\left(\frac{\pi-2\theta}{4\Delta}\right) \qquad 0<\Delta\leq\frac{\pi}{2} \tag{3.21}$$

where

$$\text{rect}(\tau) = \begin{cases} 1 & \text{if } |\tau|\leq 1/2 \\ 0 & \text{otherwise} \end{cases} \tag{3.22}$$

The function $\xi_\Delta: \mathcal{Y} \rightarrow R$ in (3.21) is a truncated impulse sheet in Radon space, that is, it is the product of an impulse sheet along the θ axis and a 2D function that is zero everywhere except when $\theta\in[\frac{\pi}{2}-\Delta,\frac{\pi}{2}+\Delta)$, where it equals unity.

Proof: See Appendix 1

Claim 2: In the discrete-view case, ξ in (3.20) is given by

$$\xi_N(t,\theta) = \sum_{j=0}^{N-1} \delta(t,\theta - \theta_j) \qquad \theta_j = j\pi/N \tag{3.23}$$

which is a train of N two-dimensional impulses uniformly spaced on $[0, \pi)$ along the θ axis in $\mathcal{Y}$.

Proof: See Appendix 1

The ambiguity function Fourier transform $A(\omega)$ in (3.19) may be obtained by noting that the ambiguity function is obtained by a convolution back-projection operation, since it is known that convolution back-projection may be written as a 2D convolution (Davison and Grunbaum, 1981). In particular, if $F(\omega)$ is the 2D Fourier transform of the object relative profile $f_o(x)$, it is shown in Appendix 2 that

$$A(\omega) = F(\omega)\tilde{F}(\omega)B_\xi(\omega) \tag{3.24}$$

Here $\tilde{F}(\omega_1,\omega_2) = \mathcal{F}_2\{\tilde{f}\} = F(-\omega_1,-\omega_2)$ and $B_\xi(\omega)$ is the 2D Fourier transform of $b_\xi(x)$, the back-projection of the Radon space function $\xi(t,\theta)$.

Combining (3.19) and (3.24), β_{ik}, the second partial derivative of the ambiguity function a(c) evaluated at the origin, is given by

$$\beta_{ik} = -4\pi^2 \mathcal{F}_2^{-1}\{\omega_i\omega_k F(\omega)\tilde{F}(\omega)B_\xi(\omega)\}_{c=0} \tag{3.25}$$

3.2 THE BACK-PROJECTION $b_\xi(x)$ AND ITS 2D FOURIER TRANSFORM

Before continuing our investigation into the error analysis, we take a moment to discuss the back-projection $b_\xi(x)$ and its 2D Fourier transform $B_\xi(\omega)$.

3.2.1 Continuous-view measurements

The back-projection of the truncated impulse sheet ξ_Δ is derived in Appendix 1, and is given by

$$b_{\xi,\Delta}(x) = \begin{cases} \frac{1}{\|x\|} & \text{if } |\phi| \le \Delta \\ 0 & \text{otherwise} \end{cases} \tag{3.26}$$

where ϕ is the angular polar coordinate of x, $\phi \in [-\frac{\pi}{2}, \frac{\pi}{2})$. In particular, in the full-view case where $\Delta = \frac{\pi}{2}$, the back-projection of $\xi_{\frac{\pi}{2}}$ is $b_{\xi,\frac{\pi}{2}}(x) = \frac{1}{\|x\|}$.

The 2D Fourier transform of $b_{\xi,\Delta}(x)$ is also derived in Appendix 1, and is given by

$$B_{\xi,\Delta}(\omega) = \begin{cases} \frac{1}{\|\omega\|} & \text{if } |\psi + \frac{\pi}{2}| \leq \Delta \\ 0 & \text{otherwise} \end{cases} \tag{3.27}$$

where ψ is the angular polar coordinate of ω, $\psi \in [-\frac{\pi}{2}, \frac{\pi}{2})$. In the full-view case, $B_{\xi,\frac{\pi}{2}}(\omega) = \frac{1}{\|\omega\|}$.

3.2.2 Discrete-view measurements

The back-projection of the impulse train ξ_N in (3.23), denoted $b_{\xi,N}(x)$, is derived in Appendix 1, and is given by

$$b_{\xi,N}(x) = \sum_{j=0}^{N-1} \delta(\underline{x}'\underline{\theta}_j) \tag{3.28}$$

This is a so-called spoke function (Riederer et al., 1978), consisting of the sum of N impulse sheets on lines through the origin uniformly spaced in angle, i.e. lines $l(t,\theta) = l(0,\theta_j)$, $j=0,1,\ldots,N-1$.

Finally, the 2D Fourier transform of $b_{\xi,N}(x)$, denoted $B_{\xi,N}(\omega)$, is also derived in Appendix 1, and is given by another spoke function

$$B_{\xi,N}(\omega) = \sum_{j=0}^{N-1} \delta(\underline{\omega}'\underline{\theta}_j^{\perp}) \qquad (3.29)$$

where $\underline{\theta}_j^{\perp} = (-\sin\theta_j \ \cos\theta_j)' = (\cos(\theta_j+\frac{\pi}{2}) \ \ \sin(\theta_j+\frac{\pi}{2}))'$ is a unit vector orthogonal to the unit vector $\underline{\theta}_j$. In Chapter 4, several specific examples are considered in which the ambiguity function in (3.20) is evaluated for the full-view, limited-view and discrete-view measurement cases.

3.3 MEASUREMENT APERTURE FUNCTION

In (2.17), the Radon space measurements are modeled as noisy projections. It should be noted that because the observations are taken along infinitely narrow lines of integration, this measurement system has an infinite bandwidth. As will be seen in Chapter 4, this leads to a degenerate Cramer-Rao bound in (3.15) for objects with a discontinuous density profile. In practice, however, the measurement system is certainly bandlimited because observations cannot be taken along infinitely narrrow lines of integration. The measurements may be more accurately modeled by replacing the projection measurement signal $g(t,\theta)$ in (2.7) with $g(t,\theta) * h(t)$ where $h(t)$ is a nonimpulsive aperture function (Bracewell, 1956); this leads to smearing or bandlimiting of the projections in the t direction.

Various aperture functions may be considered, for example the rectangular pulse aperture corresponding to strip integration as considered by Bracewell (1956), or a sinc aperture function

$$h(t) = \frac{\sin 2\pi Wt}{2\pi Wt} \tag{3.30}$$

corresponding to projections having a spatial bandwidth of W cycles per unit distance in the t direction.

An aperture function h(t) is easily included in the analysis just developed by introducing another t-direction convolution in the ambiguity function expression in (3.20),

$$a(c) = \mathcal{B}(\mathcal{R}f * h * \mathcal{R}\tilde{f} * \xi) \tag{3.31}$$

It should be noted that this expression for the ambiguity function corresponds to applying the matched filtering template (i.e. convolving kernel for the log likelihood evaluation) $\mathcal{R}f$ when the measurement signal is actually $\mathcal{R}f*h$, i.e. the matched filtering is performed as though the aperture function is impulsive. If the measurement aperture function h(t) is known precisely, then one would perform matched filtering with the kernel $\mathcal{R}f*h$. The effect of this on (3.31) is to replace h with h*h; when h(t) is the sinc function in (3.30), h*h is the same sinc

function, and the analysis is unaltered by replacing h with h*h.

It is shown in Appendix 3 that when the aperture function h(t) is nonimpulsive, the ambiguity function in (3.31) is simply a 2D filtered version of the ambiguity function in (3.20), which was obtained assuming an impulsive aperture function. It is also shown in Appendix 3 that the 2D Fourier transform for a(c) in (3.31) is given by

$$A(\omega) = F(\omega) R_h(\omega) \tilde{F}(\omega) B_\xi(\omega) \tag{3.32}$$

where $R_h(\omega)$ is a circularly-symmetric function with a central section given by $H(\omega)$, the 1D Fourier transform of h(t). The 2D inverse Fourier transform of $R_h(\omega)$ will be denoted as $r_h(x)$.

It is easily verified using the projection-slice theorem (Mersereau and Oppenheim, 1974) that for the 2D functions f and r_h, the projection of f at any angle, smeared by the aperture function h=$\mathscr{R}r_h$ (i.e. $\mathscr{R}f*\mathscr{R}r_h = \mathscr{R}f*h$) is identical to the projection at that angle of the two-dimensionally convolved functions (i.e. $\mathscr{R}(f**r_h)$). Consequently, a nonimpulsive aperture function may be used in modeling either (1) a 2D density function f from which smeared projections $\mathscr{R}f*h$ (projections $\mathscr{R}f$ smeared with aperture function h(t)) are obtained or (2) a 2D density

function $f^{**}r_h$ which is projected without smearing.

3.4 SUMMARY

At this point, an expression is available in (3.14) for Λ_e as a linear combination of conditional error covariances which may be used to approximate Λ_e. In this expression, the probabilities p_j are computed from (3.11), or some approximation thereof, and the conditional error covariances are approximated by (3.13) or bounded as in (3.15), where the Fisher's information matrix entries are obtained using the inverse Fourier transform in (3.25).

Prior to evaluating these expressions, the regions $C_j \subset C$ and points $c_j \in C_j$ must be appropriately chosen. In the next chapter, we reconsider Example 1 (the pillbox object) and Example 3 (the Gaussian object); through these examples we will be able to demonstrate the systematic use of the performance analysis machinery we have just developed. In particular, the location estimation ambiguity function is evaluated, the regions C_j and points c_j are selected, and an approximation to the estimate error covariance is obtained.

APPENDIX 1 -- Radon space sampling function

Proof of Claim 1:

From (3.7a), the continuous-view ambiguity function is

$$a_\Delta(c) = \int_{\frac{\pi}{2}-\Delta}^{\frac{\pi}{2}+\Delta}\int_{-\infty}^{\infty} g_0(t,\theta)\, g_0(t - \underline{c}'\underline{\theta},\theta)\, dt d\theta$$

$$= \int_0^{\pi} \text{rect}\left[\frac{\pi-2\theta}{4\Delta}\right] \int_{-\infty}^{\infty} g_0(t,\theta)\, g_0(t - \underline{c}'\underline{\theta},\theta)\, dt d\theta$$

$$= \mathcal{B}\left[\text{rect}\left[\frac{\pi-2\theta}{4\pi}\right] (g_0 * \tilde{g}_0)\right]$$

where $\tilde{g}_0(t,\theta) \triangleq g_0(-t,\theta)$.

$$a_\Delta(c) = \mathcal{B}\left[g_0 * \left\{\int_{-\infty}^{\infty} \tilde{g}_0(\tau,\theta)\, \delta(t-\tau)\, \text{rect}\left[\frac{\pi-2\theta}{4\Delta}\right] d\tau\right\}\right]$$

$$= \mathcal{B}\left[g_0 * \left\{\int_{-\infty}^{\infty} \tilde{g}_0(\tau,\theta)\, \xi_\Delta(t-\tau,\theta)\, d\tau\right\}\right]$$

$$= \mathcal{B}(g_0 * \tilde{g}_0 * \xi_\Delta) \qquad \text{(A1.1)}$$

which agrees with (3.20), since $\mathcal{R}\tilde{f} = \tilde{g}_0$.

Proof of Claim 2:

The discrete-view ambiguity function is, from (3.7b),

$$a_N(c) = \sum_{j=0}^{N-1} \int_{-\infty}^{\infty} g_0(t,\theta_j)\, g_0(t - \underline{c}'\underline{\theta}_j,\theta_j)\, dt$$

$$= \int_0^{\pi} \sum_{j=0}^{N-1} \delta(\theta - \theta_j) \int_{-\infty}^{\infty} g_0(t,\theta)\, g_0(t - \underline{c}'\underline{\theta},\theta)\, dt\, d\theta$$

$$= \mathcal{B}\left[\left\{ \sum_{j=0}^{N-1} \delta(\theta - \theta_j) \right\} (g_0 * \tilde{g}_0) \right]$$

$$= \mathcal{B}\left[g_0 * \int_{-\infty}^{\infty} \tilde{g}_0(\tau,\theta) \left\{ \sum_{j=0}^{N-1} \delta(t - \tau, \theta - \theta_j) \right\} d\tau \right]$$

$$= \mathcal{B}\left[g_0 * \int_{-\infty}^{\infty} \tilde{g}_0(\tau,\theta)\, \xi_N(t - \tau,\theta)\, d\tau \right]$$

$$= \mathcal{B}(\, g_0 * \tilde{g}_0 * \xi_N) \qquad \text{(A1.2)}$$

which agrees with (3.20).

Back-projection of the truncated impulse sheet

From the definition of the back-projection operator in (1.9), the back-projection of the truncated impulse sheet $\xi_\Delta(t,\theta)$ in (3.21), which is denoted $b_{\xi,\Delta}(x)$ is given by

$$b_{\xi,\Delta}(x) = \int_0^{\pi} \xi_\Delta(\underline{x}'\underline{\theta},\theta)\, d\theta = \int_0^{\pi} \delta(\underline{x}'\underline{\theta})\ \mathrm{rect}\left[\frac{\pi - 2\theta}{4\Delta}\right] d\theta$$

$$= \int_{\frac{\pi}{2}-\Delta}^{\frac{\pi}{2}+\Delta} \delta(\underline{x}'\underline{\theta})\, d\theta = \int_{\frac{\pi}{2}-\Delta}^{\frac{\pi}{2}+\Delta} \delta(r\cos(\theta - \phi))\, d\theta \qquad \text{(A1.3)}$$

where (r,ϕ) are the polar coordinates of x, $r \in (-\infty,\infty)$, $\phi \in [-\frac{\pi}{2}, \frac{\pi}{2})$. By a change of variable

$$b_{\xi,\Delta}(x) = \int_{r\cos(\frac{\pi}{2} - \phi - \Delta)}^{r\cos(\frac{\pi}{2} - \phi + \Delta)} \frac{\delta(\tau)\,d\tau}{\sqrt{r^2 - \tau^2}} \qquad \text{(A1.4)}$$

which provides

$$b_{\xi,\Delta}(x) = \begin{cases} \frac{1}{\|x\|} & \text{if } |\phi| \le \Delta \\ 0 & \text{otherwise} \end{cases} \qquad \text{(A1.5)}$$

Fourier transform of $b_{\xi,\Delta}(x)$

The 2D Fourier transform of $b_{\xi,\Delta}(x)$ in (A1.5), which is denoted $B_{\xi,\Delta}(\omega)$, is given in terms of the polar coordinates (r,ϕ) as

$$B_{\xi,\Delta}(\omega) = \int_{-\Delta}^{\Delta} \int_{-\infty}^{\infty} \frac{1}{|r|} e^{-j2\pi\, r(\omega_1\cos\phi + \omega_2\sin\phi)} |r|\,dr\,d\phi$$

$$= \int_{-\Delta}^{\Delta} d\phi \int_{-\infty}^{\infty} e^{-j2\pi\, r\, \underline{\omega}'\underline{\phi}}\, dr \qquad \text{(A1.6)}$$

where $\underline{\phi} = (\cos\phi \ \sin\phi)'$ and $\underline{\omega} = (\omega_1\ \omega_2)'$.

The second integral in (A1.6) is the 1D Fourier transform, evaluated at $\underline{\omega}'\underline{\phi}$, of a function that is unity for all r. Thus,

$$B_{\xi,\Delta}(\omega) = \int_{-\Delta}^{\Delta} \delta(\underline{\omega}'\underline{\emptyset})\, d\emptyset \qquad \text{(A1.7)}$$

Equation (A1.7) has the same form as (A1.3) and by a change of variable yields

$$B_{\xi,\Delta}(\omega) = \begin{cases} \frac{1}{\|\omega\|} & \text{if } |\psi + \frac{\pi}{2}| \leq \Delta \\ 0 & \text{otherwise} \end{cases} \qquad \text{(A1.8)}$$

where ψ is the angular polar coordinate of the point ω.

Back-projection of the N-point impulse train

Using the definition of the back-projection operator in (1.9), the back-projection of $\xi_N(t,\Theta)$, which is denoted $b_{\xi,N}(x)$, is

$$b_{\xi,N}(x) = \int_0^{\pi} \xi_N(\underline{x}'\underline{\Theta},\Theta)\, d\Theta$$

$$= \int_0^{\pi} \sum_{j=0}^{N-1} \delta(\underline{x}'\underline{\Theta},\Theta - \Theta_j)\, d\Theta = \sum_{j=0}^{N-1} \delta(\underline{x}'\underline{\Theta}_j) \qquad \text{(A1.9)}$$

Fourier transform of $b_{\xi,N}(x)$

The 2D transform of $b_{\xi,N}(x)$ in (A1.9), denoted $B_{\xi,N}(\omega)$ is given by

$$B_{\xi,N}(\omega) = \int_{-\infty}^{\infty}\int_{-\infty}^{\infty}\sum_{k=0}^{N-1}\delta(\underline{x}'\underline{\theta}_k)\ e^{-j2\pi\ \underline{x}'\underline{\omega}}\ dx_1dx_2 \qquad \text{(A1.10)}$$

By the change of variable $\underline{t} = G(\theta)\underline{x}$, where

$$G(\theta) = \begin{bmatrix} \cos\theta & \sin\theta \\ -\sin\theta & \cos\theta \end{bmatrix} \qquad \text{(A1.11)}$$

(A1.10) becomes

$$B_{\xi,N}(\omega) = \sum_{k=0}^{N-1}\int_{-\infty}^{\infty}\int_{-\infty}^{\infty}\delta(t_1)\ e^{-j2\pi\ \underline{t}'G(\theta_k)\underline{\omega}}\ dt_1dt_2$$

$$= \sum_{k=0}^{N-1}\int_{-\infty}^{\infty}\delta(t_1)e^{-j2\pi t_1\underline{\omega}'\underline{\theta}_k}\ dt_1\int_{-\infty}^{\infty}e^{-j2\pi t_2\underline{\omega}'\underline{\theta}_k^{\perp}}\ dt_2 \qquad \text{(A1.12)}$$

where $\underline{\theta}_k^{\perp} = (-\sin\theta_k\ \cos\theta_k)'$. The first integral in (A1.12) is unity and the second integral is of the same type as the second integral in (A1.6), yielding

$$B_{\xi,N}(\omega) = \sum_{k=0}^{N-1}\delta(\underline{\omega}'\underline{\theta}_k) \qquad \text{(A1.13)}$$

APPENDIX 2 -- Calculating the ambiguity function Fourier transform $A(\omega)$

In terms of the Radon transform and back-projection operators $\mathcal{R}$ and $\mathcal{B}$ introduced in Chapter 1, the CBP in (1.9) with convolving kernel $z(t,\theta)$ may be written as

$$\hat{f}(x) = \int_0^{\pi} \int_{-\infty}^{\infty} g(t,\theta) z(t - \underline{x}'\underline{\theta},\theta)\, dt d\theta$$

$$= \int_0^{\pi} \int_{-\infty}^{\infty} g(t,\theta) \tilde{z}(\underline{x}'\underline{\theta} - t,\theta)\, dt d\theta = \mathcal{B}(\mathcal{R} f * \tilde{z}) \qquad \text{(A2.1)}$$

where $\tilde{z}(t,\theta) = z(-t,\theta)$, and * denotes 1D convolution in t

$$[z_1 * z_2](\tau) = \int_{-\infty}^{\infty} z_1(t,\theta) z_2(\tau - t,\theta)\, dt \qquad \text{(A2.2)}$$

Letting ** denote 2D convolution, it is shown in Davison and Grunbaum (1981) that (A2.1) may be written as

$$\mathcal{B}(\mathcal{R} f * \tilde{z}) = f ** \mathcal{B}(\tilde{z}) \qquad \text{(A2.3)}$$

that is, CBP of $\mathcal{R}f$ with convolving kernel $z(t,\theta)$ may be written as the 2D convolution of $f(x)$ with the back-projection of $\tilde{z}(t,\theta)$.

The relationship in (A2.3) leads to an expression for the Fourier transform of the ambiguity function since, as was shown in Appendix 1 for the continuous- and discrete-view measurement cases, the ambiguity function

may be written as the back-projection of a series of convolved functions. In particular, using the previously introduced operators, the ambiguity function may be written as

$$a(c) = \mathcal{B}(\mathcal{R}f * \mathcal{R}\tilde{f} * \xi) \tag{A2.4}$$

Here, f is $f_o(x)$, the object relative profile, $\tilde{f}(x_1,x_2) \triangleq f(-x_1,-x_2)$, and ξ is the sampling function given in (3.21) and (3.23) for each of the two measurement cases, respectively. Using (A2.3) twice, (A2.4) becomes

$$a(c) = f ** \mathcal{B}(\mathcal{R}\tilde{f} * \xi) = f ** \tilde{f} ** \mathcal{B}(\xi)$$

$$\triangleq f ** \tilde{f} ** b_\xi \tag{A2.5}$$

and taking 2D Fourier transforms

$$A(\omega) = F(\omega)\tilde{F}(\omega)B_\xi(\omega) \tag{A2.6}$$

where $\tilde{F}(\omega_1,\omega_2) \triangleq F(-\omega_1,-\omega_2)$. The relationship in equation (A2.6) is shown schematically in Figure A.1.

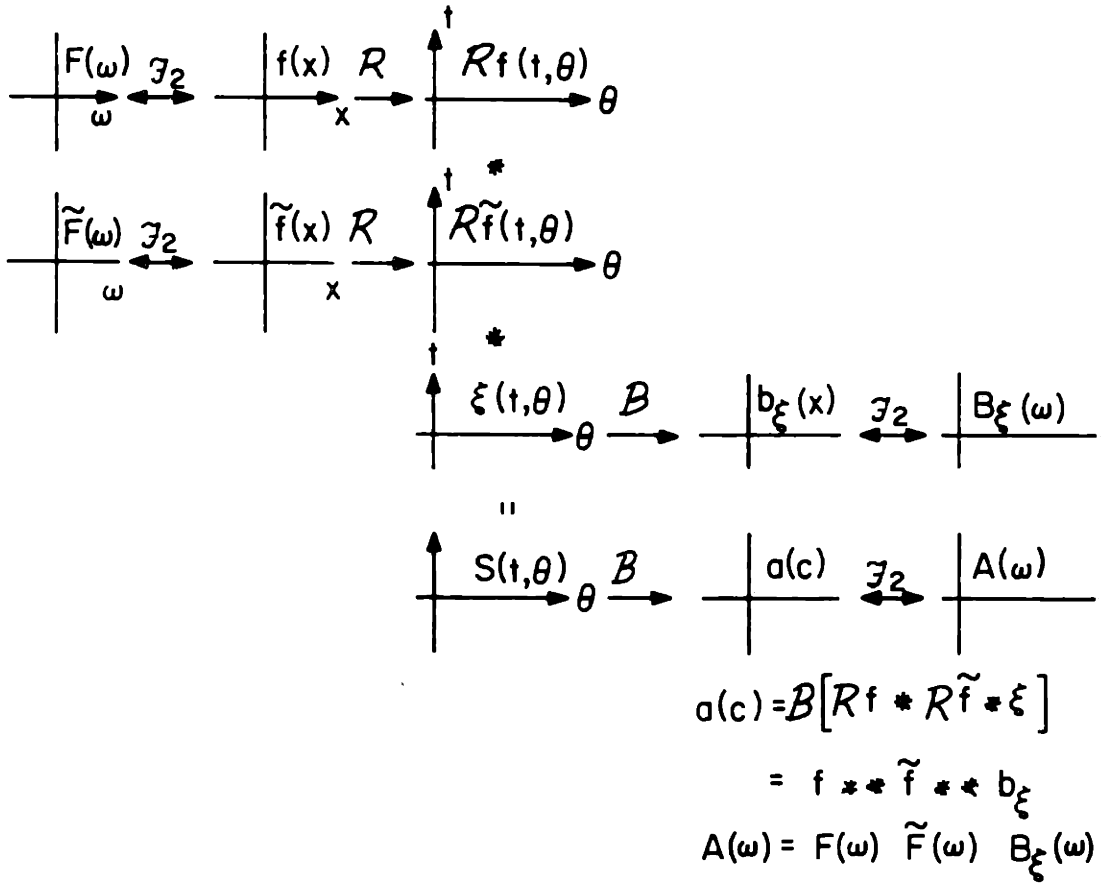

Figure A.1 Schematic representation of the relationship in (A2.6).

APPENDIX 3 -- Ambiguity function for a nonimpulsive aperature function

The ambiguity function in (3.31) is the back-projection of a Radon-space function resulting from four t-direction convolutions in Radon space. By applying (A2.3) three times, (3.31) becomes

$$a(c) = f \;**\; r_h \;**\; \tilde{f} \;**\; b_\xi \tag{A3.1}$$

and taking 2D Fourier transforms

$$A(\omega) = F(\omega) R_h(\omega) \tilde{F}(\omega) B_\xi(\omega) \tag{A3.2}$$

By the projection-slice theorem (Mersereau and Oppenheim, 1974), $R_h(\omega)$ is a circularly symmetric function (because h is Θ-independent) with a central section given by $H(\omega)$, the 1D Fourier transform of h(t). When the aperture function h(t) is nonimpulsive, then, the ambiguity function in (A3.1) is simply a two-dimensionally filtered version of the ambiguity function in (A2.5), which was obtained assuming an impulsive aperture function.

CHAPTER 4

SINGLE OBJECT LOCALIZATION
EXAMPLES AND SIMULATIONS

4.0 EXAMPLE 1 (continued)

Reconsider Example 1 in Chapter 2, involving the constant-density pillbox object with radius R. Suppose the object is located at the point $c_a \epsilon C \subset R^2$, where C is a disk of radius T

$$C = D(T) \triangleq \{x: \quad \|x\| \leq T \} \tag{4.1}$$

Since many of the expressions in this chapter will depend on T and R only through their ratio, we define the parameter

$$k \triangleq T/R \tag{4.2}$$

For example, if the object radius is one tenth of the radius of C, k equals 10; as the object size decreases, the value of k increases, and k is always greater than one.

When the object is located at the origin, its density function (i.e. its relative profile multiplied by the contrast d) is given by

$$f(x) = d \cdot f_o(x;R) = \begin{cases} d & \text{if } \|x\| < R \\ 0 & \text{otherwise} \end{cases} \tag{4.3}$$

This profile is circularly symmetric and consequently its 2D Fourier transform is also circularly symmetric (Bracewell, 1965). Letting $f(r)$ and $F(\rho)$ denote the profile in (4.3) and its 2D Fourier transform as functions of their radial polar coordinates only,

$$f(r) = d \cdot \text{rect}(r/2R) \tag{4.4}$$

where rect(t) is defined in (3.22). The function $F(\rho)$, known as the Fourier-Bessel or Hankel transform of order zero of $f(r)$ (Bracewell, 1965) is given by

$$F(\rho) = 2\pi \int_0^\infty f(r)\ J_0(2\pi\, r\rho)\ r\ dr$$

$$= (Rd/\rho)\ J_1(2\pi\, R\rho) \tag{4.5}$$

Here, $J_0(\rho)$ and $J_1(\rho)$ are Bessel functions of the first kind of order zero and one respectively.

In this example, we will consider three measurement cases, namely the full-view case, the limited view case with $\Delta < \frac{\pi}{2}$ and the discrete-view case. In all cases, we will take the measurements to be noisy projections that are smoothed by 2W times the sinc aperture function in (3.30). The 1D Fourier transform of the aperture function

is then given by

$$H(\omega) = \text{rect}(\omega/2W) \tag{4.6}$$

4.0.1 Full-view case

When projections are available over the full range of angles $\theta \in [0, \pi)$ the ambiguity function for the object location, obtained from (3.32), is

$$a(x) = f(x) \;**\; r_h(x) \;**\; \tilde{f}(x) \;**\; b_{\xi,\frac{\pi}{2}}(x) \tag{4.7}$$

where ** denotes 2D convolution, and from (3.26)

$$b_{\xi,\frac{\pi}{2}}(x) = \frac{1}{\|x\|} \tag{4.8}$$

The ambiguity function is circularly symmetric, since it is the convolution of four circularly symmetric functions. Letting a(r) denote the ambiguity function in terms of its radial polar coordinate only, it may be expressed in terms of the inverse Hankel transform (Bracewell, 1965) as

$$a(r) = 2\pi \int_0^\infty A(\rho)\, J_0(2\pi r\rho)\rho \;\; d\rho$$

$$= 2\pi \int_0^\infty F^2(\rho)\, H(\rho)\, J_0(2\pi r\rho)\, d\rho$$

$$= 2\pi R^2 d^2 \int_0^W J_1^2(2\pi R\rho)\ J_0(2\pi r\rho)\ (1/\rho^2)\ d\rho$$

By a change of variable,

$$a(r) = 2\pi d^2 R^3 \int_0^{RW} J_1^2(2\pi\rho)\ J_0(2\pi\rho r/R)\ (1/\rho^2)\ d\rho$$

$$= \left[\frac{16}{3}\pi d^2 R^3\right] \frac{3}{8} \int_0^{RW} J_1^2(2\pi\rho)\ J_0(2\pi\rho r/R)\ (1/\rho^2)\ d\rho$$

$$\triangleq \mathscr{E}\, a^*(r/R, RW) \qquad (4.9)$$

where $\mathscr{E}$ is the energy in the Radon transform (i.e. the energy in the signal part of the measurements),

$$\mathscr{E} = \int_0^{\pi}\int_{-R}^{R} \left[2d\sqrt{R^2 - t^2}\right]^2 dt d\theta = \frac{16}{3}\pi d^2 R^3 \qquad (4.10)$$

The function a^* is seen to depend on the spatial bandwidth W only through the radius-bandwidth product RW; a^* is plotted in Figure 4.1 for several values of RW.

The radius-bandwidth product RW may be interpreted in the following way; suppose at frequency W there are n cycles in the disk diameter distance 2T. Then W=n/2T and by the definition of k in (4.2), the radius-bandwidth product RW=n/2k may be seen to equal one half the number of cycles at frequency W intercepted by the circular

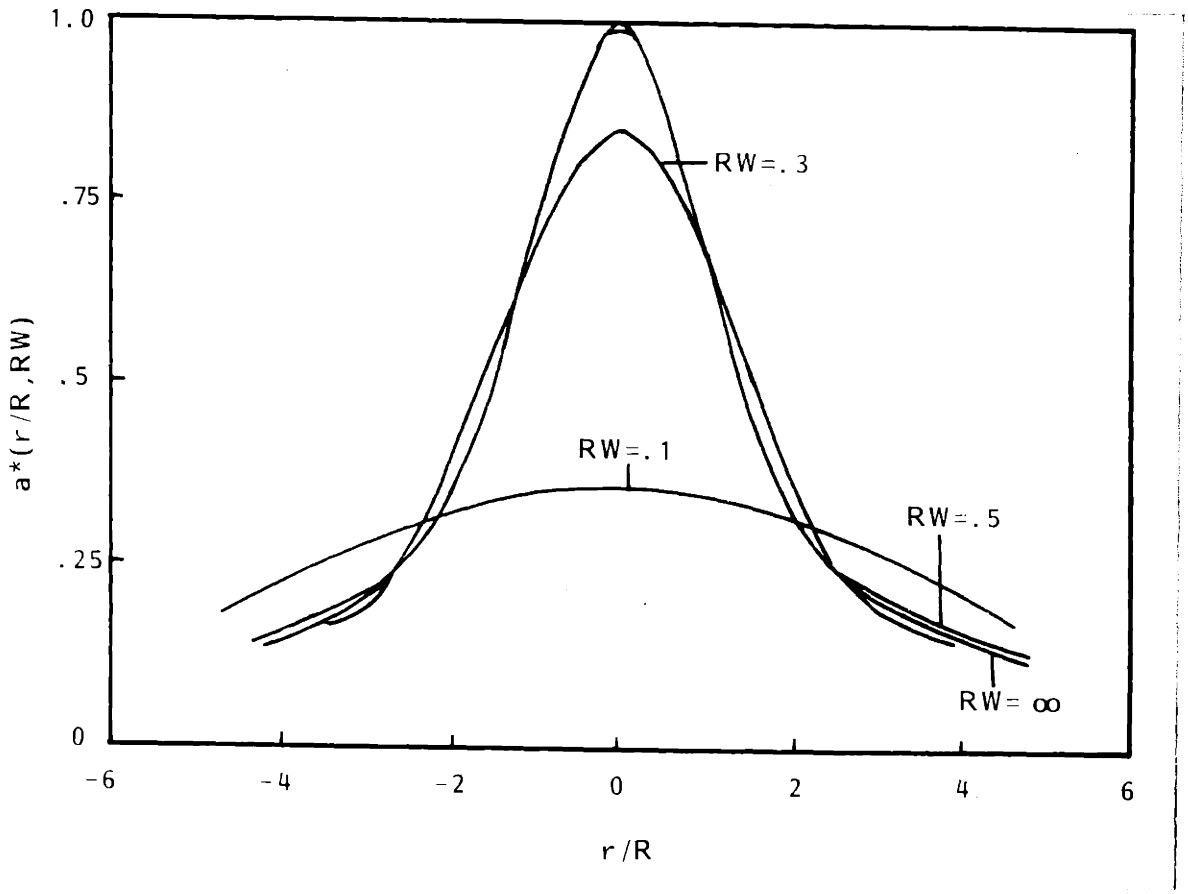

Figure 4.1 $a^*(r/R,RW)$ versus r/R.

object; said another way, the radius-bandwidth product is equal to the object radius R expressed as a number of wavelengths at frequency W.

According to Figure 4.1, the general shape of the location ambiguity function is virtually independent of the radius-bandwidth product when its value exceeds 0.5, i.e. whenever the object diameter exceeds one wavelength at frequency W. As we will show momentarily, only values

of RW in excess of 0.5 are of interest in this analysis; therefore, for the global analysis (see equation (3.10)) we will for simplicity use the ambiguity function values from the RW=∞ curve in Figure 4.1. It should be noted, however, that although for values of RW$\geq$0.5 the general shape of the ambiguity function is independent of RW, the detailed behavior of the ambiguity function is <u>not</u> independent of RW. In particular, because f(x) is discontinuous, a(r) is not twice differentiable when RW=∞ (but it is when RW is finite); consequently, the RW value will enter the Cramer-Rao bound calculation explicitly. We will discuss this point more thoroughly after the value of β_{ik} in (3.17) has been evaluated.

In this example, we will evaluate the localization performance assuming representative values of object size R=T/k and measurement system bandwidth W. In practice (for example with parallel-ray medical CAT scanners) measurements at any angular orientation are typically taken along 100 to 300 parallel lines, which corresponds at the Nyquist sampling rate to a t-direction spatial bandwidth of 50 to 150 cycles in the distance 2T. Consequently, n will be taken to be 50 in this analysis, and the performance will be evaluated for three object sizes (k=5,10,25) with corresponding RW values of 5, 2.5 and 1, all of which are larger than 0.5.

As was discussed in Chapter 3, an approximation to the error covariance of the location estimate will be obtained by partitioning the parameter space C=D(T) into M rectangular regions C_j, where c_j is a point inside C_j, and then evaluating the linear combination of conditional error covariances in (3.14). For the case being considered, C=D(T) will be partitioned into square regions of side length 2R, centered at the points

$$c_j \in \{(2Rm,2Rn): \quad (2Rm,2Rn)\in D(T),\ m,n \text{ integer}\}$$

The value of region size 2R, although somewhat arbitrarily chosen, seems appropriate in view of the discussion in Chapter 3. In particular, the regions C_j are small enough so that the log likelihood function L(c) can, for the purposes of global error analysis, be reasonably approximated by a piecewise constant function on regions C_j, yet large enough so that the statistical correlation between random variables $L_j=L(c_j)$ is small enough so that the probabilities p_j in (3.11) may be easily approximated, as we discuss shortly. Furthermore, for the local error analysis, the fine structure of L(c) is approximately quadratic, so that the Cramer-Rao bound provides a good estimate of the local error covariance.

When the regions C_j are squares having side length 2R, the number of regions in the disk D(T) is approximately the ratio of the disk area πT^2 to the region area $4R^2$, or using k in (4.2),

$$M \simeq \frac{\pi T^2}{4R^2} = \frac{\pi}{4} k^2 \tag{4.11}$$

For the values of k to be considered in this example (namely 5, 10, and 25), M in (4.11) takes on values of approximately 20, 80 and 490 respectively.

To proceed with evaluation of the approximate error covariance in (3.14), the probabilities p_j in (3.11) and the conditional error covariance Λ_0 are needed. Considering the first of these, the set of random variables $L_j = L(c_j)$ are jointly Gaussian and as indicated in (3.10) and Figure 3.1, have nonzero mean $E\{L_j\}$ and nonzero correlation $E\{L_iL_j\}$ for all i,j. Because the lattice point samples L_j are correlated, determination of the probabilities p_j in (3.11) is computationally intensive, involving an M-dimensional numerical integration if evaluated directly.

In this example, we will take advantage of the fact that the coefficient of correlation between L_i and L_j, $i \neq j$ is always less than 0.35, that is

$$\lambda_{ij} = \frac{E\{(L_i - E\{L_i\})(L_j - E\{L_j\})\}}{\sqrt{E\{(L_i - E\{L_i\})^2\}E\{(L_j - E\{L_j\})^2\}}}$$

$$= \frac{1}{\mathscr{E}} a(c_i - c_j) < 0.35 \text{ if } i \neq j \qquad (4.12)$$

We will neglect this correlation in this example, and approximate the random variables L_i and L_j as being uncorrelated when $i \neq j$. This is equivalent to assuming that the RW=∞ ambiguity function a(c) shown in Figure 4.1 equals zero for $r \geq 2R$.

The errors introduced by this approximation are minor, and in fact, this approximation makes the results somewhat pessimistic in one sense. Specifically, the probability distributions of the L_j, conditioned on $c_a=c_0$, are identical for j=1,2,...,M-1 when the L_j are approximated as being uncorrelated. If the peak lies in an incorrect region, under this approximation it is equally likely to occur in <u>any</u> one of the regions C_1, C_2,..., C_{M-1}, and

$$p_j = \frac{1-p_o}{M-1} \qquad j=1,2,...,M-1 \qquad (4.13)$$

Actually, however, since the ambiguity function is positive and monotone decreasing away from the origin, if the peak lies in an incorrect region, it will be more

likely to lie in a region close to the location of the true object, rather than far away.

Under the approximation of uncorrelated L_j, a simple approximation for the probabilities p_j in (3.11) may be easily obtained. If the true object location c_a is c_0, then the bound in Van Trees (1968) p. 263, may be used to approximate the probability of error, $1-p_0$, as

$$\text{Prob(error)} = 1 - p_0 = 1 - \text{Prob}(l_0 > l_j \ , \forall j \neq 0)$$

$$\simeq \frac{M-1}{\sqrt{2\pi \mathscr{E}/N_0}} \exp(-\frac{\mathscr{E}}{2N_0}) \qquad (4.14)$$

While the last line is an upper bound on the error probability, it is quite tight for values of $\mathscr{E}/N_0$ in excess of five or so (Van Trees, 1968); since in this example, performance will be assessed for SNR values greater than five, the expression in (4.14) is treated as an accurate approximation to the error probabilty, rather than as a bound.

For the case where the object is located at the origin (other object locations may be similarly considered, as discussed shortly), the approximate error covariance in (3.14) becomes

$$\Lambda_e \simeq \Lambda_0 p_0 + (1 - p_0) \sum_{j=1}^{M-1} \left(\frac{1}{M-1}\right) c_j c_j' \qquad (4.15)$$

The (M-1)-term summation corresponds to the covariance of a discrete 2D random variable which is equally likely to occur at any one of M-1 points on the lattice

$$\{(2Rm,2Rn): \quad (2Rm,2Rn) \in D(T),\ m,n \text{ integer, not both zero}\} \qquad (4.16)$$

A good approximation to this covariance may be obtained by considering a 2D continuous random variable uniformly distributed on the disk D(T); it has covariance $(T^2/4)I$, where I is a 2x2 identity matrix. Using this approximation, (4.15) becomes

$$\Lambda_e \simeq \Lambda_0 p_0 + (1 - p_0)(T^2/4)I \qquad (4.17)$$

Equation (4.17) is an approximation that applies when the actual object is located at the origin; for other actual object locations c_a, the $(T^2/4)I$ term is replaced by the second moment of $c-c_a$, where c is a 2D continuous random variable uniformly distributed on the disk D(T). This second moment is given by

$$\begin{bmatrix} T^2/4 + c_{a1}^2 & c_{a1}c_{a2} \\ c_{a1}c_{a2} & T^2/4 + c_{a2}^2 \end{bmatrix} \qquad (4.18)$$

In order to keep the present analysis simple, we will consider only the case where the true object location is the origin.

The next step in the performance calculation is the computation of the 2x2 Fisher's information matrix J, so that the entries of Λ_0 may be bounded using inequality (3.15). From (3.17), the ikth entry in the Fisher's information matrix is $\frac{-2}{N_0}\beta_{ik}$ where from (3.19), (3.32), and (4.5)

$$\beta_{ik} = -\mathcal{F}_2^{-1}\left\{\omega_i\omega_k \frac{(2\pi\ Rd)^2}{\|\omega\|^3} J_1^2(2\pi R\|\omega\|)\ R_h(\|\omega\|)\right\}_0$$

$$= -(2\pi Rd)^2 \int_{-\infty}^{\infty}\int_{-\infty}^{\infty} \omega_i\omega_k \frac{1}{\|\omega\|^3} J_1^2(2\pi R\|\omega\|) R_h(\|\omega\|)\, d\omega_1 d\omega_2$$

In terms of polar coordinates (ρ,ψ),

$$\beta_{ik} = -(2\pi Rd)^2 \int_0^{\pi} \nu(\psi)\, d\psi \int_{-\infty}^{\infty} J_1^2(2\pi R|\rho|) H(\rho)\, d\rho \qquad (4.19)$$

where

$$\nu(\psi) = \begin{cases} \cos^2\psi & \text{if } i=k=1 \\ \sin^2\psi & \text{if } i=k=2 \\ \cos\psi\ \sin\psi & \text{if } i\neq k \end{cases}$$

Performing the integration with respect to ψ

$$\beta_{ik} = \begin{cases} -\pi^3(2Rd)^2 \int_0^W J_1^2(2\pi R\rho)\,d\rho & \text{if } i=k \\ 0 & \text{otherwise} \end{cases} \tag{4.20}$$

Equation (4.20) indicates that by the symmetry of the problem, the Fisher's information matrix is simply a scalar times the 2x2 identity matrix. By (3.15), it follows that the diagonal entries of the conditional estimate error covariance Λ_0 are bounded by

$$[\Lambda_0]_{ii} \geq \frac{-N_o}{2\beta_{ii}} \qquad i=1,2 \tag{4.21}$$

where by (4.20) β_{ii} is given by

$$\beta_{ii} = -\pi^3(2Rd)^2 \int_0^W J_1^2(2\pi R\rho)\,d\rho = -2R(\pi d)^2 \int_0^{2\pi RW} J_1^2(\rho)\,d\rho$$

$$\triangleq -2R(\pi d)^2\,\mu(RW) = -(3\pi/8R^2)\,\mathcal{E}\mu(RW) \tag{4.22}$$

where $\mathcal{E}$ in the last line is the Radon transform energy in (4.10).

A plot of $\mu(RW)$ for $RW\in[0,10)$ is shown in Figure 4.2. On the interval [1,10) the function $\mu(RW)$ is well approximated by $0.868\sqrt[4]{RW}$, which is also plotted in this figure. In the limit as the measurement system bandwidth

W approaches infinity, the sinc aperture h(t) in (3.30) approaches an impulse, and the expected value of the measurements approaches the semi-ellipsoidal projection in (2.11), which has points of infinite first derivative. This in turn affects the error analysis; as RW approaches infinity, μ(RW) shown in Figure 4.2 becomes infinite, from which it follows that the ambiguity function a(r) is not twice differentiable, and the Cramer-Rao bound in (4.21) degenerately goes to zero. In order to obtain a meaningful error analysis, therefore, it is necessary to include a nonimpulsive aperture function in the measurement model, that is, to consider only finite values of the radius-bandwidth product.

Denoting by σ_e^2 the diagonal entries in the approximation to Λ_e in (4.17),

$$\sigma_e^2 \geq - \frac{N_0}{2\beta_{ii}} p_0 + (1 - p_0) \frac{T^2}{4}$$

$$= - \frac{N_0}{2\beta_{ii}} + \left[\frac{T^2}{4} + \frac{N_0}{2\beta_{ii}} \right] (1 - p_0) \qquad (4.23)$$

Finally, by incorporating the approximation for $(1-p_0)$ in (4.14), approximating M-1 by (4.11), and using (4.22), σ_e^2, normalized by T^2, is approximately lower bounded by the following quantity

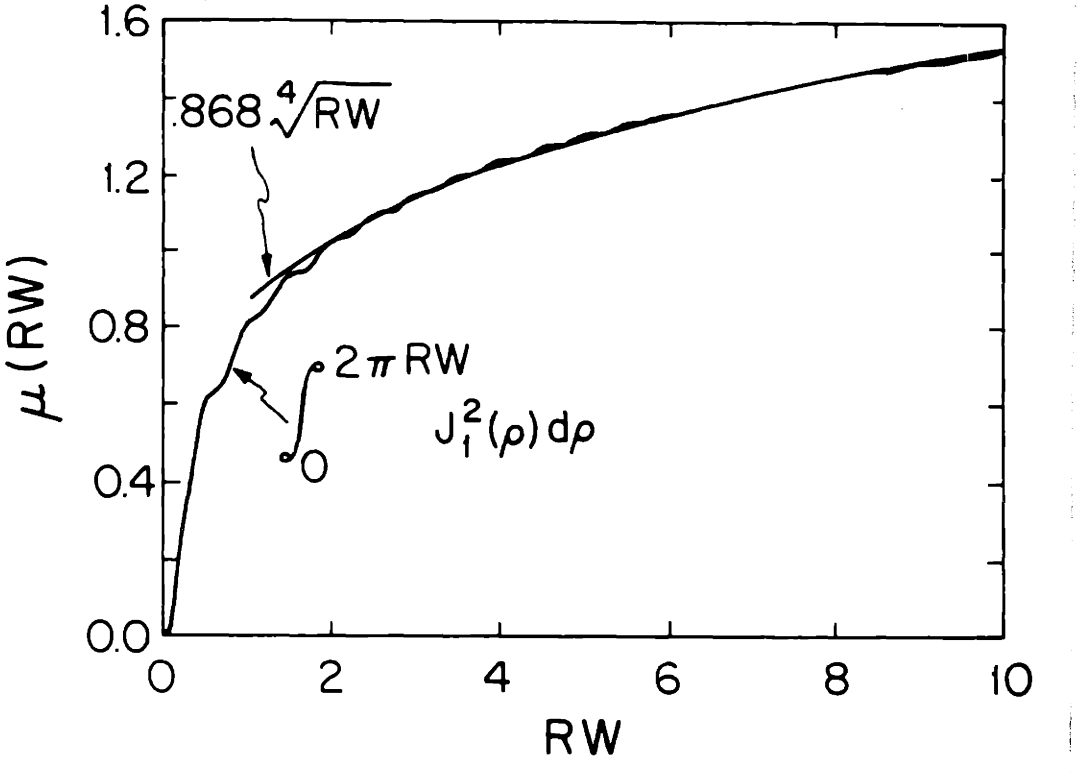

Figure 4.2 μ(RW) versus RW.

$$\left(\frac{\sigma_{LB}}{T}\right)^2 = \frac{4}{3k^2\,(\mathcal{E}/N_0)\,\mu(RW)}$$

$$+\left[\frac{1}{4} - \frac{4}{3k^2(\mathcal{E}/N_0)\,\mu(RW)}\right]\frac{\pi k^2}{4\sqrt{2\pi\mathcal{E}/N_0}}\exp\left(-\frac{\mathcal{E}}{2N_0}\right) \qquad (4.24)$$

The inverse of this normalized error variance is plotted versus SNR in Figure 4.3 for the three object sizes corresponding to k = 5, 10 and 25. These curves clearly depict a threshold behavior in the performance; for a given object size, as the SNR is decreased a point is reached beyond which the localization performance

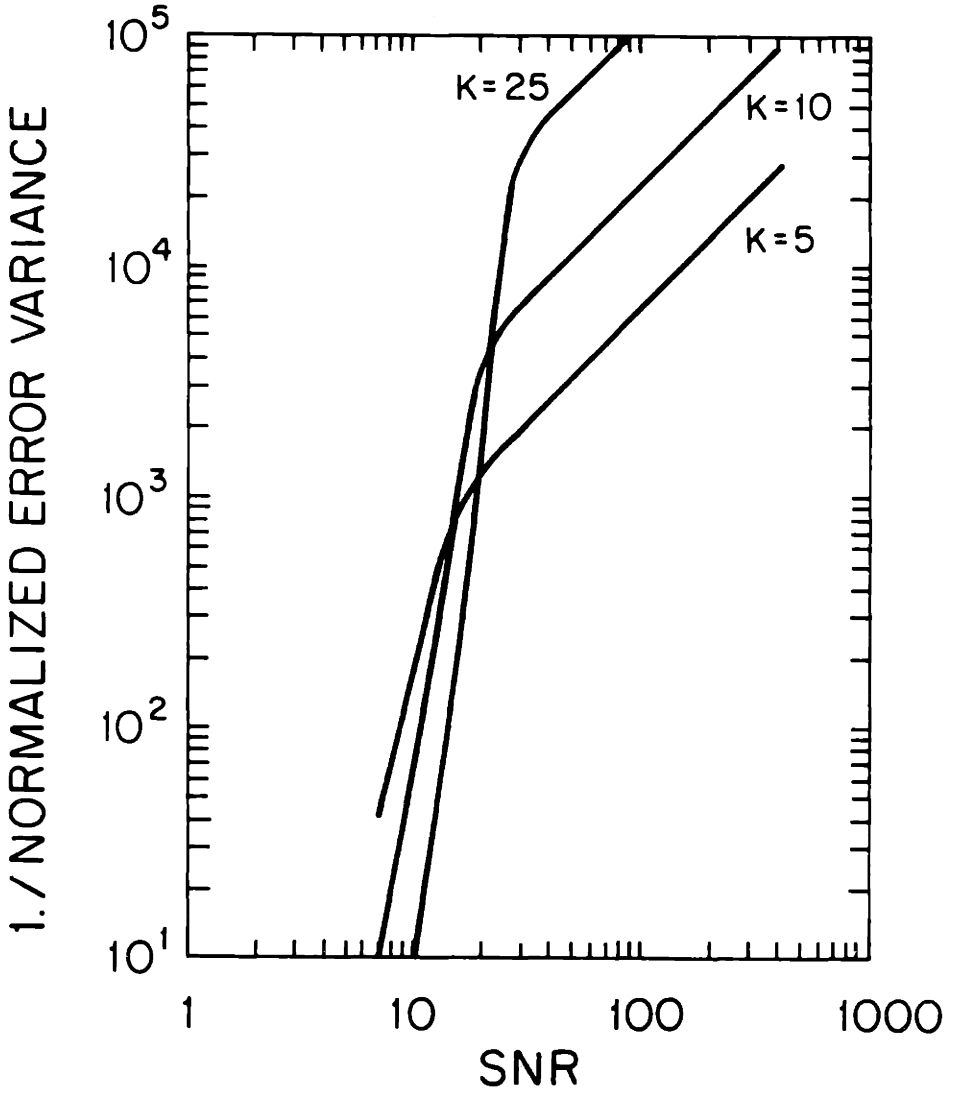

Figure 4.3 Inverse normalized error variance versus SNR.

degrades very rapidly. On either side of the threshold, one of the two sources of error (global and local) dominates; in particular, for SNR values corresponding to points below the "knee" in the performance curve, the global error term (the second term in (4.17)) dominates, and the peak has a high probability of occuring at a position far from the actual object location. For SNR values corresponding to points above the knee in the performance curve, the local error term (the first term in (4.17)) dominates because p_0 is approximately equal to one. It should be noted that the localization performances for two objects having different sizes but the same density can not be easily compared using Figure 4.3, since at a constant value of SNR (i.e. for the same value of signal energy), the smaller object is much denser than the large object.

The effect of object size (with density maintained constant) on the localization performance may be illustrated by considering (4.24), with the energy $\mathcal{E}$ given in (4.10), for fixed values of the ratio of contrast squared to noise level (d^2/N_0). The inverse normalized error is plotted versus object size R in Figure 4.4 for three values of d^2/N_0 = 60, 500 and 7500, with T normalized to unity. These d^2/N_0 values provide an energy ratio of approximately 1:8:125, which is the same energy ratio obtained for a constant density object with

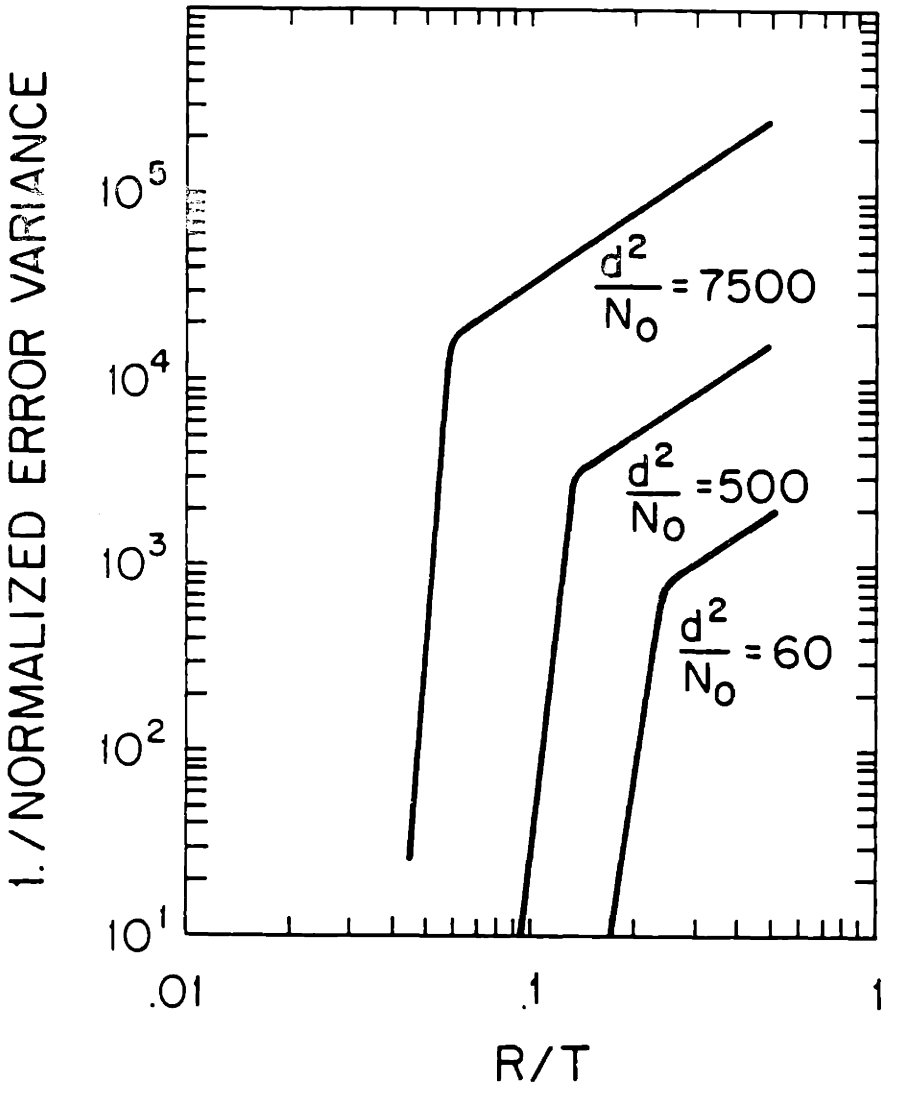

Figure 4.4 Inverse normalized error variance versus R/T.

radius varied as k = 5, 10, and 25. The curves in Figure 4.4 depict a very strong threshold behavior in performance; for a given contrast d and noise level N_o, there exists a clearly defined smallest object that can be reliably located.

In the remainder of this section, we first discuss the relationship between the Cramer-Rao bound in the full-view case and the Cramer-Rao bound in the limited- and discrete-view cases, and then we consider the Gaussian object in Example 3; we conclude with a presentation of several computer simulations.

4.0.2 Limited- and discrete-view cases

Recall from Chapter 3 that the ambiguity function for the object location is given by

$$a(c) = f ** r_h ** \tilde{f} ** b_\xi \tag{4.25}$$

In the limited-view case with projections available over the angular interval $\theta\in[\frac{\pi}{2}-\Delta,\frac{\pi}{2}+\Delta)$, $b_\xi(x)$ in (4.25) was given in (3.26) as

$$b_{\xi,\Delta}(x) = \begin{cases} \frac{1}{\|x\|} & \text{if } |\phi| \leq \Delta \\ 0 & \text{otherwise} \end{cases} \tag{4.26}$$

where ϕ is the angular polar coordinate of x. Figure 4.5a shows a surface plot of a limited view ambiguity function with $\Delta = 30^o$ for a pillbox object of radius $R = T/k = T/10$; the corresponding contour plot is shown in Figure 4.5b. The limited-view ambiguity function is seen to equal zero at points outside a bowtie shaped set centered along the c_1 axis.

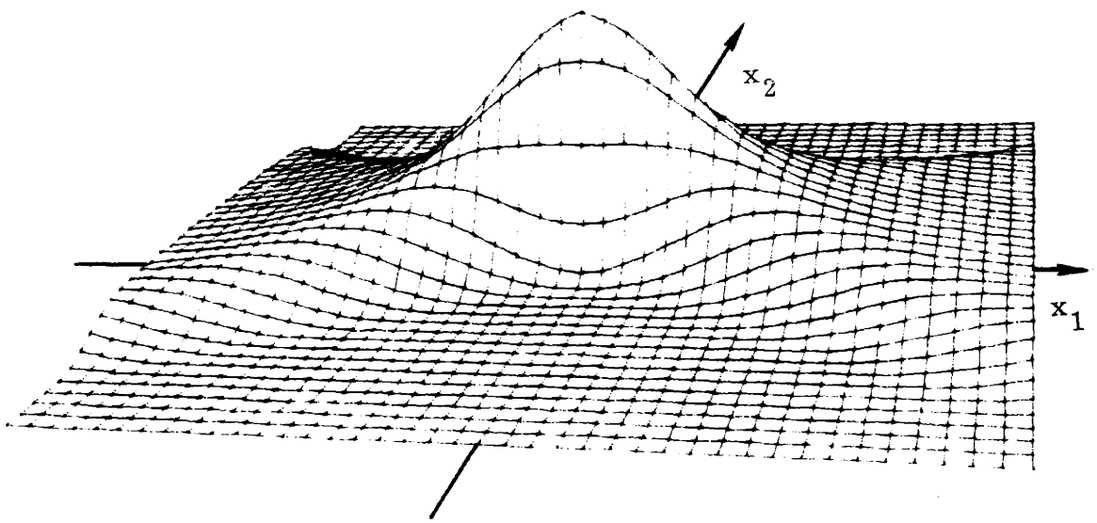

Figure 4.5 (a) Limited-view ambiguity function, $\Delta=30^{\circ}$, k=10.

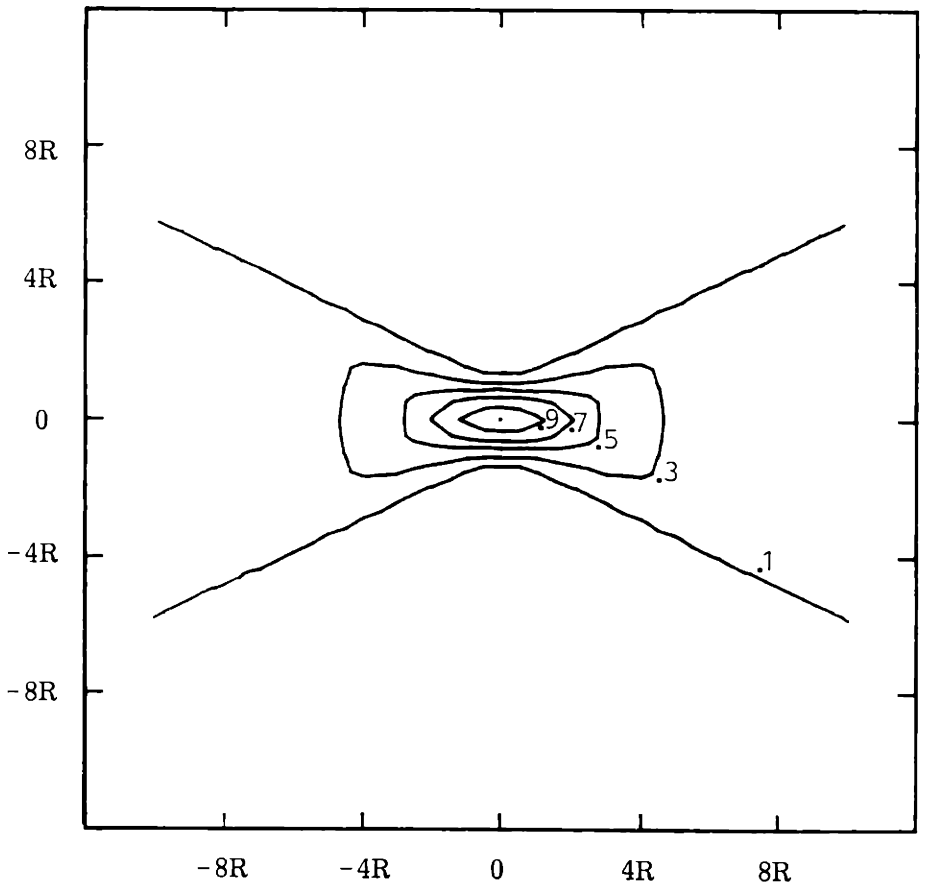

Figure 4.5 (b) Limited-view ambiguity function contour plot.

In the discrete-view case, $b_\xi(x)$ in (4.25) is the spoke function given in (3.28)

$$b_{\xi,N}(x) = \sum_{j=0}^{N-1} \delta(\underline{x}'\underline{\theta}_j) \qquad (4.27)$$

A four-view ambiguity function for a pillbox object of radius R = T/k = T/5 is shown in Figure 4.6a, and the corresponding contour plot is shown in Figure 4.6b. This ambiguity function clearly illustrates the effect of back-projecting a small number of filtered projections--along central rays oriented in the direction of the projections, the ambiguity function decreases in magnitude with increasing distance away from the origin up to a certain point, beyond which the ambiguity function takes on a constant positive value.

In order to compute the Cramer-Rao bound in (3.15) for these two measurement cases, β_{ik} in (3.17) (i.e. the second partial derivative of a(c) at the origin) must be computed. The β_{ik} may be evaluated quite easily in both the limited- and discrete-view cases by the frequency domain approach used in the full-view case. The only difference is that the integral of $\nu(\psi)$ over the interval $\psi\in[0,\pi)$ in (4.19) is replaced by an integral over the interval $[\frac{\pi}{2}-\Delta,\frac{\pi}{2}+\Delta)$ in the limited-view case and is replaced by a sum over $\theta_j = j\pi/N$, j=0,1,...,N-1 in the discrete-view case.

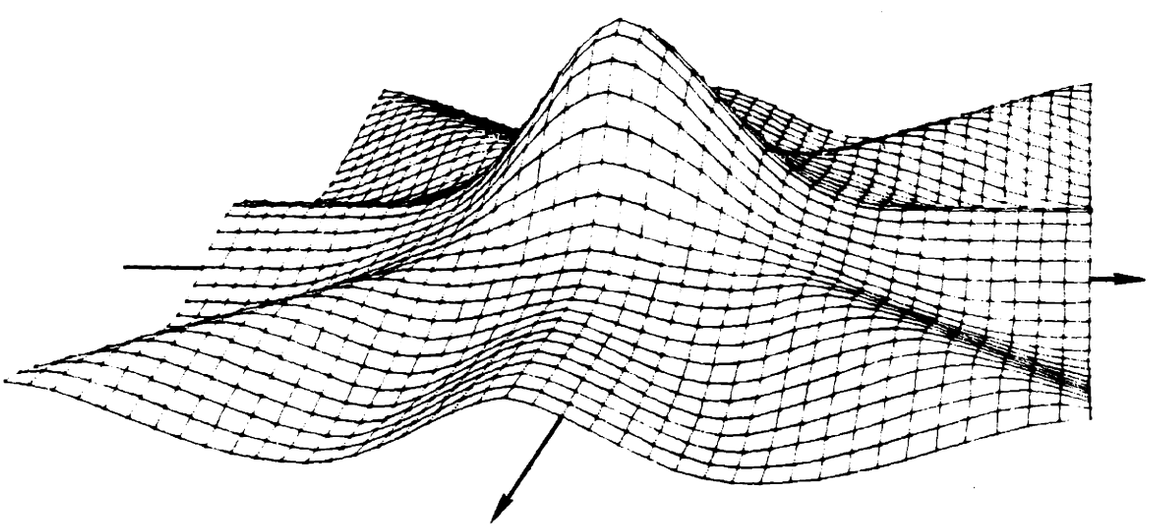

Figure 4.6 (a) Four-view ambiguity function, k=5.

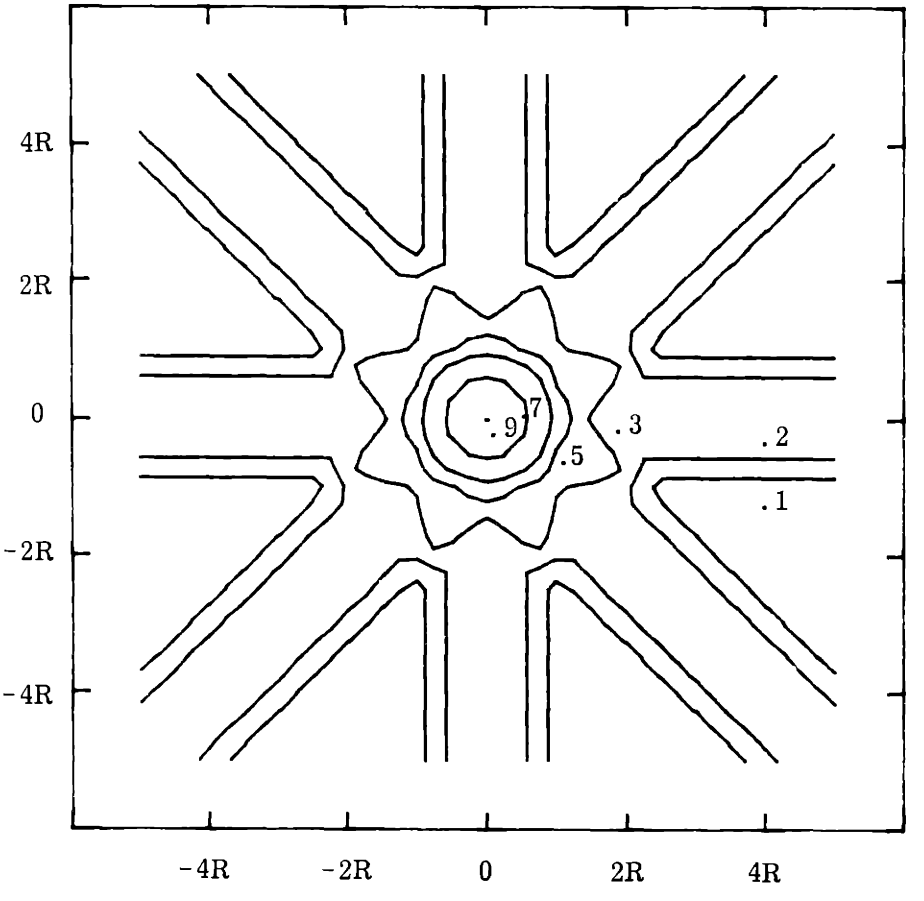

Figure 4.6 (b) Discrete-view ambiguity function contour plot.

If the projections are modeled as being convolved with a sinc aperture function (as was done in the full-view case) having the 1D Fourier transform given in (4.6), then the β_{ii} are equal to the full-view β_{ii} in (4.22) multiplied by a term that depends on Δ in the limited-view case and on N in the discrete-view case. Specifically, in the limited-view case

$$\beta_{ii} = \begin{cases} -(3\pi/8R^2)\mathcal{E}\mu(RW)\left[\frac{1}{\pi}(2\Delta - \sin 2\Delta)\right] & \text{if } i=1 \\ -(3\pi/8R^2)\mathcal{E}\mu(RW)\left[\frac{1}{\pi}(2\Delta + \sin 2\Delta)\right] & \text{if } i=2 \end{cases} \tag{4.28a}$$

As indicated by (4.28a), β_{22} is larger than β_{11} for all values of $\Delta < \frac{\pi}{2}$ so the bound on the c_1 local error variance is always larger than that of c_2; this agrees with intuition since views are taken centered about the c_1 axis. As the viewing angle 2Δ approaches π, the two terms in (4.28a) become equal to each other and equal to the full-view β_{ii} in (4.22) as expected.

In the discrete-view measurement case

$$\beta_{ii} = -\frac{N}{2}(3\pi/8R^2)\mathcal{E}\mu(RW) \qquad i=1,2 \tag{4.28b}$$

The inverse of the local error variance bound in (4.21), therefore, depends linearly on the number of discrete views N.

4.1 EXAMPLE 3 (continued)

Reconsider Example 3 from Chapter 2, involving the Gaussian relative profile

$$f(x) = d \cdot f_o(x;R) = d \cdot \exp(-\|x\|^2/R^2) \tag{4.29}$$

Since the object relative profile is circularly symmetric, it has a circularly symmetric 2D Fourier transform; let f(r) denote the relative profile as a function of its radial polar coordinate only,

$$f(r) = d \cdot \exp(-r^2/R^2) \tag{4.30}$$

The Hankel transform of order zero of f(r) is

$$F(\rho) = 2\pi \int_0^\infty f(r)\ J_0(2\pi\rho r)\ r\ dr$$

$$= d\,\pi R^2\ \exp(-\pi^2 R^2 \rho^2) \tag{4.31}$$

In this example we will evaluate the circularly symmetric ambiguity function a(r) and the local error covariance bound in (3.15) for the Gaussian object in the full-view measurement case, and compare the results to those of the pillbox object in Example 1. As was the case in Example 1, we will assume that the measurements are noisy projections smoothed by a sinc aperture function having a Fourier transform as shown in (4.6). It will be

shown that as the measurement system bandwidth W approaches infinity, the Cramer-Rao bound does not approach zero as it did in the pillbox object case. This agrees with intuition, since the Gaussian profile is continuous and its projection has a continuous first partial derivative with respect to t.

4.1.1 Ambiguity function evaluation

In this section, we will evaluate the circularly-symmetric ambiguity function for the full-view measurement case with infinite measurement system bandwidth. The assumption of an infinite bandwidth simplifies the ambiguity function evaluation considerably, and based on the results of the pillbox ambiguity function, one would expect the general shape of the Gaussian object ambiguity function to also be essentially independent of the radius-bandwidth product when the value of RW is not close to zero.

In the full-view case, the ambiguity function may be expressed as the convolution of four circularly symmetric functions, and may be obtained by inverse Hankel transformation as follows:

$$a(r) = 2\pi \int_0^\infty F^2(\rho)\ J_0(2\pi r\rho)\ d\rho$$

$$= 2\pi^3 d^2 R^4 \int_0^\infty \exp(-2\pi^2 R^2 \rho^2)\ J_0(2\pi r\rho)\ d\rho \qquad (4.32)$$

The Bessel function in this expression may be written as (Bracewell, 1965)

$$J_0(z) = (1/2\pi)\int_0^{2\pi} \exp(-jz\cos\phi)\ d\phi \qquad (4.33)$$

By substituting (4.33) into (4.32) and writing the complex exponential in terms of its cosine and sine components, the integral in (4.32) may be written as a sum of real and imaginary terms. The imaginary term contains the integral of the sine of a cosine which is easily shown to be zero, leaving

$$a(r) = \pi^2 d^2 R^4 \int_0^{2\pi}\left[\int_0^\infty \exp(-(\sqrt{2}\pi R)^2\rho^2)\cos(2\pi r\cos\phi\rho)\,d\rho\right]d\phi$$

$$= \pi\sqrt{2\pi}\ d^2 R^3 \int_0^{\frac{\pi}{2}} \exp(-0.5(r/R)^2\cos^2\phi)\,d\phi \qquad (4.34)$$

The last line follows from the equality

$$\int_0^\infty \exp(-a^2x^2)\ \cos bx\ dx = \sqrt{\pi}/2a\ \exp(-b^2/4a^2) \qquad (4.35)$$

As a check, it can be noted that a(0) evaluates to

$$\mathcal{E}_g \triangleq \sqrt{\pi/2}\,\pi^2 d^2 R^3 \tag{4.36}$$

which is easily verified to be the Gaussian object Radon-space energy from the projection expression in (2.15). When compared to the pillbox object Radon-space energy in (4.10), for the same values of contrast d and size R, the Gaussian object Radon transform energy is seen to equal about 75 percent of the pillbox object energy.

The normalized ambiguity function $a(r/R)/\mathcal{E}_g$ is plotted in Figure 4.7; it has a shape very similar to that of the infinite bandwidth pillbox object ambiguity function in Figure 4.1. In particular, it should be noted that the ambiguity function decreases to approximately 30 percent of its peak value at a distance of r = 2R.

4.1.2 Cramer-Rao bound

In this section, we evaluate β_{ii} in (3.17), i.e. the second partial derivative of the ambiguity function evaluated at the origin, for a finite value of measurement system bandwidth W ($\beta_{ik}=0$ for $i\neq k$ by the circular symmetry of the problem).

$$\beta_{ii} = \left.\frac{\partial^2 a(c)}{\partial c_i^2}\right|_0 = -\mathcal{F}_2^{-1}\{\omega_i^2\ F^2(\omega)\ R_h(\omega)\ B_\xi(\omega)\}_0$$

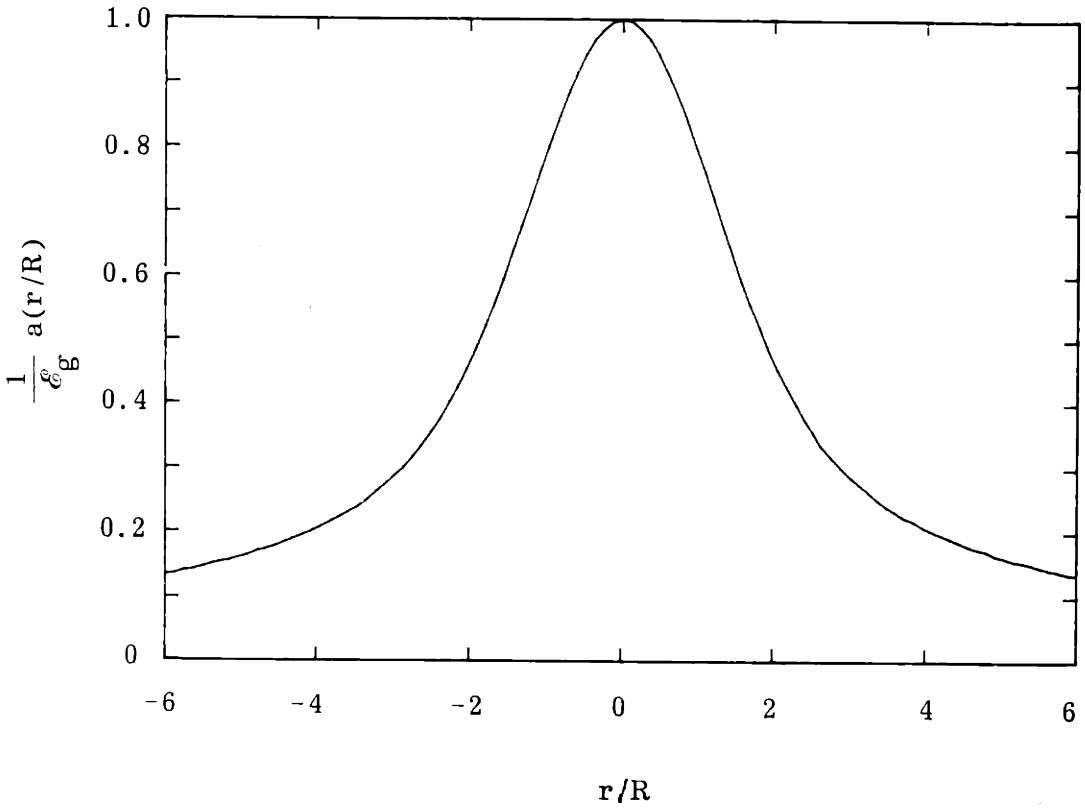

Figure 4.7 Cross-section of the Gaussian object localization ambiguity function.

$$= -\pi^3 d^2 R^4 \int_0^W \rho^2 \exp(-2\pi^2 R^2 \rho^2)\, d\rho \qquad (4.37)$$

where we have changed to polar coordinates and integrated over the angular variable. By a change of variable

$$\beta_{ii} = -(1/2\sqrt{2}) d^2 R \int_0^{2\pi RW} \rho^2 \exp(-\rho^2)\, d\rho$$

$$\triangleq -(1/2\sqrt{2})\, d^2R\, \mu_g(RW) = -(2\pi^{5/2}R^2)^{-1}\, \mathcal{E}_g \mu_g(RW) \qquad (4.38)$$

where $\mathcal{E}_g$ is the Radon space energy in (4.36). This expression resembles that for the pillbox object in (4.22), with the principle difference that $\mu(RW)$ in (4.22) approaches infinity as the bandwidth $W \to \infty$, whereas $\mu_g(RW)$ in (4.38) approaches the limit $\sqrt{\pi}/4$ as $W \to \infty$, and the Cramer-Rao bound does not degenerate to zero. This is not surprising, since the Gaussian profile, in contrast to the pillbox object, is continuous and its projection has a continuous first partial derivative.

In order to allow a comparison of the local error variance for the pillbox and Gaussian objects, we have plotted in Figure 4.8 the inverse normalized Cramer-Rao bound $(R/\sigma)^2$ versus the radius-bandwidth product RW for both objects. This figure clearly indicates that for any value of RW, the Cramer-Rao bound for the pillbox object is significantly smaller than that for the Gaussian object, which is not surprising, since the Gaussian object has a much smoother projection than does the pillbox object.

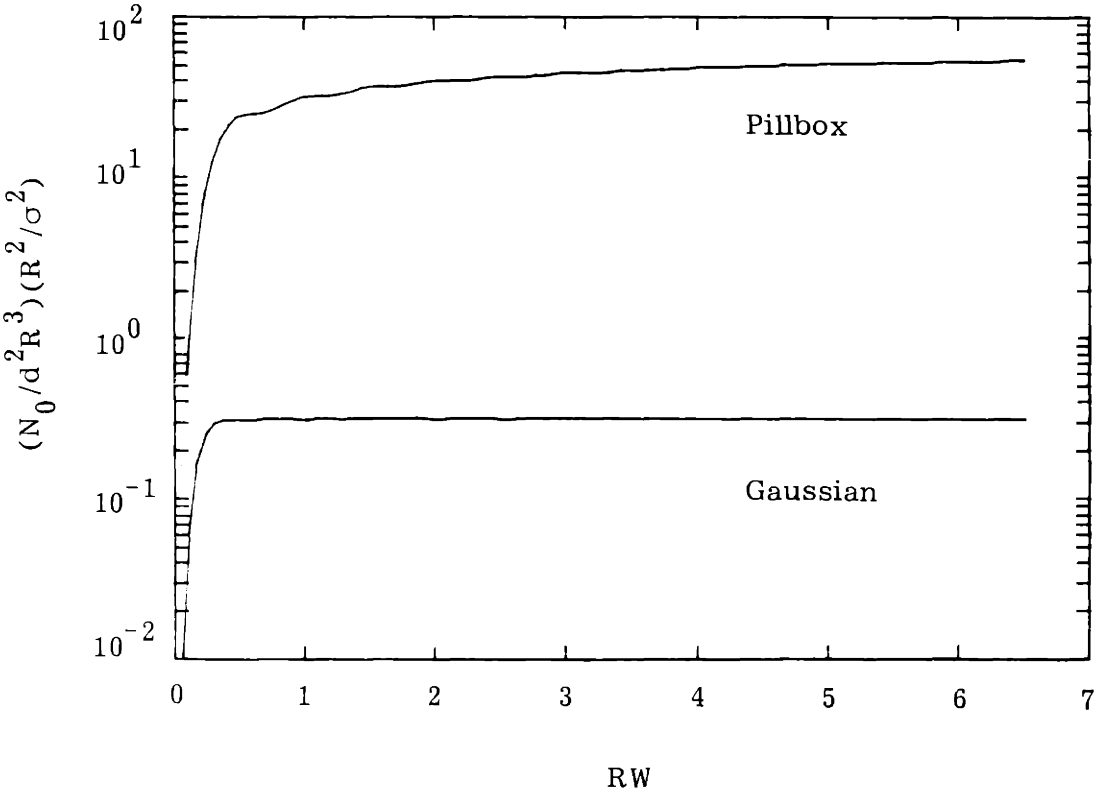

Figure 4.8 Inverse normalized Cramer-Rao bound versus RW for pillbox and Gaussian objects.

4.2 COMPUTER SIMULATIONS

4.2.1 Introduction

In this section, we report the results of several computer simulations that were performed. These simulations involve the computer generation of a limited amount of noisy projection data, which are processed in two ways, (1) by determining the log likelihood function for the unknown object location coordinates and (2) by using a conventional reconstruction algorithm to directly estimate the density profile.

In these simulations we considered the simple discontinuous pillbox profile of Example 1, that is, an indicator function on the disk D(R) lying within the disk-shaped region C = D(T) defined in (4.1); the object size was selected so that k=T/R in (4.2) equals 5. For notational convenience, we will normalize the geometry, and take the object to be situated within a circularly-shaped region of radius T=1, in which case the object has a radius of 0.2.

In all cases, a total of 105 measurements were generated by computer, corresponding to line integral measurements using a parallel-ray measurement geometry. Five views were generated at angles $\theta_j = j\pi/5$, j=0,1,...,4 (i.e. at 0, 36, 72, 108 and 144 degrees of angular rotation). Each view was comprised of 21 parallel lines of integration at t values given by $t_m = 0.1m$, m=-10,-9,...,10 (i.e. an inter-ray spacing of 0.1)

Pseudorandom white noise samples having zero mean and variance σ^2 were added to the 105 line integrals to provide noisy measurements $y(t_m,\theta_j)$. The measurement signal-to-noise ratio (SNR) in dB is defined as

$$SNR = 10 \log (\mathcal{E}_D/\sigma^2) \qquad (4.39a)$$

where $\mathcal{E}_D$, the Radon transform energy in the line integral measurements, is given by

$$\mathcal{E}_D = \sum_{j=0}^{4} \sum_{m=-10}^{10} g^2(t_m,\theta_j) \tag{4.39b}$$

and $g(t,\theta)$ is the Radon transform of the simulated density function.

The noisy data $y(t_m,\theta_j)$ were processed to develop 240x240 pixel images (16 gray levels per pixel) by using the equation

$$a(x) = \sum_{j=0}^{4} \sum_{m=-10}^{10} y(t_m,\theta_j) z(t_m - \underline{x}'\underline{\theta}_j,\theta) \tag{4.40}$$

where $|x_1|, |x_2| \leq 1$. The convolution kernel $z(t,\theta)$ in (4.40) is given by one of two functions, depending on whether the log likelihood function or a reconstructed image is being computed. In each case, a piecewise linear approximation to the ideal continuous convolving kernel was used in order to reduce the computational burden associated with the CBP operation.

The density function that was simulated corresponds to a single circular object of unit density and radius 0.2, centered at coordinates x = (0.2,0.4), i.e.

$$f(x) = \chi_{D(0.2)}(x_1-0.2,x_2-0.4) \tag{4.41}$$

An image representation of this cross-sectional density is shown in Figure 4.9. The convolving kernel for the log

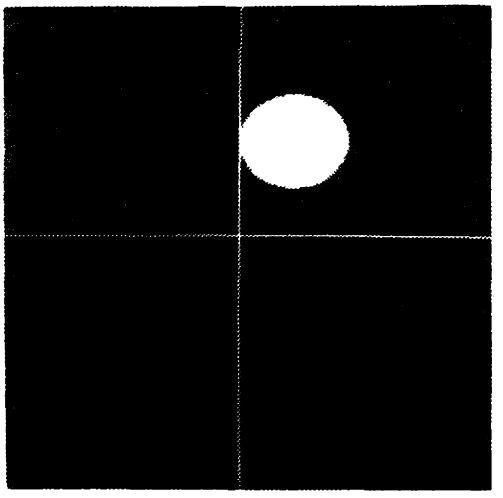

Figure 4.9 Image representation of the single-object cross-sectional density function.

likelihood function evaluation, denoted $z_{LL}(t)$, is θ-independent, and is given by the following piecewise linear approximation to the projection of a disk with radius 0.2; for t an integer multiple of 0.02

$$z_{LL}(t) = \begin{cases} 2\sqrt{(0.2)^2 - t^2} & \text{if } |t| \leq 0.2 \\ 0 & \text{if } |t| \leq 0.2 \end{cases} \qquad (4.42)$$

and if t is not an integer multiple of 0.02, the value of $z_{LL}(t)$ is obtained by linear interpolation of the two nearest values defined in (4.42).

The image reconstruction kernel, denoted $z_I(t)$ and obtained from Shepp and Logan (1974), is the θ-independent piecewise linear function

$$z_I(t) = \frac{1}{10\pi} \frac{1}{.25-k^2} \qquad \text{if } t=0.1k, \text{ k integer} \qquad (4.43)$$

and if t is not an integer multiple of 0.1, the value of $z_I(t)$ is obtained by linear interpolation of the two nearest values defined in (4.43).

4.2.2 Simulation results

Figure 4.10 is an image representation of the log likelihood function (i.e. an illustration of the image obtained using the log likelihood function kernel $z_{II}(t)$ in (4.42)) with no additive measurement noise -- that is,

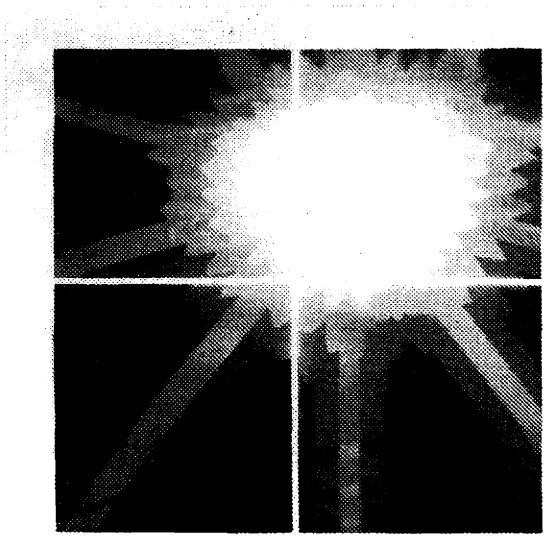

Figure 4.10 Image representation of the five-view ambiguity function.

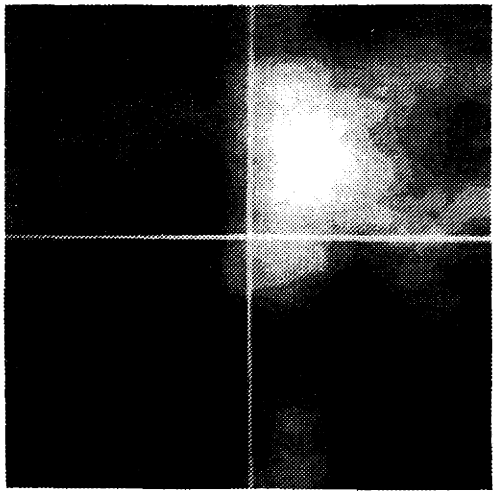

Figure 4.11 (a) log likelihood function, SNR = 5 dB, scale = [0,1].

it is the ambiguity function. Notice that the back-projection operation produces five "strips" equally-spaced in angle (corresponding to the five projection angles used) and intersecting at the true object location. The value of the ambiguity function for points not lying on these strips is zero, whereas the value for points lying on these strips does not necessarily approach zero with increasing distance from the true object location. These large ambiguity function values at points far from the true object location clearly correspond to points with an increased probability of being the location of the log likelihood function peak. This type of effect is not peculiar to the log likelihood function, rather simply corresponds to the fact that back-projection leads to a smearing of the 1D measurements back across the 2D object space. This leads to the often-discussed problem in conventional CBP reconstruction of artifacts in reconstructions from measurements of limited SNR or limited quantity (Gordon, 1973). In the conventional image reconstruction problem, such artifacts make subsequent interpretation difficult, and quantification of this effect appears to be an open problem. In contrast, in the object localization problem, such artifacts far from the true object location are completely ignored unless the measurement noise combines to make the log likelihood function peak occur within

them. Furthermore, note that the global error analysis of Chapters 3 and 4 provides us with a quantified measure of this effect, namely the probability that an artifact-induced localization error occurs.

In this simulation, two measurement SNR noise levels (see (4.39a)) were used, namely 5 dB and -10 dB, and the same noise samples were used when performing the CBP using both of the convolving kernels at each of the two noise levels. Figure 4.11a is an image representation of the log likelihood function obtained with a SNR of 5 dB. This image clearly illustrates (particularly in the vertical direction) the manner in which the back-projection operation leads to streaking when there are a small number of measurement views. In the formation of this image, the log likelihood function was first normalized so that its values lay in the interval [0,1], then the image was formed so that the smallest value (zero) corresponds to black, the largest value (one) corresponds to white, and the fourteen available intermediate gray levels are uniformly distributed between these two values. In this image representation of the log likelihood function, those areas not close to the object are characterized by low-amplitude variations that make it somewhat difficult to identify dominant features within the log likelihood function. To make the log likelihood functions and the Shepp and Logan kernel reconstructions easier to

interpret, in all of the remaining simulation photographs presented in this section, the image values are first normalized to the interval [0,1], and then the sixteen levels of gray scale are uniformly distributed on the interval [0.6,1] or [0.75,1] (that is, function values less than 0.6 or 0.75 appear black in the final image).

Figures 4.11b and 4.11c correspond to the log likelihood function and reconstructed image (using the kernel in (4.42) and (4.43), respectively), when the measurement SNR is 5 dB and the gray scale is distributed on the interval [0.6,1]. Figures 4.11d and 4.11e are the log likelihood function and reconstructed image for a SNR equal to -10 dB, with the gray scale distributed on the interval [0.75,1]. Notice that at both measurement noise levels the image reconstruction kernel $z_I(t)$ leads to sharper looking images because it is attempting to reconstruct the original field (i.e. the point spread function for the overall mapping from the original field to the reconstruction is approximately impulsive). It is well known (Mersereau and Oppenheim, 1974) that high-resolution reconstruction results in an amplification of the high frequency components in the projection measurements (including any noise present in these measurements); as can be seen in Figure 4.11, this leads to a number of spurious peaks distributed throughout the reconstruction, all having approximately the same size,

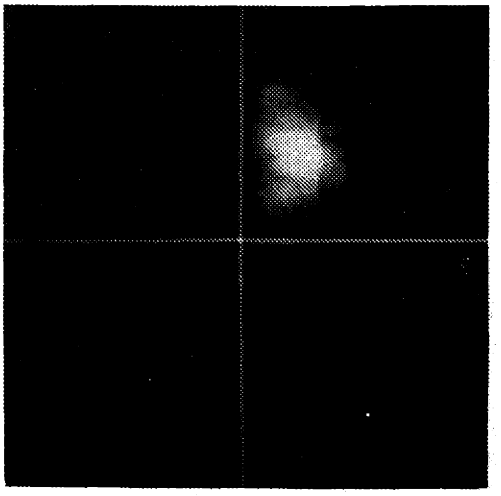

(b)

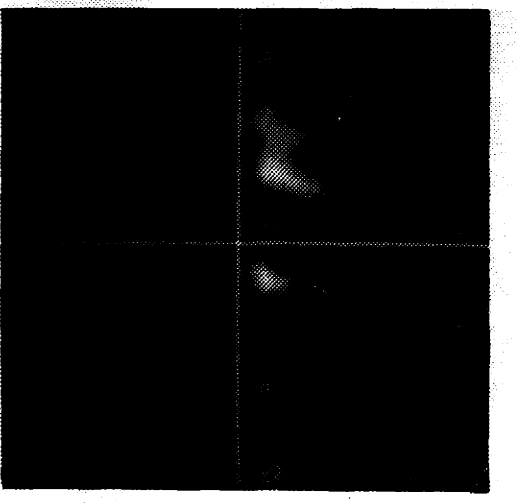

(c)

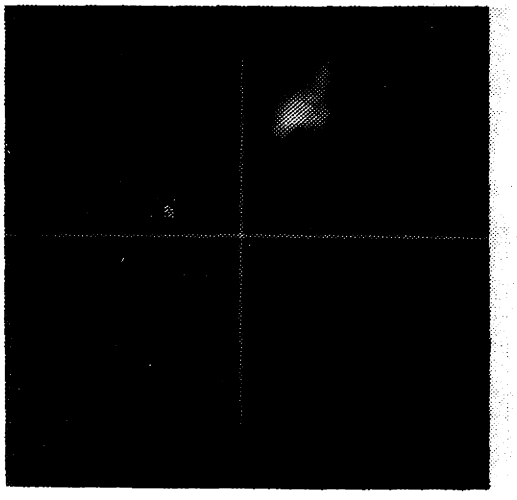

(d)

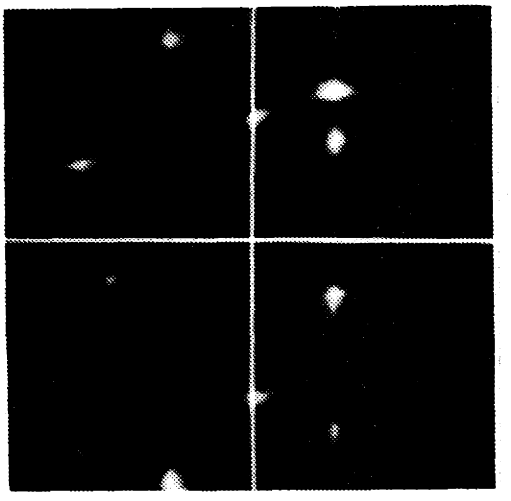

(e)

Figure 4.11 (b) log likelihood function, SNR = 5 dB, scale = [0.6,1.0].

(c) reconstructed image, SNR = 5 dB, scale = [0.6,1.0].

(d) log likelihood function, SNR = -10 dB, scale = [0.75,1.0].

(e) reconstructed image, SNR = -10 dB, scale = [0.75,1.0].

particularly for the -10 dB case. In contrast, the log likelihood function has a smeared or blurred image representation because its purpose is not to reconstruct but rather to carry out the matched filtering operation involved in ML estimation (the overall point spread function for the matched filter not only is not approximately impulsive, but is in fact positive everywhere). Because the matched filter convolving kernel attenuates high frequency components in the 1D projection measurements (compared to a conventional image reconstruction kernel like the one in (4.43)) there is a reduced probability of spurious peaks in the log likelihood function. In particular, as seen in Figure 4.11, the log likelihood function has only one peak in the 5 dB case, and it occurs very close to the true object location (in particular, at (12.2,17.2)); in the -10 dB case, the log likelihood function has several secondary peaks but the major peak occurs very close to the true object location (in particular, at (9.2,24.4)). These images indicate that the Radon-space matched filtering approach to object detection developed in this thesis is a valuable technique for determining an object's location within the cross-section. Conventionally reconstructed images (because of the relatively high gain of the convolving kernel at high spatial frequencies) contain spurious peaks which make it difficult (if not impossible)

to establish the object's location by direct examination of the reconstructed image.

Although an object's location is difficult to determine by direct examination of a noisy reconstructed image, various image post-processing operations may be considered in order to extract object location information. As discussed in Section 3.0, several researchers have investigated the problem of post-processing a reconstructed image for the purpose of delineating regions and/or detecting objects within the cross-section (e.g. Hanson, 1978). It was pointed out in this thesis and in Riederer et al. (1978) that in the presence of white measurement noise, the reconstructed image noise is <u>not</u> white; consequently, techniques for matched filtering in correlated noise must be used in the post-processing step to identify objects if truly optimal performance is desired. A suboptimal approach to post-processing for object identification purposes, and one that is quite often used in image processing, is to perform matched filtering assuming that the measurement noise is white, which in this case corresponds to correlating the reconstructed image with a pillbox object. Results of performing this procedure to post-process the reconstructed images in Figures 4.11c and 4.11e, with a 2d correlating filter

$$f_c(x) = \chi_{D(0.2)}(x) \tag{4.44}$$

are illustrated in Figure 4.12. The image in Figure 4.12a is the result of filtering the image in Figure 4.11c with $f_c(x)$, where the gray scale was distributed on [0.6,1]. Similarly, Figure 4.12b is the result of filtering the image in Figure 4.11e, with the gray scale distributed on [0.75,1]. These two images are seen to be very similar to the image representation of the log likelihood functions shown in Figures 4.11b and 4.11d. The fact that these images are so similar is an indication of the robustness of the matched filter -- even though the matched filter in (4.44) is optimal only when the additive image noise is white, it is very robust to the fact that the image noise is nonwhite.

To close this section, let us make several comments. As indicated previously, the location of an object situated within a cross-section is discerned much more easily by examining the log likelihood function than by examining a reconstructed image that has not undergone time consuming post-processing. Furthermore, notice that while suboptimal matched filtering of a conventionally reconstructed image provides an image that is useful for the detection and localization problem, it requires both a CBP and a 2D matched filtering operation. The Radon-space matched filtering approach described in this thesis

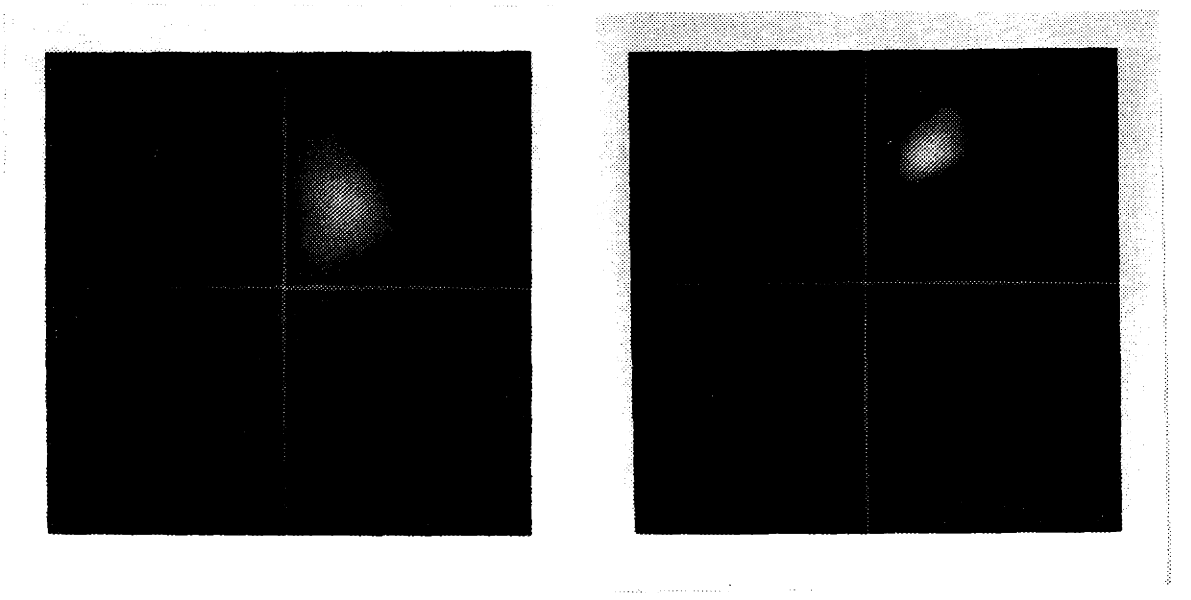

(a) (b)

Figure 4.12 (a) result of convolving the image in Figure 4.11c with $f_c(x)$; scale = [0.6,1.0].

(b) result of convolving the image in Figure 4.11e with $f_c(x)$; scale = [0.75,1.0].

produces an optimal log likelihood function using a single CBP with a correctly chosen kernel. Note also that while the use of suboptimal post-processing in object localization is robust, one might expect to encounter problems if one were to use suboptimal post-processing to determine more detailed information about the object, such as its shape (the problem of estimating object shape by direct use of noisy projection measurements is considered in Chapter 6). This implies that to extract such information from a reconstructed image with correlated reconstruction noise, one would have to decorrelate the noise which, as mentioned earlier, is nothing more than undoing the correlating effect of the convolution back-projection operation used to construct the image.

As a final point, let us note that in the case of a limited measurement view angle, our approach to object localization produces directly an optimal log likelihood function. Image reconstruction methods from limited-view measurement data are much more difficult and far less well-developed (Davison and Grunbaum, 1981). Furthermore, it is well known that such reconstruction methods may give rise to suspect features (Vest and Radulovic, 1977); in such a case, simple 2D matched filter post-processing would not be as robust as in the full-view case, and noise decorrelation or whitening would be required (which again would effectively undo the entire reconstruction) before

the optimal log likelihood function was produced.

4.3 CONCLUSIONS

In this chapter and the previous one, we have investigated the problem of locating a single object whose geometry (relative profile) is known precisely. In Chapter 3, an approximate expression was developed for the location estimate error covariance, which reflects the contribution due to both local and global errors. In Chapter 4, an approximation to this expression was evaluated for the pillbox object of Example 1; the results of this example indicate that for a fixed object contrast d and noise spectral level N_o, there exists an extremely sharp threshold effect resulting in a minimum value of object size for which reliable localization can be performed.

Also in Chapter 4, the effect on the local error covariance of limited- and discrete-view measurements was discussed, as was the localization performance for a Gaussian object. One important distinction between the local performance with a pillbox versus a Gaussian object is the behavior of the local error variance in the limit as the measurement system bandwidth W approaches infinity. In such a case, β_{ik} (the denominator of the local error variance, given in (3.17)) approaches infinity

(corresponding to a local error variance of zero) for the discontinuous pillbox object, but approaches a finite limit for the continuous Gaussian object. This indicates that care should be taken in using idealized models in performance analysis, in order to ensure that truly representative answers are obtained, rather than results which are artifacts of some detail of the simple model being used.

Finally, in Section 4.2 a computer simulation was presented which illustrates (1) the evaluation of the log likelihood function for the localization of a pillbox object from computer-generated noisy projections, as well as (2) the evaluation of a reconstructed image from the same noisy measurements. These simulations demonstrate that at high noise levels and with a limited number (five in this simulation) of projections, an object located within a cross-section is discerned much more easily by examining the log likelihood function than by examining a reconstructed image that has not been post-processed. When post-processing is performed using a 2D matched filter, it is time-consuming, suboptimal, and as already mentioned, is expected to lead to considerably less robust results in problems of estimating more detailed parameters than location (e.g. shape or geometry), or where the measurements are available only over a limited view angle.

As mentioned previously, a number of assumptions have been made throughout these two chapters regarding the measurement process, the cross-sectional field f(x) and the extent of our a priori knowledge. In the next chapter, we systematically consider in what ways the localization performance is affected when one or more of these assumptions does not hold.

CHAPTER 5

LOCALIZATION ROBUSTNESS ANALYSIS

5.0 INTRODUCTION

In the previous two chapters, we developed the problem of locating an object in a cross-section using projection measurements; the performance analysis machinery was developed in Chapter 3, and then illustrated with several examples and simulations in Chapter 4. A number of assumptions were made in the course of this development, including

- the measurements are smoothed projections corrupted by additive white noise; the evaluation of the projection at any point is given by the integral of the density field along a straight line, see (2.7) and (2.17).

- the cross-sectional field consists of exactly one object profile superimposed on a background field that is known exactly (and thus its effect may be subtracted from the measurements), see (2.3) and (2.4).

- the detailed density variations corresponding to the object are known precisely, including the contrast parameter d.

(5.1)

Assumptions (5.1) were made in Chapters 3 and 4 in order to simplify the analysis associated with the maximum likelihood localization procedure, so that insight into the structure and performance of object parameter estimation could be more easily obtained. In practice, however, assumptions (5.1) are never completely satisfied, for a variety of reasons including, for example, intentionally introduced modeling simplifications, as well as unavoidable errors in a priori information. Intentionally introduced modeling simplifications may arise, for example, when a hierarchical algorithm is employed to perform iterative estimation. With such a procedure, a very simple object model is used initially in order to extract coarse information about the cross-section, such as the number of objects and their locations; in subsequent stages of this procedure, more complex object models (making use of finer details of a priori information) are used to estimate the boundary geometry and detailed density variations within the boundary of each of the objects. When differences between the actual and the modeled density profile and

measurements exist, the performance of the localization procedure (assessed for the perfect modeling case in Chapters 3 and 4) is to some degree adversely affected.

In this chapter, we consider in a systematic way the consequences of several specific types of modeling errors, that is, specific deviations from the assumptions in (5.1). For simplicity, we continue to employ the noisy projection measurement model in (2.17), and focus our attention on the way in which localization performance is affected when one proceeds to locate a single circularly-symmetric pillbox object in a cross-section, when in fact (1) more than one object is present in the actual cross-section or (2) the density profile of the actual object differs from that of the modeled pillbox object. The analysis of robustness to the presence of one or more unmodeled objects allows us to obtain insight about the consequences of a nonzero and imperfectly known background field ($f_b(x)$ in (2.3)). For example, when the object to be located is superimposed on a background consisting of many small randomly located objects, the effect of these small objects is similar to a correlated random background field; the effect on the localization performance of this nonzero background field is much easier to analyze using the present machinery than using, say, a correlated random field background.

The two types of modeling errors just mentioned may be studied by letting the actual cross-sectional profile be given by

$$f(x) = f_b(x) + \sum_{k=1}^{N} d_k \cdot f_0(x - \tilde{c}_k; v_k) \qquad (5.2)$$

where the tilde notation denotes an object location, to avoid confusion with the jth lattice point c_j. In this field model, one object (say k=1) corresponds to the object we want to locate. The other N-1 objects may be thought of as part of the background, or as other objects that are to be estimated subsequently. Here, $f_b(x)$ corresponds to the known part (e.g. the mean value) of the background field, and without loss of generality we set it equal to zero. In Section 5.3 we consider the possibility of background uncertainty modeled as one or several additional objects lying in the background.

From (1.4), the Radon transform of f(x) is

$$g(t,\theta) = g_b(t,\theta) + \sum_{k=1}^{N} d_k \cdot g(t,\theta;\tilde{c}_k,v_k) \qquad (5.3)$$

where $g_b(t,\theta)$ is the Radon transform of the background field. In this robustness analysis, we may consider any or all of the measurement cases established in the previous chapters, namely full-view, limited-view and discrete-view measurements; in order to illustrate how one would proceed with localization robustness analysis,

we consider in this chapter the case of full-view noisy projection measurements, which are given by

$$y(t,\theta) = g(t,\theta) + w(t,\theta) \qquad (t,\theta)\in\mathcal{Y} \tag{5.4}$$

In the localization problem under assumptions (5.1), one would like to determine the location c of a single circularly-symmetric pillbox object having profile

$$d\cdot f_0(x - c;R) = d\chi_{D(R)}(x - c) \tag{5.5}$$

and Radon transform

$$g(t,\theta;d,c,R) = d\cdot g(t - \underline{c}'\underline{\theta},\theta;R) \tag{5.6}$$

using the simplified model for f(x) consisting of the sum of a known background and the single hypothesized object in (5.5). The object location c is estimated by locating the maximum of the log likelihood function computed using this simplified model, which by (2.22) is evaluated as

$$\mathcal{L}(c) = \frac{2}{N_0}\int_0^{\pi}\int_{-\infty}^{\infty} y(t,\theta)g(t,\theta;d,c,R)\,dt\,d\theta$$

$$- \frac{1}{N_0}\int_0^{\pi}\int_{-\infty}^{\infty} g^2(t,\theta;d,c,R)\,dt\,d\theta \tag{5.7}$$

In this chapter, we investigate how the performance of the localization procedure using the single-object field model in (5.5) is affected when the actual field is the multiple-object field given in (5.2) (the actual field is varied in this analysis, and as it is, we investigate how the performance is affected). The second term in (5.7) corresponds to the energy in the Radon-space matched filtering template $g(t,\theta;d,R)$, and since this energy is c-independent and the modeled object geometry is fixed, the second term in (5.7) contributes only a constant to the log likelihood function, and does not affect the location of the log likelihood function peak. Consequently, it may be disregarded, as can the scaling factor $2/N_o$, leaving

$$L(c) = \int_0^{\pi} \int_{-\infty}^{\infty} y(t,\theta)g(t,\theta;d,c,R)\,dt\,d\theta \tag{5.8}$$

Substituting the measurements and the actual multiple-object field expressions from (5.2) through (5.4), the log likelihood function becomes

$$L(c) = \int_0^{\pi} \int_{-\infty}^{\infty} g_b(t,\theta)g(t,\theta;d,c,R)\,dt\,d\theta$$

$$+ \sum_{k=1}^{N} \int_0^{\pi} \int_{-\infty}^{\infty} g(t,\theta;d_k,\tilde{c}_k,v_k)g(t,\theta;d,c,R)\,dt\,d\theta$$

$$+ \int_0^{\pi} \int_{-\infty}^{\infty} w(t,\theta) g(t,\theta;\, d,c,R)\, dt\, d\theta$$

$$\triangleq a_b(d,c,R) + \sum_{k=1}^{N} a(d,c,R;d_k,\tilde{c}_k,v_k)$$

$$+ n(d,c,R) \qquad (5.9)$$

The log likelihood function in (5.9) has N+2 terms: one due to the background field, one term for each of the N objects, and one term due to the projection measurement noise. The expression in (5.9) is a generalization of the log likelihood function in (3.5) which was developed under assumptions (5.1), i.e. for N=1, d_1 known, v_1 known, and $f_b(x)$ known and taken to be zero. As was the case in (3.5), n(d,c,R), the log likelihood component due to the zero-mean measurement noise, is a zero-mean random field with a second moment that depends only on the modeled field.

When the actual field consists of a background field with N superimposed objects, the log likelihood function in (5.9) has N more terms than the log likelihood function in (3.5); these extra terms can be thought of as noise terms (representing, for example, uncertainties in the background) which, in addition to the noise n(d,c,R), cause the peak of the log likelihood function to be shifted away from its true value (which is the location of

the peak of the ambiguity function due to the single object to be located). As was shown in the previous two chapters, the localization performance may be characterized by evaluating the degree to which the noise terms cause the log likelihood function peak to be shifted away from its true value. One approach to such a performance analysis is to develop an approximate expression for the second moment of the estimate error vector -- this is the procedure used in Chapters 3 and 4.

In previous chapters this analysis led to the consideration of two types of errors, namely local and global errors. The first of these was characterized using the Cramer-Rao bound, and the second was characterized by evaluating p_j, the probability that the maximum log likelihood function value occurs at the jth point in the M-point lattice with 2R inter-point spacing

$$\{c_j\} = \{(2Rm, 2Rn):\ (2Rm, 2Rn) \in D(T), n, m \text{ integer}\} \qquad (5.10)$$

While we may approximately characterize the second moment of the error vector in a similar way in the presence of modeling errors, we are more interested in this chapter in identifying major degradation in the performance due to modeling errors. For this reason, in this chapter we investigate the robustness to modeling errors by focusing on the probability of a global error $(1-p_0)$ when the

actual and modeled fields differ. This quantity provides valuable insight into the degree of robustness of the single-object localization procedure developed in Chapter 3 to various modeling errors.

As mentioned previously, a more detailed analysis of robustness could be performed by obtaining an approximation to the overall estimate error covariance (in much the same way as was done in Chapters 3 and 4) in the presence of modeling errors. In addition to the determination of p_0, such an analysis would involve

1) calculating the effect of modeling errors or model mismatch on the local error variance via a Cramer-Rao analysis

2) evaluating all of the p_j, which are in general not equal here.

While one could perform mismatched Cramer-Rao analysis in each of the cases we consider, this calculation is not necessary for purposes of demonstrating the robustness of the localization algorithm to various modeling errors. As an illustration of how this type of analysis is performed, however, it is carried out for one of the cases studied in this chapter, namely the robustness to shape errors in Section 5.2.

With regard to the evaluation of all of the p_j in point (2), again, this calculation is not necessary for purposes of establishing insight into the robustness of the localization algorithm to various modeling errors. As mentioned previously, we approach the object localization robustness issue in this chapter by establishing a lower bound on p_0, the probability that the log likelihood function maximum occurs at the lattice point $c_0 = c_a$. This bound provides valuable insight into the global performance under various modeling errors and SNR. The corresponding expression for the lower bound on the p_j, however, when evaluated for $j \neq 0$, provides a trivial nonpositive lower bound for the probabilities we consider. On the other hand, in the operating range of interest, p_0 is approximately equal to one and therefore this is not a real problem. If one should, however, desire more accurate estimates for the p_j values with $j \neq 0$, there are a number of ways to do so, and we discuss several of these techniques in the conclusion to this chapter. In addition, there is a simple alternate approach to obtain insight into the way in which the total global error probability $1-p_0$ is distributed among the lattice points c_j, $j \neq 0$. In particular, one may select any two lattice points, and calculate easily the probability that the log likelihood function value at one of these points exceeds the value at the other point. One can use this approach

to obtain a measure of the relative likelihood that any particular lattice point corresponds to the maximum log likelihood function value by considering various pairs of lattice points. To illustrate the basic idea behind this approach, we consider a particularly important example in Section 5.1 in the context of our discussion of size errors.

The major difference between the robustness analysis here and the performance analysis in Chapters 3 and 4 is that $\underline{m}$, the conditional expected value of the vector of lattice point log likelihood function values, has only one nonzero element in Chapters 3 and 4 (because the ambiguity function was approximated to be zero at distances greater than or equal to 2R) whereas in this chapter many elements in the vector $\underline{m}$ may simultaneously be nonzero (due to the presence of unmodeled objects or single-object modeling errors). This has the obvious effect of decreasing p_0, that is, of increasing the probability of a global error. By assessing the extent to which p_0 is decreased, as well as by performing Cramer-Rao analysis under mismatch and evaluating the relative probability of any two lattice points in the presence of global error, we can obtain insight into the robustness of the localization procedure to particular types of modeling errors, and this is the approach we pursue in this chapter.

In Chapter 4, the fact that $\underline{m}$ had only one nonzero element led to the simple bound in (4.14) for p_0. When $\underline{m}$ has more than one nonzero element, as occurs in this chapter, a similiar bound may be obtained (see Appendix 4 for the details) and is given by

$$p_j \geq 1 - \sum_{i \neq j} \int_{\Delta_{ji}/2}^{\infty} \frac{1}{\sqrt{2\pi}} \exp(\frac{-x^2}{2}) dx$$

$$\triangleq 1 - \sum_{i \neq j} \text{erfc}_*(\Delta_{ji}/\sqrt{2}) \qquad (5.11)$$

where

$$\Delta_{ji} \triangleq \frac{1}{\sigma} (m_j - m_i) \qquad (5.12)$$

and σ^2 is the log likelihood function variance at each lattice point.

The bound on p_0 in (4.14) was obtained by using the following upper bound on the Gaussian distribution error function (Van Trees, 1968)

$$\text{erfc}_*(X) = \int_X^{\infty} \frac{1}{\sqrt{2\pi}} \exp(-\frac{x^2}{2}) dx$$

$$< \frac{1}{\sqrt{2\pi}X} \exp(-\tfrac{1}{2}X^2) \quad , \quad X>0 \qquad (5.13)$$

In contrast to the argument of the error function which

was bounded in Chapter 4, the $\Delta_{ji}/\sqrt{2}$ error function argument in (5.11) may take on both negative and positive values (e.g. the value is negative when a small, dense unmodeled object exists at some lattice point c_j, $j \neq 0$). Consequently, the error function bound in (5.13) can not be simply applied to (5.11). In this analysis, rather than using different error function bounds for positive and negative values of Δ_{ji}, we instead express the lattice point probability bounds directly in terms of error functions as in (5.11). In the examples that are evaluated in this chapter, these error functions are computed using readily available numerical subroutines.

In the remainder of this chapter, we consider three specific types of modeling errors, and evaluate the lattice point probability p_0 (i.e. one minus the probability of a global error) for each case in order to obtain insight into how quickly the localization performance degrades in the presence of modeling errors. In Section 5.1 we investigate the localization performance when only a single object is present, but its contrast and size are not known precisely a priori. It is demonstrated that localization global performance is not affected by a priori errors in the object contrast (not surprisingly, since the measurements are linear in the contrast parameter d) and that if size modeling errors occur, performance degrades more quickly when object size is

underestimated rather than overestimated. In addition, in this section we provide analysis indicating that if a global error is made it is decidedly more likely to lead to a location estimate near the actual object rather than far away. In Section 5.2, we consider the robustness of the location estimation procedure to errors in the shape of the modeled object, in particular, when the modeled object is circularly-symmetric but the actual object is elongated. In that section, in addition to investigating the behavior of p_0 in the presence of shape modeling errors, we also illustrate the evaluation of the Cramer-Rao bound under mismatch, which in this case provides insight into the effect of shape modeling errors on the local error covariance. In Section 5.3, we consider the robustness of the location estimation procedure to the presence of multiple objects; included in this section are the results of a multiple-object computer simulation. In Section 5.4, the conclusions, we summarize the results of this robustness analysis, and also discuss techniques for obtaining more accurate bounds for the probabilities p_j, particularly for $j \neq 0$.

5.1 ROBUSTNESS TO SIZE AND CONTRAST ERRORS

In this section, we investigate the way in which localization performance degrades when the size and contrast of the actual object are known imprecisely a priori. As mentioned previously, the modeled field we will consider corresponds to a single pillbox object; in this section, we consider the problem of location estimation when the actual object is also a pillbox, but its size (radius) and contrast are known imperfectly. More precisely, suppose that the actual field consists of a single pillbox object of size R_a and contrast d_a, and the modeled object is a pillbox with contrast d and size R (not necessarily equal to d_a and R_a). In this case, the location estimation log likelihood function in (5.9) is

$$L(c) = \int_0^{\pi} \int_{-\infty}^{\infty} g(t,\theta;d_a,c_a,R_a)\, g(t,\theta;d,c,R)\, dt\, d\theta + n(d,c,R)$$

$$= d_a d R_a R \int_0^{\pi} \int_{-\infty}^{\infty} g(1/R_a(t - \underline{c}_a'\underline{\theta}),\theta)\, g(1/R(t - \underline{c}'\underline{\theta}),\theta)\, dt\, d\theta + n(d,c,R) \qquad (5.14)$$

By a change of variable,

$$L(c) \triangleq \mathcal{E}_a (d/d_a) a^*(1/R(c - c_a), R/R_a) + n(d,c,R) \qquad (5.15)$$

where $\mathcal{E}_a$ denotes the Radon-space energy in the actual object

$$\mathcal{E}_a = d_a^2 R_a^3 \mathcal{E}_0 \qquad (5.16)$$

and

$$a^*(\frac{1}{R}c, R/R_a)$$

$$= (1/\mathcal{E}_0)(R/R_a)^2 \int_0^{\pi} \int_{-\infty}^{\infty} g(\frac{R}{R_a} t, \theta) g(t - \frac{1}{R} \underline{c}' \underline{\theta}, \theta) dt d\theta \qquad (5.17)$$

Notice the effect of imprecise knowledge of the contrast d; the normalized ambiguity function in (5.17) does not depend on d or d_a, whereas the log likelihood function in (5.14) depends on the product $d_a d$. In the example that follows, it is shown that the Δ_{ij} terms given in (5.12) (which is the set of information sufficient to determine the p_j probabilities) do <u>not</u> depend on the modeled contrast parameter d, and depend on the actual contrast d_a only through the actual object energy in (5.16). Thus, localization performance does not depend on discrepancies between d and d_a.

EXAMPLE 1 (continued)

Consider the case where the actual and modeled objects are both circularly-symmetric pillbox functions in (4.4),

$$f(r) = d \cdot \text{rect}\ (r/2R) \tag{5.18}$$

and let the modeled object size be given by R = T/10 (see (4.2)). Since the objects are circularly-symmetric, the normalized ambiguity function in (5.17) is also circularly-symmetric, and a central section of it is illustrated in Figure 5.1a for several values of R/R_a. Figure 5.1b is an illustration of these curves normalized by their peak values; notice that the width of the peak (relative to R) is essentially constant when the modeled size exceeds the actual size, and the width of the peak increases when the actual size exceeds the modeled size. That is, the width is determined essentially by the size of the larger of the modeled and actual objects.

In order to determine how p_0 (one minus the global error probability) is affected by incorrect knowledge of the object size, we first evaluate the vector of lattice point log likelihood function means $\underline{m}$ and the log likelihood function variance σ^2, conditioned on the actual object location being $c_0=0$, and then use these values to evaluate the lattice point probability bound in

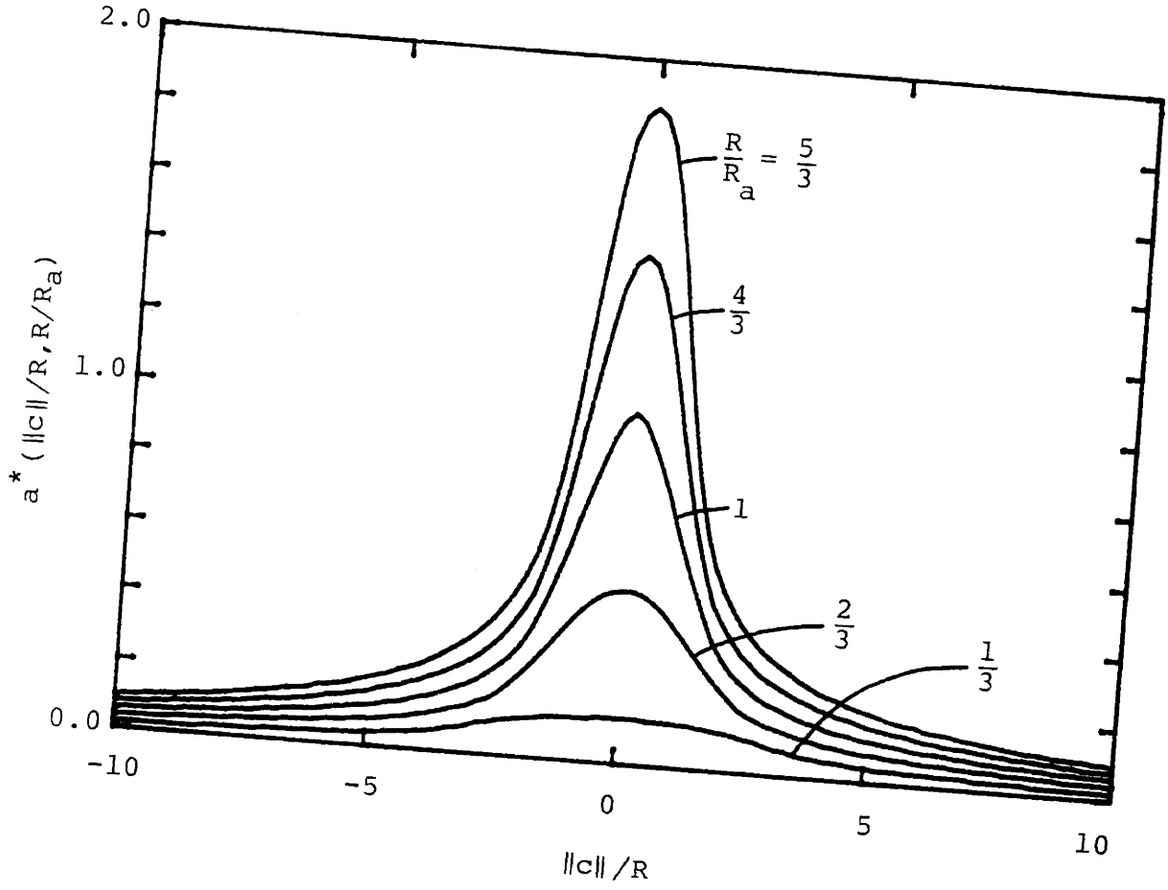

Figure 5.1 (a) Location ambiguity function in the presence of size modeling error.

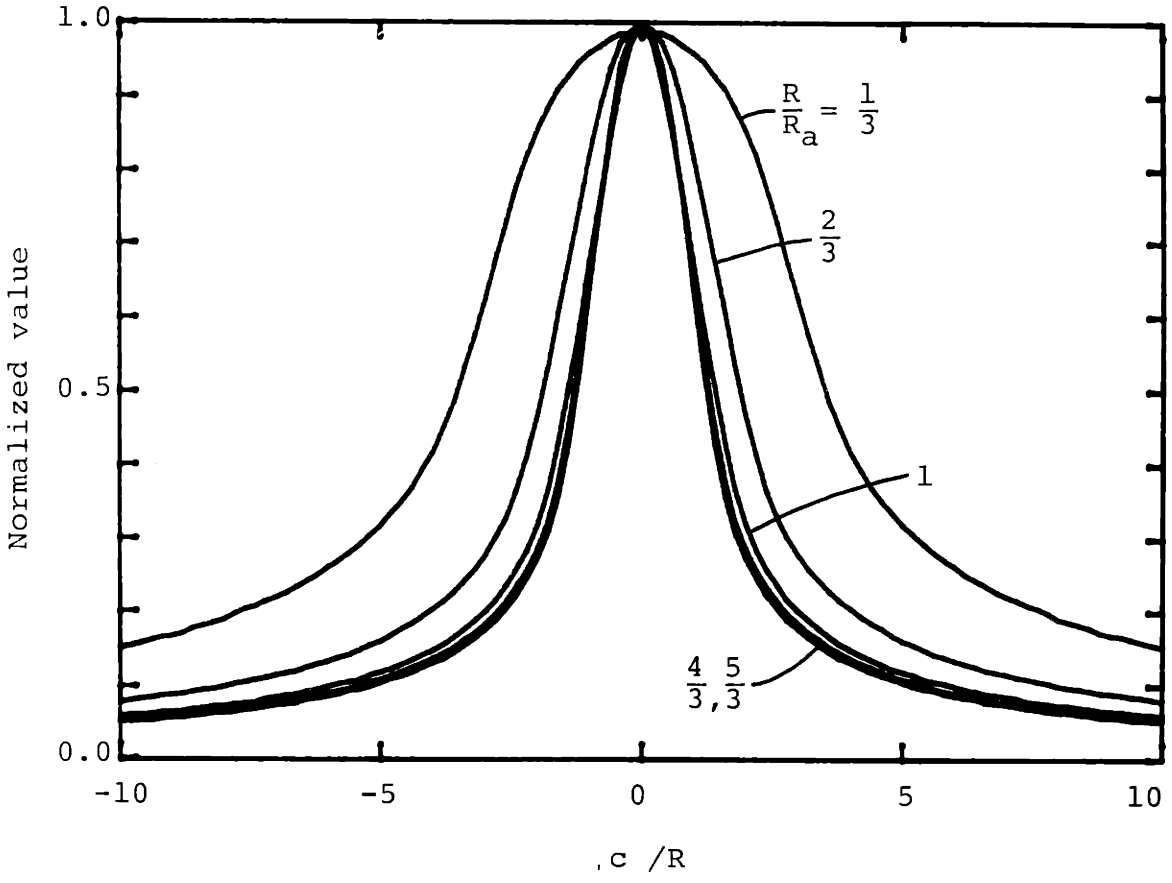

Figure 5.1 (b) Location ambiguity function in the presence of size modeling error, normalized by peak value.

(5.11). The mean value of the log likelihood function at lattice point c_j, from (5.17), is

$$m_j = E\{L(c_j)\} = \mathcal{E}_a (d/d_a) a^*(\frac{1}{R}c_j, R/R_a) \tag{5.19}$$

The variance of the log likelihood function is

$$\sigma^2 = E\{n^2(d,c,R)\} = \frac{N_0}{2}\mathcal{E}a^*(0,1) = \frac{N_0}{2}\mathcal{E} \tag{5.20}$$

where $\mathcal{E}$ denotes the energy in the modeled object, $\mathcal{E} = d^2R^3\mathcal{E}_o$. By using (5.11) and (5.12), a bound may be obtained for the probability p_0, in particular, p_0 is bounded as in (5.11) and (5.12) where

$$\frac{m_j}{\sigma} = \frac{1}{\sqrt{\mathcal{E}N_0/2}}\mathcal{E}_a(d/d_a)a^*(\frac{1}{R}c_j, R/R_a)$$

$$= \sqrt{\frac{\mathcal{E}_a}{N_0/2}}(R/R_a)^{-\frac{3}{2}}a^*(\frac{1}{R}c_j, R/R_a) \tag{5.21}$$

Figure 5.2 illustrates the relationship between the lower bound on p_0 and the measurement SNR (actual object energy divided by N_o) for R/R_a equal to 1/3, 2/3, 1, 4/3, 5/3. As indicated by this figure, the best global performance corresponds to perfect knowledge of the object size (R/R_a=1); notice that the SNR at which p_0 decreases from a value of essentially unity (at $\mathcal{E}_a/N_o \tilde{=} 10$) corresponds closely to the SNR at the "knee"

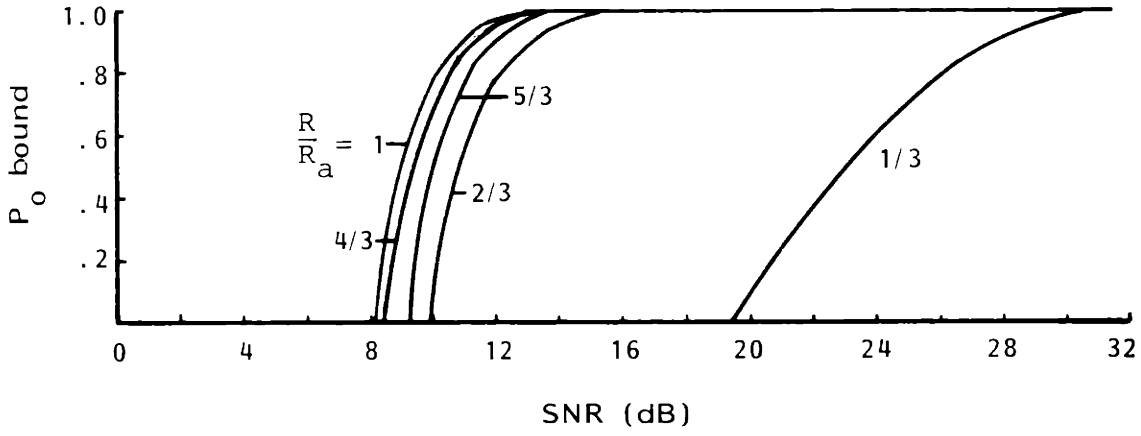

Figure 5.2 Lower bound on p_0 versus measurement SNR in the presence of size modeling error.

in the k=10 performance curve in Figure 4.3 (i.e. to the threshold SNR below which global errors dominate). When size modeling errors occur, Figure 5.2 indicates (1) for a constant value of SNR, the amount by which the global performance measure p_0 decreases or, looked at differently, (2) the amount by which the measurement SNR would have to be increased for the global performance to remain unaffected. The obvious conclusion from this figure is that localization performance is quite robust to moderately-sized modeling errors -- even when modeling errors on the order of 50 percent of the true size occur, the measurement SNR must only be increased by 2 dB or so to overcome global performance degradation caused by the mismatch between the actual and modeled object size.

In this robustness analysis, we have evaluated a bound on p_0, the probability that the value of log likelihood function at lattice point $c_0 = c_a$ exceeds the log likelihood value at all of the other lattice points. As seen in Figure 5.2, this quantity provides insight into the extent to which the localization procedure is robust to size modeling errors. If one desired a more complete analysis of localization robustness, an approximation to the overall error covariance under mismatch could be calculated, as discussed in the introduction, by performing mismatched Cramer-Rao analysis and evaluating all of the p_j, which

are in general not equal here. As was noted in the introduction, when the expression in (5.11) is used directly to compute a bound on p_j for $j \neq 0$, the lower bound is nonpositive, and therefore is useless for the overall error covariance analysis. In the concluding section of this chapter, we discuss several techniques for obtaining more accurate estimates for the p_j values with $j \neq 0$. In addition to these techniques, there is a simple alternate approach to obtain insight into the way in which the total global error probability $1-p_0$ is distributed among the lattice points c_j, $j \neq 0$. In particular, one may select any two lattice points, and calculate easily the probability that the log likelihood function value at one of these points exceeds the value at the other point. One can use this approach to obtain a measure of the relative likelihood that any particular lattice point corresponds to the maximum log likelihood function value by considering various pairs of lattice points.

To illustrate the basic idea behind this approach, we consider in the remainder of this section one particular pair of lattice points. Specifically, we consider the case where one lattice point is close to the actual object at $c_c=(2R,0)$, and the other is far from the object at $c_f=(8R,0)$; we evaluate p_{cf}, the probability that the log likelihood function value at lattice point c_c exceeds the value at c_f. The quantity p_{cf} can be

thought of as an estimate of the probability that, conditioned on the log likelihood maximum not occuring at c_0 (i.e. conditioned on a global error), the maximum value occurs at a point close to the actual object location rather than far away.

The log likelihood function values at these two lattice points are jointly Gaussian and uncorrelated with means m_c and m_f and variance σ^2 given in (5.19) and (5.20); this probability is easily obtained as the following error function

$$p_{cf} = \Pr\left\{ L(c_c) > L(c_f) \right\}$$

$$= 1 - \mathrm{erfc}_*(\Delta/\sqrt{2}) \tag{5.22}$$

where

$$\Delta = \frac{1}{\sigma}(m_c - m_f) \tag{5.23}$$

and $\mathrm{erfc}_*(X)$ is given in (5.13).

The probability p_{cf} was calculated versus SNR for the five R/R_a values in Figure 5.2, and the following was observed:

1) at a fixed value of SNR, smaller values of R/R_a result in larger values of p_{cf} (this agrees with intuition, since when R_a is larger than R, the ambiguity function peak widens, as shown in Figure 5.1).

2) for a fixed value of R/R_a, p_{cf} is a monotone increasing function of SNR; this is also intuitive, since we expect the probability that the peak occurs close to the actual object location to increase with increasing SNR.

3) for a fixed value of R/R_a, and for values of SNR in the range which produces meaningful p_0 bounds in Figure 5.2 (i.e. SNR > 9 dB), $p_{cf} \in (.7,1]$.

The third point confirms the intuitive notion that for a given object size and a SNR value in the range of interest, if a global error does occur, the maximum log likelihood function value is more likely to occur at a lattice point close to the true object rather than far away.

5.2 ROBUSTNESS TO SHAPE ERRORS

In this section, we investigate the way in which localization performance is affected when the shape of the actual object is not known precisely a priori. To illustrate this, we focus our attention on one likely type of shape error, namely, a case in which the actual object is oblong but we do not model it as such. In particular, we consider the case where the actual object is an indicator function on an ellipsoidal region centered at the origin given by

$$\frac{x_1^2}{\lambda} + \lambda x_2^2 \leq R_a^2 \tag{5.24}$$

This object can be thought of as the result of starting with a radius R_a pillbox object in Example 1 and applying the coordinate transformation

$$\tilde{x} = \begin{bmatrix} \sqrt{\lambda} & 0 \\ 0 & 1/\sqrt{\lambda} \end{bmatrix} x \tag{5.25}$$

When the actual object is such a function and the modeled object is a circularly-symmetric pillbox of radius R, the log likelihood function for the location estimate is

$$L(c) = \int_0^{\pi} \int_{-\infty}^{\infty} g(t,\theta;d_a,\lambda,R_a)\, g(t,\theta;d,c,R)\, dt d\theta + n(d,c,R)$$

$$= \mathcal{E}_a \left(\frac{d}{d_a}\right) a^*\left(\frac{1}{R}\, c, \frac{R}{R_a}, \lambda\right) + n(d,c,R) \tag{5.26}$$

where $\mathcal{E}_a$ denotes the Radon-space energy in the ellipsoidally-shaped object

$$\mathcal{E}_a = d_a^2 R_a^3 \mathcal{E}_0(\lambda) \tag{5.27}$$

and

$$a^*\left(\frac{1}{R}\, c, \frac{R}{R_a}, \lambda\right)$$

$$= \frac{1}{\mathcal{E}_0(\lambda)} \left(\frac{R}{R_a}\right) \int_0^{2\pi} \int_{-\infty}^{\infty} g\left(\frac{R}{R_a} t, \Theta; \lambda\right) g\left(t - \frac{1}{R}\, \underline{c} \cdot \underline{\Theta}, \Theta\right) dt\, d\Theta \tag{5.28}$$

In order to determine how p_0 (one minus the probability of a global error) is affected by mismatch between the actual and modeled object shapes, we evaluate, as in the previous section, the vector of lattice point log likelihood function means $\underline{m}$ and the log likelihood function variance σ^2, and then use these values in (5.11) and (5.12) to obtain a bound on the probability p_0. The mean value of the log likelihood function at the point c_j, from (5.26), is

$$m_j = E\left\{L(c_j)\right\} = \mathcal{E}_a\left(\frac{d}{d_a}\right) a^*\left(\frac{1}{R}\, c, \frac{R}{R_a}, \lambda\right) \tag{5.29}$$

The variance of the log likelihood function is $\mathcal{E}N_o/2$ as previously, where $\mathcal{E}$ denotes the energy in the modeled object, $\mathcal{E} = d^2R^3\mathcal{E}_o$. By using (5.11) and (5.12), a bound may be obtained for the probability p_0; in particular p_0 is bounded by (5.11) where

$$\begin{aligned}\frac{m_i}{\sigma} &= \sqrt{\frac{2}{N_0\mathcal{E}}}\ \mathcal{E}_a\left(\frac{d}{d_a}\right) a^*\left(\frac{1}{R}\, c_i, \frac{R}{R_a}, \lambda\right) \\ &= \sqrt{\frac{\mathcal{E}_a}{N_0/2}}\left(\frac{R}{R_a}\right)^{-3/2}\left(\frac{\mathcal{E}_0(\lambda)}{\mathcal{E}_0}\right)^{1/2} a^*\left(\frac{1}{R}\, c_i, \frac{R}{R_a}, \lambda\right)\end{aligned} \tag{5.30}$$

Figure 5.3 illustrates the lower bound on p_0 versus the measurement SNR in dB (i.e. 10 log $\mathcal{E}_a/N_o$) for actual object eccentricity values of 1, 2, 4 and 9. As indicated by this figure, the global localization performance is quite robust to eccentricity modeling errors. This suggests, for example, that it may be possible to use a simple circularly-symmetric pillbox object model in the initial stages of an iterative estimation procedure, even if the actual object is not circularly-symmetric. Once a location and possibly a coarse size estimate are obtained (see Section 6.1), more complicated noncircularly-symmetric object models may be

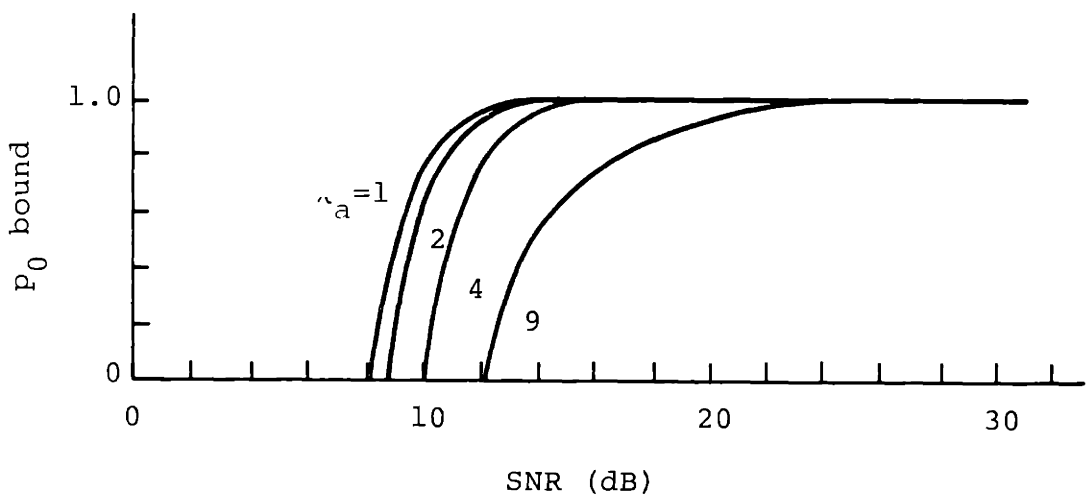

Figure 5.3 Lower bound on p_0 versus measurement SNR in the presence of shape modeling error.

used to estimate finer details of the object profile (the structure of an algorithm along these lines is described more completely in Section 6.4, after the geometry estimation problem has been addressed).

A more detailed robustness analysis may be performed by evaluating an approximation to the overall error covariance; as described in the introduction, this involves estimating each of the p_j probabilities, as well as evaluating the Cramer-Rao bound under mismatch (i.e. in the presence of modeling errors). When the bound in (5.11) is evaluated directly for $j \neq 0$, a nonpositive lower bound is obtained which is useless for the evaluation of the overall error covariance. There are a number of alternative techniques exist for obtaining useful estimates for the p_j, and one such technique is described in the conclusions to this chapter. As discussed in Section 5.1, in the event of a global error, the relative likelihood of lattice points other than c_0 may be assessed by considering lattice points pairwise, and the analysis in that section can be directly applied in the case of shape modeling errors as well. In addition to estimates for the p_j, investigation into the overall error covariance requires evaluation of the local error, which depends on the shape (in particular the width of the main peak) of the ambiguity function under mismatch. We next carry out this step of the analysis in detail in the

present context in order to illustrate the procedure involved and the types of conclusions that can be drawn.

As was shown in previous chapters (see (4.7)), the location estimation ambiguity function may be expressed in terms of four 2D convolutions, namely the convolution of the actual object profile, the modeled object profile, the function $r_h(x)$ arising from a nonimpulsive aperture, and $b_\xi(x)$, the back-projection of the Radon-space sampling function $\xi(t,\theta)$ (which equals $1/\|x\|$ in the full-view case). This convolution representation provides insight into the general shape of the ambiguity function; for example, with regard to the peak of the ambiguity function, it can be no narrower (i.e. sharper) than the broadest peak of the four component functions. One example of this is illustrated in Figure 5.1b, for the case where the actual and modeled objects are both circularly-symmetric pillboxes; when the modeled and actual object sizes R and R_a are not equal, the wider of the two functions can be seen to dominate the general shape of the location ambiguity function.

For the case being considered in this section, where the actual object is an indicator function on an ellipse (taken, for simplicity, to have its long axis in the x_1 direction) but where the modeled object is a pillbox, it is apparent, from the convolution representation for the

ambiguity function, that because the ellipse is centrally-symmetric, the peak of the ambiguity function occurs at the correct object location; also, the actual object dominates the sharpness of the ambiguity function peak in the x_1 direction, and the pillbox modeled object dominates in the x_2 direction. This suggests that when the actual object is very eccentric, object location estimates based on an assumed pillbox shape for the modeled object are somewhat more likely to be obtained which lie outside of the boundary of the actual object (particularly in the x_2 direction). In order to develop some insight into the extent to which this type of shape modeling error will affect localization performance, we consider in the remainder of this section the Cramer-Rao bound for the location estimate error covariance in the presence of shape modeling errors.

As discussed in Section 3.1.2, the Cramer-Rao bound provides an accurate estimate of the local error covariance matrix Λ_0; in particular, from (3.15) through (3.17),

$$\left[\Lambda_0\right]_{ii} \geq \left[J^{-1}\right]_{ii} \tag{5.31}$$

where

$$\left[J\right]_{ik} = -\frac{2}{N_0}\left[\frac{\partial a^2(c)}{\partial c_i\, \partial c_k}\right]_{c=0} = -\frac{2}{N_0}\beta_{ik} \tag{5.32}$$

One derivation of this expression comes from examining the error covariance of a linearized version of the problem (linearized about the actual object location), and this analysis holds for both perfect and imperfect modeling. In the latter case, the local error analysis corresponds to determining the estimation error covariance for a linear estimation problem in which the measurement model used is inaccurate.

For the case being considered in the section, the modeled object is a pillbox

$$f(x) = d \cdot \text{rect}\,(\|x\|/2R) \tag{5.33}$$

and the actual object is an indicator function on the ellipsoidal region given in (5.24), i.e.

$$f_a(x) = d \cdot \text{rect}\left(\frac{1}{2R}\sqrt{\frac{1}{\lambda}x_1^2 + \lambda x_2^2}\right) \tag{5.34}$$

When the measurement aperture function h(t) is the sinc function in (4.6), the expression for β_{ik} resembles that in (4.19), and is given by

$$\beta_{ik} = -4\pi R d^2 \int_0^{\pi} \frac{\nu(\psi)\, d\psi}{\sqrt{\lambda\cos^2\psi + 1/\lambda\sin^2\psi}} \int_0^{2\pi RW} J_1\left(\rho\sqrt{\lambda\cos^2\psi + \frac{1}{\lambda}\sin^2\psi}\right) J_1(\rho)\, d\rho \tag{5.35}$$

where $\nu(\psi)$ is given in (4.19). As a check, note that when $\lambda = 1$ (perfect modeling of a pillbox), equation (5.35) reduces to (4.22).

The expression in (5.35) may be written in a form very similar to (4.22); by using $\mathscr{E}_a$, the Radon-space energy given in (5.27) for the ellipsoidally-shaped object, one obtains

$$\beta_{ik} = (-4\pi/R^2 \mathscr{E}_0(\lambda))\ \mathscr{E}_a \mu_\lambda^{ik}(RW) \tag{5.36}$$

where

$$\mu_\lambda^{ik}(RW)$$

$$= \int_0^\pi \frac{\nu(\psi)\, d\psi}{\sqrt{\lambda\cos^2\psi + 1/\lambda\sin^2\psi}} \int_0^{2\pi RW} J_1\left(\rho\sqrt{\lambda\cos^2\psi + \frac{1}{\lambda}\sin^2\psi}\right) J_1(\rho)\, d\rho \tag{5.37}$$

For purposes for illustration, this expression has been evaluated for values of actual object eccentricity of 1, 2, 4 and 9, with the radius-bandwidth product RW = 1, and the results are tabulated in Table 1. Not surprisingly, by the central symmetry of the problem, β_{ik} is zero for $i \neq k$. This implies that the Fisher's information matrix is diagonal, in which case it is sufficient to consider σ_{11} and σ_{22}, the diagonal elements in the inverse Fisher's information matrix (i.e. the local error covariance matrix, see (5.31)). From (5.31), (5.32), and (5.36),

$$\sigma_{ii} = \frac{R}{\sqrt{\mathcal{E}_a/N_0}} \sqrt{\frac{\mathcal{E}_0(\lambda)}{8\pi \mu_\lambda^{ii}(RW)}} \tag{5.38}$$

The value of the second term on the right-hand side is also indicated in Table 1.

	$\mu_\lambda^{ik}(1)$			$\sqrt{\mathcal{E}_o(\lambda)/8\pi\mu_\lambda^{ik}(1)}$	
	i=k=1	i=k=2	i≠k	i=k=1	i=k=2
λ=1	1.29	1.29	0.0	0.72	0.72
λ=2	0.71	1.26	0.0	0.95	0.72
λ=4	0.27	0.92	0.0	1.49	0.81
λ=9	0.09	0.58	0.0	2.32	0.94

Table 1. Values of the expressions in (5.37) and (5.38) for λ = 1, 2, 4 and 9.

Equation (5.38) is an expression for the standard deviation of the localization error in the x_1 and x_2 directions when shape modeling errors have been made. In order to develop some insight into the relationship between these two standard deviations and the likelihood that a location estimate is obtained which lies outside

the actual object boundary, we may use (5.38), for a given SNR, to identify an error ellipse, that is, the set of estimate points lying inside an ellipse centered at the actual object location, with semi-axis lengths equal to the standard deviations σ_{11} and σ_{22}. Notice from (5.38) that the size of this ellipsoidal region is inversely proportional to the square root of the SNR; thus the size of this ellipse will shrink as SNR is increased. For given values of SNR, radius-bandwidth product RW, and eccentricity λ, the error ellipse may be calculated and compared to the actual ellipsoidal object boundary; Figure 5.4 illustrates the error ellipse specified by (5.38) for two representative eccentricities, namely $\lambda = 2$ and 9, and a SNR value of 10 dB. As indicated by this figure, the 10 dB error ellipse is completely contained within the boundary of the actual ellipsoidal object (this is also true for the cases where λ equals 1 and 4). The results of this analysis provide insight into the effect of shape modeling errors on the local estimate error -- even when the actual object is highly eccentric with λ equal to 9 (and the modeled object is a pillbox), the location estimate has a high probability of lying within the actual object boundary. Note that according to Figure 5.3, 10 dB is not a particularly high SNR; for example, for $\lambda = 2$, a SNR of 13 or 14 dB is needed for p_0 to be sufficiently close to

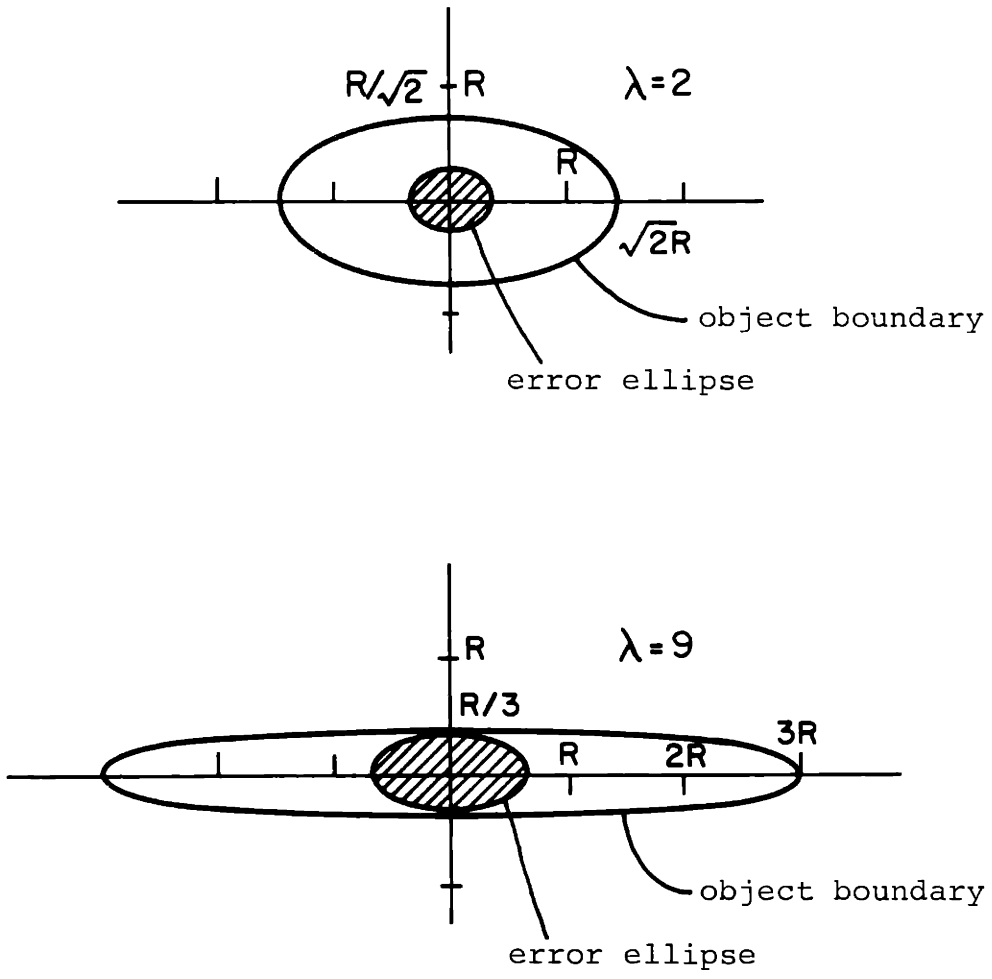

Figure 5.4 10 dB error ellipse in the presence of shape modeling error.

one, and for $\lambda = 9$, the SNR must be close to 25 or so.

The information obtained from the analysis in this section can be used in several ways:

1) It can be thought of as an indication of the measurement SNR that is needed if one is unsure of the shape of the actual object and uses a circularly-symmetric modeled profile.

2) For a given SNR, the information in this section (see Figure 5.3) can be used to identify the maximum eccentricity of an object that can be located reliably using a circularly-symmetric modeled shape. If there is some likelihood that the actual object is more eccentric than this, an iterative procedure (such as the one described in Section 6.4) may be necessary to obtain an accurate location estimate.

This last point deserves a bit more comment. As described in Chapter 6, if one uses a modeled object which is eccentric, the object <u>orientation</u> is a quantity that must also be estimated if it is not already known. In particular, when object location is being determined using a modeled object which is eccentric but which has an orientation which is different from the actual object, localization robustness may be assessed using the same

general ideas developed in this chapter. In fact, in this case, the location ambiguity function may be shown by symmetry to have ellipsoidal contours with a major axis oriented at an angle that is the average of the modeled and actual orientation angles.

In Section 6.3 we consider the object geometry estimation problem when the location is perfectly and imperfectly known; in that section we show that even if the object location is known imprecisely, certain aspects of the object's geometry (for example, size) can be estimated quite reliably. These results, together with the results of the present section, suggest that a simple circularly-symmetric profile can be useful in the initial stages of an iterative procedure (even if the actual object is not circularly-symmetric) to estimate object location and geometry parameters. We discuss this point more completely in Section 6.4.

5.3 ROBUSTNESS TO THE PRESENCE OF UNMODELED OBJECTS

5.3.1 A bound on p_0

In this section, we investigate the way in which localization performance degrades when in addition to the object being located, one or more unmodeled objects exist within the cross-section. Suppose that the actual field

consists of N objects, where the kth has contrast d_k, location $\tilde{c}_k$ and size R_k; the object to be located will be denoted as the first (k=1) object, and objects with k=2,...,N correspond to unmodeled objects. As discussed in Section 5.1, these N-1 unmodeled objects (which contribute N-1 extra terms to the log likelihood function) may be thought of as corresponding to uncertainty in the background field $f_b(x)$. From (5.9), the log likelihood function is given by

$$L(c) = \sum_{k=1}^{N} \int_0^{\pi} \int_{\infty}^{\infty} g(t,\Theta;d_k,\tilde{c}_k,v_k)\, g\,(t,\Theta;d,c,R)\, dt d\Theta + n(d,c,R) \tag{5.39}$$

which by a change of variable may be written as

$$L(c) = \sum_{k=1}^{N} \mathscr{E}_k \left(\frac{d}{d_k}\right) a^* \left(\frac{1}{R}\,(c - \tilde{c}_k), \frac{R}{R_k}\right) + n(d,c,R) \tag{5.40}$$

where $\mathscr{E}_k$ denotes the Radon-space energy in the kth object,

$$\mathscr{E}_k = d_k^2 R_k^3 \mathscr{E}_0 \tag{5.41}$$

and

$$a^*\left(\frac{1}{R}(c - \tilde{c}_k),\ \frac{R}{R_k}\right)$$

$$= \frac{1}{\mathcal{E}_0}\left(\frac{R}{R_k}\right)^2 \int_0^{\pi}\int_{\infty}^{\infty} g\left(\frac{R}{R_k}t,\Theta\right) g\left(t - \frac{1}{R}(\underline{c} - \underline{\tilde{c}}_k)\cdot\underline{\theta},\Theta\right) dt\, d\Theta \qquad (5.42)$$

This expression resembles that in (5.17), and when the actual and modeled objects are both pillboxes (see (5.18)), the normalized ambiguity function for the k<u>th</u> object in (5.42) may be obtained from Figure 5.1 by replacing R/R_a with R/R_k.

In order to determine how the probability p_0 (one minus the probability of a global error) is affected by the presence of unmodeled objects in the cross-section, we first evaluate the vector of lattice point log likelihood function means $\underline{m}$ and the log likelihood function variance σ^2, and then we use these values in (5.11) and (5.12) to obtain a bound on p_0. The mean values of the log likelihood function at the point c_j, obtained from (5.40), is

$$m_j = E\left\{L(c_j)\right\} = \sum_{k=1}^{N} \mathcal{E}_k\left(\frac{d}{d_k}\right) a^*\left(\frac{1}{R}(c_j - \tilde{c}_k),\ \frac{R}{R_k}\right) \qquad (5.43)$$

The variance of the lattice point measurements is $\mathcal{E}N_o/2$, as previously, where $\mathcal{E}$ denotes the energy in the modeled object, $\mathcal{E} = d^2R^3\mathcal{E}_o$. By using (5.11) and (5.12), a

bound may be obtained for the probability p_0; in particular, p_0 is bounded as in (5.11) where

$$\frac{m_i}{\sigma} = \sqrt{\frac{2}{N_0 \mathscr{E}}} \sum_{k=1}^{N} \mathscr{E}_k \left(\frac{d}{d_k}\right) a^* \left(\frac{1}{R}(c_i - \tilde{c}_k), \frac{R}{R_k}\right)$$

$$= \sqrt{\frac{\mathscr{E}_1}{N_0/2}} \left[\left(\frac{R}{R_1}\right)^{-3/2} a^* \left(\frac{1}{R}(c_i - \tilde{c}_1), \frac{R}{R_1}\right) \right.$$

$$\left. + \left(\frac{R}{R_1}\right)^{3/2} \sum_{k=2}^{N} \left(\frac{R}{R_k}\right)^{-3} \left(\frac{d_k}{d_1}\right) a^* \left(\frac{1}{R}(c_i - \tilde{c}_k), \frac{R}{R_k}\right) \right] \qquad (5.44)$$

Two specific examples are investigated, the first involving a single unmodeled object, and the second involving the presence of numerous small objects distributed throughout the cross-section (as discussed at the beginning of this section, such an example may be thought of in a sense as corresponding to modeling the presence of unknown random fluctuations in the actual background field, which is assumed to be known perfectly in the model used in the localization procedure).

As mentioned, in all of the problems considered in this chapter, the modeled field corresponds to a pillbox object of radius T/10, and the lattice has 2R spacing as shown in (5.10). In the first example of this section, we investigate the effect on global performance when the

actual field consists of a pillbox of size R_1=R=T/10 (perfectly matched to the model) situated at the origin, plus a single unmodeled object with size R_2 and contrast d_2 situated at the coordinates (6R,0). In this example we examine the way in which the lower bound on p_0 depends on the measurement SNR and the unmodeled object size and contrast. As was the case in the previous two sections, we focus our attention on the bound for p_0 because it provides a useful measure of localization robustness to the presence of unmodeled objects. More detailed robustness results may be obtained by performing Cramer-Rao analysis as illustrated in Section 5.2. Also, as in the previous sections, the bounds on p_j for $j\neq 0$, when calculated directly using (5.11), result in values that are nonpositive. Useful bounds on the p_j for $j\neq 0$ may be obtained either by using the method described in Section 5.1 for evaluating the relative likelihood of any two lattice points, or by using one of the approaches discussed in the conclusions to this chapter.

For the case of an extra, unmodeled object of size and contrast R_2 and d_2, Figure 5.5 illustrates the lower bound on p_0 versus the contrast ratio d_2/d_1 for size ratio values of R/R_2 equal to 1/3, 2/3, 1, 4/3 and 5/3, when the value of $\mathcal{E}_1/N_o$ equals 20 dB (i.e. $\mathcal{E}_1/N_o$ = 100). This figure clearly illustrates the graceful manner in which global performance degrades

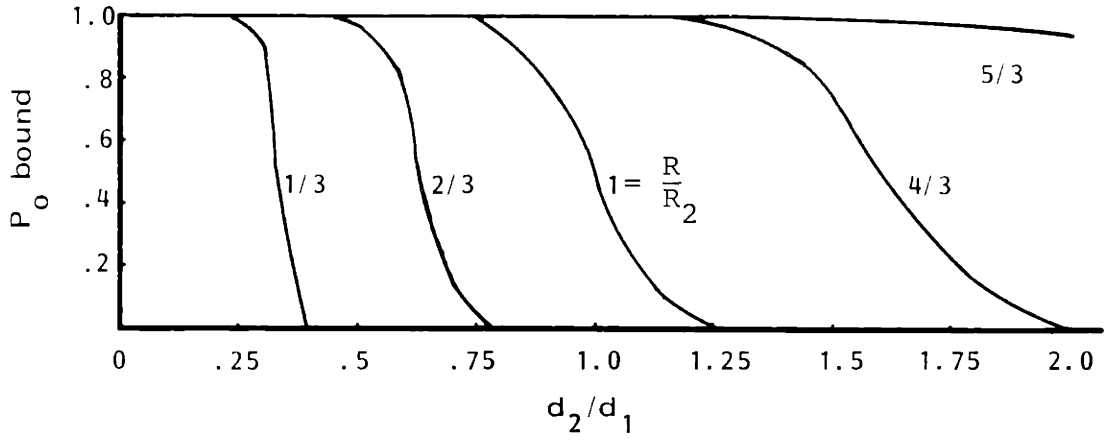

Figure 5.5 Lower bound on p_0 versus unmodeled object contrast ratio d_2/d_1.

when an unmodeled object is present in the cross-section. Namely, when the unmodeled object is smaller than the modeled object (R/R_a = 5/3 and 4/3 curves), even if its contrast is equal to the value of the actual object contrast, global performance is virtually unaffected. Notice in particular the case of a smaller unmodeled object with a radius of 0.6 times the actual object radius -- this unmodeled object can be <u>far</u> denser than the actual object without significant degradation in the ability to locate the main object by using an algorithm which does not take into account the possibility of more than one object.

When the unmodeled object size is approximately the same as the actual object (or larger), the global performance can be seen to degrade quite rapidly with increasing unmodeled object contrast. What these results indicate is that (1) there is essentially no performance degradation due to the presence of unmodeled objects when one is locating the largest object in the field, and (2) if one wants to locate smaller objects in the cross-section, it is necessary to also locate any larger ones that are present. The latter of these two points is not surprising; the former is surprising only insofar as the extraordinary level of insensitivity of the localization performance to the presence of a smaller object.

In the second example of this section, we investigate the effect on global performance when numerous small unmodeled objects are distributed throughout the cross-section. As mentioned, these "objects" may be thought of in a sense as corresponding to random fluctuations in the background field, which in all of our models for object estimation is assumed to be perfectly known. The specific example we consider is the global error performance (i.e. p_0) when the actual field consists of a pillbox of size R_1=R=T/10 (perfectly matched to the model) situated at the origin, plus twenty smaller unmodeled pillbox objects located at the coordinates shown in Table 2, each having size R_u and density d_u. Figure 5.6 illustrates the distribution of objects within the cross-section when R/R_u=2, i.e. when each of the unmodeled objects has a radius of one-half that of the central object.

Figure 5.7 illustrates the lower bound on p_0 versus the contrast ratio d_u/d_1 for $\mathcal{E}_1/N_o$ equal to 20 dB and values of R/R_u = 2 and 4/3 (that is, each of the unmodeled objects has a radius of one-half the actual object radius in the first case, and a radius of 0.75 times the actual object radius in the second case). As indicated by this figure, the global localization performance is extraordinarily robust to the presence of smaller unmodeled objects, even if there are many of them.

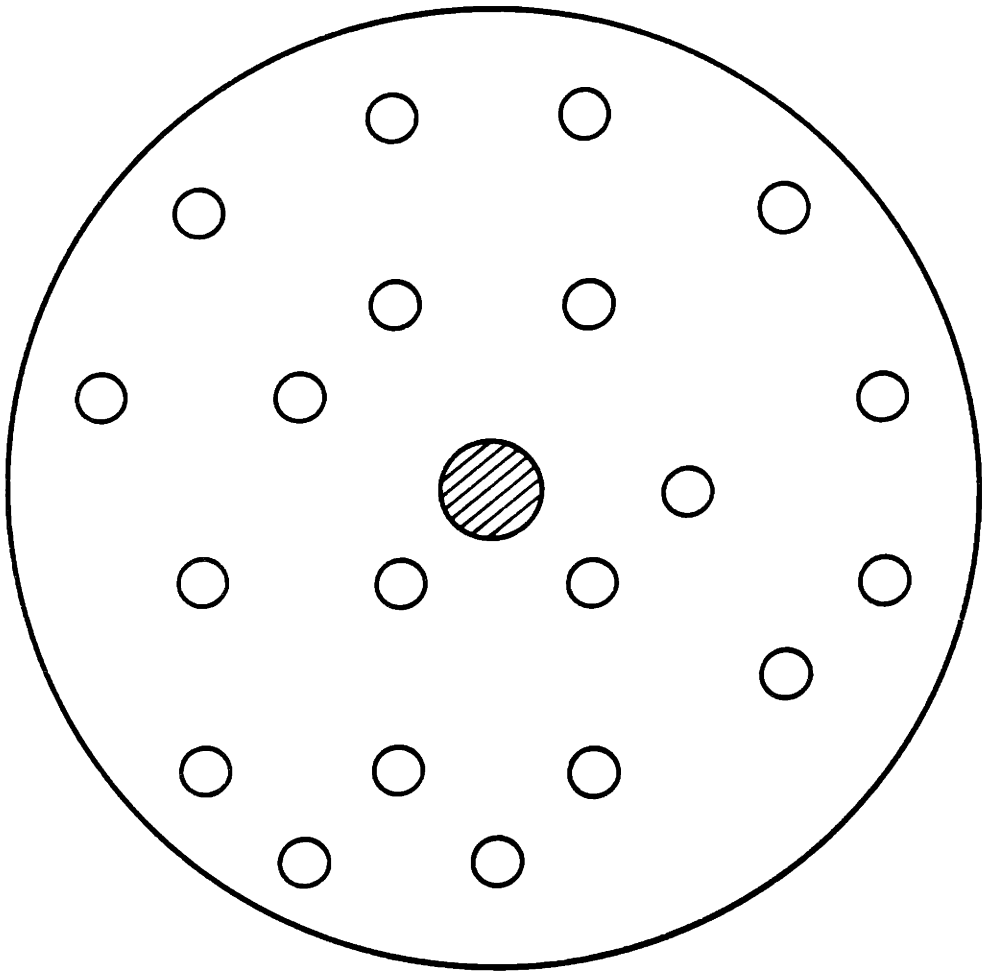

Figure 5.6 Distribution of unmodeled objects in the cross-section.

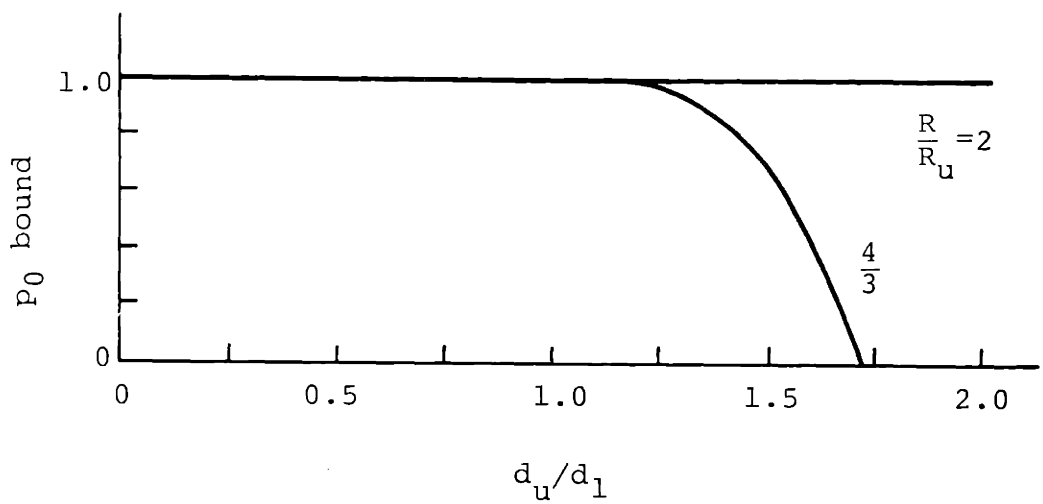

Figure 5.7 Lower bound on p_0 versus the contrast ratio d_u/d_l; 20 unmodeled objects.

OBJECT	LOCATION	OBJECT	LOCATION
2	2R,8R	12	-2R,-2R
3	-6R,6R	13	2R,-2R
4	-2R,4R	14	8R,-2R
5	2R,4R	15	6R,-4R
6	6R,6R	16	-6R,-6R
7	-8R,2R	17	-2R,-6R
8	-4R,2R	18	2R,-6R
9	8R,2R	19	-4R,-8R
10	4R,0	20	0,-8R
11	-2R,8R	21	-6R,-2R

Table 2. Locations of the twenty unmodeled objects in Figure 5.6

In particular, when the unmodeled object size is one-half the actual object size, the global performance is unaffected for values of the contrast of the unmodeled objects up to twice that of the central object. Even when the object size is 0.75 times the actual object size, the global performance is unaffected for unmodeled object contrast values less than or equal to the actual object contrast. The results of this robustness analysis, then, suggest that our localization procedure, which assumes that $f_b(x)$ is known, is quite robust to random

fluctuations in the background field about its assumed nominal distribution.

5.3.2 Simulations

In this section we present the results of a multiple-object computer simulation in which a limited number of computer-generated noisy line integrals were processed using the algorithm in (4.40), to create both a log likelihood function and a reconstructed image by using the kernels in (4.42) and (4.43) respectively. The same measurement geometry is used here as was used in the single-object simulation described in Section 4.2. In this simulation, the actual field consists of three objects situated within a circularly-shaped region normalized to have a radius of T=1. The first object (the object to be located) is given in (4.41) of the single object simulations, namely a unit-contrast pillbox of radius 0.2 centered at (0.2,0.4). The other two objects (which are not modeled in the localization algorithm) are each a unit-contrast pillbox of radius 0.1; one is centered at (-0.4,0.2) and the other is centered at (0.5,-0.5). An image representation of this three-object cross-sectional density function is shown in Figure 5.8.

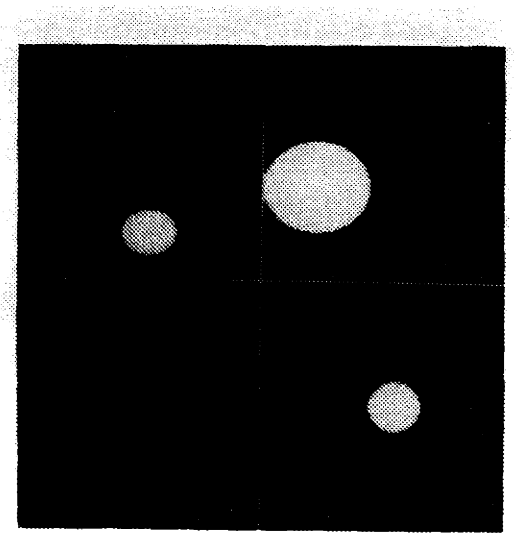

Figure 5.8 Image representation of the three-object cross-sectional density function.

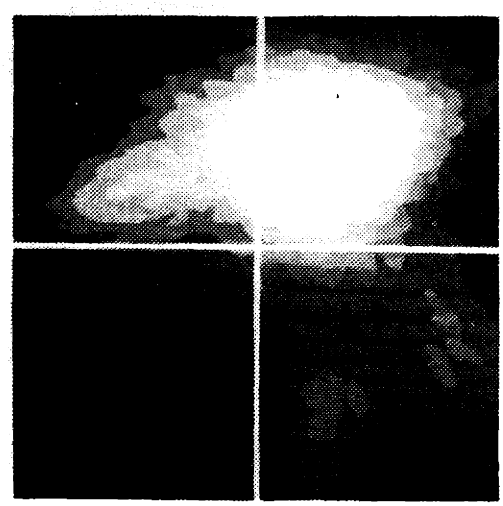

Figure 5.9 Image representation of the five-view noise-free log likelihood function.

Figure 5.9 is an illustration of the image obtained using the log likelihood kernel $z_{LL}(t)$ in (4.22) with no additive measurement noise. As was the case in the single-object simulation in Section 4.2, the back-projection operation is seen to produce a series of strips intersecting at the object locations, and the value of the function at points not lying on these strips is zero.

In this multiple object simulation, two measurement noise levels (see (4.39a)) were used, namely 5 dB and 0 dB, and at each noise level, the same noise samples were used in performing the CBP using both convolving kernels. Figure 5.10a is an image representation of the log likelihood function obtained with an SNR of 5 dB, with the gray scale distributed on the interval [0.6,1]. Notice that the two objects having a radius of 0.1 do not contribute visible peaks in this image at their center locations. This is because the value of the noise-free log likelihood function at the centers of these two unmodeled objects is approximately 25 percent of the value at the center of the object at (0.1,0.2) (see (5.40) and Figure 5.1a); because this value is less than 0.6, it is imaged in black.

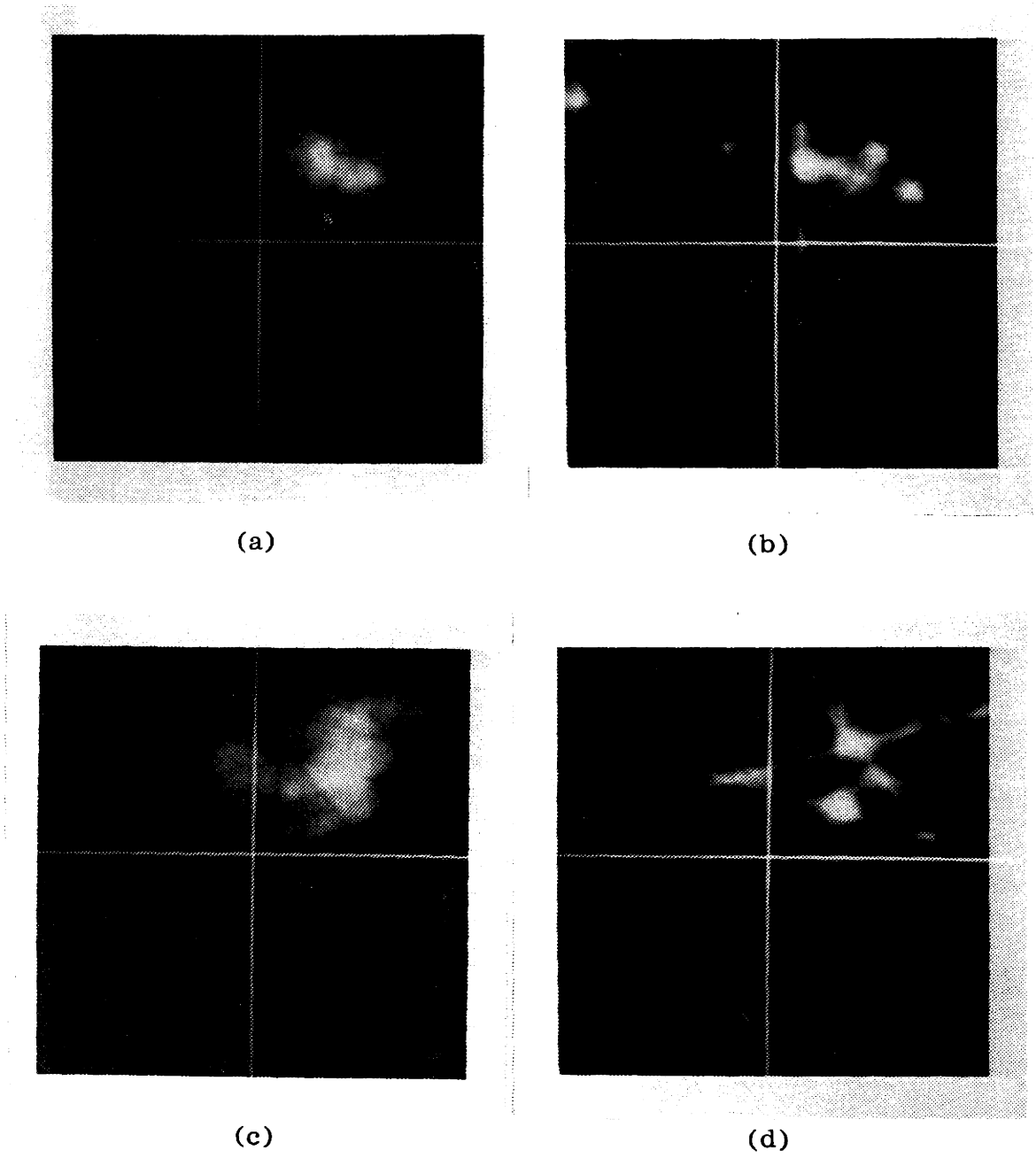

Figure 5.10 (a) log likelihood function, SNR = 5 dB, scale = [0.6,1.0].
(b) reconstructed image, SNR = 5 dB, scale = [0.6,1.0].
(c) log likelihood function, SNR = 0 dB, scale = [0.6,1.0].
(d) reconstructed image, SNR = 0 dB, scale = [0.6,1.0].

Figure 5.10b corresponds to the reconstructed image (obtained using the kernel in (4.43)) with a SNR of 5 dB, with the gray scale distributed on the interval [0.6,1]. Figures 5.10c and 5.10d are the log likelihood function and reconstructed image at a SNR value of 0 dB with the gray scale distributed on the interval [0.6,1]. As was the case in the single-object simulation in Section 4.2, the image reconstruction kernel $z_I(t)$ in (4.43), because of its higher gain at high frequencies as compared to $z_{LL}(t)$, leads to multiple spurious peaks throughout the cross-section, complicating the localization of the pillbox having a radius of 0.2. In contrast, for each of the noise levels, the log likelihood function has only one peak, which occurs very close to the true object location.

In order to investigate the way in which post-processing the reconstructed image improves one's ability to detect and locate objects, we post-processed the reconstructed images in Figures 5.10b and 5.10d using the 2D correlating function $f_c(x)$ described in the single-object simulation (see (4.44)). The image in Figure 5.11a is the result of post-processing the image in Figure 5.10b, with the gray scale distributed on the interval [0.6,1]. Similarly, Figure 5.11b is the result of post-processing the image in Figure 5.10d, with the gray scale distributed on [0.6,1]. As in Section 4.2, these two images are seen to be very similar to the log

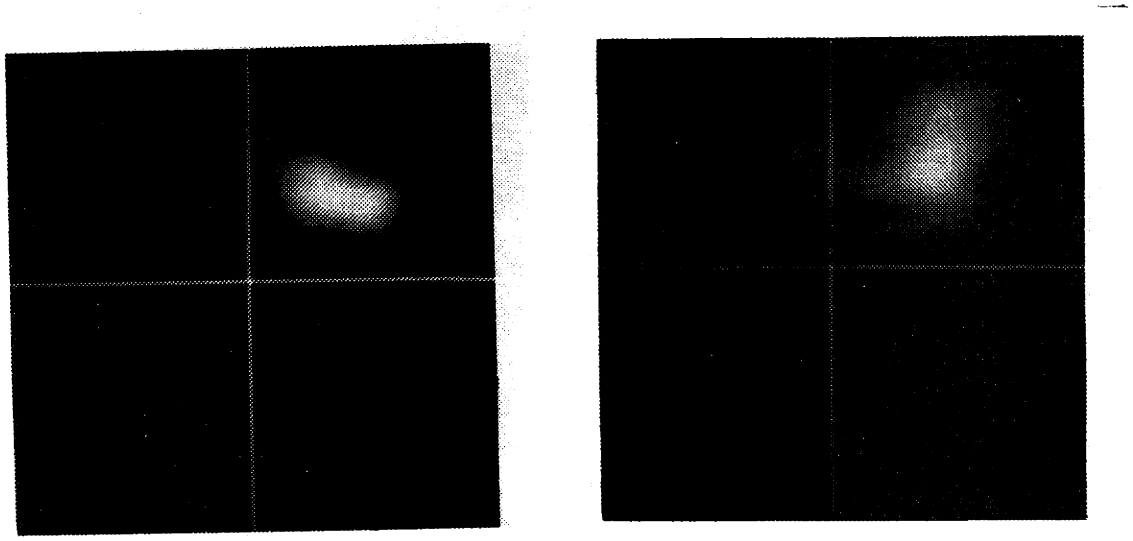

(a) (b)

Figure 5.11 (a) result of convolving the image in Figure 5.10b with $f_c(x)$; scale = [0.6,1.0].

(b) result of convolving the image in Figure 5.10d with $f_c(x)$; scale = [0.6,1.0].

likelihood functions (imaged in Figures 5.10a and 5.10c), although the log likelihood functions were computed directly in much less time, and, unlike Figures 5.11a and 5.11b, are the result of optimal matched filtering. The similarity in appearance of the log likelihood functions and post-processed images is (as in Section 4.2) again an indication of the robustness of the matched filter to nonwhite image noise.

These multiple-object simulations provide a visualization of the difference between the log likelihood function with modeling errors (an incorrectly modeled number of objects) and a conventionally reconstructed image. As was the situation with the single object simulation, an object located within the cross-section is discerned much more easily by examining the log likelihood function (even in the presence of modeling errors) than by examining a reconstructed image that has not undergone time consuming post-processing. The relative advantages of direct log likelihood function evaluation (it is faster, optimal, and applicable to the estimation of other object parameters) discussed in Section 4.2.2 apply here as well.

5.4 CONCLUSIONS

In this chapter, we have investigated the way in which the single object localization performance analysis in Chapters 3 and 4 is affected when the modeling assumptions in (5.1) do not all hold. In particular, size and shape modeling errors were investigated, as was the presence of unmodeled objects within the cross-section. Equation (5.9) also shows how the background field $f_b(x)$ enters the log likelihood function; if $f_b(x)$ is not known deterministically, but is instead a zero-mean random field, $g_b(t,\Theta)$ and $a_b(d,c,R)$ are both zero-mean random fields. In this chapter, we continued to assume that $f_b(x)$ is known, but the effect of random fluctuations in the background field was essentially investigated via an analysis of the robustness to the presence of many small, unmodeled objects.

As discussed in Section 5.0, one could approach this robustness analysis by performing detailed covariance analysis similar to that developed and applied in Chapters 3 and 4. This type of analysis requires evaluation of the Cramer-Rao bound (for an estimate of the local variance) as well as all of the probabilities p_j. In this chapter, we have illustrated the behavior of p_0 in the presence of a variety of modeling errors, and the Cramer-Rao bound was evaluated in the analysis of

robustness to shape modeling errors in Section 5.2. Also, in the analysis of robustness to size modeling errors in Section 5.1, we investigated the relative likelihood that any given lattice point has a larger log likelihood function value than any other given lattice point.

It was mentioned in Section 5.1 that for $j \neq 0$, the lower bound on p_j in (5.11) is not positive. More useful bounds on the probabilities p_j may be obtained in several ways; we take a moment now to discuss one such technique. In particular, by use of the procedure illustrated in this chapter, p_0 may be bounded easily, and for SNR values large enough so that this bound is positive, one minus this bound is a good approximation to $(1-p_0)$, the probability that the log likelihood function maximum occurs at some lattice point other than c_0. Consider the reduced set of lattice points $c_1,\ldots,c_{M-1}$; if lattice point c_k has the largest mean of these M-1 lattice points, p_k is given by

$$p_k = \Pr\left\{ l_k \geq l_j \text{ , } j=1,2,\ldots,M-1 \;\middle|\; c_0 \text{ not maximum lattice point} \right\} (1 - p_0) \tag{5.45}$$

By considering the reduced set of lattice points $c_1,\ldots,c_{M-1}$, the procedure presented in Appendix 4 may

be used to obtain an estimate of the first probability on the right-hand side of (5.45), and as just discussed, $(1-p_0)$ may be approximated using (5.11). This calculation may be continued by considering an increasingly reduced set of lattice points, and leads to more useful bounds on the probabilities p_j, $j \neq 0$, than are obtained by using (5.11) directly. The problem of obtaining bounds on the probability that any one of a set of jointly Gaussian random variables is the maximum is an open problem, particularly when the random variables are correlated (as occurs for our problem in the limited- and discrete-view measurement cases); some work has been done, however, see Gallager and Helstrom (1969).

In conclusion, the results of this chapter indicate that the ML localization procedure developed in Chapter 3 is quite robust to a variety of modeling errors. In Section 5.1 it was demonstrated that no major degradation in global performance occurs when the object size is in error by up to approximately 50 percent of the actual object size. In Section 5.2, it was shown that when the actual object shape differs from the modeled shape (an eccentric object was modeled as being circularly-symmetric), the localization performance is again very insensitive to modeling errors. Finally, it was shown in Section 5.3 that global performance is not affected significantly by the presence of unmodeled

objects (even if there are many of them) that are smaller than approximately three-quarters of the size of the object to be located; this is true even when the value of their contrast is equal to that of the object being located (and in fact, their contrast can exceed that of the object to be located if they are half its size or smaller).

APPENDIX 4 -- Lattice point probability bound

Let $\underline{L}$ denote the M-vector of lattice point measurements, which is a Gaussian random vector having mean $\underline{m}$ and covariance $\sigma^2 I$. As in Chapter 3, we let p_j denote the probability of E_j, the event that the lattice point c_j has the largest log likelihood function value. Using the fact that the lattice point measurements are uncorrelated, $(1-p_j)$ may be bounded using the approach in Van Trees (1968), p. 263,

$$1 - p_j = \Pr\left\{ \text{any } l_i > l_j,\ i \neq j \right\}$$

$$= \Pr\left\{ l_1 > l_j \text{ or } l_2 > l_j \text{ or} \ldots \ l_m > l_j \right\}$$

$$\leq \Pr\left\{ l_1 > l_j \right\} + \Pr\left\{ l_2 > l_j \right\} + \ldots + \Pr\left\{ l_m > l_j \right\}$$

$$= \sum_{i \neq j} \int_{-\infty}^{\infty} p_{l_j}(L_j) \int_{L_j}^{\infty} p_{l_i}(L_i)\, dL_i\, dL_j \qquad \text{(A4.1)}$$

Substituting the Gaussian distribution and simplifying,

$$p_j \geq$$

$$1 - \sum_{i \neq j} \int_{-\infty}^{\infty} \frac{1}{\sqrt{2\pi}} \exp\left(-\frac{1}{2}(x_j - \Delta_{ji})^2\right) \int_{x_j}^{\infty} \frac{1}{\sqrt{2\pi}} \exp\left(-\frac{x_i^2}{2}\right) dx_i dx_j \qquad \text{(A4.2)}$$

where

$$\Delta_{ji} = \frac{1}{\sigma} (m_j - m_i) \qquad \text{(A4.3)}$$

By a change of variable corresponding to a 45^{o} coordinate system rotation, (A4.2) may then be written as

$$p_j \geq 1 - \sum_{i \neq j} \int_{\Delta_{ji}/\sqrt{2}}^{\infty} \frac{1}{\sqrt{2\pi}} \exp\left(-\frac{x^2}{2}\right) dx \qquad \text{(A4.4)}$$

CHAPTER 6

OBJECT SIZE, ECCENTRICITY AND ORIENTATION ESTIMATION

6.0 INTRODUCTION

Up to this point we have considered the problem of using noisy projection measurements to locate an object in a cross-section when its relative profile $f_o(x;v)$ is known. This is a special case of the more general problem, introduced in Chapter 2, of using noisy projection data to estimate the object density, location and relative profile (i.e. the detailed density variations corresponding, for example, to object size, shape and orientation). In this chapter, we consider the object relative profile estimation problem, that is, the problem of estimating the finite-dimensional profile parameter v for a single object whose contrast d and location c are known (the location c is taken without loss of generality to be the origin).

The focus of this chapter will be on obtaining insight into the geometry estimation problem and on developing a methodology for assessing estimation performance. Consequently, one particular parameterization for the object geometry is selected which has a small number of degrees of freedom and is

well-suited for the approach in this chapter. A framework is then developed for addressing a number of specific issues, such as

- estimation performance -- determining under what conditions unbiased ML estimates are obtained, and evaluating estimation accuracy, as a function of projection measurement noise level, by using the Cramer-Rao bound.

- robustness to modeling errors -- determining the effect of modeling errors on the performance; e.g. the effect of modeling an elongated object as circularly-symmetric when estimating object size.

- selecting the model complexity -- simple models (e.g. circularly-symmetric profiles) are computationally attractive and may be useful, especially if limited measurement data are available, for extracting simple object information such as size. Extracting more detailed information about an object requires the use of more complex models, which in turn requires the availability of more measurement data (either more views or higher SNR). Given a set of measurements, what questions about an object can one reasonably expect to answer, or how does one select an object model whose complexity is appropriate for the

measurement quantity and SNR?

- the effect of limited projection data -- in what ways does estimation performance degrade when the total number of projections or the view angle is decreased?

In Chapter 2, several potentially useful profile representations were mentioned. One simple relative profile is an indicator function on a subset $K \subset R^2$ which is located at the origin. In this case the object relative profile is completely specified by the set boundary ∂K, and in order to approach this problem as a finite dimensional optimal estimation problem, the boundary ∂K must be either exactly or approximately parameterized by a finite dimensional parameter v. In the next section, we discuss this issue.

6.0.1 Geometry parameterizations

Several parameterizations of the boundary ∂K were mentioned in Section 2.1.1, including (1) a set K that has a simple geometric shape that is parameterized by a small set of numbers, (2) a set K that is convex and approximately parameterized by the coefficients in a truncated series expansion for its support function (Santalo, 1976), and (3) a set K whose boundary is represented by a sequence of horizontally and vertically

directed edge segments (Cooper et al., 1980). While the results of Cooper et al. suggest that the last representation may be very robust, this parameterization generally involves a large number of unknowns. Since our focus in this chapter is on obtaining insight into the geometry estimation problem, we concentrate instead on parameterizations having fewer unknowns.

The convex set representation for K is attractive for several reasons: (1) convex sets are intersected at most once by a line in the plane, which simplifies the Radon transform computation, (2) the support function for a convex set corresponds in Radon space to the boundary of the support region for the Radon transform (the region on which the Radon transform is nonzero) and (3) if the support function is represented as a truncated Fourier series, the first harmonic coefficients affect only the object's location in the plane, which leads to a natural separation of the localization and relative profile estimation problems. The parameterization of a convex set K by approximating its support function with a truncated Fourier series expansion, and the calculation of the Radon transform for such a representation are discussed in Appendix 5.

One potential drawback of this representation, however, (and the reason we do not pursue it here), is that elongated, narrow objects can not be well approximated using only a few terms in the support function series. For example, if the support function for K (located at the origin so the first harmonic coefficients are zero) is restricted to have no higher than second order harmonics, the support function is $h(\emptyset) = v_0 + v_{2c}\cos 2\emptyset + v_{2s}\sin 2\emptyset$. The convexity requirement of $h + h'' > 0$ (Santalo, 1976) implies that the maximum value of the length/width ratio for this object is two; this situation does not change rapidly as higher order harmonics are included in the support function.

Since we would like to consider geometry estimation for objects having length/width ratios in excess of two, we turn to the representation of an object using simple geometric shapes. For example, in order to develop insight into the geometry estimation problem, we may consider approximately representing an object's relative profile by using an indicator function on a set such as a disk or an ellipsoid of given eccentricity and orientation, or by using an indicator function on a square or a rectangle with given side lengths and orientation. Ellipsoids and rectangles are the result of scaling, stretching and rotating unit sized disks and squares, respectively; this idea may be generalized very easily,

as mentioned in Section 2.1.3, to encompass a class of relative profiles that are obtained from an arbitrary profile f(x) by coordinate system scaling, stretching and/or rotation transformation.

Since the focus of this chapter is on developing insight into the problem of estimating object geometry from projections, this representation (in spite of its apparent simplicity and the restricted class of profiles that can be generated) will be pursued because of its analytic simplicity. This representation should also prove useful in some practical problems, for example, in obtaining a preliminary, coarse reconstruction of a cross-section containing one or more high contrast objects, or in problems where one is interested only in locating and sizing a group of objects distributed in a cross-section.

6.0.2 Size, eccentricity and orientation estimation

In this chapter we consider profiles (and their 2D Fourier transforms) that are obtained from a given profile by scaling, stretching and rotation, so we take a moment now to state precisely these transformations. Consider an initial, normalized (i.e. unit sized) object relative profile f(x) (denoted as $f_p(r,\emptyset)$ in polar coordinates) having unit contrast and located at the origin; f(x) need

not be circularly-symmetric. The 2D Fourier transform of $f(x)$ will be denoted $F(\omega) = F(\omega_1,\omega_2)$, and as $F_p(\rho,\psi)$ in polar coordinates.

The object whose geometry is being estimated will be thought of as arising from $f(x)$ by applying one, two, or all three of the following coordinate system transformations: (1) scaling to obtain an object of <u>size</u> R, (2) stretching and compressing in the direction of the coordinate axes to obtain an object with <u>eccentricity</u> λ, and (3) rotation to obtain an object with <u>orientation</u> $\emptyset$. These three transformations correspond to the coordinate transformation, repeated from (2.5)

$$\tilde{x} = \begin{bmatrix} \cos\emptyset & \sin\emptyset \\ -\sin\emptyset & \cos\emptyset \end{bmatrix} \begin{bmatrix} \lambda & 0 \\ 0 & 1/\sqrt{\lambda} \end{bmatrix} \begin{bmatrix} R & 0 \\ 0 & R \end{bmatrix} x$$

For example, if $f(x)$ is an indicator function on a unit-radius disk centered at the origin, one may obtain an object that is an indicator function on an arbitrary ellipse centered at the origin by using these three transformations. Note that the first two operations commute, as do the first and last operations; the last two operations do not commute. The object geometry estimation problem, then, involves estimating the size, eccentricity and orientation parameters R, λ and $\emptyset$.

A profile of size R, obtained by isotropically scaling the initial profile, may be expressed in terms of the initial profile as

$$f\left(\frac{x_1}{R}, \frac{x_2}{R}\right) \quad \underline{\text{or}} \quad f_p\left(\frac{r}{R}, \phi\right) \tag{6.1a}$$

with 2D Fourier transform (obtained using the Fourier transform scaling property (Bracewell, 1965)) given by

$$R^2 F(R\omega_1, R\omega_2) \quad \underline{\text{or}} \quad R^2 F_p(R_\rho, \psi) \tag{6.1b}$$

Consider now a profile with eccentricity λ, obtained by scaling a given (possibly scaled) profile by a factor $\sqrt{\lambda}$ in the x_1 direction and $1/\sqrt{\lambda}$ in the x_2 direction; this profile can be expressed as

$$f\left(\frac{x_1}{\sqrt{\lambda}}, \sqrt{\lambda}\, x_2\right) \quad \underline{\text{or}}$$

$$f_p\left(r\sqrt{\frac{1}{\lambda}\cos^2\phi + \lambda\sin^2\phi}, \arctan(\lambda\tan\phi)\right) \tag{6.2a}$$

with 2D Fourier transform

$$F(\sqrt{\lambda}\,\omega_1, \omega_2/\sqrt{\lambda}) \quad \underline{\text{or}}$$

$$F_p\left(\rho\sqrt{\lambda\cos^2\psi + \frac{1}{\lambda}\sin^2\psi}, \arctan\left(\frac{1}{\lambda}\tan\psi\right)\right) \tag{6.2b}$$

Finally, consider a (possibly scaled and eccentric) initial profile $f(x)$ or $f_p(r,\phi)$ that is oriented in the direction of the x_1 axis (obtained, for example, from an initial profile by the transformations in (6.1) and (6.2)); an object with orientation ϕ_o, measured counterclockwise from the x_1 axis, is expressed as

$$f\left(x_1\cos\phi_0 + x_2\sin\phi_0,\ -x_1\sin\phi_0 + x_2\cos\phi_0\right) \qquad \underline{\text{or}}$$

$$f_p(r,\phi-\phi_0) \tag{6.3a}$$

with 2D Fourier transform

$$F\left(\omega_1\cos\phi_0 - \omega_2\sin\phi_0, \omega_1\sin\phi_0 + \omega_2\cos\phi_0\right) \qquad \underline{\text{or}}$$

$$F_p\left(\rho, \psi+\phi_0\right) \tag{6.3b}$$

The log likelihood function in (2.22) for the general parameter estimation problem contains a term corresponding to the energy in the Radon-space matched filter template. While the Radon transform energy was seen in Chapter 3 to be independent of location, it is <u>not</u> independent of object geometry. For convenience, we use the shorthand notation $\mathcal{E}(d,R,\lambda)$ to denote the energy in an object with

contrast d, size R and eccentricity λ (the energy is independent of the orientation), when the measurement system bandwidth is infinite (i.e. the measurement aperture function is impulsive). It is easy to show that

$$\mathcal{E}(d,R,\lambda) = d^2\mathcal{E}(1,R,\lambda) = R^3\mathcal{E}(d,1,\lambda) \tag{6.4}$$

In the special case of a circularly-symmetric profile with Radon transform energy $\mathcal{E}(d,R,1) = d^2R^3\mathcal{E}_o$, it can also be shown (see Appendix 6 for details) that if the eccentricity transformation in (6.2) is applied, the resulting profile has Radon transform energy

$$\mathcal{E}(d,R,\lambda) = d^2R^3\mathcal{E}_0\, q(\lambda) \tag{6.5}$$

where

$$q(\lambda) = \frac{2}{\pi}\int_0^{\frac{\pi}{2}} \left(\lambda\cos^2\psi + \frac{1}{\lambda}\sin^2\psi\right)^{\frac{1}{2}} d\psi \tag{6.6}$$

Notice that $q(\lambda) = q(1/\lambda)$ and $q(1)=1$; a plot of $q(\lambda)$ on the interval $\lambda \in [1,20]$ is shown in Figure 6.1.

In this chapter, we investigate the object profile estimation problem by using the size, eccentricity and orientation profile parameterizations in (6.1) through (6.3). One approach to the problem of estimating an object's size, orientation and eccentricity parameters from noisy projection measurements is to use the ML

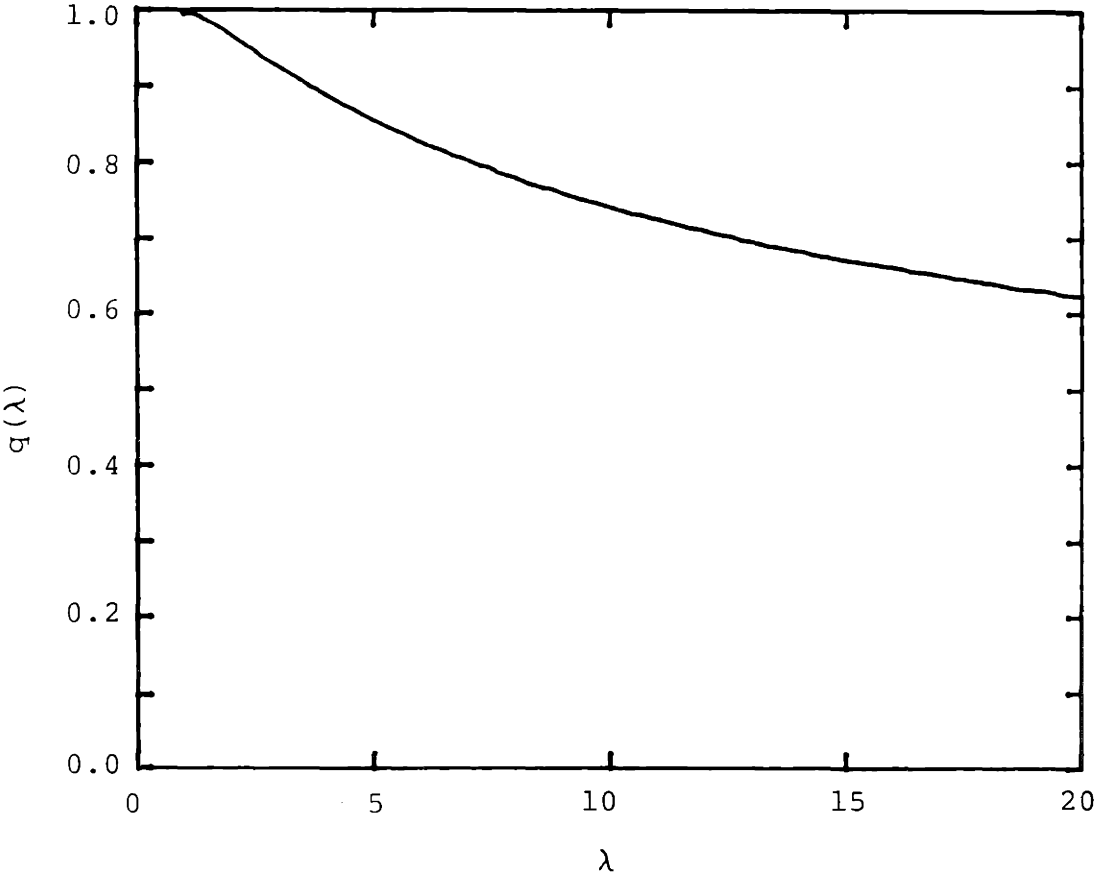

Figure 6.1 Radon transform energy dependence on eccentricity λ.

estimation procedure developed in Section 2.4 and simultaneously estimate all three parameters. However, more insight may be obtained into the parameter estimation problem by considering the issue of how accurately profile parameters can be estimated independently or jointly, when the remaining parameters are perfectly or imperfectly known. This issue is relevant not only in the case where some aspects of the object profile are known precisely a priori, but also when one considers the development of efficient, iterative methods for object-based reconstruction in which at each stage one updates estimates of one or more parameters while keeping the others fixed. For example, one might conceive of using a simple circularly-symmetric profile model during the initial stages of a reconstruction to determine, say, how many objects are present in a cross-section, as well as to obtain a coarse estimate of each object's location and size. In subsequent stages, more complicated object models may be used to estimate finer details regarding each object's density profile and to refine estimates of location and size. Indeed, as we discuss in Section 6.4, the analysis in this chapter supports the intuitive notion that this is an appropriate sequence in which to estimate geometry iteratively.

In such a setting, myriad questions suggest themselves with regard to the accuracy with which one or more of the parameters can be estimated at any stage from noisy projections when the remaining parameters are either perfectly known, in a "best case" analysis, or imperfectly known, in a robustness or sensitivity analysis. In addition, from such analysis we can gain insight into how one might structure an iterative algorithm in terms of the optimal order in which shape parameters should be estimated.

In this chapter we expose and systematically investigate these issues in the context of the specific geometry parameterization introduced previously. To this end, we consider a sequence of specific problems (described in Section 6.0.4) involving the estimation of size, eccentricity and orientation parameters one or two at a time, when the remaining parameter(s) are perfectly or imperfectly known. Considering such a series of well-defined individual and joint parameter estimation problems allows us to obtain insight into the "best case" performance, as well as insight into the specific issues of interest which were listed in the beginning of this chapter. In addition, in Section 6.3 we discuss the impact of imprecise object location information, as well as the effect when the actual object profile is not within the class of modeled profiles.

The specific problems to be considered may be viewed as restrictions of the general problem where all three parameters are estimated simultaneously, and consequently we begin by considering this more general problem in the next section. Evaluating the ambiguity function once for the general three-parameter estimation problem saves us having to derive it a number of times independently for each of the special cases we consider. Before begining, it should be noted that while the ambiguity function for the three-parameter estimation problem is rather cumbersome, for the special cases of interest in this chapter the expression simplifies considerably, as we will show.

6.0.3 The three parameter estimation problem

Suppose $f(x)$ or $f_p(r,\phi)$ is an arbitrary initial relative profile (i.e. unit contrast and located at the origin, but not necessarily circularly-symmetric) with Radon transform energy $\mathcal{E}_o$. If the actual object is obtained by scaling, stretching and rotating this relative profile, followed by multiplication by the known contrast d, it follows from equations (6.1) through (6.3) that the actual object is given by

$$df_p\left(\frac{r}{R_a}\sqrt{\frac{1}{\lambda_a}\cos^2(\phi-\phi_a)+\lambda_a\sin^2(\phi-\phi_a)}\right),$$

$$\arctan(\lambda\tan\phi) - \phi_a\Big) \tag{6.7}$$

with 2D Fourier transform

$$dR_a^2 F_p\left(R_a\rho\sqrt{\lambda_a\cos^2(\psi+\phi_a) + \frac{1}{\lambda_a}\sin^2(\psi+\phi_a)}\right.,$$

$$\arctan(\frac{1}{\lambda_a}\tan\psi) + \phi_a\Big) \tag{6.8}$$

Here R_a, λ_a and ϕ_a denote the actual values of the object size, eccentricity and orientation. The actual object Radon transform will be denoted

$$g(t,\theta;d,R_a,\lambda_a,\phi_a) = dR_a g(t/R_a,\theta-\phi_a;\lambda_a) \tag{6.9}$$

and it has energy

$$\mathcal{E}(d,R_a,\lambda_a) = d^2R_a^3\mathcal{E}(1,1,\lambda_a) \tag{6.10}$$

In the special case where f(x) is circularly-symmetric, $\mathcal{E}(d,R_a,\lambda_a) = d^2R_a^3q(\lambda_a)\mathcal{E}_o$.

If the modeled object (with parameters d, R, λ and ϕ) is similarly denoted, the log likelihood function for the size, eccentricity and orientation parameters, obtained from (2.22), is given by

$$\mathcal{L}(R,\lambda,\phi) = \frac{2}{N_0}\int_0^{\pi}\int_{-\infty}^{\infty} y(t,\theta)g(t,\theta;d,R,\lambda,\phi)\,dt\,d\theta$$

$$-\frac{1}{N_0}\int_0^{\pi}\int_{-\infty}^{\infty} g^2(t,\theta;d,R,\lambda,\phi)\,dt\,d\theta \qquad (6.11)$$

If the measurements are noisy projections smoothed by an aperture function h(t) as discussed in Section 3.3, then the ambiguity function (the expected value of the log likelihood function) is given by

$$a(R,\lambda,\phi;R_a,\lambda_a,\phi_a)$$

$$= \frac{2}{N_0}\int_0^{\pi}\int_{-\infty}^{\infty} [g(t,\theta;d,R_a,\lambda_a,\phi_a) * h(t)]g(t,\theta;d,R,\lambda,\phi)\,dt\,d\theta$$

$$-\frac{1}{N_0}\int_0^{\pi}\int_{-\infty}^{\infty} g^2(t,\theta;d,R,\lambda,\phi)\,dt\,d\theta \qquad (6.12)$$

The first term in this expression is the result of evaluating a CBP operation at the origin, and the second term may be written as $(1/N_o)d^2R^3\mathcal{E}(1,1,\lambda)$. Consider the case where the aperture function h(t) is the sinc function in (3.22) corresponding to an ideal low-pass filter with spatial bandwidth W cycles per unit distance. It is shown in Appendix 7 that for given values of the actual object parameters R_a, λ_a and ϕ_a, this

ambiguity function depends on R only through the ratio R/R_a, and is given by

$$a(R,\lambda,\emptyset;R_a,\lambda_a,\emptyset_a) = \frac{\mathcal{E}_a}{N_0}\, a^*\left(\frac{R}{R_a},\lambda,\lambda_a,\emptyset,\emptyset_a,R_aW\right) \tag{6.13}$$

where $\mathcal{E}_a$ is the actual object energy

$$\mathcal{E}_a = d^2R_a^3\mathcal{E}(1,1,\lambda_a) \tag{6.14}$$

and

$$a^*\left(\frac{R}{R_a},\lambda,\lambda_a,\emptyset,\emptyset_a,R_aW\right) = \frac{2}{\mathcal{E}(1,1,\lambda_a)}\left(\frac{R}{R_a}\right)^2 \cdot$$

$$\int_0^{2\pi}\int_0^{R_aW} F_p\left(\rho\sqrt{\lambda_a\cos^2(\psi+\emptyset_a)+\frac{1}{\lambda_a}\sin^2(\psi+\emptyset_a)},\emptyset_a+\arctan\left(\frac{1}{\lambda_a}\tan\psi\right)\right)\cdot$$

$$F_p\left(\frac{R}{R_a}\rho\sqrt{\lambda\cos^2(\psi+\emptyset)+\frac{1}{\lambda}\sin^2(\psi+\emptyset)},\ \emptyset+\arctan\left(\frac{1}{\lambda}\tan\psi\right)\right)$$

$$-\frac{\mathcal{E}(1,1,\lambda)}{\mathcal{E}(1,1,\lambda_a)}\left(\frac{R}{R_a}\right)^3 \tag{6.15}$$

As noted previously, the expression for the three-parameter ambiguity function is involved, but it simplifies considerably in the special cases to be investigated. In particular, when the initial profile f(x) is circularly-symmetric, the following simplifications occur: (1) $F(\rho,\psi)$ depends only on its first argument, (2) $\mathcal{E}(1,1,\lambda_a) = q(\lambda_a)\mathcal{E}_o$, (3) the

ratio $\mathscr{E}(1,1,\lambda)/\mathscr{E}(1,1,\lambda_a)$ is given by $q(\lambda)/q(\lambda_a)$, and (4) the ambiguity function depends on $\emptyset$ and $\emptyset_a$ only through their difference. Even if f(x) is not circularly-symmetric, the ambiguity function simplifies substantially in the case where only the first and last of the transformations in (6.1) through (6.3) are applied (i.e. a possibly noncircularly-symmetric profile is scaled and rotated, but the eccentricity transformation is not applied, and $\lambda = \lambda_a = 1$). In this case (1) the arctangent operations disappear and (2) the ambiguity function depends on $\emptyset$ and $\emptyset_a$ only through their difference.

As mentioned, in the course of this chapter, we investigate a sequence of several important special cases of (6.15); in order to get some insight into the geometry estimation problem, the results obtained are illustrated through the use of several examples. In particular, the results are occasionally evaluated for the pillbox object in Example 1, however, for this object the calculations are performed numerically rather than analytically because the Fourier transform for the pillbox contains a Bessel function, and the integrals involving this function cannot be evaluated in closed form. The Gaussian object in Example 3 is used more frequently to illustrate the results obtained in this chapter, as in many cases the results can be evaluated analytically for this object in the limit as the measurement system bandwidth W approaches

infinity. (As discussed earlier, the results for the Gaussian object with infinite bandwidth are quite similar to results for other circularly-symmetric objects such as the pillbox with finite bandwidth.) For future reference, we present the ambiguity function in (6.15) for the Gaussian relative profile.

Example 3 (continued)

Suppose f(x) is the circularly-symmetric Gaussian object

$$f_p(r) = \exp(-r^2) \tag{6.16}$$

with 2D Fourier transform

$$F_p(\rho) = \pi \exp(-\pi^2 \rho^2) \tag{6.17}$$

and Radon transform energy

$$\mathscr{E}_0 = \sqrt{\frac{\pi}{2}}\, \pi^2 \tag{6.18}$$

In Appendix 8, the normalized ambiguity function in (6.15) is evaluated for this object, in the limit as the measurement system bandwidth W approaches infinity, and is given by

$$a^*\left(\frac{R}{R_a}, \lambda, \lambda_a, \Delta\phi\right) = \frac{2\sqrt{2}}{q(\lambda_a)}\left(\frac{R}{R_a}\right)^2 \cdot$$

$$\left[\frac{1}{\pi}\int_0^{\pi}\left\{\lambda_a\cos^2\psi + \lambda\left(\frac{R}{R_a}\right)^2\cos^2(\psi+\Delta\phi) + \frac{1}{\lambda_a}\sin^2\psi + \frac{1}{\lambda}\left(\frac{R}{R_a}\right)^2(\psi+\Delta\phi)\right\}^{-\frac{1}{2}} d\psi\right]$$

$$- \frac{q(\lambda)}{q(\lambda_a)}\left(\frac{R}{R_a}\right)^3 \qquad (6.19)$$

6.0.4 Chapter outline

In this chapter, we investigate the issue of size, orientation and eccentricity estimation when a priori information (perfect and imperfect) is available about one or more of these parameters. We consider a hierarchy of problems of increasing complexity.

The size estimation problem is investigated first -- the actual object is modeled as an initial (not necessarily circularly-symmetric) profile isotropically scaled, as in (6.1), by an unknown size factor R which is to be estimated. Estimation performance is assessed in Section 6.1 for the case of perfect and imperfect knowledge of the initial profile. The size estimate obtained in the presence of a priori errors in the knowledge of the profile f(x) is shown to be biased (in particular, when an elongated object is modeled

incorrectly as being either circularly-symmetric or eccentric with the incorrect value of eccentricity). In order to obtain an unbiased size estimate, the eccentricity and orientation must be accounted for, and this leads in a natural way to the problem of estimating the object's eccentricity and orientation, which is treated in Section 6.2.

After the joint eccentricity and orientation ambiguity function has been calculated, it is shown that orientation and eccentricity are amenable to independent estimation (in that order), and that an unbiased estimate of elongated object orientation can be obtained even if the eccentricity of the object is not precisely known.

The Cramer-Rao bound for the eccentricity and orientation estimation problems is calculated in Sections 6.2.2 and 6.2.3. When the eccentricity is known, the Cramer-Rao bound may be used to show (not surprisingly) that for a given SNR, the orientation of an eccentric object is more accurately determined than is the orientation of a nearly circular object. In Section 6.2.4, we use the Cramer-Rao bound to develop a decision rule for selecting between the use of a simple (circularly-symmetric) versus a more complex object model that makes use of knowledge of the SNR and the estimate of object eccentricity.

In Section 6.3, we address the question of how sensitive the analysis in this chapter is to the assumption of a centrally-symmetric object profile (leading to symmetric Radon transforms) whose location is precisely known, since in practice, these assumptions hold, at best, only approximately. In the concluding section 6.4, we discuss the implications of our analysis, with an emphasis on how one might structure an iterative algorithm for practically implementing the estimation of an object's relative profile.

6.1 SIZE ESTIMATION

Suppose f(x) corresponds to some initial (not necessarily circularly-symmetric) relative profile with Radon transform energy $\mathcal{E}_o$, and that the actual object, denoted $d \cdot f(x/R_a)$, is obtained from f(x) by the scaling transformation in (6.1) and multiplication by the known object contrast d.

6.1.1 Size estimation ambiguity function

The size ambiguity function, assuming f(x) is known perfectly a priori, is the ambiguity function in (6.13) through (6.15) evaluated when $\lambda = \lambda_a = 1$ (the eccentricity transformation is not applied) and $\phi = \phi_a = 0$ (the rotation transformation is not applied); namely

$$a(R,R_a) = \frac{\mathcal{E}_a}{N_0}\, a^*\left(\frac{R}{R_a}, R_a W\right) \tag{6.20}$$

where

$$a^*\left(\frac{R}{R_a}, R_a W\right)$$

$$= \frac{2}{\mathcal{E}_0}\left(\frac{R}{R_a}\right)^2 \int_0^{2\pi}\int_0^{R_a W} F_p(\rho,\psi)\, F_p\left(\frac{R}{R_a}\rho,\psi\right) d\rho d\psi - \left(\frac{R}{R_a}\right)^3 \tag{6.21}$$

Notice that in contrast to the location estimation ambiguity function in (3.7), the Radon transform energy here depends on the parameter being estimated (object size), and consequently the ambiguity function is the difference between two terms.

EXAMPLES

In order to get some insight into the size estimation problem, we now calculate the normalized ambiguity function in (6.21) for two specific objects in the limiting case when the measurement system bandwidth W approaches infinity. For the circularly-symmetric Gaussian object $f_p(r) = \exp(-r^2)$ described in (6.16) through (6.18), the normalized ambiguity function a* is a special case of (6.19) where $\lambda = \lambda_a = 1$ and $\emptyset = \emptyset_a = 0$, and is given by

$$a^*\left(\frac{R}{R_a}, \infty\right) = \frac{2\sqrt{2}\left(\frac{R}{R_a}\right)^2}{\sqrt{1+\left(\frac{R}{R_a}\right)^2}} - \left(\frac{R}{R_a}\right)^3 \qquad (6.22)$$

This function is plotted in Figure 6.2, along with the normalized ambiguity function a* for the pillbox object $f_p(r,\emptyset) = \text{rect}(r/2R_a)$ with $W = \infty$, which was determined by numerically evaluating the Radon-space double integral in (6.12). The peaks of these two normalized ambiguity functions are seen to lie at the true value of the size parameter, and these curves are seen to have approximately the same overall shape.

It should be noted that the unnormalized ambiguity function in (6.20) depends linearly on the actual object energy, which for the same value of contrast d and size R_a, is larger for the pillbox than for the Gaussian. The normalized ambiguity function a*, of which we make extensive use in this chapter, is useful for presenting a qualitative visualization of the estimation performance. The normalized ambiguity functions shown in Figure 6.2 suggest, at least for circularly-symmetric objects, that it should be possible to estimate the size quite reliably (since the ambiguity function value drops rapidly away from the true parameter value), and if some amount of estimation error does occur, it is more likely that the

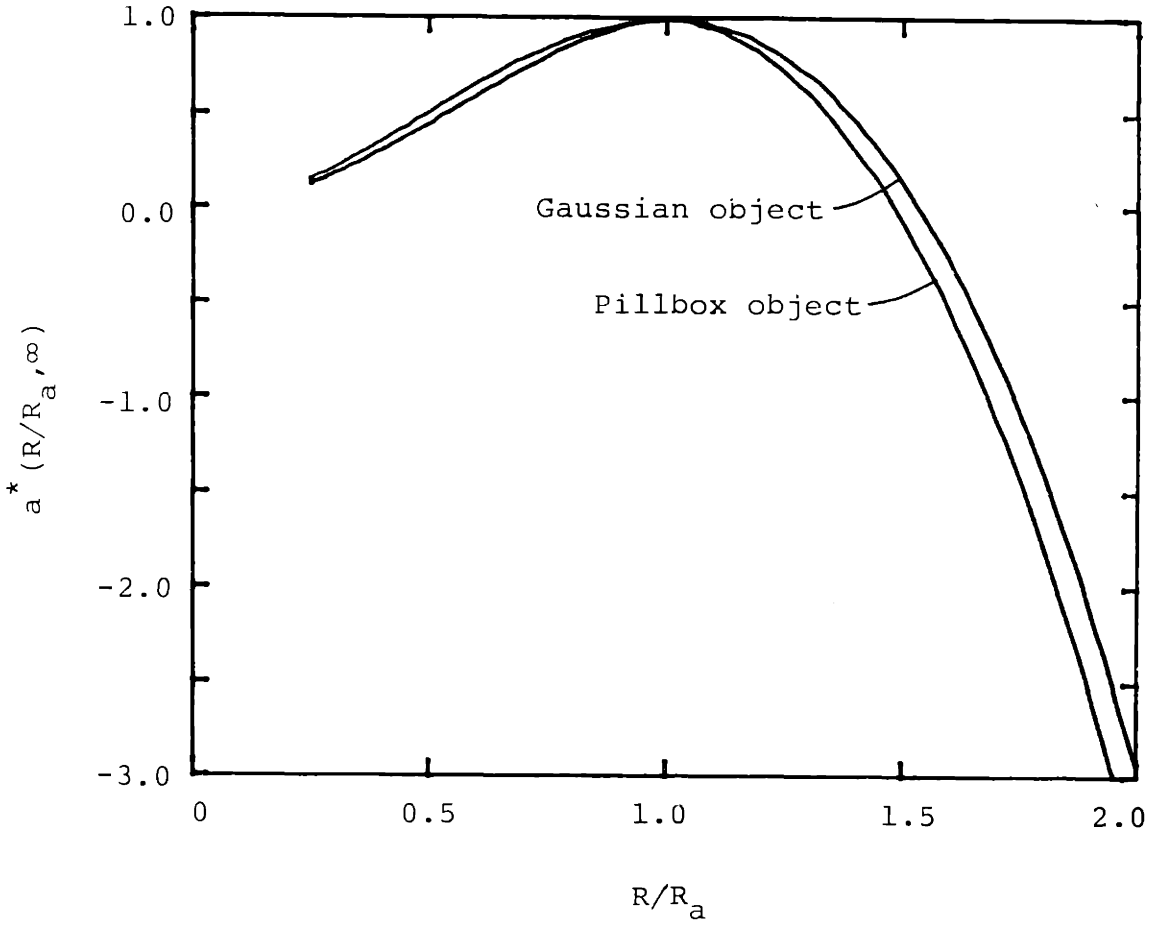

Figure 6.2 Size ambiguity function for a Gaussian and pillbox object.

size parameter will be underestimated rather than overestimated.

It can be shown that for a circularly-symmetric initial profile f(x), in the limit as the measurement system bandwidth goes to infinity, the normalized size ambiguity function a* in (6.21) is independent of the eccentricity of an object obtained from f(x) by the eccentricity transformation in (6.2). In particular, it is shown in Appendix 9 that if an arbitrary circularly-symmetric object has a normalized size ambiguity function $a^*(R/R_a,\infty)$, then any object obtained from it by applying the eccentricity transformation in (6.2) has exactly the same normalized ambiguity function. The object eccentricity, then, enters the size estimation problem only via the energy term in (6.14), and affects the magnitude, but not the shape, of the size estimation ambiguity function.

6.1.2 Cramer-Rao bound for size estimation

The Cramer-Rao bound for the size estimation problem may be obtained by finding the second partial derivative of the ambiguity function in (6.20) with respect to the parameter R. If the first and second partial derivatives of $F_p(\rho,\psi)$ with respect to ρ are denoted F' and F'', the Cramer-Rao bound on the size estimate error variance is

(see Appendix 10 for details)

$$\sigma_R^2 \geq \left[-E \left\{ \frac{\partial^2 a(R,R_a)}{\partial R^2} \right\}_{R=R_a} \right]^{-1} = \frac{N_0}{2d^2(3\mathscr{E}_0 - \gamma(R_a W))R_a} \tag{6.23}$$

where

$$\gamma(R_a W)$$

$$\triangleq \int_0^{2\pi} \int_0^{R_a W} F(\rho,\psi) \left[2F(\rho,\psi) + 4\rho F'(\rho,\psi) + \rho^2 F''(\rho,\psi) \right] d\rho d\psi \tag{6.24}$$

EXAMPLE 1 (continued)

Consider the pillbox object $f_p(r,\emptyset) = \text{rect}(r/2R_a)$ with 2D Fourier transform $F_p(\rho,\psi) = J_1(2\pi\rho)/\rho$. Taking advantage of recurrence relationships for the Bessel function derivatives (Hildebrand, 1976), (6.24) may be written as

$$\gamma(R_a W) = 4\pi^2 \int_0^{2\pi R_a W} \left[J_1^2(\rho)\left(\frac{2}{\rho^2}-1\right) - \frac{1}{\rho} J_1(\rho) J_2(\rho) \right] d\rho \tag{6.25}$$

where $J_1(\rho)$ and $J_2(\rho)$ are Bessel functions of the first kind of order one and two respectively. Evaluation of equation (6.25) involves a tedious numerical computation which we do not carry out here. Rather, we

evaluate instead the Cramer-Rao bound for the Gaussian object.

EXAMPLE 3 (continued)

When the initial object profile f(x) is the circularly-symmetric Gaussian object in (6.16) through (6.18), $\gamma(R_aW)$ in (6.24) is given by

$$\gamma(R_aW) = \sqrt{2}\,\pi^2 \int_0^{\sqrt{2}\pi R_a W} e^{-\rho^2} [2-5\rho^2 + \rho^4] d\rho \tag{6.26}$$

While $\gamma(R_aW)$ may be numerically evaluated for any finite value of radius-bandwidth product R_aW, we consider the limit as the measurement system bandwidth approaches infinity. In the limit as $W \to \infty$, $\gamma(R_aW)$ may be determined analytically and is equal to $(\pi/2)^{5/2}$, and the Cramer-Rao bound in (6.23) is given by

$$\sigma_R^2 \geq \frac{N_0}{2d^2[3\mathscr{E}_0 - \left(\frac{\pi}{2}\right)^{\frac{5}{2}}] R_a} = \left(\frac{2}{\pi}\right)^{\frac{5}{2}} \frac{N_0}{22d^2 R_a} \tag{6.27}$$

With infinite bandwidth measurements, then, the size estimation Cramer-Rao bound for the Gaussian object is inversely related to the actual object size, indicating that size estimation performance improves rapidly with increasing object size.

6.1.3 Size estimation in the presence of a priori profile modeling errors

In the analysis just described, it was assumed that the object profile f(x) is known perfectly a priori, and that the only unknown is the object size R, which is estimated. In this section, we investigate how the size estimation performance degrades in the face of a priori uncertainty in the object's relative profile.

In particular, for analytic simplicity, we focus on the case where both the modeled and actual objects are eccentric, but the actual object eccentricity is not perfectly known. The actual and modeled object will be obtained from the same initial profile by scaling with the size factor R, followed by application of the eccentricity transformation in (6.2).

The size ambiguity function, evaluated in the presence of eccentricity mismatch (i.e. when the modeled and actual eccentricities differ), is a special case of the three parameter ambiguity function in (6.13) when $\emptyset = \emptyset_a = 0$ (the rotation transformation is not applied), and is given by

$$a(R,\lambda;R_a,\lambda_a) = \frac{\mathscr{E}_a}{N_0}\, a^*\left(\frac{R}{R_a},\lambda,\lambda_a,R_aW\right) \tag{6.28}$$

where

$$a^*\left(\frac{R}{R_a}, \lambda, \lambda_a, R_a W\right) = \frac{2}{\mathscr{E}(1,1,\lambda_a)}\left(\frac{R}{R_a}\right)^2 \cdot$$

$$\int_0^{2\pi}\int_0^{R_a W} F_p\left(\rho\sqrt{\lambda_a \cos^2\psi + \frac{1}{\lambda_a}\sin^2\psi}\,,\ \arctan\left(\frac{1}{\lambda_a}\tan\psi\right)\right) \cdot$$

$$F_p\left(\frac{R}{R_a}\rho\sqrt{\lambda\cos^2\psi + \frac{1}{\lambda}\sin^2\psi}\,,\ \arctan\left(\frac{1}{\lambda}\tan\psi\right)\right) d\rho\, d\psi$$

$$- \frac{\mathscr{E}(1,1,\lambda)}{\mathscr{E}(1,1,\lambda_a)}\left(\frac{R}{R_a}\right)^3 \tag{6.29}$$

EXAMPLE 3 (continued

When the profile f(x) is the circularly-symmetric Gaussian object in (6.16) through (6.18), the normalized ambiguity function evaluated in the limit as $W \to \infty$ is a special case of (6.19) with $\emptyset = \emptyset_a = 0$, given by

$$a^*\left(\frac{R}{R_a}, \lambda, \lambda_a, \infty\right) = \frac{2\sqrt{2}}{q(\lambda_a)}\left(\frac{R}{R_a}\right)^2 \cdot$$

$$\frac{1}{\pi}\int_0^{\pi} \left\{ \left(\lambda_a + \left(\frac{R}{R_a}\right)^2 \lambda\right)\cos^2\psi + \left(\frac{1}{\lambda_a} + \left(\frac{R}{R_a}\right)\frac{1}{\lambda}\right)\sin^2\psi \right\}^{-\frac{1}{2}} d\psi$$

$$- \frac{q(\lambda)}{q(\lambda_a)}\left(\frac{R}{R_a}\right)^3 \tag{6.30}$$

Notice that when $\lambda = \lambda_a$ (perfect eccentricity knowledge), (6.30) reduces to (6.22) (the size ambiguity function for the Gaussian object when eccentricity is known perfectly),

and the peak occurs at $R/R_a=1$. A contour plot of the ambiguity function in (6.30), in the variables R/R_a and λ, is shown in Figure 6.3, for the case where the actual eccentricity is taken to be $\lambda_a=4$. Several sections of this function for various λ values are shown in Figure 6.4a.

These figures indicate that when the eccentricity is not accurately known a priori, the peak of the size ambiguity function does <u>not</u> occur at $R/R_a=1$ (this shift in the peak value is more dramatic when the eccentricity is modeled as being too small rather than too large), and in this case the size estimate that is obtained is <u>biased</u>. While this shift in the peak location with eccentricity modeling error is not negligible, it should be noted that the extent of peak shift is relatively mild -- the peak shifts downward by less than 3 percent when the eccentricity is overmodeled by a factor of 4, and shifts downward by about 7 percent when the eccentricity is undermodeled by a factor of 4 (i.e. when the object with eccentricty 4 is modeled as being circularly-symmetric).

This last case is interesting in its own right, since in practice, one may have no reason to believe, a priori, that an object is eccentric, or even if it is, one may not have any reason to expect the object to have a particular orientation. Consequently, it would seem reasonable in

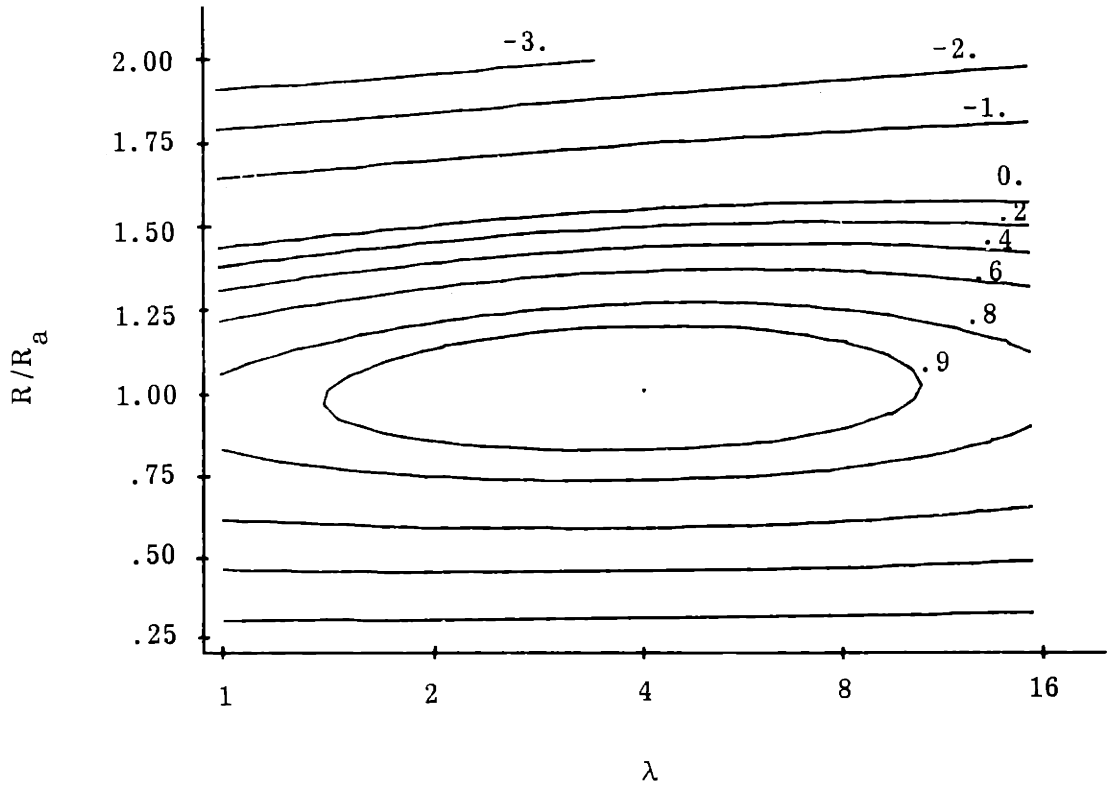

Figure 6.3 Joint size and eccentricity ambiguity function contour plot; $\lambda_a = 4$.

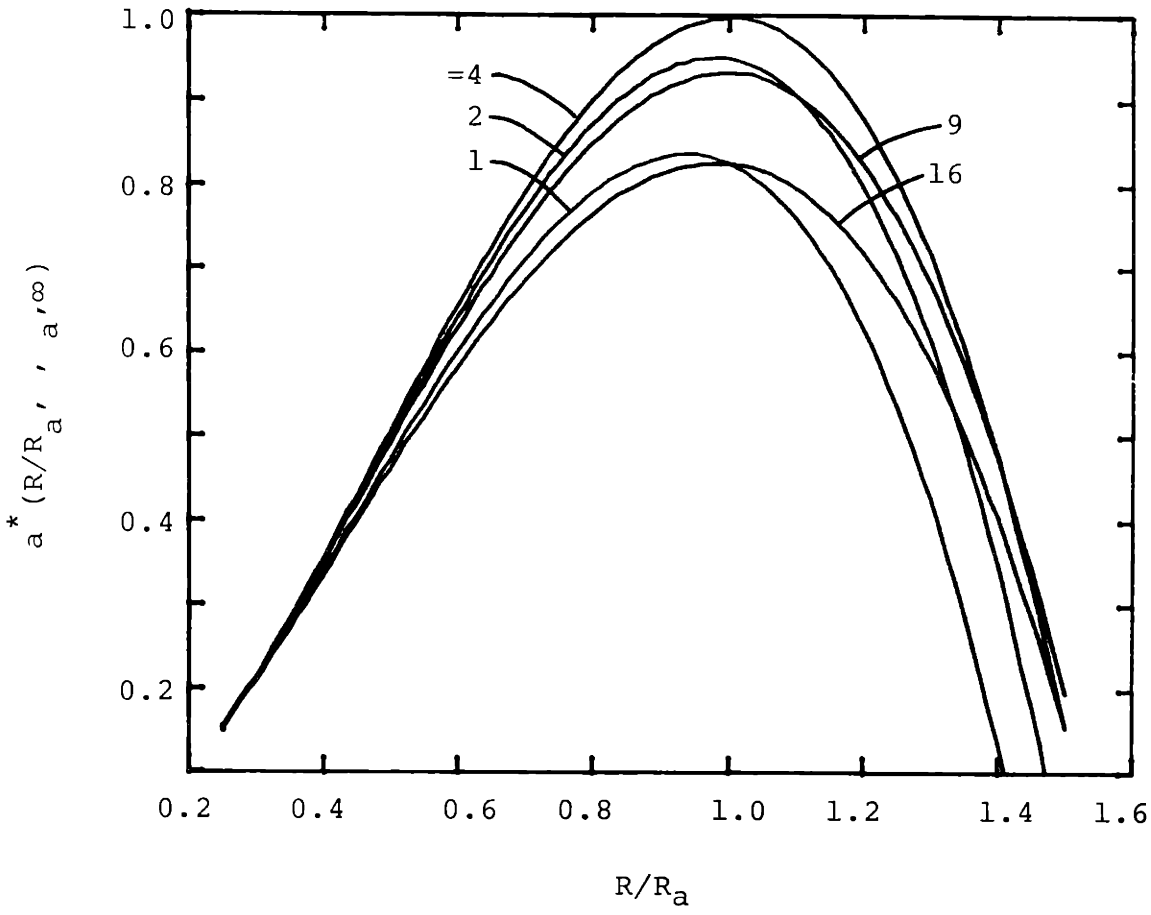

Figure 6.4 (a) Size ambiguity function in the presence of eccentricity modeling errors; $_a$=4.

such a situation to use a circularly-symmetric object model to determine object size, even if it is not known whether the actual object is circularly-symmetric. Figure 6.4b is a plot of the normalized size ambiguity function in (6.30) for the case where a circularly-symmetric (λ=1) modeled object is used to estimate the size of an actual object that is either circularly-symmetric or eccentric with λ_a = 4, 9 and 16. Here, the ambiguity function peak occurs at the true parameter value only when the eccentricity is correctly modeled (λ_a=1); when the eccentricity is undermodeled (by using a circularly-symmetric model when λ_a = 4,9 and 16) the peak location is shifted downward to R/R_a values of .94, .84 and .75 respectively.

Consequently, estimating the size of an eccentric object by using a circularly-symmetric model results in a biased size estimate. It should be noted, however, that (1) the extent of bias may be determined once the eccentricity is known, so that the size estimate can be corrected accordingly, and (2) the amount of bias is relatively modest -- modeling an object with eccentricity λ_a=16 as being circularly-symmetric represents a very significant modeling error, yet it results in a shift of only 25 percent in the location of the size ambiguity function peak.

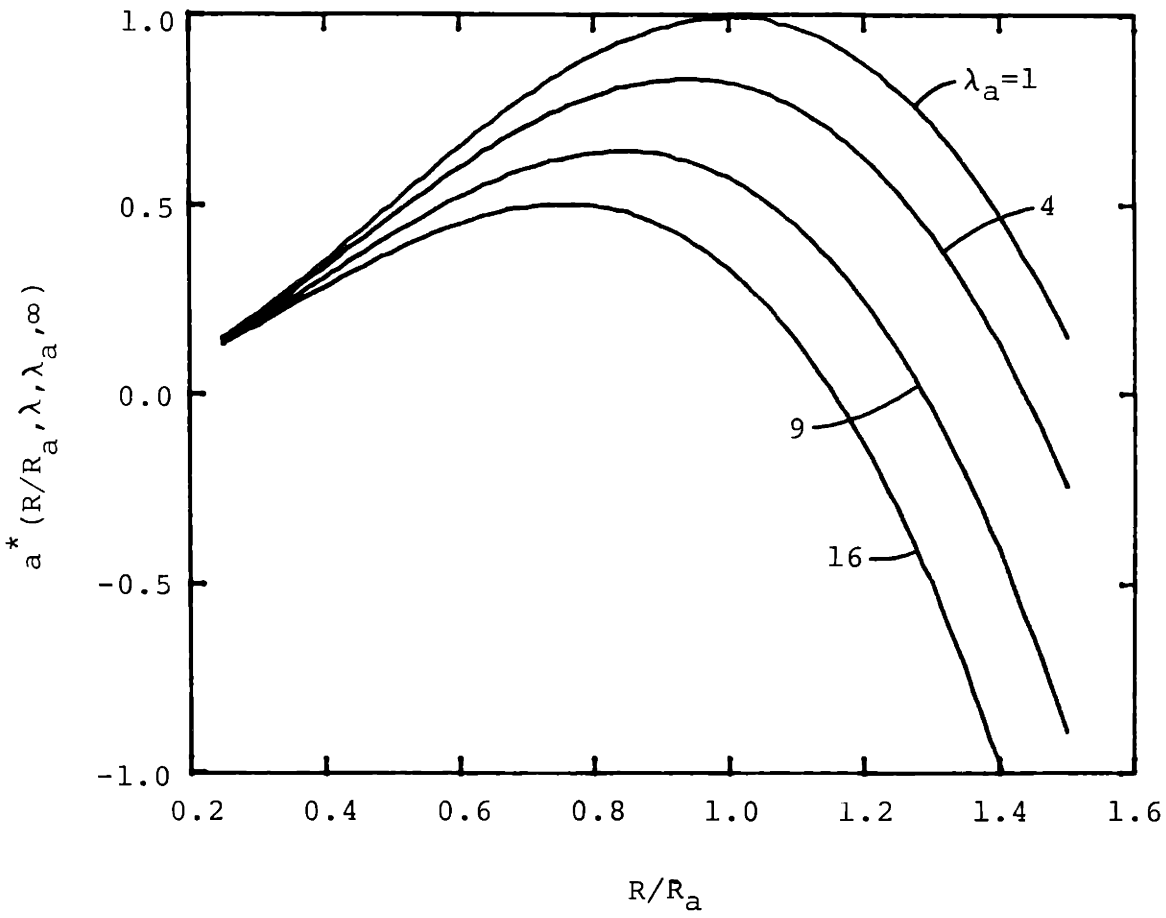

Figure 6.4 (b) Size ambiguity function when the modeled object is circularly-symmetric (λ=1) but the actual object has eccentricity λ_a=1,4,9,16.

In summary, the ambiguity function in (6.29), along with Figures 6.3 and 6.4, indicate that an unbiased size estimate cannot be obtained when the actual object's eccentricity is unknown and is modeled incorrectly. However, our results indicate that the magnitude of the bias in a size estimate is a slowly increasing function of eccentricity, both indicating that useful initial estimates can be obtained using a circularly-symmetric model and suggesting an iterative approach in which a refinement in size estimate can be made after eccentricity is estimated.

Since an object's eccentricity clearly can not be estimated accurately until its orientation is known, some amount of recursive or joint parameter estimation is necessary when the orientation and eccentricity are both unknown. In the following section, we take up the problem of jointly estimating the orientation and eccentricity of an object, when its location and size are assumed to be known.

6.2 ORIENTATION AND ECCENTRICITY ESTIMATION

In this section we investigate the problem of using noisy full-view projection measurements to estimate the orientation and eccentricity of an elongated object whose size and location are assumed to be known. It is assumed

throughout this section that the actual object is obtained from a circularly-symmetric relative profile. This assumption simplifies the calculations considerably, allowing us to glean several important insights from this problem.

Suppose, then, that the actual object is obtained from a circularly-symmetric object of known size (not necessarily unity), which will be denoted $f_p(r)$, by application of the eccentricity transformation in (6.2) and rotation by the angle ϕ_a as in (6.3). In section 6.2.1, we evaluate the joint eccentricity and orientation ambiguity function and illustrate it for the Gaussian profile as special cases of (6.13) through (6.18). In the subsequent two sections, we treat the eccentricity and orientation estimation problems individually, by examining in each case the 1D ambiguity function and the Cramer-Rao bound on the error variance. The orientation Cramer-Rao bound is then used in Section 6.2.4, where we develop one approach to the problem of appropriately selecting the complexity of the modeled object.

6.2.1 Joint orientation and eccentricity ambiguity function

Consider a circularly-symmetric relative profile f(x) or $f_p(r)$, with Radon transform energy $\mathcal{E}_o$. Suppose that the actual object is obtained by applying the eccentricity and rotation transformations in (6.2) and (6.3) with unknown parameters λ_a and ϕ_a (which are to be estimated), and then by multiplying by the known contrast d. The problem of jointly estimating the object's orientation and eccentricity, assuming its size, contrast and location are known, has an ambiguity function that is the special case of (6.13) where $R=R_a$ and $F_p(\rho,\psi)$ depends only on its first argument and will be denoted $F_p(\rho)$; it depends on ϕ and ϕ_a only through their difference $\Delta\phi = \phi-\phi_a$, and is given by

$$a(\lambda,\phi;\lambda_a,\phi_a) = \frac{\mathcal{E}_a}{N_0}\, a^*(\lambda,\lambda_a,\Delta\phi,R_aW) \tag{6.31}$$

where

$$a^*(\lambda,\lambda_a,\Delta\phi,R_aW)$$

$$= \frac{2}{q(\lambda_a)\mathcal{E}_0}\int_0^{2\pi}\int_0^{R_aW} F_p\left(\rho\sqrt{\lambda_a\cos^2\psi + \frac{1}{\lambda}\sin^2\psi}\right)\cdot$$

$$F_p\left(\rho\sqrt{\lambda\cos^2(\psi+\Delta\phi) + \frac{1}{\lambda}\sin^2(\psi+\Delta\phi)}\right)\rho\,d\rho\,d\psi - \frac{q(\lambda)}{q(\lambda_a)} \tag{6.32}$$

EXAMPLE 3 (continued)

When the initial object is the Gaussian profile in (6.16) through (6.18), the ambiguity function in the limit as $W \to \infty$ is the special case of (6.19) when $R=R_a$, and is given by

$$a^*(\lambda, \lambda_a, \Delta\emptyset, \infty) = \frac{2\sqrt{2}}{q(\lambda_a)} \cdot$$

$$\left[\frac{1}{\pi}\int_0^{\pi} \left\{\lambda_a \cos^2\psi + \lambda\cos^2(\psi + \Delta\emptyset) + \frac{1}{\lambda_a}\sin^2\psi + \frac{1}{\lambda}\sin^2(\psi + \Delta\emptyset)\right\}^{-\frac{1}{2}} d\psi\right]$$

$$- \frac{q(\lambda)}{q(\lambda_a)} \qquad (6.33)$$

A contour plot of the ambiguity function in (6.33) is shown in Figure 6.5 for the case where the actual eccentricity $\lambda_a=4$. Notice in this figure that the peak of the ambiguity function occurs at the true parameter values.

In the next two sections, we investigate two single-parameter estimation problems. In Section 6.2.2 we evaluate the 1D ambiguity function and the Cramer-Rao bound for the eccentricity estimation problem; in Section 6.2.3 we do the same for the orientation estimation problem, and also consider the effect of incorrect eccentricity knowledge on the accuracy of the orientation estimate.

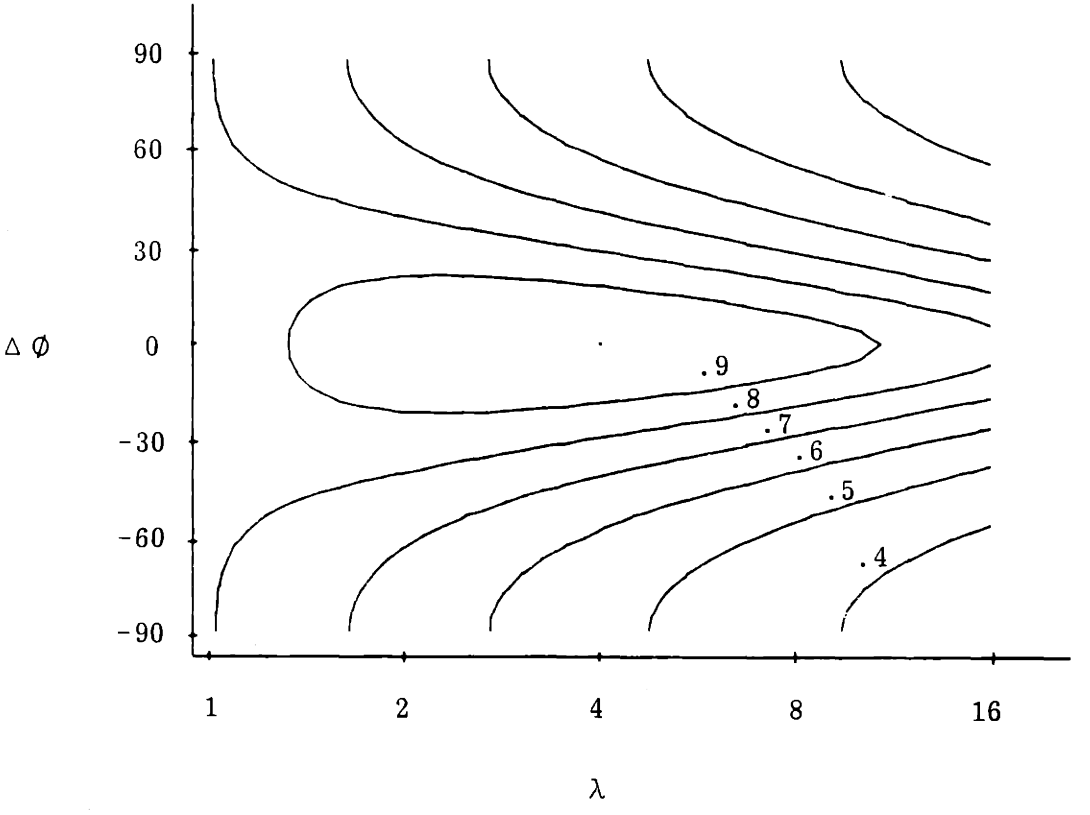

Figure 6.5 Joint orientation and eccentricity ambiguity function contour plot; $\lambda_a = 4$.

6.2.2 Ambiguity function and Cramer-Rao bound for the eccentricity estimation problem

In this section, we consider the problem of estimating an object's eccentricity, assuming all other parameters are known. We first write an expression for the ambiguity function, which is a special case of (6.13), and then evaluate it for the Gaussian object, which is a special case of (6.19). We then investigate the Cramer-Rao bound on the eccentricity estimation error variance for the Gaussian object, and illustrate the dependence of the bound on the actual object eccentricity.

Consider an initial circularly-symmetric profile $f(x)$ or $f_p(r)$ with Radon transform energy $\mathscr{E}_o$. Suppose that the actual object is obtained by applying the eccentricity transformation in (6.2) with unknown parameter λ_a, and then multiplying the profile by the known contrast d. The problem of estimating the eccentricity, assuming all other parameters are known, is the special case of (6.15) where $R = R_a$, $F_p(\rho,\psi) = F_p(\rho)$ and $\emptyset = \emptyset_a$, and is given by

$$a(\lambda,\lambda_a) = \frac{\mathscr{E}_a}{N_0} a^*(\lambda,\lambda_a,R_aW) \tag{6.34}$$

where

$$a^*(\lambda,\lambda_a,R_aW) = \frac{2}{q(\lambda_a)\mathscr{E}_0} \cdot$$

$$\int_0^{2\pi}\int_0^{R_aW} F_p\left(\rho\sqrt{\lambda_a\cos^2\psi + \frac{1}{\lambda_a}\sin^2\psi}\right) F_p\left(\rho\sqrt{\lambda\cos^2\psi + \frac{1}{\lambda}\sin^2\psi}\right) d\rho d\psi$$

$$- \frac{q(\lambda)}{q(\lambda_a)} \tag{6.35}$$

Note that as one would expect, the normalized ambiguity function in (6.35) does not depend on the actual value of $\emptyset_a$ when it is known.

EXAMPLE 3 (continued)

When the normalized object is the Gaussian profile in (6.16) through (6.18), the ambiguity function in (6.35), in the limit as $W \to \infty$, is the special case of (6.19) where $R = R_a$ and $\Delta\emptyset = 0$, given by

$$a^*(\lambda,\lambda_a,\infty) = \frac{2\sqrt{2}}{q(\lambda_a)} \cdot$$

$$\left[\frac{2}{\pi}\int_0^{\frac{\pi}{2}} \left\{(\lambda + \lambda_a)\cos^2\psi + \left(\frac{1}{\lambda} + \frac{1}{\lambda_a}\right)\sin^2\psi\right\}^{-\frac{1}{2}} d\psi\right]$$

$$- \frac{q(\lambda)}{q(\lambda_a)} \tag{6.36}$$

By using $q(\lambda)$ defined in (6.6), this may be rewritten as

$$a^*(\lambda,\lambda_a,\infty)$$

$$= \frac{2\sqrt{2}\sqrt[4]{\lambda\lambda_a}}{\sqrt{\lambda+\lambda_a}} \frac{q(\sqrt{\lambda\lambda_a})}{q(\lambda_a)} - \frac{q(\lambda)}{q(\lambda_a)} \qquad (6.37)$$

Figure 6.6 is a plot of (6.37) for the case where $\lambda_a=4$. Although the peak of the ambiguity function occurs at the true parameter value, it should be noted that the function value does not decrease rapidly as the modeled eccentricity value moves away from the true value. This indicates that the estimation of object eccentricity (even if all other parameters are known perfectly) requires a high measurement SNR.

The eccentricity estimation Cramer-Rao bound is obtained by taking two derivatives with respect to λ of the ambiguity function in (6.34). To provide some specific results, we evaluate the eccentricity Cramer-Rao bound for the special case of the Gaussian object, as this serves to illustrate how the bound depends on the actual object eccentricity. The details associated with the Cramer-Rao bound calculation are given in Appendix 11, and yield the following expression

$$\sigma_\lambda^2 \geq \frac{8N_0}{3\mathscr{E}(d,R,1)} \cdot$$

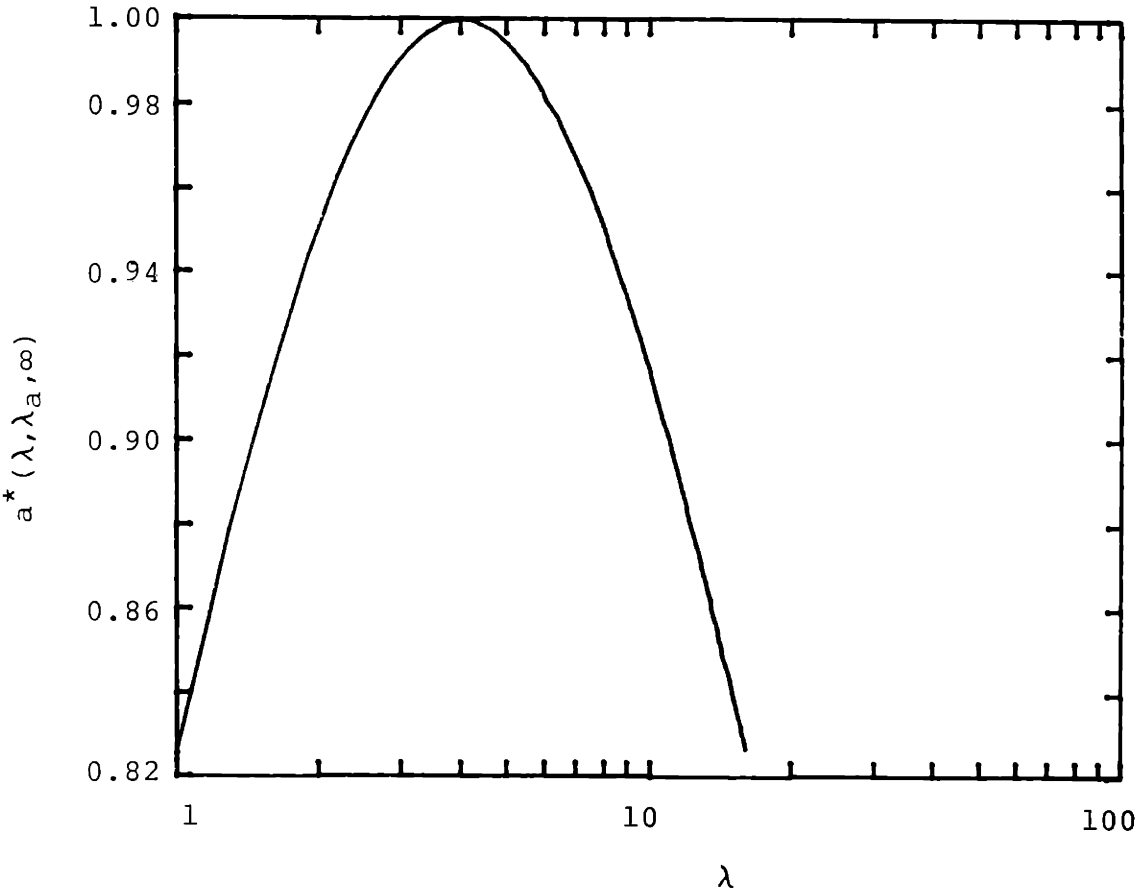

Figure 6.6 Normalized ambiguity function for the eccentricity estimation problem; $\lambda_a=4$.

$$\left\{\frac{2}{\pi}\int_0^{\frac{\pi}{2}}\left[\lambda_a\cos^2\psi+\frac{1}{\lambda_a}\sin^2\psi\right]^{-\frac{5}{2}}\left[\cos^2\psi-\frac{1}{\lambda_a^2}\sin^2\psi\right]^2 d\psi\right\}^{-1} \tag{6.38}$$

The inverse normalized Cramer-Rao bound (λ_a^2 times the term in braces in (6.38)) is plotted versus λ_a in Figure 6.7. As this figure indicates, the normalized Cramer-Rao bound is essentially independent of λ_a. Consequently, the standard deviation of the estimate error is proportional to the actual object's eccentricity λ_a, indicating that the more eccentric an object is, the greater its eccentricity error variance will be.

6.2.3 Ambiguity function and Cramer-Rao bound for the orientation estimation problem

In this section, we consider the second of the two single-parameter estimation problems discussed at the end of Section 6.2.1, namely the problem of using full-view projection measurements to estimate the orientation of an eccentric object, assuming all other parameters (including the object eccentricity) are known. The ambiguity function for this problem, and the evaluation of it for the Gaussian object, are special cases of (6.13) through (6.15) and (6.19) where $R = R_a$, $\lambda = \lambda_a$, $F_p(\rho,\psi) = F_p(\rho)$, and the resulting ambiguity function depends on ϕ only through the difference $\Delta\phi = \phi - \phi_a$. The

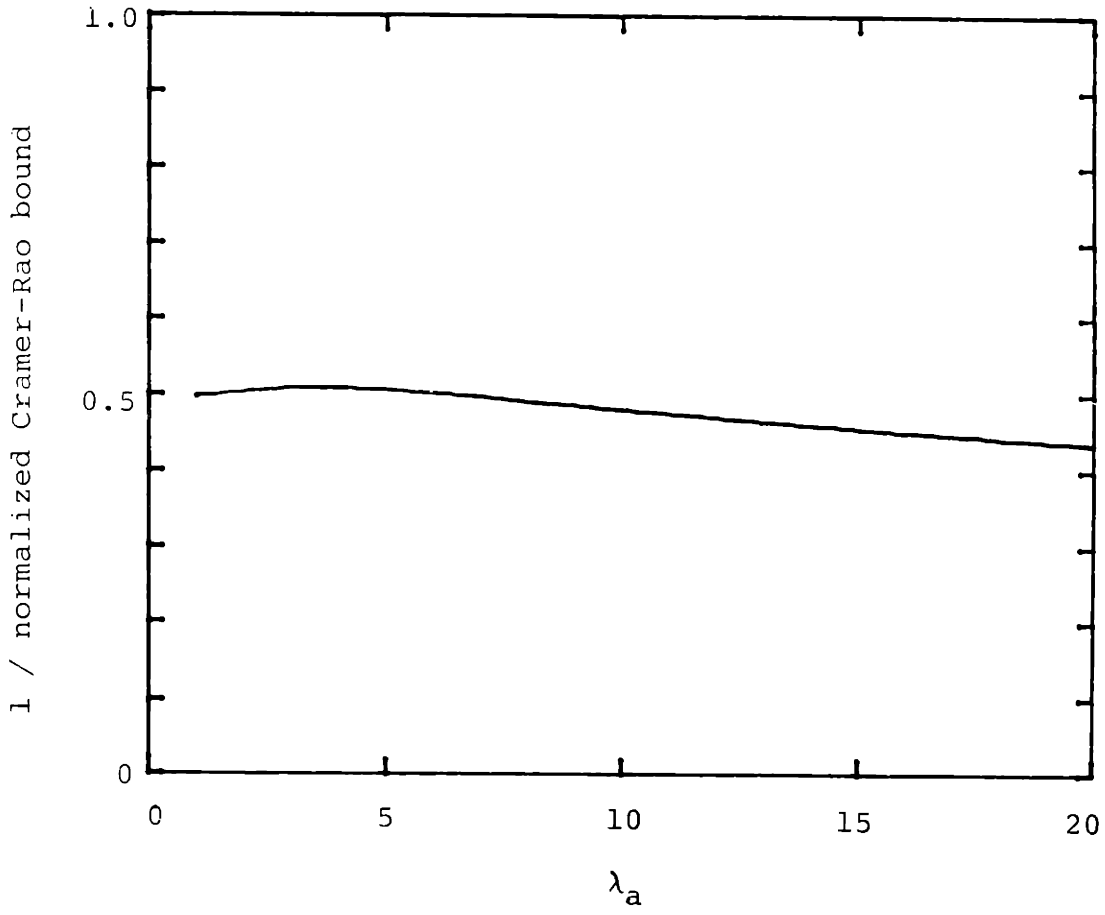

Figure 6.7 Inverse of the normalized Cramer-Rao bound for the eccentricity estimation problem.

orientation estimation ambiguity function is given by

$$a(\Delta\phi,\lambda) = \frac{\mathcal{E}_a}{N_0}\, a^*(\Delta\phi,\lambda_a,R_aW) \tag{6.39}$$

where

$$a^*(\Delta\phi,\lambda_a,R_aW) = \frac{2}{q(\lambda_a)\mathcal{E}_0}\int_0^{2\pi}\int_0^{R_aW} F_p\left(\rho\sqrt{\lambda_a\cos^2\psi + \frac{1}{\lambda_a}\sin^2\psi}\right)\cdot$$

$$F_p\left(\rho\sqrt{\lambda_a\cos^2(\psi+\Delta\phi) + \frac{1}{\lambda_a}\sin^2(\psi+\Delta\phi)}\right)\rho\,d\rho\,d\psi - 1 \tag{6.40}$$

Notice that a^* is symmetric in $\Delta\phi$, and that $a^*(\Delta\phi,\lambda_a,R_aW) = a^*(\Delta\phi,1/\lambda_a,R_aW)$, which it should since these are ambiguity functions for the same object rotated by 90 degrees.

EXAMPLE 3 (continued)

For the case of the Gaussian normalized profile in (6.16), the ambiguity function is a special case of (6.19) given by

$$a^*(\Delta\phi,\lambda_a,\infty) = \frac{2\sqrt{2}}{q(\lambda_a)}\cdot$$

$$\left[\frac{1}{\pi}\int_0^{\pi}\left\{\lambda_a\cos^2\psi + \frac{1}{\lambda_a}\sin^2\psi + \lambda_a\cos^2(\psi+\Delta\phi) + \frac{1}{\lambda_a}\sin^2(\psi+\Delta\phi)\right\}^{-\frac{1}{2}} d\psi\right]$$

$$- 1 \tag{6.41}$$

Figure 6.8 is a plot of the orientation ambiguity function in (6.41) for several values of object eccentricity λ_a. The results presented in this figure agree with intuition -- narrower objects have a narrower orientation ambiguity function, implying that the orientation of very eccentric objects can be estimated more accurately than can the orientation of nearly circular objects.

The result suggested by this figure may be verified by actually computing the Cramer-Rao bound for the estimation error variance. We evaluate the orientation Cramer-Rao bound for the special case of the Gaussian object, which illustrates the dependence of the bound on the actual object eccentricity. The details associated with this calculation are given in Appendix 12, and lead to the following Gaussian object orientation error Cramer-Rao bound

$$\sigma_{\phi}^2 \geq \frac{N_0}{\mathcal{E}(d,R,1)} \cdot$$

$$\left\{\frac{3}{8}\left(\frac{1}{\lambda_a} - \lambda_a\right)^2 \left[\frac{2}{\pi}\int_0^{\frac{\pi}{2}} \left(\lambda_a \cos^2\psi + \frac{1}{\lambda_a}\sin^2\psi\right)^{-\frac{5}{2}} \sin^2 2\psi \, d\psi\right]\right.$$

$$\left. + \left(\frac{1}{\lambda_a} - \lambda_a\right)\left[\frac{2}{\pi}\int_0^{\frac{\pi}{2}} \left(\lambda_a \cos^2\psi + \frac{1}{\lambda_a}\sin^2\psi\right)^{-\frac{3}{2}} \cos 2\psi \, d\psi\right]\right\}^{-1} \qquad (6.42)$$

Figure 6.9 is a plot of $\mathcal{E}(d,R,1)/N_0$ times the Cramer-Rao bound versus the object eccentricity λ_a. This figure

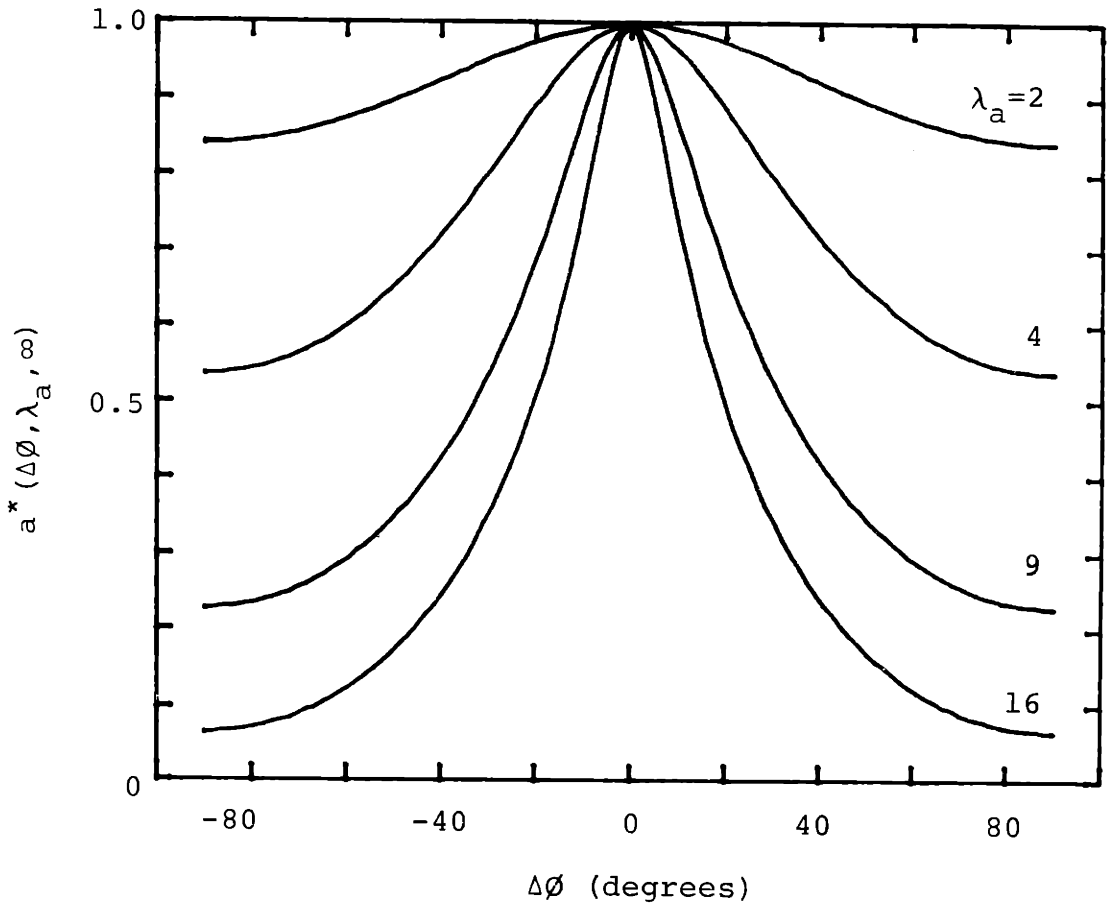

Figure 6.8 Orientation ambiguity function when eccentricity is known perfectly.

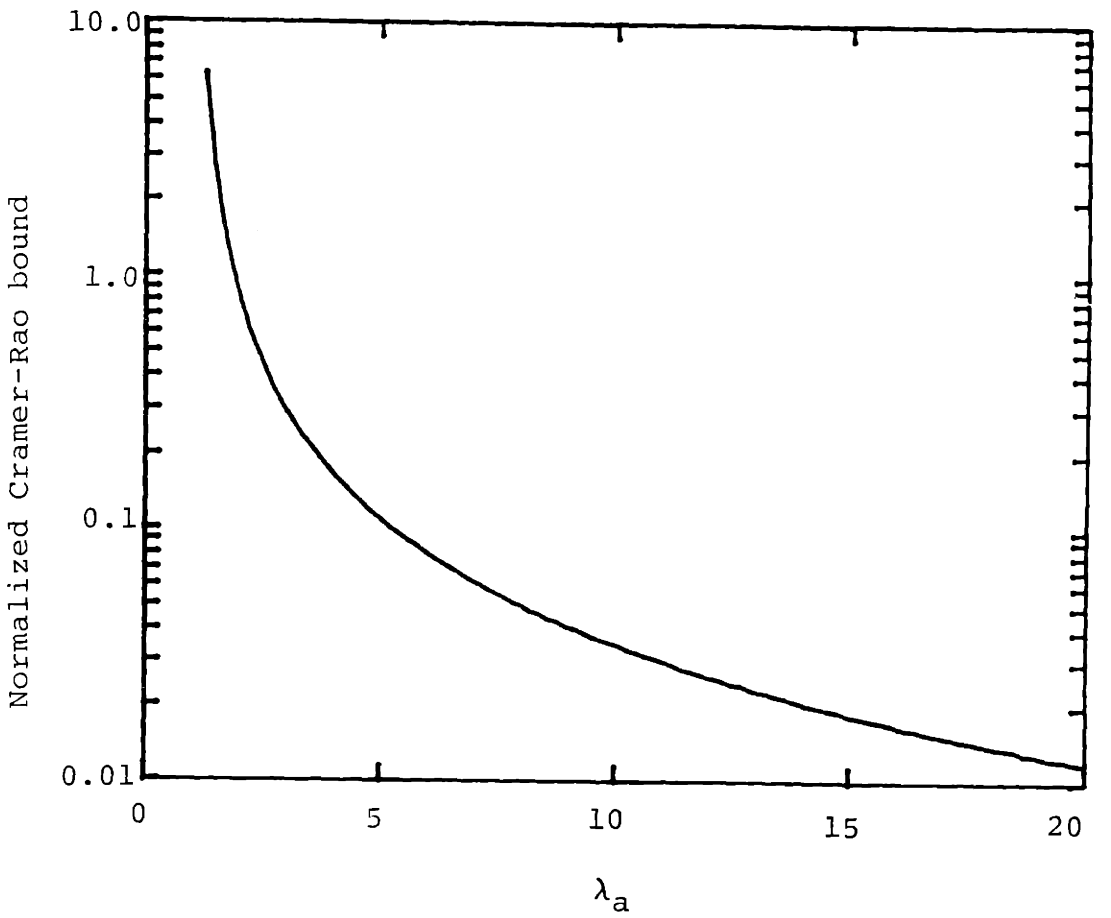

Figure 6.9 Normalized Cramer-Rao bound for the orientation estimation problem.

serves to reinforce the previous observation, based on Figure 6.8, that for fixed values of density, size and noise level, as the object's eccentricity is decreased, it becomes increasingly difficult to reliably estimate the object's orientation.

Up to this point in this section, we have evaluated the ambiguity function and Cramer-Rao bound for the orientation estimation problem, assuming all other parameters (including the eccentricity) are known perfectly. In practice, however, it is unlikely that the actual object eccentricity is known precisely. In the remainder of this section, we consider the robustness of the orientation estimation problem to a priori eccentricity modeling errors. In particular, we evaluate the orientation ambiguity function when the actual and modeled eccentricities differ.

The 1D orientation ambiguity function, in the presence of eccentricity modeling errors, may be obtained by evaluating the joint eccentricity and orientation ambiguity function given in (6.31) and (6.32) and illustrated for the Gaussian object with $\lambda_a = 4$ in Figure 6.5. Cross-sections of the joint ambiguity function at various values of λ shown in Figure 6.10 correspond to the 1D ambiguity function for the problem of estimating the orientation when the modeled value for the

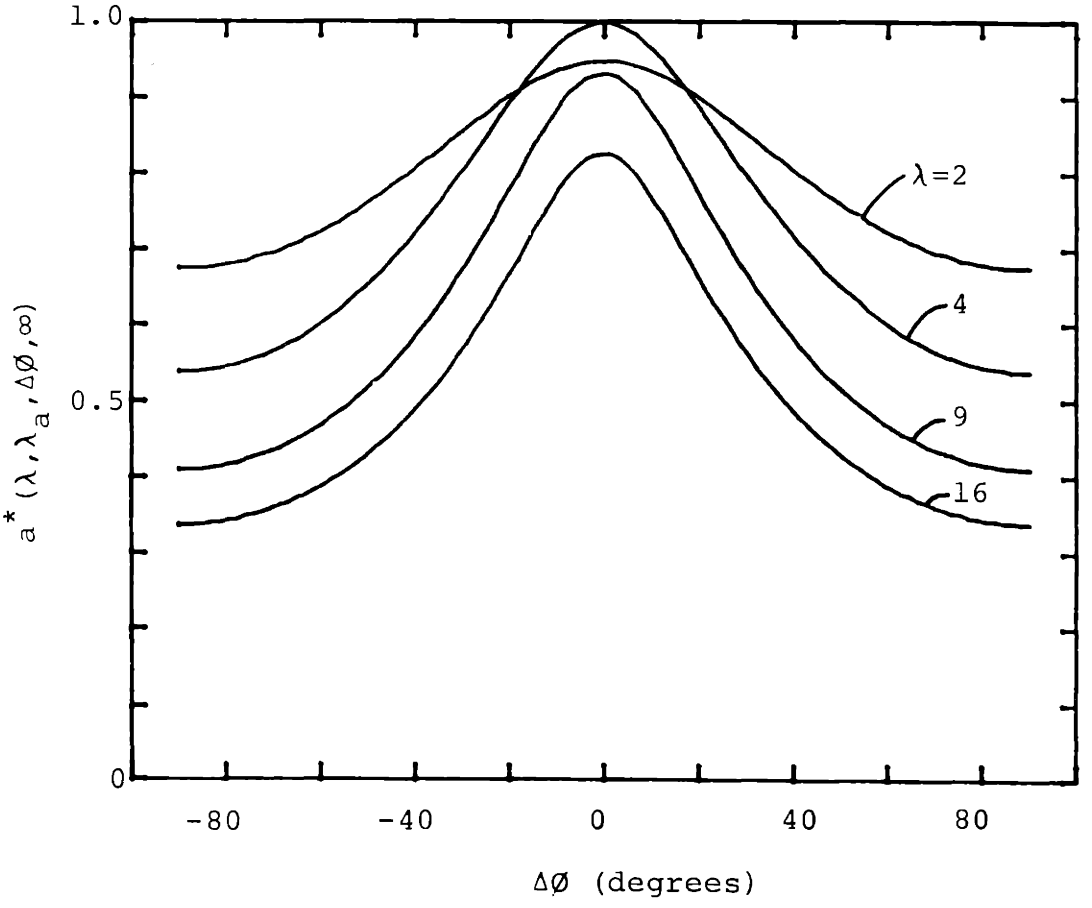

Figure 6.10 Orientation ambiguity function in the presence of eccentricity modeling errors; $\lambda_a=4$.

object eccentricity is fixed and possibly is in error. Even with eccentricity modeling errors, the orientation ambiguity function is seen to be symmetric with a peak at the true orientation value. Consequently, if one were to hypothesize a value of λ and estimate only the orientation $\emptyset$, the resulting estimate would be unbiased. When a value of eccentricity is selected that is smaller than the true value, the ambiguity function has a broader peak then it does when the true value is used, indicating that the orientation can not be estimated as accurately as it can when the true eccentricity is known. When a value of eccentricity is used that is larger than the true value, the ambiguity function has approximately the same degree of sharpness, but the peak value is smaller than it is when the true value is known.

This suggests that while the best estimation performance is obtained in the matched case (i.e. the true eccentricity value is known), the orientation estimation performance is relatively insensitive to errors in the a priori eccentricity value. That is, even if an object's eccentricity is not known precisely, the orientation estimation problem may be approached by using some nominal (but possibly incorrect) value of eccentricity. It should be noted that Figure 6.10 indicates that it is preferable to overestimate, rather than underestimate, the eccentricity.

6.2.4 Selecting the complexity of the modeled object

Figure 6.9 in the previous section clearly illustrates the relationship between an object's eccentricity and the accuracy with which its orientation can be determined. In particular, for values of λ_a near unity (i.e. the contours of the object profile nearly circular) the orientation is nearly impossible to estimate accurately. On the other hand, when the object is nearly circularly-symmetric, object orientation is essentially meaningless, and certainly is a far less important parameter than say, object size (which can be determined in such a case by using a circularly-symmetric modeled profile).

An object model incorporating size, eccentricity and orientation has more degrees of freedom associated with it than does a circularly-symmetric model, and consequently, a higher measurement SNR is required to accurately estimate these additional degrees of freedom. Said another way, even if the actual object is somewhat eccentric, the measurement SNR may not be high enough to simultaneously determine accurate estimates for both the eccentricity and orientation; in such a case, a simpler circularly-symmetric profile would be more appropriate.

In the concluding section of this chapter, we discuss an iterative approach to the problem of estimating an object's geometry parameters. In the final step of this procedure (once the size, eccentricity and orientation estimates are available), the question arises of whether there is enough measurement information for the object eccentricity and orientation estimates to be statistically meaningful. Intuitively, in a low SNR case, one would expect that only extremely eccentric objects would be distinguishable from circularly-symmetric ones, and thus one would not put much weight on the eccentricity and orientation estimates if the estimated value of the eccentricity is small. In this section we turn this intuitive notion into a precise real-time decision rule for deciding, based on knowledge of the SNR and the estimate obtained for object eccentricity, between the following two hypotheses:

$$\begin{aligned} H_0&: \text{the object is approximately circularly-symmetric } (\lambda_a \simeq 1) \\ H_1&: \text{the object has an elongated geometry } (\lambda_a > 1) \end{aligned} \tag{6.43}$$

Various optimization criteria may be used to develop a decision rule for the hypotheses in (6.43), and the criterion we use is simple and intuitive. In particular, our rule is based on the fact that circularly-symmetric

objects do not have well-defined orientations, while eccentric objects do. Thus, if the available amount of information does not provide us with an orientation estimate in which we have much confidence, we may as well assume the object to be circularly-symmetric. More precisely, since the orientation Cramer-Rao bound is a decreasing function of both SNR and object eccentricity, we will decide H_1 only when (1) the object is eccentric enough and (2) the SNR is high enough for the orientation to be accurately estimated. In particular, suppose that one has established an a priori limit ζ on the maximum acceptable orientation estimate error variance. The decision rule we propose is to decide H_1 if and only if the orientation estimate variance does not exceed ζ, i.e.

$$\text{decide } H_1 \text{ iff } \sigma_{\phi}^2 < \zeta \tag{6.44}$$

The orientation Cramer-Rao bound in (6.42) is inversely related to the SNR, and is a decreasing function of the object eccentricity as shown in Figure 6.9; for a fixed value of ζ, the inequality in (6.44) corresponds to a continuous region of SNR and λ_a values for which an accurate orientation estimate may be obtained. For a given SNR, denoted $\mathcal{E}/N_o$, from (6.42) and Figure 6.9 it follows that there is an eccentricity value $\lambda_{\min}(\mathcal{E}/N_o)$ such that (using the eccentricity estimate as though it were the actual eccentricity) the decision

rule in (6.44) is equivalent to the decision rule

$$\text{decide } H_1 \text{ iff } \hat{\lambda} > \lambda_{min}(\mathcal{E}/N_o) \tag{6.45}$$

These ideas are more clearly illustrated with an example, and we return to the Gaussian object in Example 3.

EXAMPLE 3 (continued)

Consider a Gaussian profile, for which the orientation Cramer-Rao bound is given in (6.42) and for which σ_ϕ^2 versus λ_a is plotted in Figure 6.9. Suppose that the orientation of this object must be estimated from projection measurements with an error variance not exceeding ζ_d degrees^2 or $\zeta_r = (\frac{\pi}{180})^2 \zeta_d$ radians^2. By setting the Cramer-Rao bound σ_ϕ^2 equal to the maximum acceptable error variance ζ_r, Figure 6.9 may be thought of as a plot of $\frac{\mathcal{E}}{N_0}\zeta_r$ versus λ_{min}, or switching the role of the abcissa and ordinate and rescaling, a plot of λ_{min} versus $\frac{\mathcal{E}}{N_0}$.

For example, if the maximum acceptable orientation estimate error variance is $\zeta_d = (20 \text{ degrees})^2$, then $\zeta_r = (\pi/9 \text{ radians})^2$, which leads to the plot of minimum eccentricity versus SNR shown in Figure 6.11. What this figure illustrates is the decision rule in (6.45); for a given measurement SNR $\mathcal{E}/N_o$, the eccentricity estimate must be greater than or equal to

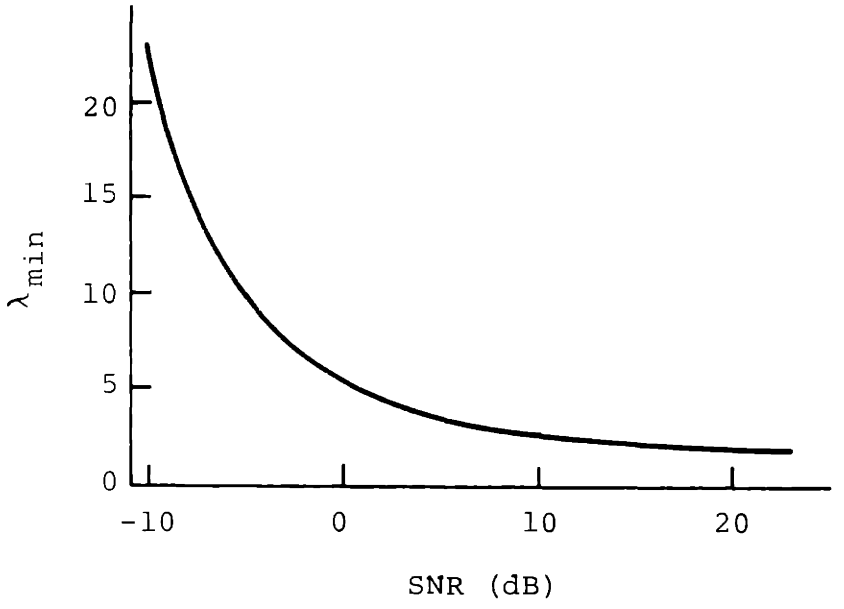

Figure 6.11 Minimum eccentricity versus measurement SNR.

λ_{min} in order for an orientation estimate to be obtained that satisfies $\sigma_{\phi}^2 < \zeta$.

At this point, we close our discussion about size, eccentricity and orientation estimation performance, and briefly turn to the issue of the robustness of these estimation procedures to two common types of modeling errors -- inaccurate a priori location information, and an actual object profile that does not belong to the class of modeled objects.

6.3 ROBUSTNESS ANALYSIS

Thus far in this chapter, we have addressed the problem of estimating the detailed density variations corresponding to an object, assuming that its location is perfectly known and that its relative profile lies within the class of modeled object profiles. In Sections 6.1.3 and 6.2.3, we addressed several robustness issues, in particular, the effect of eccentricity modeling errors on the estimation of size and orientation parameters, respectively. In this section, we consider two specific examples that illustrate the robustness of the geometry estimation procedure to location modeling errors, as well as errors in the assumption that the relative profile lies within the class of modeled profiles. In Section 6.3.1, we consider a problem where the actual object profile does

not lie within the modeled class of profiles -- the modeled object is an indicator function on an ellipse, the actual object is an indicator function on a rectangle, and we consider the size and orientation estimation problem. In Section 6.3.2, we consider geometry estimation in the presence of incorrect a priori knowledge of the object location -- the modeled and actual objects are both either pillboxes or indicator functions on ellipses, and several geometry estimation problems are considered when the modeled and actual object locations differ.

6.3.1 Robustness to relative profile inaccuracy

In this section, we investigate the way in which geometry estimation performance is affected when the actual object does not lie within the class of modeled objects. In particular, we consider the problem where the class of modeled object relative profiles is the set of indicator functions on ellipses centered at the origin, but where the actual object is an indicator function on a rectangle. The actual object will be taken to be the result of applying the scaling, eccentricity and rotation coordinate transformations in (6.1) through (6.3) to the relative profile

$$f_0(x) = \chi_I(x) \tag{6.46}$$

where $I \triangleq \{x: |x_1| \leq 1, |x_2| \leq 1\}$. Letting $g_r(t,\Theta)$

denote the Radon transform for an indicator function on a rectangle, the ambiguity function for the 3-parameter geometry estimation problem in (6.12), as $W \rightarrow \infty$, is given by

$$a(R,\lambda,\emptyset;R_a,\lambda_a,\emptyset_a) = \frac{2}{N_0} \cdot$$

$$\int_0^{\pi}\int_{-\infty}^{\infty} g_r(t,\Theta;d,R_a,\lambda_a,\emptyset_a)\, g(t,\Theta;d,R,\lambda,\emptyset)\, dt d\Theta$$

$$- \frac{1}{N_0} d^2 R^3 q(\lambda) \mathcal{E}_0 \qquad (6.47)$$

Consider the problem of estimating the object orientation when the size and eccentricity parameters R_a and λ_a are known, with λ_a taken to equal 9. In this case, the ambiguity function, which depends on $\emptyset$ and $\emptyset_a$ only through their difference $\Delta\emptyset \triangleq \emptyset - \emptyset_a$, is shown in Figure 6.12 (where the magnitude has been normalized for comparison purposes) along with the $\lambda_a = 9$ orientation ambiguity function when both the actual and modeled objects are indicator functions on ellipses (see Figure 6.8). This figure clearly demonstrates that orientation estimation is very robust to differences between the actual and modeled profile class. In particular, the peak of the ambiguity function is at $\Delta\emptyset = 0$, and in fact, it is not difficult to see that the orientation estimate is

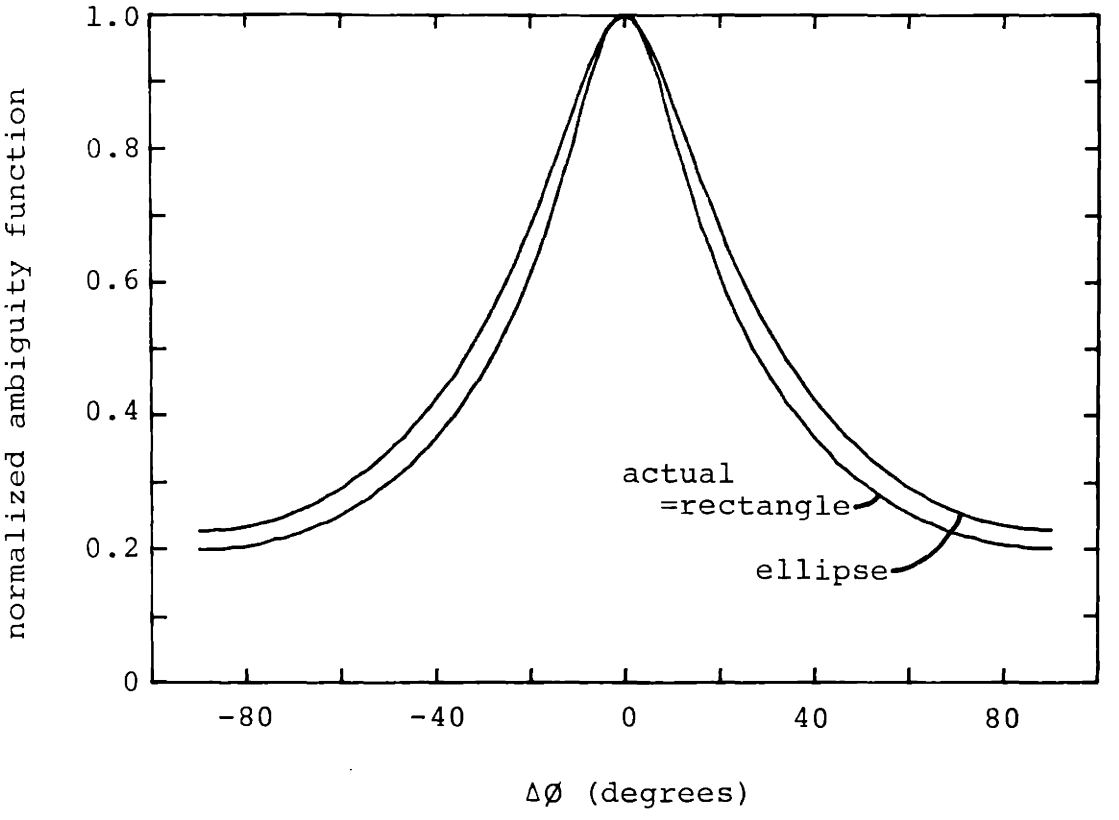

Figure 6.12 Orientation ambiguity function with profile class modeling error; λ_a=9.

unbiased. Note also that because the indicator function on a rectangle has a discontinuous projection at certain angles, the orientation ambiguity function for this case has a narrower peak than when the actual object is an indicator function on an ellipse. In the case where both the actual and modeled objects are indicator functions on rectangles, the orientation ambiguity function would even be somewhat more peaked than it is in Figure 6.12.

One may similarly consider the size estimation problem when the actual and modeled objects belong to different profile classes. Consider the problem where the actual object is an indicator function on a square, and where object size is estimated using a pillbox modeled object. The ambiguity function for this problem is a special case of the ambiguity function in (6.47), where $\lambda = \lambda_a$ and $\emptyset = \emptyset_a = 0$. Figure 6.13 illustrates the size ambiguity function for this case, which has a shape resembling the size ambiguity function when the actual object relative profile is known perfectly (see Figure 6.2). The peak of this ambiguity function occurs at the value of $R/R_a = 1.16$; this corresponds to a modeled object size that represents a very good fit of a disk to a square, in the sense that this value lies between the radii of disks that inscribe (R=1) and circumscribe (R=1.414) the square. Furthermore, the area of the square is $(2R_a)^2$, and a disk having the same area has radius

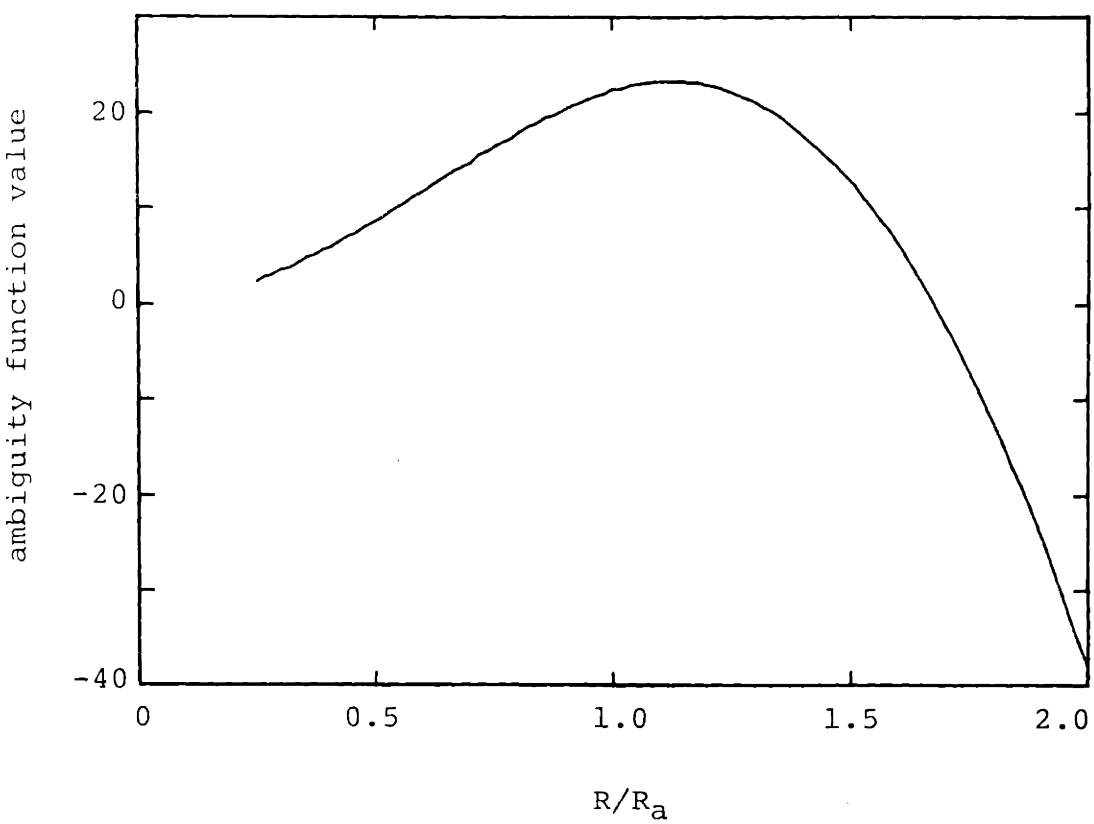

Figure 6.13 Size ambiguity function, actual=box object, modeled=pillbox object.

R which satisfies $R/R_a = 4/\pi = 1.13$, which is seen to be extremely close to the value at which the ambiguity function peak occurs.

The two examples considered in this section verify the intuitive notion that estimation of the gross geometrical structure of an object should be relatively insensitive to detailed differences between the actual and modeled profiles. In the next section, we consider in what ways the geometry estimation performance is affected when the location is known imprecisely.

6.3.2 Robustness to location modeling errors

In this section we consider the problem of size, eccentricity and orientation estimation when the actual and modeled objects have the same relative profile and are both either pillboxes or indicator functions on ellipses, but where the actual object location is not known precisely. This issue is very important when one considers using a hierarchical estimation algorithm, where objects are located first using a modeled object having a simple geometry, after which the object geometry is estimated.

First, consider the problem in which the actual and modeled objects are both pillboxes and size is estimated, but where the actual object is centered at c_a =

$(c_{al},0)$, with c_{al}/R_a = 0, 0.25, 0.5, 0.75, and 1, rather than at the origin. That is, we are considering location offsets of up to one full radius (i.e. offsets up to the case where the actual object center is located on the boundary of the modeled object when $R = R_a$). The size estimation ambiguity function for this case is shown in Figure 6.14. According to this figure, as the actual and modeled locations become increasingly separated, the magnitude of the ambiguity function decreases, its shape flattens, and the peak location shifts downward slightly. This figure demonstrates, however, that size estimation is very robust to location modeling errors, even when the actual object is centered at a point on the boundary of the modeled object when $R = R_a$.

It should be noted that the localization robustness analysis of Section 5.1 (see Figure 5.2) indicated that even when the size of an object is not known precisely, the location estimate has a high probability of lying within a distance R of the true object location (because the probability p_o of the event E_o is high). This analysis, together with Figure 6.14, indicates that object location and size estimation can be performed in a nested fashion, in which location is estimated first by using a nominally-sized object, and then the size parameter is estimated by treating the location estimate as though it were the true object location.

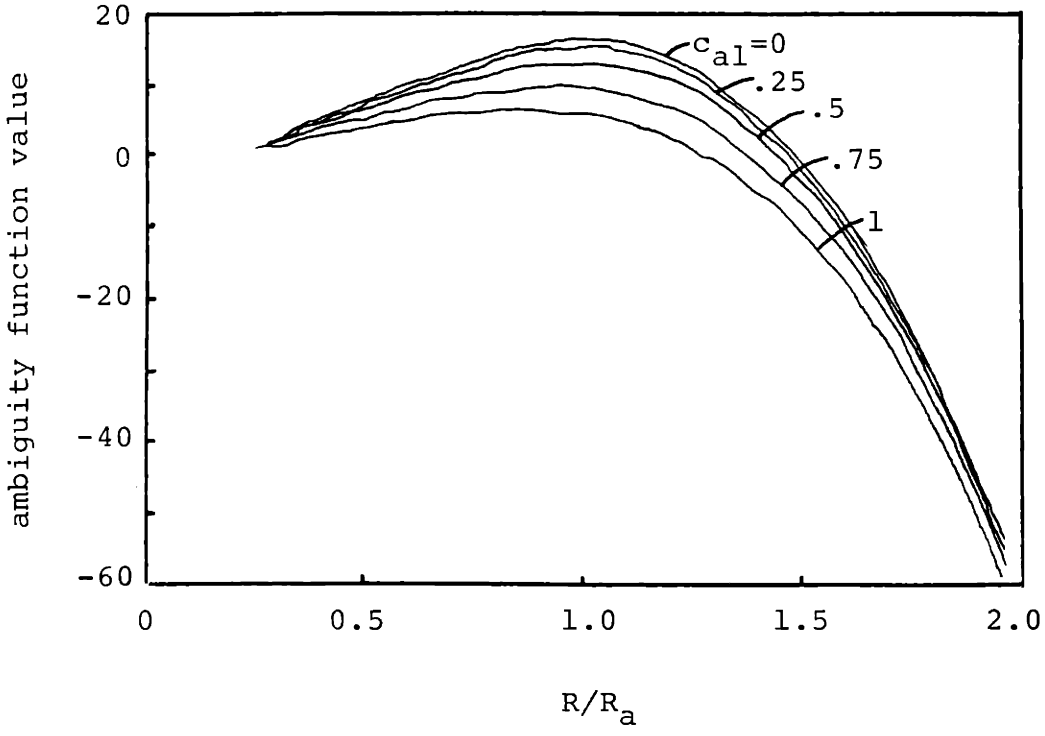

Figure 6.14 Size ambiguity function in the presence of location modeling errors; $c_a=(c_{a1},0)$.

We now turn to the effect of location errors on the estimation of eccentricity, when the actual object is an "off-center" pillbox, and geometry is estimated using the size, eccentricity and orientation parameterization. In such a case, one might conjecture that the resulting estimated geometry will be that of a somewhat eccentric object (with eccentricity directed along the vector from the assumed to the actual location). To test this, we consider the problem where the actual object is a pillbox centered at $(c_{al},0)$, and the modeled object is an indicator function on an ellipse centered at the origin and oriented at 0^{o}. Figure 6.15 indicates the eccentricity estimation ambiguity function for such a case, with c_{al}/R =0, 0.25, 0.5, 0.75 and 1. Indeed, as the actual and modeled object locations become separated, the peak of the ambiguity function does shift to increasingly higher eccentricity values (for the five values of c_{al} studied, the peak occurs at 1.0, 1.2, 1.4, 2.8 and 4.9), although this shift is relatively mild for $c_{al}<0.5R$. This implies that in a hierarchical approach to the estimation of location and then geometry, in order for accurate geometry estimation to be performed in the second step, the pillbox object location must be determined with an error not exceeding 0.5R. For a given application, the localization analysis performed in Chapters 3 and 4 and characterized by the performance

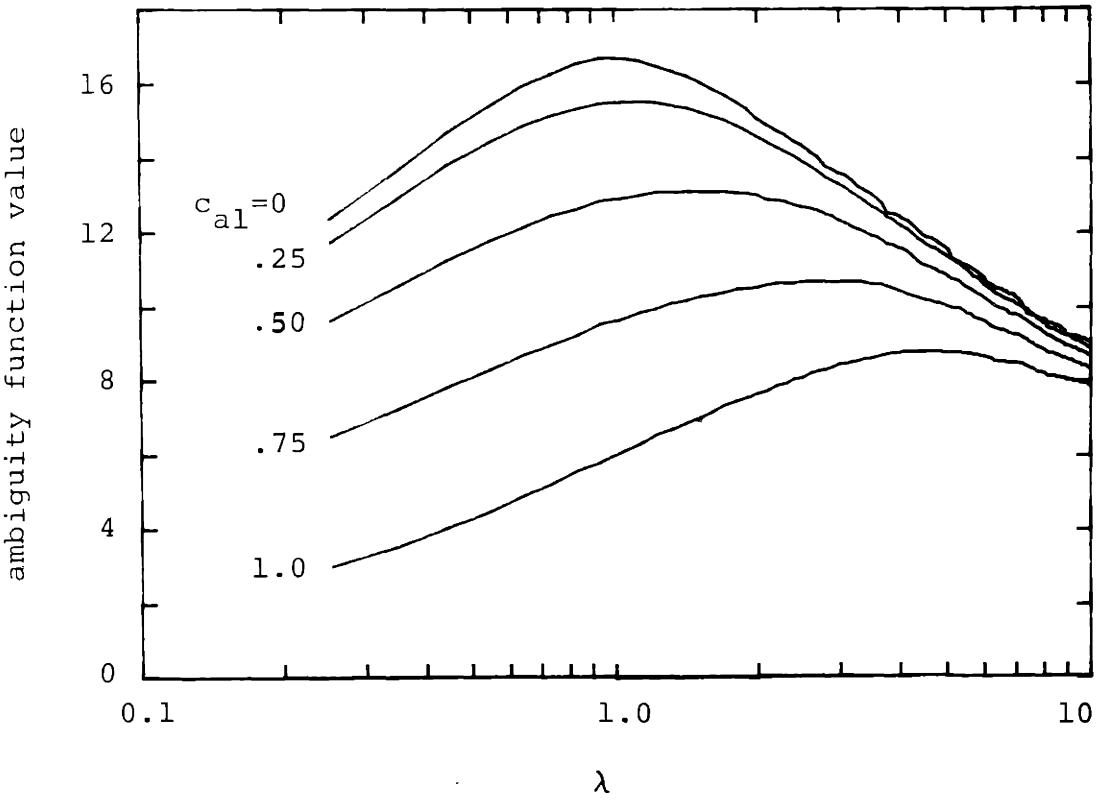

Figure 6.15 Eccentricity ambiguity function in the presence of location modeling errors; $c_a=(c_{a1},0)$.

curves in Figure 4.4 (or the robustness analysis in the presence of modeling errors in Section 5.2) may be used to determine for what SNR and measurement conditions the location can be estimated to within this accuracy. For example, if the actual and modeled objects are equally-sized pillboxes, the $\lambda_a = 1$ curve in Figure 5.3 indicates that for SNR exceeding 12 dB or so, p_0 is essentially equal to one. Furthermore, conditioned on the occurrence of no global errors, the expression for the error standard deviation in (5.38), along with the $\lambda = 1$ entry in Table 1, may be used to deduce that for SNR exceeding 12 dB the local error standard deviation is less than 0.18R; this is less than the value 0.5R needed for accurate geometry estimation.

In the problem just discussed, we considered estimating the geometry of an off-center pillbox. In the remainder of this section, we consider estimating the size and orientation of an ellipsoidally-shaped actual object when its location is not known precisely. For purposes of illustration, we take the actual object eccentricity to be $\lambda_a = 9$ (i.e. an ellipse with semiaxis lengths 3 and 1/3), and consider size and orientation estimation when the actual object location is (0,0), (3/2,0), (0,1/6) and (3/2,1/6), that is the object location is in error by various combinations of one-half the semiaxis length in each direction.

Consider first the size estimation problem; Figure 6.16 illustrates the size ambiguity function (assuming the eccentricity is known perfectly) for these values of actual object location. As was the case with pillbox objects illustrated in Figure 6.14, the magnitude of the ambiguity function decreases and the peak location shifts downward slightly in the presence of location modeling errors, but overall, the size estimation procedure is very robust to location modeling errors.

Finally, consider the orientation estimation problem in the presence of location modeling errors. Figure 6.17 indicates the orientation ambiguity function when the actual and modeled objects are both indicator functions on an ellipse with eccentricity equal to 9, and where the actual object location takes on the four values given previously. When the vector between the actual object location and the modeled object location takes on values along either of the two coordinate axes, the magnitude of the ambiguity function decreases but the peak remains at $\Delta\emptyset=0$, and unbiased estimates are obtained. When the actual object location differs from the modeled object location in <u>both</u> coordinates, the ambiguity function magnitude decreases and the peak location <u>shifts</u>; intuitively, this makes sense, because the modeled object "fits" the actual object best, under these conditions, when it is rotated slightly.

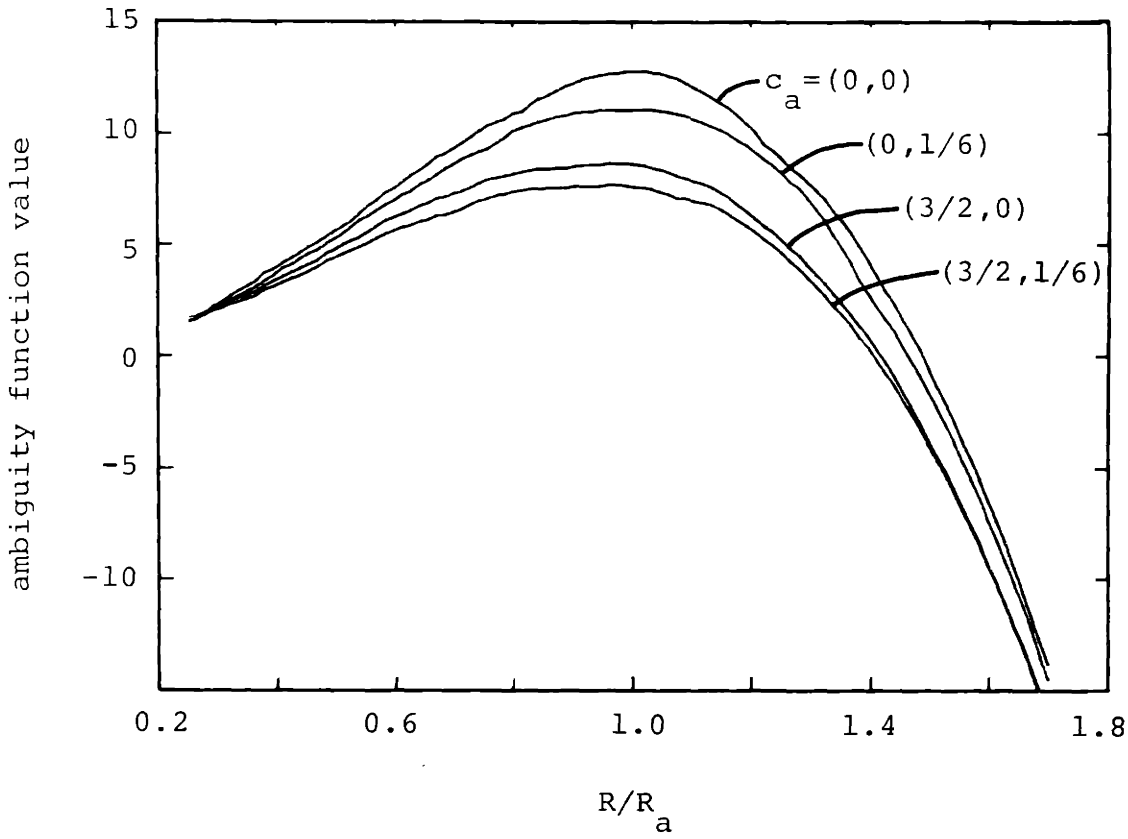

Figure 6.16 Size ambiguity function in the presence of location modeling errors; λ_a=9.

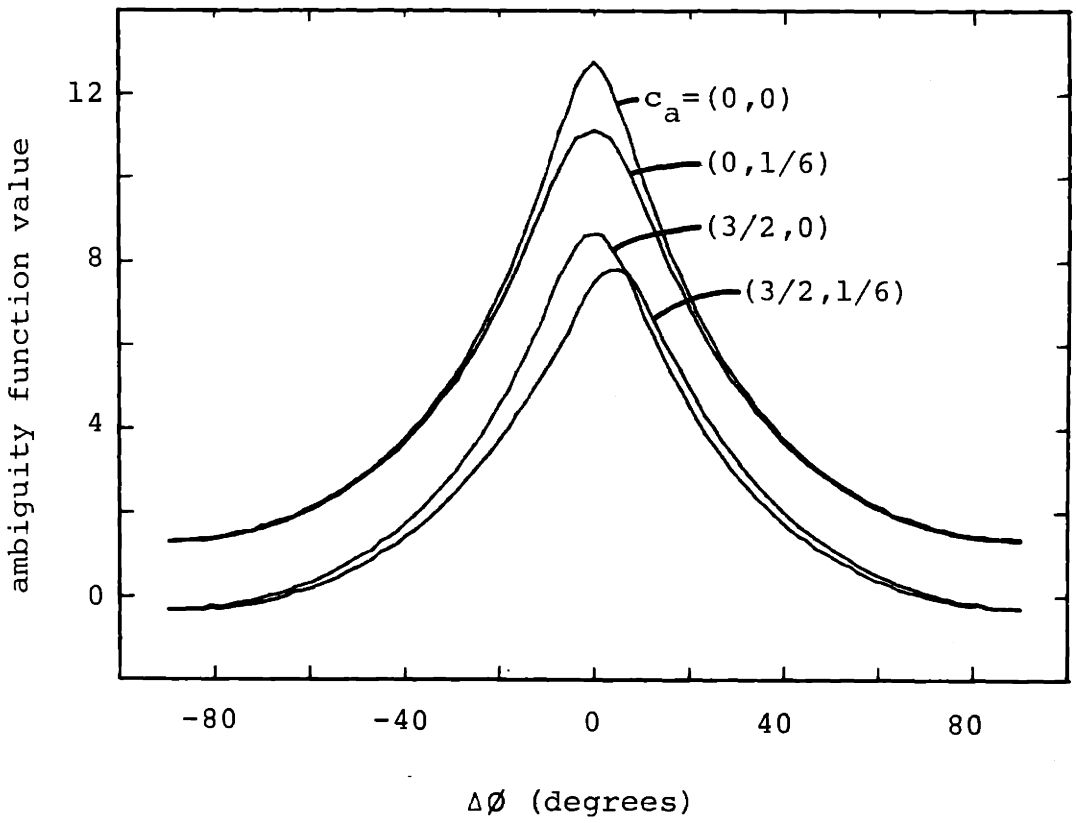

Figure 6.17 Orientation ambiguity function in the presence of location modeling errors; λ_a=9.

The results of this analysis indicate that even if an eccentric object's location is known only approximately (to within half a semiaxis length in each coordinate direction), its geometry can still be estimated quite reliably. The localization robustness analysis results in Section 5.2 (see Figures 5.3 and 5.4), however, demonstrate that even in the presence of shape modeling errors, if the SNR exceeds 15 dB or so, p_0 is approximately equal to one and if no global errors occur, the location estimate is characterized by a standard error ellipse with semiaxis lengths much smaller than half the actual object semiaxis lengths. This analysis, along with Figures 6.16 and 6.17, indicates that object location, size and orientation estimation can be approached in a nested manner, where the location is estimated first by using a nominally-sized object profile, and then the size and orientation parameters are estimated by treating the location estimate as though it were the true object location. Note, as shown in Section 6.2, that eccentricity estimation requires a high SNR, and for such SNR values, the location may be estimated very accurately.

Combining all of these conclusions plus several others from earlier chapters, we can readily determine an object estimation algorithm which will perform well. This is described in the concluding section of this chapter.

6.4 CONCLUSIONS

In this chapter, we have investigated the problem of using noisy projection measurements to estimate the (finitely-parameterized) relative profile of an object. In particular, the focus of this chapter has been on developing insight into the geometry estimation problem by selecting for study one particular relative geometry parameterization having a small number of degrees of freedom, and investigating the performance of the estimation procedures, as well as the robustness to particular modeling errors. Figure 6.18 presents an overview of the problems addressed in this chapter, along with a summary of important results and insights obtained from this analysis.

In this section we discuss the implications of the foregoing analysis, with an emphasis on how one might use the results of this chapter in structuring an iterative algorithm to accomplish reliable location and geometry estimation in practice. In particular, one may conceive of recursively processing the projection measurements. For example, a simple circularly-symmetric profile model may be used during the initial stages of such a procedure to determine coarse estimates of object location and size, and in subsequent stages, additional a priori information (regarding probable object shapes and orientations) and

SIZE ESTIMATION

1) relative profile known	• size ambiguity fn. • Cramer-Rao bound	• peak at $R = R_a$ • $\sigma_R^2 \sim 1/R^2$ (Gaussian object)
2) relative profile unknown	• size ambiguity fn.	• estimate is mildly biased

ECCENTRICITY ESTIMATION

all other parameters known	• eccentricity ambiguity fn. • Cramer-Rao bound	• peak at λ_a • requires a high SNR • $\sigma_\lambda^2 \sim \lambda_a^2$ (Gaussian object)

ORIENTATION ESTIMATION

1) $\lambda = \lambda_a$	• orientation ambiguity fn.	• peak at ϕ_a, unbiased • λ_a large $\Rightarrow$ narrow peak • σ_ϕ monotone decreasing in λ_a
2) $\lambda \neq \lambda_a$	• orientation ambiguity fn.	• peak at λ_a, unbiased • best performance for λ known • in presence of eccentricity modeling errors, better to overestimate λ.

Figure 6.18 Summary of problems in Chapter 6.

more complicated object models may be employed to estimate finer details of the object's density profile. While many approaches to recursive estimation of object size, orientation and eccentricity are possible, the results of this chapter suggest one approach, as outlined in Figure 6.19.

The localization results in Chapters 3 through 5 and the size estimation robustness results in Section 6.1.3 suggest that even if the actual object is not circularly symmetric, a circularly-symmetric profile may be used for the initial localization and sizing stage of the signal processing, where a priori information about the cross-section is incorporated in selecting the initial profile type (e.g. discontinuous, continuous) and its size. Based on the results of Chapters 3 through 5, for a measurement SNR exceeding a minimum value (which may be determined by the procedure that led to Figure 4.4), the location may be estimated reliably, even in the presence of size and shape modeling errors or the presence of other, small unmodeled objects. For example, we have shown in Chapter 4 that an unbiased location estimate is obtained when the actual and modeled objects are centrally-symmetric (e.g. the actual object could be ellipsoidal while the modeled object is taken to be circularly-symmetric).

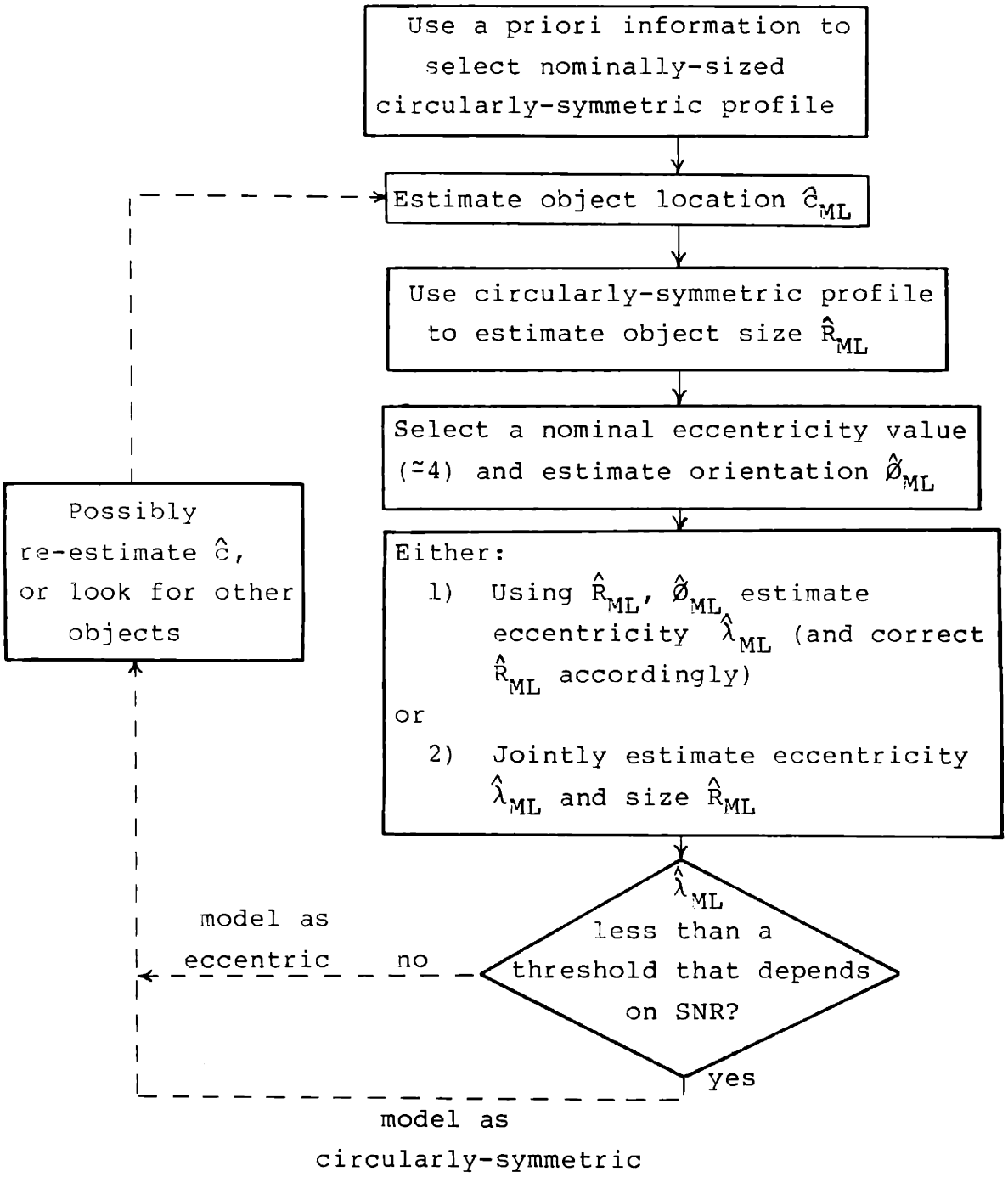

Figure 6.19 An iterative approach to object-based reconstruction.

The results of Section 6.1 suggest that after the object location has been estimated, a circularly-symmetric modeled profile may be used (even if the actual object is not circularly-symmetric) in estimating the object size. According to Figure 6.2, an accurate size estimate may be obtained when the actual and modeled relative profiles are the same; in the presence of shape modeling errors, mildly biased size estimates are obtained, as illustrated in Figure 6.4b (the peak of the ambiguity function is located at a value of the size parameter that is somewhat smaller than the true size parameter value). Such biases can be removed at a later processing stage as described shortly.

Once an ML size estimate is obtained through the use of a circularly-symmetric profile, one can address the question of whether the actual object is approximately circularly-symmetric or eccentric. In particular, the second stage of the iterative estimation procedure outlined in Figure 6.19 involves examining the directional characteristics of the object. In Section 6.2 (see Figures 6.8 and 6.10), it was shown that ML orientation estimation is relatively insensitive to eccentricity modeling errors; this suggests that the object orientation may be estimated reliably by using some nominal (perhaps incorrect) value of object eccentricity (say, in the range of 4 to 10). In particular, an

unbiased estimate is obtained when the actual object is centrally-symmetric. As indicated by Figure 6.10, the width of the orientation ambiguity function peak depends on the smaller of the actual and modeled eccentricities (as the modeled eccentricity decreases, the ambiguity function peak width increases); for this reason, it is better in the orientation estimation problem to slightly overestimate, rather than underestimate the object eccentricity.

Once the size estimate $\hat{R}_{ML}$ (obtained using a circularly-symmetric profile) and the orientation estimate $\hat{\emptyset}_{ML}$ are available, one may consider in the next stage of the parameter estimation problem either (1) estimating the eccentricity alone (and subsequently correcting the size estimate given knowledge of the size estimation bias in the presence of shape modeling errors, see Figure 6.4b), or (2) jointly estimating the size and eccentricity parameters. In Section 6.2.2, eccentricity estimation was seen to require a high measurement SNR (see Figure 6.6); in fact, the results of this chapter indicate that, for a given measurement SNR, eccentricity is the most difficult parameter to estimate accurately.

At the conclusion of the third iteration, object size, eccentricity and orientation estimates are available, and the issue of selecting the modeled object

complexity (discussed in Section 6.2.4) arises. In that section, it was shown that if the object is not very eccentric (λ near 1), the orientation can only be estimated accurately at very high measurement SNR. A decision rule was described in Section 6.2.4 for assessing whether object eccentricity and measurement SNR are high enough for orientation to be estimated to within a prescribed accuracy. Such a decision rule is incorporated into the final step of the iterative algorithm presented in Figure 6.19, leading to one of two conclusions: (1) the object is eccentric (in which case the orientation may perhaps be reestimated using the eccentricity estimate $\hat{\lambda}_{ML}$) or (2) the object is approximately circularly-symmetric with size $\hat{R}_{ML}$.

It should be noted that the geometry estimation procedures alluded to in the latter stages of the iterative algorithm in Figure 6.19 (which assume that the location is known perfectly) have been shown in Section 6.3.2 and Chapters 3 through 5 to be very insensitive to object location modeling errors. In particular, it was demonstrated in Section 6.3.2 that object size can be estimated quite accurately, even if the actual object off-center to the extent that it is located on the boundary of the modeled object. Also, it was shown reliable orientation and eccentricity estimates may be obtained even when the location is known imprecisely (see

Figures 6.15 and 6.16). Consequently, useful geometry estimates may be obtained even if the location estimate from the initial stages of this iterative procedure is taken as though it were the actual object location.

As indicated by the recursive algorithm outlined in Figure 6.19, one may, after completing one pass through this algorithm, return to the beginning of this procedure in order to determine a more accurate estimate of the object location; alternatively, one may return to the beginning of the algorithm and attempt to identify other objects in the cross-section. Our results in Chapter 5 suggest that if more than one object is present, one should first estimate the parameters associated with the largest object, and then consider any smaller ones. As we mention in the next and concluding chapter, the problem of recursively estimating parameters when more than one object is present is an area for future research, which may be pursued within the framework developed in this thesis.

Appendix 5 -- Representation of a convex object

Consider a relative profile that is an indicator function on a set K that is a two-dimensional convex body, i.e. it is a closed, bounded, convex set in the plane (Benson, 1966). By the definition of a relative profile, K contains the origin, and the support function $h(\Theta)$ of K, relative to the origin, is a periodic function of Θ given by the length of the vector at angle Θ normal to the supporting or tangent line (see Figure A.1a). The support function can be written as (Kelly and Weiss, 1979)

$$h(\Theta) = \sup_{x \in K} \underline{x}'\underline{\Theta} \tag{A5.1a}$$

and the width of K is defined as

$$w(\Theta) \triangleq h(\Theta) + h(\Theta+\pi) \tag{A5.1b}$$

Let K_c denote the c-translate of K (i.e. the result of translating the set K from the origin to the point c). The set K_c has support and width, relative to the origin, of

$$h_c(\Theta) = h(\Theta) + \underline{c}'\underline{\Theta} \tag{A5.2a}$$

$$w_c(\Theta) = w(\Theta) \tag{A5.2b}$$

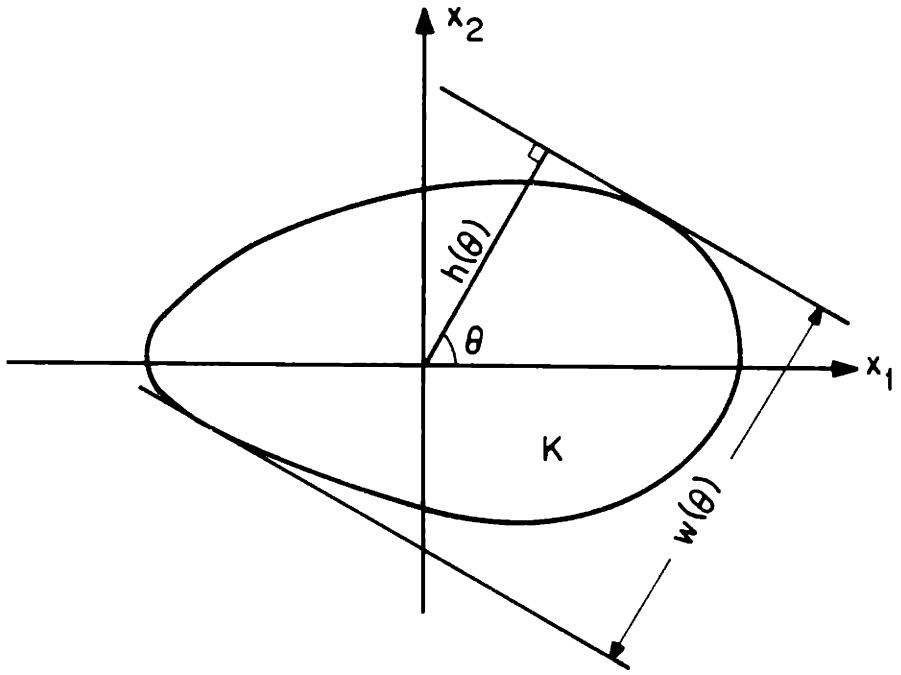

Figure A.1 (a) Support function for the set K.

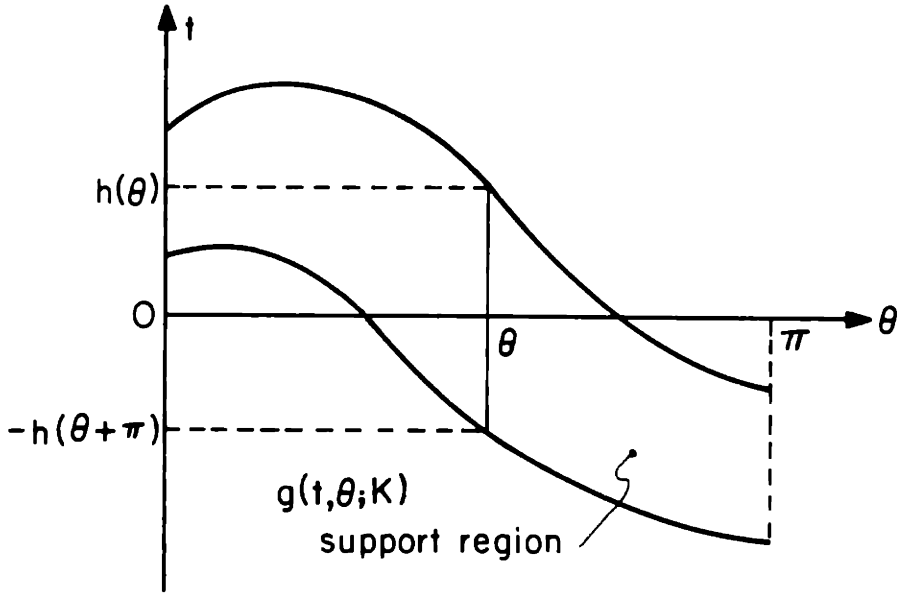

Figure A.1 (b) Relationship between the support function h and the Radon transform support set.

The support and width functions for K are both differentiable in Θ (Kelly and Weiss, 1979) and a necessary and sufficient condition for a periodic function h to be the support function for a convex set K (Santalo, 1976) is

$$h(\Theta) + h''(\Theta) > 0 \qquad \text{(A5.3)}$$

where h'' is the second derivative of h with respect to Θ. As shown in Figure A.1b, the support function $h(\Theta)$ for a convex set K corresponds directly to the region of support for the two-dimensional Radon transform $g(t,\Theta;K)$ for set K.

Consider the 1D projection $g(t,\Theta;K)$ at angle Θ; in the neighborhood of the end points of the support interval $[-h(\Theta + \pi),h(\Theta)]$, the Radon transform generally takes on values close to zero. The first partial derivative $\partial g/\partial t$, however, is typically discontinuous at the support interval endpoints (in particular, this occurs whenever the set K has a boundary following a curve with a finite radius of curvature (Galvin and Bjarngard, 1975)) and possibly infinite (e.g. consider a circular object with semi-ellipsoidal projection). One could consider approaching the object geometry determination problem by using the measurements $y(t,\Theta)$, perhaps by differentiating, to estimate the Radon transform support region boundary

$h(\Theta)$. Such a Radon space boundary following approach requires a high SNR to be successful, since in the region of the boundary, $g(t,\Theta)$ is small.

Fourier series representation for $h(\Theta)$

As an alternative to procedures of the type alluded to in the previous paragraph, one can consider estimating a parametric representation of the object boundary. For example, one might consider representing the boundary of a convex object K using an approximate, truncated Fourier series expansion for the periodic support function $h(\Theta)$, i.e.

$$h(\Theta) \cong h(\Theta;v)$$

$$\triangleq v_0 + \sum_{k=1}^{M} v_{ck}\cos(k\Theta) + v_{sk}\sin(k\Theta) \qquad \text{(A5.4)}$$

Here the boundary is completely characterized by v, the (2M+1)-vector of series coefficients. Using the support function in (A5.4) to characterize a convex set, K(v) object boundary estimation becomes a problem of estimating the Fourier series coefficients on the set V of coefficients corresponding to a convex object:

$$V \triangleq \{v: v\epsilon R^{2M+1}, h(\Theta;v) + h''(\Theta;v) > 0\} \qquad \text{(A5.5)}$$

It should be noted that except for very small values of M,

the set $V \subset R^{2M+1}$ has a complex description. Note also that the Fourier series (A5.4) is used to represent the support function rather than the width function because the width function $w(\theta)$ of a convex set does not uniquely specify the set shape. In particular,

$$w(\theta) = h(\theta) + h(\theta+\pi)$$

$$= 2v_0 + \sum_k v_{ck}[\cos(k\theta) + \cos(k(\theta+\pi))] + v_{sk}[\sin(k\theta) + \sin(k(\theta+\pi))]$$

$$= 2v_0 + 2 \sum_{k \text{ even}} v_{ck}\cos(k\theta) + v_{sk}\sin(k\theta) \qquad \text{(A5.6)}$$

The width function contains only even Fourier series terms (i.e. less information than the support function) and consequently does not uniquely specify the geometry of a convex set. For example, the circle and Reuleaux triangle, shown in Figure A.2, are convex sets having a constant width function but different support functions (Lyusternik, 1963).

From equation (A5.2a), which relates the support function for a set and its c-translate, it is seen that the first harmonic terms $v_{c1}\cos\theta$ and $v_{s1}\sin\theta$ in (A5.4) affect only the translation of the set K and not its relative geometry. If $v = (v_o\ v_{c1}\ v_{s1}\ v_{c2}\ \ldots)$ specifies the support function in (A5.4) for a convex set and $\underline{v} \triangleq (v_{c1}\ v_{s1})'$, then

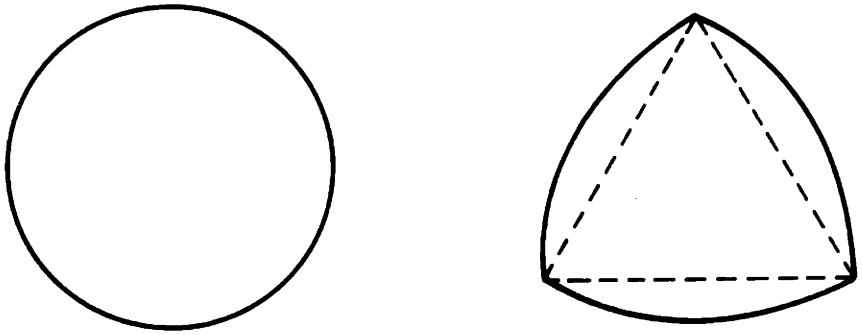

Figure A.2 Convex sets of constant width.

$$g(t,\Theta;v) = g(t - \underline{v}'\underline{\Theta},\Theta;(v_0\ 0\ 0\ v_{c2}\ldots)) \qquad \text{(A5.7)}$$

This is the Radon transform cosinusoidal displacement property discussed in Chapter 2. Put another way, for a convex object specified by v above, coefficients v_{c1} and v_{s1}, unlike all of the other coefficients, affect the Radon transform only by translation.

In Chapter 2, the location of the object K was arbitrarily defined to be a point c internal to the set K that serves as a reference point for defining the relative object profile. Because coefficients v_{c1} and v_{s1} in (A5.4) affect the translation of the set K(v), but not its boundary shape, the point (v_{c1},v_{s1}) may be considered to be the location c of the object K(v). If the location

(v_{c1}, v_{s1}) is known (or assumed known based on the estimate produced by solving an object localization problem), then estimating the object relative profile involves estimating the Fourier series coefficients v_o, v_{c2}, v_{s2},... in (A5.4).

The various harmonic coefficients v_{ck} and v_{sk} affect the shape, size, orientation, and detailed boundary of the set K(v) in object space in very specific ways. For example, $h(\theta) = v_o$ corresponds to a circular set centered at the origin. When only zero and second order harmonics are included in $h(\theta;v)$, K(v) has an ellipsoidal character (although it does not correspond precisely to an ellipse). As higher-order harmonics are added in $h(\theta)$, the set K(v) attains a variety of shape characteristics; one advantage of the Fourier series support function parameterization is the apparently large class of possible shapes that can be generated using relatively few harmonic components. It should be noted, however, that because of the condition (A5.3), an arbitrarily eccentric ellipse-like object may <u>not</u> be generated using only zero and second order harmonics; in particular, using only these harmonics, the maximum value of object length/width ratio that may be generated is two.

The 1D projection of object K(v), i.e. the Radon transform $g(t,\theta;v)$ as a function of t, clearly depends on the Fourier series coefficients v. Although the area under the projection function at any projection angle is constant, and equals the contrast d times the cross-sectional area of the object K(v), details of the width, shape, and symmetry of the projection depend on v. Generally, even harmonic components correspond to centrally-symmetric objects (with respect to the center c) having symmetric projections, and odd harmonics correspond to non-centrally-symmetric objects having nonsymmetric projections.

Radon transform for a convex object

We now develop an expression for $g(t,\theta;v)$, the Radon transform of the indicator function on the set K(v), evaluated at the point (t,θ) in Radon space. From Figure A.3, the Radon transform for the indicator function on an arbitrary convex set K(v) is the chord length of intersection

$$g(t,\theta;v) = \begin{cases} t_2^+(t,\theta;v) - t_2^-(t,\theta;v) & \text{if } -h(\theta+\pi;v) < t < h(\theta;v) \\ 0 & \text{otherwise} \end{cases} \qquad \text{(A5.8)}$$

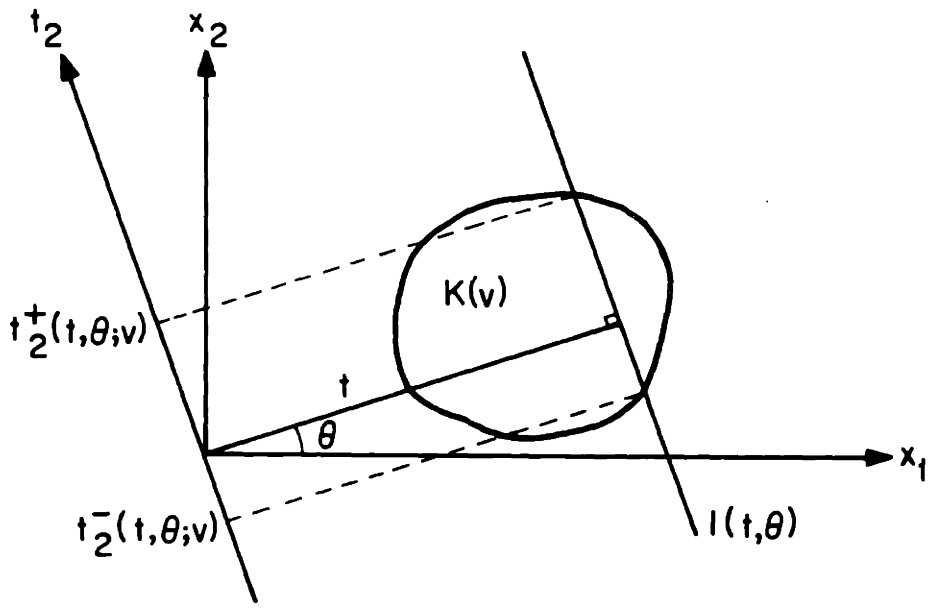

Figure A.3 Convex set and measurement line geometry.

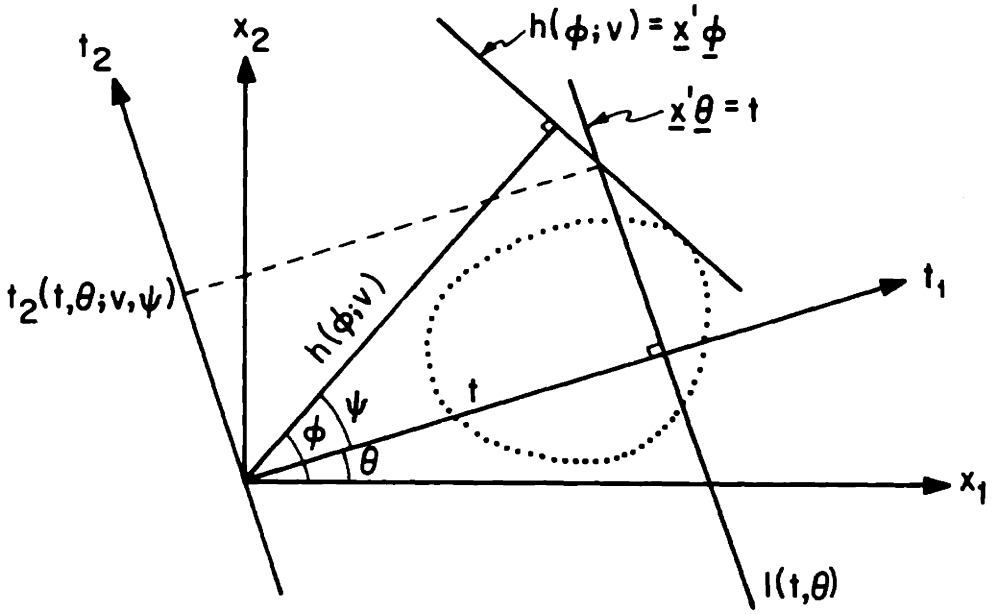

Figure A.4 Convex set support function.

For a given projection line $l(t,\theta)$, the values of $t_2^+(t,\theta;v)$ and $t_2^-(t,\theta;v)$, which clearly depend on the set boundary parameter v, may be obtained in the following way (we discuss t_2^+ in detail, t_2^- follows similarly). Consider the convex set support line at angle ϕ satisfying $\underline{x}'\underline{\phi} = h(\phi;v)$ and shown in Figure A.4, where $\theta<\phi<\theta+\pi$. This line intersects the projection line $l(t,\theta)$ at a point whose coordinates, with respect to the t-coordinate system, are $(t,t_2(t,\theta;v,\psi))$, where $\psi \triangleq \phi-\theta$. The value of $t_2^+(t,\theta;v)$ in Figure A.3 may be obtained by noting that as ψ is varied over the range $\psi\epsilon(0,\pi)$, $t_2(t,\theta;v,\psi)$ in Figure A.4 varies from infinity to some minimum value, and then returns to infinity. The minimum value of $t_2(t,\theta;v,\psi)$ is $t_2^+(t,\theta;v)$ in Figure A.3.

To state this more precisely, the line $h(\phi;v) = \underline{x}'\underline{\phi}$ may be rewritten in terms of the t-coordinate system by using the 2x2 orthogonal rotation matrix $G(\theta)$ in (A1.11) where $\underline{t}=G(\theta)\underline{x}$. The representation of this line with respect to the t coordinate system is

$$\underline{\phi}'G(\theta)^{-1}\underline{t} = h(\phi;v)$$

or

$$(\underline{\theta}+\underline{\psi})'G(\theta)'\underline{t} = h(\theta+\psi;v) \qquad \text{(A5.9)}$$

For fixed values of θ and v, (A5.9) specifies the support

line for the set K(v) at the angle ψ with respect to the t coordinate system. The value of $t_2(t,\theta;v,\psi)$ corresponds to the t_2 value of the point of intersection of the line in (A5.9) and the line given by $t = t_1$; setting $t_1 = t$ in (A5.9) and solving for t_2,

$$t_2(t,\theta;v,\psi) = (\sin\psi)^{-1}[h(\theta+\psi;v) - t\cos\psi] \qquad 0<\psi<\pi \tag{A5.10}$$

As just discussed, as ψ varies over the interval $(0,\pi)$, $t_2(t,\theta;v,\psi)$ starts at infinity, decreases to a minimum value of $t_2^+(t,\theta;v)$ in Figure A.3, then returns to infinity, so that

$$t_2^+(t,\theta;v) = \min_{0<\psi<\pi} t_2(t,\theta;v,\psi) \tag{A5.11a}$$

and performing the same analysis for $-\pi<\psi<0$,

$$t_2^-(t,\theta;v) = \max_{-\pi<\psi<0} t_2(t,\theta;v,\psi) \tag{A5.11b}$$

Finally, equations (A5.11) may be substituted into (A5.8) to determine the Radon transform $g(t,\theta;v)$.

Summarizing, for a fixed convex set geometry parameter v and a fixed value of (t,θ), the Radon transform $g(t,\theta;v)$ is obtained by subtracting the values of $t_2(t,\theta;v,\psi)$ at two stationary points with respect to ψ. The two stationary points provide the values $t_2^+(t,\theta;v)$ and $t_2^-(t,\theta;v)$ (see Figure A.3) which are

the t_2-coordinate values of the two points where the boundary of the set K(v) intersects the line $l(t,\theta)$. The stationary points $t_2^+(t,\theta;v)$ and $t_2^-(t,\theta;v)$ in (A5.11) may be obtained by finding the zeroes of the first partial derivative of $t_2(t,\theta;v,\psi)$ with respect to ψ. The function $t_2(t,\theta;v,\psi)$ appears to be a well behaved function inside the intervals $(-\pi,0)$ and $(0,\pi)$, even for convex sets with sharp corners. Because of this, it is expected that the first partial derivative zeroes can be determined recursively quite rapidly, by using for example both function and derivative information with a Newton-Raphson technique. Alternatively, the stationary points may be determined as functions of v for a given number of Fourier coefficients, and stored in a look-up table for on-line use.

APPENDIX 6 -- Radon transform energy for an eccentric object

Consider a circularly-symmetric profile $d \cdot f_p(r/R)$ with contrast d and size R, having a circularly-symmetric Fourier transform $d \cdot R^2 F_p(R\rho)$. In the case of infinite measurement system bandwidth, the object's Radon transform energy is

$$\mathcal{E}(d,R,1) = \int_0^{\pi} \int_{-\infty}^{\infty} g^2(t,\theta;d,R)\,dt\,d\theta$$

$$= d^2R^3\int_0^{\pi}\int_{-\infty}^{\infty} g^2(t/R,\Theta)dtd\Theta = d^2R^3\int_0^{\pi}\int_{-\infty}^{\infty} g^2(t,\Theta)dtd\Theta \qquad \text{(A6.1)}$$

and since this is the result of a CBP operation evaluated at the origin, it may be written as

$$\mathscr{E}(d,R,1) = d^2R^3\left[f_p \;**\; f_p \;**\; \frac{1}{\|x\|}\right]_0$$

$$= d^2R^3\mathscr{F}_2^{-1}\left\{F_p^2(\rho)\frac{1}{\rho}\right\}_0$$

$$= d^2R^3\int_0^{2\pi}\int_0^{\infty} F_p^2(\rho)d\rho \triangleq d^2R^3\mathscr{E}_0 \qquad \text{(A6.2)}$$

An object formed by applying the eccentricity transformation in (6.2) has Radon transform energy

$$\mathscr{E}(d,R,\lambda) = \int_0^{\pi}\int_{-\infty}^{\infty} g^2(t,\Theta;d,R,\lambda)dtd\Theta$$

$$= d^2R^3\mathscr{F}_2^{-1}\left\{F_p^2\left(\rho\sqrt{\lambda\cos^2\psi + \frac{1}{\lambda}\sin^2\psi}\right)\frac{1}{\rho}\right\}_0$$

$$= d^2R^3\int_0^{2\pi}\int_{-\infty}^{\infty} F_p^2\left(\rho\sqrt{\lambda\cos^2\psi + \frac{1}{\lambda}\sin^2\psi}\right)d\rho\,d\psi$$

$$= d^2R^3\int_0^{2\pi}\int_{-\infty}^{\infty}\left(\lambda\cos^2\psi + \frac{1}{\lambda}\sin^2\psi\right)^{\frac{-1}{2}} d\psi\int_0^{\infty} F_p^2(\rho)d\rho \qquad \text{(A6.3)}$$

where the last line follows by a change of variable. Using (A6.2), and noting that the first integrand in (A6.3) is periodic in $\pi/2$,

$$\mathcal{E}(d,R,\lambda) = d^2R^3q(\lambda)\mathcal{E}_0 \tag{A6.4}$$

where

$$q(\lambda) \triangleq \frac{2}{\pi}\int_0^{\frac{\pi}{2}}\left(\lambda\cos^2\psi + \frac{1}{\lambda}\sin^2\psi\right)^{-\frac{1}{2}} d\psi \tag{A6.5}$$

APPENDIX 7 -- Size, eccentricity and orientation ambiguity function

Consider an initial relative profile $f_p(r,\phi)$ with 2D Fourier transform $F_p(\rho,\psi)$ and Radon transform energy $\mathcal{E}_o$. Let the actual object be the result of scaling, stretching and rotating this profile, followed by multiplication by the known contrast d. The log likelihood function, from (6.12), is

$$a(R,\lambda,\phi;R_a,\lambda_a,\phi_a)$$

$$= \frac{2}{N_0}\int_0^{\pi}\int_{-\infty}^{\infty}\Big[g(t,\theta;d,R_a,\lambda_a,\phi_a)*h(t)\Big]g(t,\theta;d,R,\lambda,\phi)dtd\theta$$

$$- \frac{1}{N_0}\,d^2R^3\mathcal{E}(1,1,\lambda_a)$$

$$\triangleq \frac{\mathcal{E}_a}{N_0}\left[\frac{2}{R_a^3\mathcal{E}(1,1,\lambda_a)}\,\bar{a}(R,\lambda,\phi;R_a,\lambda_a,\phi_a) - \frac{\mathcal{E}(1,1,\lambda)}{\mathcal{E}(1,1,\lambda_a)}\left(\frac{R}{R_a}\right)^3\right] \tag{A7.1}$$

where $\mathcal{E}_a$ is the actual object Radon transform energy in

(6.10) and

$$\bar{a}(R,\lambda,\phi;R_a,\lambda_a,\phi_a)$$

$$= \mathcal{F}_2^{-1}\Big\{ R_a^2 F_p\Big(R_a\rho\sqrt{\lambda_a\cos^2(\psi+\phi_a) + \frac{1}{\lambda_a}\sin^2(\psi+\phi_a)},\phi_a + \arctan(\frac{1}{\lambda_a}\tan\psi)\Big)$$

$$\cdot R^2 F_p\Big(R\rho\sqrt{\lambda\cos^2(\psi+\phi) + \frac{1}{\lambda}\sin^2(\psi+\phi)},\phi + \arctan(\frac{1}{\lambda}\tan\psi)\Big) R_h(\rho)B_\xi(\rho)\Big\}_0$$

(A7.2)

In the case where the aperture function is the sinc function in (3.30) corresponding to a projection spatial bandwidth of W cycles per unit t-direction distance, by a change of variable, the ambiguity function in (A7.1) becomes

$$a(R,\lambda,\phi;R_a,\lambda_a,\phi_a) = \frac{\mathcal{E}_a}{N_0} a^*(\frac{R}{R_a},\lambda,\lambda_a,\phi,\phi_a,R_aW) \tag{A7.3}$$

where

$$a^*(\frac{R}{R_a},\lambda,\lambda_a,\phi;\phi_a,R_aW)$$

$$= \frac{2}{\mathcal{E}(1,1,\lambda_a)}\left(\frac{R}{R_a}\right)^2\int_0^{2\pi}\int_0^{R_aW} F_p\Big(\rho\sqrt{\lambda_a\cos^2(\psi+\phi_a) + \frac{1}{\lambda_a}\sin^2(\psi+\phi_a)},$$

$$\phi_a + \arctan(\frac{1}{\lambda_a}\tan\psi)\Big) F_p\Big(\frac{R}{R_a}\rho\sqrt{\lambda\cos^2(\psi+\phi) + \frac{1}{\lambda}\sin^2(\psi+\phi)},$$

$$\phi + \arctan(\frac{1}{\lambda}\tan\psi)\Big) - \frac{\mathcal{E}(1,1,\lambda)}{\mathcal{E}(1,1,\lambda_a)}\left(\frac{R}{R_a}\right)^3 \tag{A7.4}$$

APPENDIX 8 -- Three-parameter Gaussian object ambiguity function

Substituting the circularly-symmetric Gaussian object Fourier transform into the three-parameter ambiguity function in (6.15), in the limit as $W \to \infty$,

$$a^*\left(\frac{R}{R_a}, \lambda, \lambda_a, \Delta\emptyset, \infty\right)$$

$$= \frac{2\pi^2}{q(\lambda_a)\mathscr{E}_0}\left(\frac{R}{R_a}\right)^2 \int_0^{2\pi}\int_0^{\infty} \exp\left\{-\pi^2\rho^2\left[\lambda_a\cos^2\psi + \lambda\left(\frac{R}{R_a}\right)^2\cos^2(\psi+\Delta\emptyset)\right.\right.$$

$$\left.\left. + \frac{1}{\lambda_a}\sin^2\psi + \frac{1}{\lambda}\left(\frac{R}{R_a}\right)^2\sin^2(\psi+\Delta\emptyset)\right]\right\} d\rho\, d\psi - \frac{q(\lambda)}{q(\lambda_a)}\left(\frac{R}{R_a}\right)^3 \qquad \text{(A8.1)}$$

Making use of the fact that

$$\int_0^{\infty} e^{-a\rho^2} d\rho = \sqrt{\pi}\,/2a \qquad \text{(A8.2)}$$

and noting that the integrand is periodic in π, equation (A8.1) becomes

$$a^*\left(\frac{R}{R_a}, \lambda, \lambda_a, \Delta\emptyset, \infty\right)$$

$$= \frac{2\sqrt{2}}{q(\lambda_a)}\left(\frac{R}{R_a}\right)^2 \left[\frac{1}{\pi}\int_0^{\pi}\left\{\lambda_a\cos^2\psi + \lambda\left(\frac{R}{R_a}\right)^2\cos^2(\psi+\Delta\emptyset)\right.\right.$$

$$\left.\left. + \frac{1}{\lambda_a}\sin^2\psi + \frac{1}{\lambda}\left(\frac{R}{R_a}\right)^2\sin^2(\psi+\Delta\emptyset)\right\}^{-\frac{1}{2}} d\psi\right] - \frac{q(\lambda)}{q(\lambda_a)}\left(\frac{R}{R_a}\right)^3 \qquad \text{(A8.3)}$$

APPENDIX 9 -- Size ambiguity function for an eccentric object

Consider a circularly-symmetric object $f_p(r,\theta)$, denoted in terms of its radial polar coordinate as f(r) with Radon transform energy $\mathcal{E}_o$; the 2D Fourier transform, $F_p(\rho,\psi)$ is also circularly-symmetric, and is denoted in terms of its radial polar coordinate as $F(\rho)$. In the limit as the measurement system bandwidth goes to infinity, the size ambiguity function in (6.21) is given by

$$a^*\left(\frac{R}{R_a},\infty\right) = \frac{4\pi}{\mathcal{E}_0}\left(\frac{R}{R_a}\right)^2\int_0^\infty F(\rho)F\left(\frac{R}{R_a}\rho\right)d\rho - \left(\frac{R}{R_a}\right)^3 \qquad \text{(A9.1)}$$

An object obtained from f(r) by applying the eccentricity transformation in (6.2) has Radon transform energy $\mathcal{E}_o q(\lambda)$ and by (6.2b), has the 2D Fourier transform

$$F\left(\rho\sqrt{\lambda\cos^2\psi + \frac{1}{\lambda}\sin^2\psi}\right)$$

and by (6.21) has size ambiguity function

$$a_\lambda^*\left(\frac{R}{R_a},\infty\right) = \frac{2}{q(\lambda)\mathcal{E}_0}\left(\frac{R}{R_a}\right)^2\int_0^{2\pi}\int_0^\infty F\left(\rho\sqrt{\lambda\cos^2\psi + \frac{1}{\lambda}\sin^2\psi}\right)$$

$$\cdot F\left(\frac{R}{R_a}\rho\sqrt{\lambda\cos^2\psi + \frac{1}{\lambda}\sin^2\psi}\right)d\rho d\psi - \left(\frac{R}{R_a}\right)^3 \qquad \text{(A9.2)}$$

By a change of variable and the definition of $q(\lambda)$ in (6.6),

$$a_\lambda^*\left(\frac{R}{R_a},\infty\right)$$

$$= \frac{2}{q(\lambda)\mathscr{E}_0}\left(\frac{R}{R_a}\right)^2 \int_0^{2\pi} \left(\lambda\cos^2\psi + \frac{1}{\lambda}\sin^2\psi\right)^{-\frac{1}{2}} d\psi \int_0^\infty F(\rho)F\left(\frac{R}{R_a}\rho\right) d\rho - \left(\frac{R}{R_a}\right)^3$$

$$= \frac{4\pi}{0}\left(\frac{R}{R_a}\right)^2 \int_0^\infty F(\rho)F\left(\frac{R}{R_a}\rho\right) d\rho - \left(\frac{R}{R_a}\right)^3 = a^*\left(\frac{R}{R_a},\infty\right)$$

(A9.3)

The eccentric object size ambiguity function, then, is the same as that for the circularly-symmetric object.

APPENDIX 10 -- Cramer-Rao bound for size estimation

The Cramer-Rao bound for the size estimation problem is obtained by taking two partial derivatives of the ambiguity function in (6.20); taking two derivatives and evaluating the result for $R = R_a$ (for the local error variance), one obtains

$$\left.\frac{\partial^2 a(R,R_a)}{\partial R^2}\right|_{R=R_a} = (2d^2R_a/N_0)\left\{-3\mathscr{E}_0 \right.$$

$$\left. + \int_0^{2\pi}\int_0^{R_aW} F_p(\rho,\psi)\left[2F_p(\rho,\psi) + 4\rho F_p'(\rho,\psi) + \rho^2 F_p''(\rho,\psi)\right] d\rho d\psi \right\}$$

$$\triangleq (2d^2R_a/N_0)\left\{-3\mathscr{E}_0 + \gamma(R_aW)\right\}$$

(A10.1)

and the Cramer-Rao bound is given by

$$\sigma_R^2 \geq \frac{N_0}{2d^2[3\mathscr{E}_0 - \gamma(R_a W)]R_a} \qquad \text{(A10.2)}$$

APPENDIX 11 -- Gaussian object eccentricity Cramer-Rao bound

The Cramer-Rao bound for the Gaussian object eccentricity estimation problem is obtained by taking two partial derivatives of $\mathscr{E}_a/N_o$ times the ambiguity function in (6.36); taking two derivatives with respect to λ, and evaluating the result for $\lambda = \lambda_a$ provides

$$\frac{\mathscr{E}_a}{N_0} \left.\frac{\partial^2 a^*(\lambda, \lambda_a, \infty)}{\partial \lambda^2}\right|_{\lambda=\lambda_a} = (-3\mathscr{E}_a/4\pi q(\lambda_a)N_0)$$

$$\cdot \int_0^{\frac{\pi}{2}} (\lambda_a \cos^2\psi + \frac{1}{\lambda_a}\sin^2\psi)^{-\frac{5}{2}} (\cos^2\psi - \frac{1}{\lambda_a^2}\sin^2\psi)\, d\psi \qquad \text{(A11.1)}$$

The eccentricity Cramer-Rao bound, then, is given by

$$\sigma_\lambda^2 \geq (8N_0/3\mathscr{E}(d, R, 1))$$

$$\cdot \left\{ \frac{2}{\pi} \int_0^{\frac{\pi}{2}} (\lambda_a \cos^2\psi + \frac{1}{\lambda_a}\sin^2\psi)^{-\frac{5}{2}} (\cos^2\psi - \frac{1}{\lambda_a^2}\sin^2\psi)^2\, d\psi \right\}^{-1} \qquad \text{(A11.2)}$$

where equation (6.14) has been used to obtain the last equality.

APPENDIX 12 -- Gaussian object orientation Cramer-Rao bound

The Gaussian object orientation Cramer-Rao bound is obtained by taking two partial derivatives of $\mathscr{E}_a/N_o$ times the normalized ambiguity function in (6.41); taking two partial derivatives with respect to $\Delta\phi$, and evaluating the result at $\Delta\phi = 0$ provides

$$\frac{\mathscr{E}_a}{N_0} \left.\frac{\partial^2 a^*(\Delta\phi,\lambda_a,\infty)}{\partial\Delta\phi^2}\right|_{\Delta\phi=0}$$

$$= (-3\mathscr{E}_a/8q(\lambda_a)N_0)\left(\frac{1}{\lambda_a} - \lambda_a\right)^2 \left[\frac{2}{\pi}\int_0^{\frac{\pi}{2}} u(\lambda_a,\psi)^{-\frac{5}{2}} \sin^2 2\psi d\psi\right]$$

$$- (\mathscr{E}_a/q(\lambda_a)N_0)\left(\frac{1}{\lambda_a} - \lambda_a\right)\left[\frac{2}{\pi}\int_0^{\frac{\pi}{2}} u(\lambda_a,\psi)^{-\frac{3}{2}} \cos 2\psi d\psi\right] \qquad \text{(A12.1)}$$

where

$$u(\lambda,\psi) \triangleq \lambda\cos^2\psi + \frac{1}{\lambda}\sin^2\psi \qquad \text{(A12.2)}$$

The orientation Cramer-Rao bound, then, is given by

$$\sigma_\phi^2 \geq$$

$$[N_0/\mathscr{E}(d,R,1)]\left\{\frac{3}{8}\left(\frac{1}{\lambda_a} - \lambda_a\right)^2 \left[\frac{2}{\pi}\int_0^{\frac{\pi}{2}} u(\lambda_a,\psi)^{-\frac{5}{2}} \sin^2 2\psi d\psi\right]\right.$$

$$\left. + \left(\frac{1}{\lambda_a} - \lambda_a\right)\left[\frac{2}{\pi}\int_0^{\frac{\pi}{2}} u(\lambda_a,\psi)^{-\frac{3}{2}} \cos 2\psi d\psi\right]\right\}^{-1} \qquad \text{(A12.3)}$$

where equation (6.14) has been used to obtain the last equality.

CHAPTER 7

CONCLUSIONS AND FURTHER DIRECTIONS

7.0 CONCLUSIONS

In this thesis we have described a method for utilizing a priori information directly in an inverse problem. In particular, we have explored the problem of object-based reconstruction of a two-dimensional medium from noisy projection measurements. As discussed in Chapter 1, the direct utilization of a priori information offers the potential for significant improvements in applications where (1) attempts to perform direct inversion result in severely degraded reconstructions and (2) the ultimate goal of the processing is to obtain specific pieces of information concerning the cross-section, rather than simply a reconstruction. We have focused our attention in this thesis on the single-object problem in order to obtain insight into the structure, performance and robustness of object parameter estimation procedure, and to demonstrate the nature and viability of our approach.

In Chapter 2, a probabilistic object-based field model was developed and used in formulating a finite-dimensional maximum likelihood estimation problem for the object parameters. Two special cases of this

general N-object problem were studied, namely the single object location estimation problem (in Chapters 3 through 5) and the single object geometry estimation problem (in Chapter 6).

In Chapters 3 and 4, the performance of the single object localization problem was analyzed. It was shown that the log likelihood function for the object location coordinates is evaluated by a convolution back-projection operation, and this fact was exploited in developing a frequency-domain approach to the evaluation of the Cramer-Rao bound for the local estimate error covariance. Also, the ambiguity function for the object localization problem was calculated, and was used in characterizing global estimation errors.

In Chapter 4, the performance analysis developed in Chapter 3 was applied to the problem of locating a single pillbox object using full-view measurements. In this chapter, it was demonstrated that for a fixed value of object contrast and noise spectral level, there exists a minimum value of object size (as illustrated in Figure 4.4) for which objects can be estimated reliably. Other measurement scanning geometries and the Gaussian object profile were also investigated in Chapter 4, and image representations of the log likelihood function and images reconstructed using conventional methods were presented

and discussed.

In Chapter 5, we investigated the robustness of the single object localization procedure to several types of modeling errors. In particular, object size and shape modeling errors were studied, as was the presence of one or more unmodeled objects in the cross-section. The results of Chapter 5 indicate that the single object localization problem is quite robust to both geometry modeling errors and the presence of smaller unmodeled objects.

The problem of determining the geometry of a single object was investigated in Chapter 6. In this chapter, the geometry of an object was characterized by size, eccentricity and orientation parameters. This is a simple parameterization of object geometry that has a small number of degrees of freedom and its use, together with the analytical tools developed in Chapter 6, allowed us to develop insight into the problem of geometry estimation from projections. In Chapter 6, it was shown that the size and orientation parameters can be estimated reliably (orientation estimation accuracy improves with object elongation, as shown in Figures 6.8 and 6.9), even in the presence of certain types of modeling errors, as discussed in Section 6.3. Eccentricity was shown to require a comparatively high SNR to estimate accurately (see Figure

6.6). These results, as well as those obtained in previous chapters, led directly to the determination of a useful structure for an iterative algorithm for recursive location and geometry estimation; this topic was discussed in the conclusion to Chapter 6.

Collectively, the results obtained in this thesis indicate that object-based signal processing is a potentially valuable approach to certain types of problems involving reconstruction from projections. In particular, object-based reconstruction appears to be especially attractive for problems where (1) the measurements are of limited quantity, view angle, and/or quality (SNR) and (2) the ultimate goal of the signal processing is to extract specific pieces of object-related information about the cross-section.

7.1 FURTHER DIRECTIONS

In this thesis, we have developed a framework for addressing the problem of object-based reconstruction from projections; there are a variety of open problem areas that may be investigated in this framework. These include:

1) Implementation and algorithmic issues -- in this thesis, we have not considered the implementation of ML object localization algorithms or of the iterative algorithm described in Chapter 6; also, we have not examined algorithmic issues such as efficient procedures for locating the log likelihood function peak.

2) Multiple object fields -- with the exception of a discussion regarding robustness to the presence of unmodeled objects, we have concentrated exclusively on the single object problem. Interesting questions arise in the consideration of the multiple object problem, particularly with regard to the geometric relationships between the measurement scanning geometry and the object locations and geometries. It appears that the framework developed (and the insights obtained) in the single object problem will be valuable in the study of the multiple object problem. One intriguing approach to the multiple object problem is via analysis in Radon space -- the multiple object problem may be pursued by identifying and characterizing the multiple cosinusoidal "tracks" along which energy is distributed in Radon space.

3) Applications -- in this thesis we have made reference to a number of applications for which the framework we have developed is potentially useful, for example detecting flaws in materials in quality-control nondestructive testing, or locating and characterizing Gulf-stream cold-core rings in oceanography. The application of the ideas and techniques of this thesis to a specific practical problem would serve to expose other issues that need to be considered to make our approach practical.

4) Other field and measurement models -- in Appendix 5, we developed an expression for the Radon transform of an indicator function on a convex set, but we did not pursue geometry estimation using this particular parameterization. (which may prove useful in estimating boundary details in certain reconstruction problems) Also, an area we have not investigated, but which represents an interesting extension of the framework developed in this thesis, is measurement models other than integrals taken along straight lines; for example, models incorporating refraction and diffraction. In fact, for some particular applications, e.g. ultrasound probing of a medium, it may very well be necessary to employ more complex measurement models in order to avoid excessive modeling errors.

5) The application of model-based signal processing to other inverse problems -- the framework developed in this thesis led to extensive insights and to a potentially useful approach to one particular inverse problem, by focusing on modeling and identifying structural features of the field under investigation. A similar approach applied to other inverse problems, particularly those that are ill-posed or poorly conditioned, may provide valuable insights and/or a fruitful approach to their solution.

REFERENCES

Anastassiou, D., D.J. Sakrison. 1981. A probability model for simple closed random curves. IEEE Trans. Inform. Theory IT-27:376-381.

Backus, R.H., G.R. Flierl, D.R. Kester, D.B. Olson, P.L. Richardson, A.C. Vastano, P.H. Wiebe, J.H. Wormuth. 1981. Gulf Stream cold-core rings: their physics, chemistry, and biology. Science 212:1091-1100.

Belanger, M.G., W.A. Yasnoff, R.D. Penn, J.W. Bacus. 1979. Automated scene analysis of CT scans. Computerized Tomography 3:201-211.

Benson, R.V. 1966. Euclidean geometry and convexity. McGraw Hill, New York.

Bracewell, R. 1956. Two-dimensional aerial smoothing in radio astronomy. Aust. J. Phys. 9:297-314.

Bracewell, R. 1965. The Fourier transform and its applications. McGraw-Hill, New York.

Brownell, G.L., C.A. Burnham, D.A. Chesler, J.A. Correia, J.E. Correll, B. Hoop, Jr., J.A. Parker, R. Subramanyam. 1977. Transverse section imaging of radionuclide distributions in heart, lung, and brain. In: Reconstruction tomography in diagnostic radiology and nuclear medicine, M.M. Ter-Pogossian, M.E. Phelps, G.L. Brownell, J.R. Cox, Jr., D.O. Davis, R.G. Evans, eds. University Park Press, Baltimore, 293-307.

Cho, Z.H., J. Burger. 1977. Construction, restoration, and enhancement of 2- and 3-dimensional images. IEEE Trans. Nucl. Sci. NS-24:886-899.

Chu, P.L., C. Saekeang. 1979. Nondestructive determination of refractive-index profile and cross-sectional geometry of optical-fibre preform. Electron. Lett. 15:635-637.

Cooper, D.B., H. Elliott, F. Cohen, L. Reiss, P. Symosek. 1980. Stochastic boundary estimation and object recognition. Computer Graphics and Image Processing. 12:326-356.

Cormack, A. 1963. Representation of a function by its line integrals, with some radiological applications. J. Appl. Phys. 34:2722-2727.

Cormack, A. 1964. Representation of a function by its line integrals, with some radiological applications, II. J. Appl. Phys. 35:2908-2913.

Das, Y., W.M. Boerner. 1978. On radar target shape estimation using algorithms for reconstruction from projections. IEEE Trans. Antennas Propogat. AP-26:274-279.

Davison, M.E., F.A. Grunbaum. 1981. Tomographic reconstruction with arbitrary directions. Comm. in Pure and Appl. Math. 34:77-120.

Dennis, M.J., R.G. Waggener, W.D. McDavid, W.H. Payne, V.J. Sank. 1977. Preprocessing x-ray transmission data in CT scanning. Optical Engineering 16:6-10.

Denton, R.V., A.J. Rockmore, B. Friedlander, J.S. Malin. 1978. An image reconstruction approach to target association. Proc. 12th Asilomar Conf. on Circuits, Systems, and Computers 304-308.

DeRosier, D., P. Moore. 1970. Reconstruction of three-dimensional images from electron micrographs of structures with helical symmetry. J. Molec. Biol. 52:355-369.

Dines, K.A., R.J. Lytle. 1979. Computerized geophysical tomography. Proc. IEEE 67:1065-1073.

Elliott, H., L. Srinivasan. 1981. An application of dynamic programming to sequential boundary estimation. Colorado State University Technical Report AP81-DELENG-1.

Gallager, R.G., C.W. Helstrom. 1969. A bound on the probability that a Gaussian process exceeds a given function. IEEE Trans. Inform. Theory IT-15:163-166.

Galvin, J.M., B.E. Bjarngard. 1975. A defence of Johann Radon. Phys. Med. Biol. 20:839-343.

Glover, G.H., J.C. Sharp. 1977. Reconstruction of ultrasound propagation speed distributions in soft tissue: time-of-flight tomography. IEEE Trans. Sonics Ultras. SU-24:229-234.

Gordon, R. 1973. Artifacts in reconstructions made from a few projections. Proc. First Int. Joint Conf. on Pattern Recog. 275-285.

Gordon, R. 1974. A tutorial on ART (algebraic reconstruction techniques). IEEE Trans. Nucl. Sci. NS-21:78-93.

Greenleaf, J.F., S.A. Johnson, A.H. Lent. 1978. Measurement of spatial distribution of refractive index in tissues by ultrasonic computer assisted tomography. Ultras. Med. Biol. 3:327-339.

Gullberg, G.T., T.F. Budinger. 1981. The use of filtering methods to compensate for constant attenuation in single-photon emission computed tomography. IEEE Trans. Biomed. Eng. BME-28:142-157.

Hanson, K.M. 1978. Detectability in the presence of computed tomographic reconstruction noise. Proc. SPIE 127, Medicin VI, 304-312.

Herman, G. 1973. ART: mathematics and applications. J. Theor. Biol. 42:1-32.

Herman, G., A. Lent. 1976. A computer implementation of a Bayesian analysis of image reconstruction. Info. and Control 31:364-384.

Hildebrand, B.P., T.P. Harrington. 1981. Mapping of materials stress with ultrasonic tomography. Materials Evaluation 39:383-390.

Hildebrand, F.B. 1976. Advanced Calculus for Applications. Prentice-Hall, New Jersey.

Horn, B.K.P. 1978. Density reconstruction using arbitrary ray-sampling schemes. Proc. IEEE 66:551-562.

Hounsfield, G.N. 1973. Method and apparatus for measuring X or γ-radiation absorption or transmission at plural angles and analyzing the data. U.S. Patent 3 778 614, 11 Dec 1973.

Kashyap, R., M. Mittal. 1973. Picture reconstruction from projections. Proc. First Int. Joint Conf. on Pattern Recog. 286-292.

Kelly, P.J., M.L. Weiss. 1979. Geometry and convexity -- a study in mathematical methods. John Wiley and Sons, New York.

Klyuev, V.V., E.I. Vainberg, I.A. Kazek, V.P. Kurozaev. 1980. Computational tomography - a new radiation method of nondestructive testing, I, II. Soviet J. Nondestr. Testing 16:180-185,186-193.

Kowalski, G. 1979. Multislice reconstruction from twin-cone beam scanning. IEEE Trans. Nucl. Sci. NS-26:2895-2903.

Krishnamurthy, E.V., T. Mahadeva Rao, K. Subramanian, S.S. Prabhu. 1974. Reconstruction of objects from their projections using generalized inverses. Comp. Graphics and Image Proc. 3:336-345.

Lakshminarayanan, A.V. 1975. Reconstruction from divergent ray data. Dept. Computer Science, State Univ. New York, Buffalo Tech. Rep. TR-92.

Ledsham, W.H., D.H. Staelin. 1978. An extended Kalman-Bucy filter for atmospheric temperature profile retrieval with a passive microwave sounder. J. Appl. Meteor. 17:1023-1033.

Lyusternik, L.A. 1963. Convex figures and polyhedra. Dover Publications, New York.

McKinnon, G.C., R.H.T. Bates. 1981. Towards imaging the beating heart usefully with a conventional CT scanner. IEEE Trans. Biomed. Eng. BME-28:123-127.

Mersereau, R.M., A.V. Oppenheim. 1974. Digital reconstruction of multidimensional signals from their projections. Proc. IEEE 62:1319-1338.

Morris, R.A., R.P. Kruger, G.W. Wecksung. 1979. Tomographic detection of cracks in reactor piping. 39th National ASNT Fall Conference, St. Louis 15-18 Oct 1979.

Munk, W., C. Wunsch. 1979. Ocean acoustic tomography: a scheme for large scale monitoring. Deep Sea Research 26A:123-161.

Radcliff, R.D., C.A. Balanis. 1979. Reconstruction algorithms for geophysical applications in noisy environments. Proc. IEEE 67:1060-1064.

Radon, J. 1917. Uber die Bestimmung von Funktionen durch ihre Integralwarte langes Gewisser Mannigfaltigkeiten (On the determination of functions from their integrals along certain manifolds). Ber. Verk. Sachs. Akad. 69:262-277.

Riederer, S.J., N.J. Pelc, D.A. Chesler. 1978. The noise power spectrum in computed x-ray tomography. Phys. Med. Biol. 23:446-454.

Rockmore, A.J. 1980. Multi-array surveillance processing using image reconstruction. IEEE Conf. Record of the Fourteenth Asilomar Conf. on Circuits, Systems, and Computers, 119-123.

Rockmore, A.J., R.V. Denton, B. Friedlander. 1979. Direct three-dimensional image reconstruction. IEEE Trans. Antennas Propagat. AP-27:239-241.

Rockmore, A.J., Macovski, A. 1976. A maximum likelihood approach to transmission image reconstruction from projections. Ph.D. disseration Stanford Univ., Stanford, CA.

Rohler, D., P.S. Krishnaprasad. 1981. Radon inversion and Kalman reconstructions: a comparison. IEEE Trans. Automat. Contr. AC-26:483-487.

Rowland, S.W. 1979. Computer implementation of image reconstruction formulas. Chapter 2 in Image reconstruction from projections. Implementation and applications (Topics in applied physics; v. 32). Ed. G.T. Herman. Springer-Verlag, New York.

Santalo, L.A. 1976. Integral geometry and geometric probability. Encyclopedia of mathematics and its applications I. Addison-Wesley, Reading, MA.

Selfridge, P.G., J.M.S. Prewitt. 1981. Organ detection in abdominal computerized tomography scans: application to the kidney. Comp. Graphics and Image Proc. 15:265-278.

Shepp, L.A., B.F. Logan. 1974. The Fourier reconstruction of a head section. IEEE Trans. Nucl. Sci. NS-21:21-43.

Snyder, D.L., J.R. Cox. 1977. An overview of reconstructive tomography and limitation imposed by a finite number of projections. In: Reconstructive tomography in diagnostic radiology and nuclear medicine. Univ. Park Press, Baltimore, 3-32.

Spindel, R.C. 1979. An underwater acoustic pulse compression system. IEEE Trans. Acoust., Speech, Signal Processing ASSP-27:723-728.

Stark, H., J.W. Woods, I. Paul, R. Hingorani. 1981. An investigation of computerized tomography by direct Fourier inversion and optimum interpolation. IEEE Trans. Biomed. Eng. BME-28:496-505.

Sweeney, D.W., C.M. Vest. 1973. Reconstruction of three-dimensional refractive index fields from multidirectional interferometric data. Appl. Optics 12:2649-2664.

Tasto, M. 1974. A probabalistic object model for computerized transverse axial tomography. Proc. Second Int. Joint Conf. on Pattern Recog. 396-400.

Tasto, M. 1976. Maximum likelihood reconstruction of random objects from noisy objects. Proc. Third Int. Joint Conf. on Pattern Recog. 551-553.

Van Trees, H.L. 1968. Detection, estimation, and modulation theory, part I. John Wiley and Sons, New York.

Van Trees, H.L. 1971. Detection, estimation, and modulation theory, Part III, Radar-sonar signal processing and Gaussian signals in noise. John Wiley and Sons, New York.

Vest, C.M., P.T. Radulovic. 1977. Measurement of three-dimensional temperature fields by holographic interferometry. In Proc. of the Intl. Conf. on Appl. of Holography and Optical Processing. Ed. E. Marom, A.A. Friesem, E. Wiener-Avnear. Pergamon Press, New York.

Willsky, A.S., H.S. Jones. 1976. A generalized likelihood ratio approach to the detection and estimation of jumps in linear systems. IEEE Trans. Aut. Control AC-21:108-112.

Wood, S.L., M. Morf. 1981. A fast implementation of a minimum variance estimator for computerized tomography image reconstruction. IEEE Trans. Biomed. Eng. BME-28:56-68.